UNCLASSIFIED

AD NUMBER
AD385910
CLASSIFICATION CHANGES
TO: unclassified
FROM: confidential
LIMITATION CHANGES
TO: Approved for public release, distribution unlimited
FROM: Distribution authorized to U.S. Gov't. agencies and their contractors; Administrative/Operational Use; DEC 1967. Other requests shall be referred to Air Force Rocket Propulsion Laboratory, Attn: Rppr-Stinfo] Edwards AFB, CA 93523.
AUTHORITY
31 dec 1979 DoDD 5200.10; AFRPL LTR 5 FEB 1986

THIS PAGE IS UNCLASSIFIED

GENERAL DECLASSIFICATION SCHEDULE

IN ACCORDANCE WITH
DOD 5200.1-R & EXECUTIVE ORDER 11652

THIS DOCUMENT IS:

CLASSIFIED BY_____

Subject to General Declassification Schedule of Executive Order 11652-Automatically Downgraded at 2 Years Intervals-DECLASSIFIED ON DECEMBER 31,____.

BY

Defense Documentation Center
Defense Supply Agency
Cameron Station
Alexandria, Virginia 22314

THIS REPORT HAS BEEN DELIMITED
AND CLEARED FOR PUBLIC RELEASE
UNDER DOD DIRECTIVE 5200.20 AND
NO RESTRICTIONS ARE IMPOSED UPON
ITS USE AND DISCLOSURE.

DISTRIBUTION STATEMENT A

APPROVED FOR PUBLIC RELEASE;
DISTRIBUTION UNLIMITED.

SECURITY MARKING

The classified or limited status of this report applies to each page, unless otherwise marked.
Separate pages printouts MUST be marked accordingly.

THIS DOCUMENT CONTAINS INFORMATION AFFECTING THE NATIONAL DEFENSE OF THE UNITED STATES WITHIN THE MEANING OF THE ESPIONAGE LAWS, TITLE 18, U.S.C., SECTIONS 793 AND 794. THE TRANSMISSION OR THE REVELATION OF ITS CONTENTS IN ANY MANNER TO AN UNAUTHORIZED PERSON IS PROHIBITED BY LAW.

NOTICE: When government or other drawings, specifications or other data are used for any purpose other than in connection with a definitely related government procurement operation, the U. S. Government thereby incurs no responsibility, nor any obligation whatsoever; and the fact that the Government may have formulated, furnished, or in any way supplied the said drawings, specifications, or other data is not to be regarded by implication or otherwise as in any manner licensing the holder or any other person or corporation, or conveying any rights or permission to manufacture, use or sell any patented invention that may in any way be related thereto.

Best
Available
Copy

5476 2550-A
RDD SUB-CONTROL STA. 92

PATENT SECRECY NOTICE

Material in this publication relating to
RADIAL CERAMIC INSERTION, LAMINATED
CHAMBER COOLING MEANS, and A VARIABLE
AREA INJECTION ORIFICE

reveals subject matter contained in U.S. Patent Application Serial Nos. 426,711, 319,047, and 390,521 entitled "Rocket Injector," "High Pressure Rocket and Cooling Means" and "Controllable Injector for Rockets," respectively, which have been placed under Secrecy Orders issued by the Commissioner of Patents. These Secrecy Orders have been modified by SECURITY REQUIREMENTS PERMITS and a PERMIT "A", respectively.

A Secrecy Order prohibits publication or disclosure of the invention, or any material information with respect thereto. It is separate and distinct, and has nothing to do with the classification of Government contracts.

By statute, violation of a Secrecy Order is punishable by a fine not to exceed $10,000 and/or imprisonment for not more than two years.

A SECURITY REQUIREMENTS PERMIT authorizes disclosure of the invention or any material information with respect thereto, to the extent set forth by the security requirements of the Government contract which imposes the highest security classification on the subject matter of the application, except that export is prohibited.

A PERMIT "A" authorizes disclosure of the subject matter of the patent application to any person of the classes hereinafter specified if such person is known to be concerned directly in an official capacity with the subject matter, provided that all reasonable safeguards are taken to otherwise protect the invention from unauthorized disclosure. The specified classes are:

(a) Any officer or employee of any department, independent agency, or bureau of the Government of the United States.

(b) Any person designated specifically by the head of any department, independent agency or bureau of the Government of the United States, or by his duly authorized subordinate, as a proper individual to receive the disclosure of the above indicated application.

A PERMIT "A" also authorizes disclosure to the minimum necessary number of persons of known loyalty and discretion, employed by or working with United Aircraft Corporation or its licensees and whose duties involve cooperation in the development, manufacture or use of the subject matter by or for the Government of the United States, provided such persons are advised of the issuance of the Secrecy Order.

Disclosure of these inventions or any material information with respect thereto is prohibited except by written consent of the Commissioner of Patents or as authorized by the respective permits.

The foregoing does not in any way lessen responsibility for the security of the subject matter as imposed by any Government contract or the provisions of the existing laws relating to espionage and national security.

AD 385910

(UNCLASSIFIED TITLE)

ADVANCED CRYOGENIC ROCKET ENGINE PROGRAM STAGED-COMBUSTION CONCEPT

FINAL REPORT

R. R. ATHERTON

PRATT & WHITNEY AIRCRAFT
DIVISION OF UNITED AIRCRAFT CORPORATION
FLORIDA RESEARCH AND DEVELOPMENT CENTER

TECHNICAL REPORT AFRPL-TR-67-298-VOL I
DECEMBER 1967

DECLASSIFIED AFTER 12 YEARS, DOD DIR. 5200.10

PATENT SECRECY NOTICE

PORTIONS OF THIS DOCUMENT CONTAIN SUBJECT MATTER COVERED BY A U.S. PATENT OFFICE SECRECY ORDER WITH MODIFYING SECURITY REQUIREMENTS PERMIT AND MODIFYING PERMIT "A". HANDLING SHALL BE IN ACCORDANCE WITH THE PERMIT AS DESCRIBED ON PAGE A AND INDICATED HEREIN. VIOLATORS MAY BE SUBJECT TO THE PENALTIES PRESCRIBED BY TITLE 35, U. S. C. (1952), SECTIONS 186 AND 190.

THIS DOCUMENT CONTAINS INFORMATION AFFECTING THE NATIONAL DEFENSE OF THE UNITED STATES WITHIN THE MEANING OF THE ESPIONAGE LAWS, TITLE 18 U. S. C., SECTIONS 793 AND 794. ITS TRANSMISSION OR THE REVELATION OF ITS CONTENTS IN ANY MANNER TO AN UNAUTHORIZED PERSON IS PROHIBITED BY LAW.

UNCLASSIFIED

Best Available Copy

COPIES OF AFRPL REPORTS MAY BE OBTAINED FROM
Edwards, Calif. 93523

FOREWORD

This final report describes the Phase I program for A High Performance Cryogenic Staged-Combustion Rocket Engine conducted during the period 1 March 1966 to 30 September 1967, and is submitted in accordance with the requirements of Contract AF 04(611)-11401.

This publication was prepared by the Pratt & Whitney Aircraft Florida Research and Development Center as report PWA FR-2597.

This report contains no classified information extracted from other classified documents.

This Technical Report has been reviewed and is approved.

Robert E. Probst
Captain, USAF
Project Engineer
Air Force Rocket Propulsion Laboratory

Ernie D. Braunschweig
Captain, USAF
Program Manager
Air Force Rocket Propulsion Laboratory

UNCLASSIFIED ABSTRACT

Phase I of the Advanced Development Program for a High Performance Oxygen/Hydrogen Rocket Engine, which was sponsored by the Air Force Rocket Propulsion Laboratory at Pratt & Whitney Aircraft, was an evaluation of the critical technology associated with the staged-combustion bell nozzle engine system. Experimental evaluation was conducted in the areas of preburner, main chamber, nozzle, turbopump bearings, and engine controls. In addition, engine system (module) preliminary design and applications studies were conducted. In the Module Design Study, a system cycle balance, steady-state off-design analyses, transient analyses, component and system design studies, a weight study, and a parametric engine study were completed. The Applications Study was completed, and a separate final report, AFRPL-TR-67-270, was issued. Under the Cooling Investigation, 50K staged combustion tests were conducted that demonstrated high impulse efficiency and the two-position translating nozzle. Under the Turbopump Components investigation, endurance testing of the hydrogen turbopump bearing demonstrated long life is feasible, but roller skewing remains a significant problem. Under the Module Control System investigation, the oxidizer flow divider valve, the mixture ratio valve, and ignition systems were designed, manufactured, and tested with the preburner and main burner. Continued development is needed to improve seal performance. The Preburner Demonstration investigation was completed, and ignition, control, and dynamic combustion stability were demonstrated; however, additional development is required to reduce the hot gas temperature profile. Under the 250K Staged Combustion investigation, the 250K main chamber was tested, and the performance and feasibility of the full-scale tandem concept, including the two-position nozzle and dynamic combustion stability, was demonstrated at various thrust levels.

CONTENTS

SECTION		PAGE
	ILLUSTRATIONS	
	TABLES	
	LIST OF ABBREVIATIONS AND SYMBOLS	
I	INTRODUCTION	1
II	SUMMARY	5
III	CONCLUSIONS AND RECOMMENDATIONS	7
	A. Module Design Studies	7
	B. Applications Studies	8
	C. Cooling Investigation	8
	D. Turbopump Components	8
	E. Control System	9
	F. Preburner	9
	G. Staged Combustion	10
IV	MODULE DESIGN	11
	A. Introduction	11
	B. Summary	11
	C. Configuration Analysis	13
	1. Demonstrator Engine Analysis	13
	2. Flight Engine and Parametric Performance Data	92
	3. Dual-Preburner Cycle Study	104
V	APPLICATIONS STUDY	117
VI	COOLING INVESTIGATION	123
	A. Introduction	123
	B. Summary and Conclusions	123
	1. Summary	123
	2. Conclusions	124
	C. Hardware Description	125
	D. Test Program and Test Results	149
	1. Introduction	149
	2. Combustion Performance	152
	3. Uncooled Testing	156
	4. Cooled Testing	161
	5. Two-Position Nozzle Testing	168

CONTENTS (Continued)

SECTION		PAGE
	E. Heat Transfer Studies and Materials Evaluation.	172
	1. Introduction.	172
	2. Grooved Wafer Analytical Heat Transfer Model.	175
	3. Rigimesh Analytical Heat Transfer Model	185
	4. Material Evaluation	185
	5. Cooled Convergent Tests Sections. . . .	190
	F. Test Facilities and Procedures.	192
	1. B-2B Test Facility.	192
	2. 50K Test Procedures	193
VII	TURBOPUMP COMPONENTS.	199
	A. Introduction.	199
	B. Summary and Conclusions	199
	C. Hardware Description.	200
	1. Bearing Test Rig.	200
	2. Bearing Configuration Selection	201
	D. Test Program and Test Results	212
	1. Cage Spin Testing	212
	2. Cage and Bearing Geometry Screening . .	217
	3. Endurance Tests	236
	E. Test Facility and Procedures.	244
	1. Test Facility	244
	2. Test Procedures	244
VIII	MODULE CONTROL SYSTEM	247
	A. Introduction and Summary	247
	B. Mixture Ratio Valve and Seal Rig.	248
	1. Hardware Description.	248
	2. Test Program and Test Results	284
	3. Test Facilities and Procedures.	347
	4. Conclusions	352

CONTENTS (Continued)

SECTION		PAGE
	C. Flow Divider Valve and Seal Rig.	354
	1. Hardware Description	354
	2. Test Program and Test Results.	392
	3. Test Facilities and Procedures	435
	4. Conclusions.	440
	D. Thrust Control	441
	1. Hardware Description	441
	E. Chamber Coolant Valve and Seal Rig	468
	1. Hardware Description	468
	2. Design of Selected Configuration	471
	3. Test Program and Test Results.	474
	4. Summary and Conclusions.	486
	F. Electrical Ignition Systems	486
	1. Hardware Description	486
IX	PREBURNER DEMONSTRATION.	497
	A. Introduction	497
	B. Summary and Conclusions.	500
	C. Hardware Description	504
	D. Testing.	529
	1. Facility Checkout	529
	2. Preburner Torch Igniter Testing. . . .	531
	3. Preburner Testing.	537
	E. Facilities and Procedures.	599
X	250K STAGED COMBUSTION	603
	A Introduction	603
	B. Summary and Conclusions.	603
	1. Summary.	603
	2. Conclusions.	603
	C. 250K Staged-Combustion Hardware Description.	604
	D. Test Program and Test Results.	617
	1. Introduction	617
	2. Staged-Combustion Performance.	621
	3. Preburner Tests.	621

CONTENTS (Continued)

SECTION		PAGE
	4. Main Chamber Coolant Optimization and Performance Tests	621
	5. Two-Position Nozzle	637
	6. Main Chamber Combustion Stability Tests	637
E.	Test Facilities and Procedures	645
	1. Test Facilities	645
	2. 250K Test Procedures	648
APPENDIX I -	Acceleration Load Analysis	651
APPENDIX II -	A Simulation for Controls Study of the Advanced Cryogenic Rocket Engine	655
A.	Introduction	655
B.	Engine Cycle Description	655
	1. Fuel Pump Discharge Valve	658
	2. Preburner Fuel Injector Control	658
	3. Dump Coolant Control	658
	4. Preburner Oxidizer Flow Divider Valve	658
	5. Main Chamber Oxidizer Control	659
	6. Oxidizer Inducer Turbine Area Control	659
	7. Engine Operating Limits	659
C.	Analog Simulation	660
	1. General	660
	2. Equations, Constants, and Functions	660
D.	Equation Assumptions and Bases	690
	1. Fluid Flow - General	691
	2. Liquid Flow	695
	3. Gas Flow	695
	4. Gas Pressures	696
	5. Pumps	697
	6. Regenerative Nozzle Sections (Heat Exchangers)	697
	7. Preburner and Main Turbines	698
	8. Main Combustion Chamber	699
E.	Digital Transient Program	700
	1. Program Input Parameters	701

CONTENTS (Continued)

SECTION		PAGE
	2. Program Output Parameters	704
	3. Program Formulation	707
F.	Program Operating Instructions	715
APPENDIX III -	Parametric Data	717
A.	Performance Data	717
	1. General	717
	2. Performance	718
B.	Weight and Envelope	719
APPENDIX IV -	Performance Data Reduction	785
A.	Nozzle Throat Area	785
	1. Uncooled Chamber Tests	785
	2. Cooled Chamber Tests	787
B.	Nozzle Exit Area	787
	1. 50K Model Tests	787
	2. 250K Tests	787
C.	Nozzle Area Ratio	787
D.	Stagnation Chamber Pressure	787
E.	Propellant Flow Rate	788
F.	Mixture Ratio	788
G.	Thrust	788
	1. 50K Model Tests	788
	2. 250K Tests	789
H.	Chamber Heat Loss	789
I.	Nozzle Heat Loss	789
J.	Propellant Injector Parameters	790
	1. Fuel Injection Velocity	790
	2. Oxidizer Injection Velocity	790
	3. Injection Velocity Ratio	790
K.	Specific Impulse	790
L.	Impulse Efficiency	790
	1. Nozzle Retracted	790
	2. Nozzle Extended	791

CONTENTS (Continued)

SECTION		PAGE
M.	Thrust Coefficient	791
N.	Thrust Coefficient Efficiency	791
	1. Nozzle Retracted	791
	2. Nozzle Extended	791
O.	Characteristic Velocity	791
P.	Characteristic Velocity Efficiency	791
Q.	Test Duration and Data Point Time	792
R.	Test Instrumentation Error Analysis	792
	1. 50K Data	792
	2. 250K Data	793
S.	Analytical Performance Models	796
	1. Combustion Gas Profile	796
	2. Transpiration Cooling Mixture Ratio Profile Model	798
REFERENCES		808
DISTRIBUTION LIST		809

ILLUSTRATIONS

FIGURE		PAGE
1	Propellant Flow Schematic.	11
2	250K Engine Component Arrangement.	12
3	Demonstrator Engine Operating Range.	16
4	Effect of Turbine Area on Fuel Pump Speed.	18
5	Effect of Turbine Area on Fuel Pump Pressure Rise. .	18
6	Effect o. . cal Turbine Area on Turbine Area Ratio	19
7	Effect of Turbine Area on Oxidizer Pump Speed. . . .	19
8	Effect of Turbine Area on Oxidizer Pump Pressure Rise.	20
9	Main Oxidizer Turbine Efficiency vs Mean Velocity Ratio	22
10	Comparison of Oxidizer Turbine Assemblies.	22
11	Main Fuel Turbine Efficiency vs Mean Velocity Ratio	23
12	Effect of Turbine Vane Exit Angle on Fuel Pump Discharge Pressure	25
13	Preburner Fuel Injector Pressure Drop for Fixed Fuel Area.	27
14	Preburner Fuel Injector Pressure Drop - Variable Fuel Area	28
15	Required Fuel Preburner Injector Area vs Expansion Ratio	29
16	Load Control System (4-Valve Configuration) Operating Region and Control Areas	37
17	Load Control System (3-Valve Configuration) Operating Region (Control Point 7 Scheduled for Minimum Chamber Cooling Flow).	38
18	Load Control System (3-Valve Configuration) Operating Region (Control Point 6 Orifice Area Too Small).	38
19	Load Control System (3-Valve Configuration) Operating Region and Control Areas (Control Point 7 Scheduled for Injector Stability).	39
20	Load Control System (2-Valve Configuration) Operating Region	39
21	Demonstrator Engine Control System	40

ILLUSTRATIONS (Continued)

FIGURE		PAGE
22	Control System Accuracy Comparison.	42
23	Flow Measurement Control System Precision	42
24	Vacuum Specific Impulse vs Thrust (Upper Stage) . .	47
25	Altitude Performance for Booster Application. . . .	47
26	Fuel Valve Pressure Drop Schedule	48
27	Propellant Flow Schematic	49
28	Demonstrator Engine Preliminary Installation Drawing (Booster Application)	52
29	Demonstrator Engine Preliminary Installation Drawing (Upper Stage)	53
30	Oxidizer Low-Speed Inducer.	55
31	Fuel Low-Speed Inducer.	58
32	Oxidizer Turbopump.	60
33	Fuel Turbopump.	63
34	Transition Case - Component and Cooling Liner Arrangement	66
35	Estimated Demonstrator Engine Start Transient to 20% Thrust, r = 5.	70
36	Valve Sequence for Start Transient.	71
37	Demonstrator Engine 3-Second Acceleration 20% to 100% Thrust.	73
38	Demonstrator Engine 1-Second Deceleration 100% to 20% Thrust.	74
39	Estimated Demonstrator Engine Shutdown Transient from 20% Thrust, r = 6.0.	75
40	Estimated Shutdown Transient from Rated Thrust. . .	79
41	Effect of Shutoff Valve Timing on Shutdown Characteristics	80
42	Response of Chamber Pressure to Preburner Oxidizer Control Area	81
43	Response of Chamber Mixture Ratio to Main Chamber Oxidizer Control Area	81
44	Response of Chamber Pressure With Varying Coolant Passage Volume.	82
45	Response of Chamber Pressure With Varying Oxidizer Turbopump Inertia.	82

ILLUSTRATIONS (Continued)

FIGURE		PAGE
46	Response of Chamber Pressure to Preburner Oxidizer Control Area.	83
47	Response of Chamber Mixture Ratio to Main Chamber Oxidizer Control Area.	83
48	Fuel Pump Performance During 10-Second Ramp Between 20% and 100% Thrust (Open-Loop Control System)	85
49	ADP Analog Simulation, Effects of Fuel Turbopump Torque Disturbance	86
50	ADP Analog Simulation, 95 psi Pressure Loss Case Results.	87
51	ADP Analog Simulation, Effects of Fuel Pump Inlet Pressure Disturbance.	88
52	Control Area Influence at 30% Thrust	89
53	Control Area Influence at 60% Thrust	90
54	Control Area Influence at 90% Thrust	90
55	Control System Logic Diagram	91
56	Stability Analysis Data.	91
57	Main Chamber Pressure vs Mixture Ratio - Analog Simulation.	93
58	Preburner Chamber Pressure vs Mixture Ratio - Analog Simulation.	93
59	Acceleration and Deceleration Transient Simulation	94
60	Preliminary Flight Engine Installation Drawing.	101
61	Dual-Preburner Cycle Control Schematic	105
62	Single Preburner Cycle Propellant Flow Schematic	105
63	Oxidizer Pump Pressure Rise vs Mixture Ratio	106
64	Oxidizer Pump Speed vs Mixture Ratio	107
65	Fuel Pump Pressure Rise vs Mixture Ratio	107
66	Fuel Pump Pressure Rise vs Fuel Pump Flow.	108
67	Total Turbine Flow Available vs Mixture Ratio. . . .	109
68	Fuel and Oxidizer Pump Horsepower vs Mixture Ratio.	110

ILLUSTRATIONS (Continued)

FIGURE		PAGE
69	Turbine Areas vs Mixture Ratio.	112
70	Fuel Turbine Flow Ratio vs Mixture Ratio.	112
71	Fuel Turbine Pressure Ratio vs Mixture Ratio.	113
72	Preburner Temperature vs Mixture Ratio.	113
73	Dual-Preburner Engine Component Arrangement	115
74	Dual-Preburner Engine Radial Arrangement.	116
75	Application Study Vehicles, 250K Engines.	117
76	Application Study Vehicles, 350K Engines.	118
77	Ground Test Staged-Combustion Configuration	126
78	320-Element Preburner Injector.	127
79	54-Concentric-Element Preburner Injector Assembly . .	127
80	50K Multiple Concentric Element Preburner Injector. .	128
81	Preburner Chamber Acoustic Liner.	130
82	Preburner Chamber Thermocouple Rake	130
83	50K, 20-Spraybar Main Injector.	131
84	Swirler Spraybar and Rigimesh Faceplate	131
85	50K Thrust Level 20-Spraybar Main Burner Injector Assembly	132
86	24-Spraybar 50K Injector Schematic.	133
87	Dual Tangential Slot Swirler Element Configuration. .	133
88	Tangential Entry Liquid Oxygen Injector Elements Shown in Rigimesh Injector Face Slot.	134
89	Tailored Fuel Slot.	135
90	50K Main Burner Injector Faces.	137
91	Uncooled Chamber, Variable Geometry Hardware.	137
92	50K Main Burner Variable Geometry Chambers and Associated Hardware	138
93	50K Uncooled Chamber Nozzle Insert.	139
94	50K Uncooled Chamber Liners	139
95	Main Chamber Uncooled Copper Liner.	140
96	50K Cooled Main Chamber Configuration	141
97	50K Contraction Ratio of 3, Cooled Chamber.	141
98	Wafer Cooling Concept	142

ILLUSTRATIONS (Continued)

FIGURE		PAGE
99	50K Cooled Wafer Geometry.	143
100	50K Cooled Chamber Temperature and Pressure Locations.	145
101	Surface Temperature Plating Indications for 50K Cooled Chamber	146
102	50K, Area Ratio 90, Uncooled Nozzle Skirt.	146
103	Primary Nozzle With Area Ratio of 4.75 to 20 Showing Cooling Water Holes.	147
104	50K Translatable Nozzle in Closed Position Mounted in Assembly and Transportation Fixture . . .	148
105	50K Translatable Nozzle in Open Position Mounted in Assembly and Transportation Fixture . . .	148
106	50K Translatable Nozzle in Open Position Mounted in Asse[illegible]y and Transportation Fixture . . .	149
107	Effect of [illegible]on Combustion Performance ,	150
108	Starting and O[illegible]iant Mass Flux	151
109	50K Two-Posi[illegible]rformance (Test No. 5[illegible])	152
110	50K Performance Tren[illegible]	155
111	50K Preburner Combustion Chamber Temperature Profiles	157
112	Sources of Performance Losses.	158
113	Main Injectors After the Uncooled Test Series. . . .	159
114	24-Spraybar Injector, Post-Test No. 50N3C.	159
115	Film-Cooled Copper Liner Wall Erosion Patterns (Post-Test 50SC5).	160
116	50K Cooled Chamber Pretest Condition	162
117	50K Transpiration Cooling Requirements	163
118	50K Transpiration Cooling Flux - Distribution 1. . .	164
119	50K Transpiration Cooling Flux - Distribution 2. . .	165
120	50K Transpiration Cooling Flux - Distribution 3. . .	166
121	50K Cooled Chamber, Post-Test 50SC7C. 3 O'Clock Position	167
122	Closeup of Throat, Post-Test 50SC7C.	168
123	Vibration Traces for Cooled Test, Uncooled Test, and RL10 Production Engine	169

ILLUSTRATIONS (Continued)

FIGURE		PAGE
124	50K Translating Nozzle, Chamber Pressure Ratio and Side Load.	171
125	Load Cell Data for Secondary Nozzle.	172
126	50K Translating Nozzle Tests	173
127	Translating Skirt Wall Pressure and Temperature. . .	174
128	Grooved Wafer and Rigimesh Cooling Concepts.	175
129	Transpiration Heat Transfer Analysis	177
130	Mass Addition Film Effect (η_f)	178
131	Transpiration Section Wall Efficiency (θ_w)	179
132	Influence of Wafer Groove Geometry on Required Coolant Mass Flux	179
133	Effect of Wafer Axial Thickness on Coolant Mass Flux Requirements	180
134	Material Thermal Conductivity vs Temperature	181
135	Typical Plating Thickness Requirements for 2500°R Wall Temperature.	181
136	Grooved Wafer Cooling Requirements vs Thermal Conductivity (Contraction Area Ratio Equal to 3.0).	182
137	Grooved Wafer Cooling Requirements vs Thermal Conductivity (Expansion Area Ratio Equal to 1.0).	183
138	Grooved Wafer Cooling Requirements vs Thermal Conductivity (Expansion Area Ratio Equal to 4.0).	183
139	Rigimesh Coolant Mass Flux vs Thermal Conductivity (Nozzle Throat)	186
140	Wafer and Rigimesh Coolant Mass Flux Requirements	189
141	Effect of Thermal Conductivity and Surface Wall Temperature on Wafer and Rigimesh Throat Cooling Requirements.	189
142	Cooled Convergent Nozzle Test Rig.	190
143	Transpiration Cooled Convergent Test Section	191
144	Rigimesh Cooled Convergent Test Section.	192
145	Liquid Propellant Research Facility Test Stand Layout.	193

ILLUSTRATIONS (Continued)

FIGURE		PAGE
146	B-28 Test Stand Schematic.	194
147	B-28 Data Acquisition System Schematic	195
148	50K Thrust Level Staged-Combustion Test Rig Control System	195
149	50K Thrust Uncooled Staged-Combustion Test Sequence.	198
150	Roller Bearing Test Rig Cross Section.	200
151	Roller Bearing Test Rig.	201
152	Radial Spring Rate vs Inner Race Speed (Single Ball Bearing).	203
153	Radial Spring Rate vs Radial Load (Single Ball Bearing, 600-lb Thrust Load)	203
154	Radial Spring Rate vs Radial Load (Single Ball Bearing, 1000-lb Thrust Load)	204
155	Radial Spring Rate vs Radial Load (Single Ball Bearing).	204
156	Ball Bearing Load Capacity	205
157	Radial Spring Rate vs Radial Load (Single Ball Bearing).	205
158	Ball Bearing Load Capacity	206
159	Radial Spring Rate vs Radial Load (Single Ball Bearing).	206
160	Ball Bearing Load Capacity	207
161	Radial Spring Rate vs Radial Load (Roller Bearings).	208
162	Radial Spring Rate vs Radial Load (Roller Bearings).	208
163	Roller Bearing Fatigue Life vs Radial Load (50,000 rpm)	209
164	Radial Spring Rate vs Radial Load (Roller Bearings).	209
165	Roller bearing Fatigue Life vs Radial Load (50,000 rpm)	210
166	Radial Spring Rate vs Radial Load (Roller Bearings).	210

ILLUSTRATIONS (Continued)

FIGURE		PAGE
167	Predicted 250K Fuel Turbopump Critical Speeds.	211
168	250K Fuel Pump Maximum Radial Loading of Rear Bearing (Loaded 47.4 Degrees from Vehicle Axis)	213
169	250K Fuel Pump Maximum Radial Loading of Front Bearing (Loaded 47.4 Degrees from Vehicle Axis)	214
170	250K Fuel Pump Maximum Radial Loading of Front Bearing Vector Load Diagram	215
171	Bearing Configurations.	220
172	Armalon Cage from Bearing S/N B-1 Showing Delamination After 15 Minutes at 48,000 rpm.	221
173	Rollers from Bearing S/N B-1 After 15 Minutes at 48,000 rpm.	222
174	Rollers from Bearing S/N B-2 Showing End Wear After 15 Minutes at 48,000 rpm	222
175	Inner Race from Bearing S/N C-2 Showing Worn Side Rails After Operation at Speed Less than 1000 rpm.	223
176	Armalon Cage With Failed Pockets from Bearing S/N C-2A After 7 Minutes at 48,000 rpm. . . .	224
177	Rollers from Bearing S/N C-2A Showing End Wear After 7 Minutes at 48,000 rpm.	225
178	Inner Race from Bearing S/N C-1 Showing Side Rail Wear After 7 Minutes at 48,000 rpm.	225
179	Polyimide (SP-1) Cage from Bearing S/N C-1 After 7 Minutes at 48,000 rpm	226
180	Rollers from Bearing S/N C-1 Showing Light (0.0005 inch) End Wear After 7 Minutes at 48,000 rpm.	226
181	New Condition Bearing Details, S/N F-2A	227
182	New Condition bearing Details, S/N F-1A	228
183	Bearing S/N F-1A Post-Test Condition Showing Cage Failure After 1 Minute at 48,000 rpm	228
184	Bearing S/N F-2A Post-Test Condition Showing No Roller End Wear After 1 Minute at 48,000 rpm . . .	229
185	Halok-M Cage from Bearing S/N F-1A Showing Cracks at Rivet Locations After 1 Minute at 48,000 rpm	229

ILLUSTRATIONS (Continued)

FIGURE		PAGE
186	Salox-M Cage from Bearing S/N F-2A Showing Several Axial Cracks at Rivet Locations After 1 Minute at 48,000 rpm.	230
187	Bearing S/N H-2 Post-Test Condition Showing Polyimide (SP-1) Cage After Failure During Acceleration.	231
188	Outer Race Assembly and Failed Shrouded Salox-M Cage (S/N N-1).	232
189	Outer Race Assembly Showing Damaged Polyimide SP-4 Insert (S/N N-2)	233
190	Salox-M Cage Assembly (S/N N-2)	233
191	Outer Race Assembly Showing Failed Leaded-Bronze Inserts (S/N P-1)	234
192	Outer Race Assembly Showing Side Rail Wear (S/N P-2)	235
193	Post-Test No. 11 Condition of Inner Race from the Reaction Bearing.	236
194	Post-Test No. 11 Condition of Cage from Reaction Bearing Showing Rub Areas on Cage Armor.	236
195	Post-Test No. 7 Condition of Reaction Bearing After 1 Hour and 32 Minutes at Design Speed.	237
196	Post-Test No. 12 Condition of Load Bearing After 1 Hour and 32 Minutes at Design Speed	237
197	Post-Test No. 14 Condition of Load Bearing S/N S-2 After 7 Hours and 26 Minutes at Design Speed.	239
198	Post-Test No. 15 Condition of Load Bearing S/N T-2 After 1 Hour and 19 Minutes at Design Speed.	240
199	Post-Test No. 16 Condition of Outer Race from Load Bearing S/N U-2 Showing Cracked Outer Race After 3 Hours and 50 Minutes of Testing at 48,000 rpm.	241
200	Post-Test No. 16 Condition of Rollers from Load Bearing S/N U-2 Showing One Failed Roller and the Good Condition of the Remaining Rollers After 3 Hours and 50 Minutes of Testing at 48,000 rpm . . .	242

ILLUSTRATIONS (Continued)

FIGURE		PAGE
201	Post-Test No. 16 Condition of Bearing S/N S-1 Showing Good Condition After 12 Hours and 35 Minutes of Testing at 48,000 rpm.	243
202	Post-Test No. 16 Condition of Load Ring and Outer Race OD Showing the Fretting Between These Two Parts in Area in Line With the Applied Radial Load.	243
203	B-13 Roller Bearing Test Facility	246
204	Mixture Ratio Valve Operating Requirements.	249
205	Mixture Ratio Valve, Sleeve Type.	250
206	Sleeve Valve Geometric Area vs Percent Thrust (Mixture Ratio Valve).	252
207	Maximum Width of Constant Area Error Contoured Port vs Stroke of Sleeve Valve (Mixture Ratio Valve)	252
208	Sleeve Valve Diameter vs Stroke (Mixture Ratio Valve).	253
209	Port Area vs Stroke for Constant Percentage Port Contour on Sleeve Valve (Mixture Ratio Valve).	253
210	Sleeve Port Contour for 2.0-inch Stroke (Mixture Ratio Valve, ...	254
211	Sleeve Port Contour for 2.5-inch Stroke (Mixture Ratio Valve)	254
212	Sleeve Port Contour for 3.0-inch Stroke (Mixture Ratio Valve)	255
213	Percent Area Error vs Percent Stroke Error for Various Valve Turndown Ratios (Mixture Ratio Valve).	255
214	Axial Flow Forces vs Percent Thrust at r = 5 (Mixture Ratio Valve).	256
215	Horsepower Required to Overcome Flow Forces vs Percent Thrust at r = 5 (Mixture Ratio Valve). . .	256
216	Mixture Ratio Valve, Pintle Orifice Type.	257

ILLUSTRATIONS (Continued)

FIGURE		PAGE
217	Pintle Valve Sizing Criteria (Mixture Ratio Valve)	258
218	Required Geometric Flow Area vs Percent Thrust (Mixture Ratio Valve)	258
219	Percent Pressure Recovery vs Percent Thrust (Mixture Ratio Valve)	259
220	Axial Force vs Percent Thrust (Mixture Ratio Valve)	259
221	Net Axial Force vs Percent Thrust as a Function of Mixture Ratio (Mixture Ratio Valve)	260
222	Throat Pressure vs Percent Thrust for Noncavitating Venturi Pintle Scheme (Mixture Ratio Valve)	261
223	Mixture Ratio Valve, Cavitating Venturi Type	262
224	Venturi Throat Pressure vs Percent Thrust for Cavitating Venturi Scheme (Mixture Ratio Valve)	262
225	Mixture Ratio Valve, Ball Type	263
226	K Factor for Ball Valve vs Angular Rotation	264
227	Pressure Drop vs Diameter of Ball Passage (Mixture Ratio Valve)	265
228	Angular Opening of Ball vs Percent Thrust (Mixture Ratio Valve)	266
229	Effective Area of Ball Valve vs Angular Position (Mixture Ratio Valve)	266
230	Area Error for Ball Valve and Constant Percentage Valve (Mixture Ratio Valve)	267
231	Dynamic Torque vs Percent Thrust (Ball Valve)	268
232	Mixture Ratio Valve, Butterfly Type Candidate	269
233	Butterfly Position vs Throat Diameter (Mixture Ratio Valve)	270
234	Butterfly Angular Opening vs Percent Thrust for 3.0-inch Inlet Diameter (Mixture Ratio Valve)	270
235	Butterfly Angular Opening vs Effective Area for 3.0-inch Inlet Diameter (Mixture Ratio Valve)	271

ILLUSTRATIONS (Continued)

FIGURE		PAGE
236	Area Error Per Degree in Percent vs Disk Angle. . . .	271
237	Butterfly Dynamic Torque vs Percent Thrust for 3.0-inch Inlet Diameter (Mixture Ratio Valve) . .	272
238	Butterfly Dynamic Torque vs Angular Opening for 3.0-inch Inlet Diameter (Mixture Ratio Valve) . .	272
239	Mixture Ratio Valve Initial Design.	277
240	Mixture Ratio Valve Final Design.	278
241	Mixture Ratio Valve Shutoff Seal.	279
242	Mixture Ratio Valve Torque vs Percent Thrust.	279
243	Rotary Shaft Seal Test Rig Parts.	280
244	Rotary Shaft Seal Test Rig.	284
245	Mixture Ratio Valve Assembly F-33466-1.	288
246	Mixture Ratio Valve Assembly Mounted in B-21 Water Flow Test Stand	289
247	Mixture Ratio Valve Effective Area vs Shaft Position, Rig F-33466-1	289
248	Mixture Ratio Valve Torque vs Differential Pressure, Rig F-33466-1	290
249	Disk Seal Piston Ring After Test on Rig F-33466-1 . .	291
250	Tensile Failed Areas of Disk Seal Piston Ring After Test on Rig F-33466-1	291
251	Sheared Area of Disk Seal Piston Ring After Test on Rig F-33466-1	292
252	Revised Actuator Mount.	293
253	Mixture Ratio Valve Leakage vs Actuation Cycles, Rig F-33466-2	294
254	Butterfly Shaft After Test of Rig F-33466-2	294
255	Bearing Sleeve After Test of Rig F-33466-2.	295
256	Outboard Tufram-Coated Bushing After Test of Rig F-33466-2	295
257	Mixture Ratio Valve Effective Area vs Shaft Position, Rig F-33466-3	296
258	Shaft Disk After Test of Rig F-33466-3.	297
259	Shaft Disk After Test of Rig F-33466-3 Showing Crack in Metal Spray.	297
260	Shaft Disk After Test of Rig F-33466-3 Showing Chips in Metal Spray.	298

ILLUSTRATIONS (Continued)

FIGURE		PAGE
261	Disk Seal After Test of Rig F-33466-3.	298
262	Mixture Ratio Valve Effective Area vs Shaft Position, Rig F-33466-4.	299
263	Leakage vs Cycles, Mixture Ratio Valve Rig F-33466-5.	301
264	Control System Schematic, Mixture Ratio Valve Rig F-33466-5.	302
265	Hysteresis vs Shaft Position (Fixed Step Increments).	302
266	Nonlinearity vs Valve Shaft Position (Fixed Step Increments).	303
267	Nonlinearity vs Shaft Position (Increasing Step Increments)	303
268	Amplitude Ratio vs Frequency (Inlet Pressure = 0 psig)	304
269	Amplitude Ratio vs Frequency (Inlet Pressure = 3000 psig).	304
270	Lower Thrust Bearing After Test of Rig F-33466-5.	305
271	Shaft and Shaft Disk After Test of Rig F-33466-5.	305
272	Disk Seal After Test of Rig F-33466-5.	306
273	Primary Lip Seal After Test of Rig F-33466-5	306
274	Disk Seal Leakage vs Shaft Cycles, Mixture Ratio Valve Rig F-33466-6.	308
275	Shaft Disk After Test of Rig F-33466-6	309
276	Lower Thrust Bearing After Test of Rig F-33466-6 . .	309
277	Lip Seal After Test of Rig F-33466-6	310
278	Leakage vs Actuation Cycles, Rig F-33466-7	311
279	Leakage vs Actuation Cycles, Rig F-33466-8	313
280	250K Mixture Ratio Valve Housing Assembly Showing Stresscoat Patterns Due to 6000 psig Internal Proof Pressure.	314
281	250K Mixture Ratio Valve Housing Assembly Showing Stresscoat Patterns Due to 6000 psig Internal Proof Pressure.	315

ILLUSTRATIONS (Continued)

FIGURE		PAGE
282	250K Mixture Ratio Valve Housing Assembly Showing Stresscoat Patterns on Bearing Cap Due to 6000 psig Internal Proof Pressure.	315
283	Mixture Ratio Valve Effective Area vs Shaft Position, Rig F-35106-1	318
284	Torque vs Differential Pressure for Mixture Ratio Valve Rig F-35106-1	318
285	Teflon Disk Seal After Test of Rig F-35106-1. . . .	319
286	Mixture Ratio Valve Effective Area vs Shaft Position, Rig F-35106-2	320
287	Laminated Kapton-FEP Teflon Disk Seal After Test of Rig F-35106-2	320
288	Leakage vs Cycles, Mixture Ratio Valve Rig F-35106-3	322
289	Leakage vs Cycles, Mixture Ratio Valve Rig F-35106-4	322
290	Leakage vs Cycles, Mixture Ratio Valve Rig F-35106-5	324
291	Rotary Shaft Seal Test Rig Leakage vs Cycles for Rig F-33443-2	329
292	Primary Bal-Seal After Test	330
293	Primary Lip Seal After Test	330
294	Rotary Shaft Seal Test Rig Leakage vs Cycles for Rig F-33443-3	331
295	Primary Bal-Seal After Test	332
296	Rotary Shaft Seal Test Rig Leakage vs Cycles for Rig F-33443-4.	333
297	Primary Bal-Seal After Test	334
298	Primary Lip Seal After Test	334
299	All Dynamic Seals Tested on Rig F-33443-4	335
300	Rotary Shaft Seal Test Rig Leakage vs Cycles for Rig F-33443-5	336
301	Primary Lip Seal After Test on Rig F-33443-5. . . .	337
302	Secondary Lip Seal After Test on Rig F-33443-5. . .	338
303	All Dynamic Seals Tested on Rig F-33443-5	338
304	Rotary Shaft Seal Test Rig Leakage vs Cycles for Rig F-33443-6	339

ILLUSTRATIONS (Continued)

FIGURE		PAGE
305	Primary Lip Seal After Test on Rig F-33443-6. . . .	340
306	Rotary Shaft Seal Test Rig Leakage vs Cycles for Rig F-33443-7.	341
307	Primary Lip Seal After Test on Rig F-33443-7. . . .	342
308	Rotary Shaft Seal Test Rig Leakage vs Cycles for Rig F-33443-8	343
309	Primary Lip Seal After Test on Rig F-33443-8. . . .	344
310	Rotary Shaft Seal Test Rig Leakage vs Cycles for Rig F-33443-9	345
311	Rotary Shaft Seal Test Rig Leakage vs Cycles for Rig F-33443-10.	346
312	Primary Lip Seal After Test on Rig F-33443-10 . . .	348
313	B-21 Control Calibration Facility	348
314	B-22 Cryogenic Static Cycle Stand	349
315	Mixture Ratio Valve Assembly Mounted in B-21 Waterflow Test Stand.	350
316	Mixture Ratio Valve Instrumentation Schematic (B-21 Stand).	350
317	Flow Torque Test Installation	351
318	Mixture Ratio Valve Rig F-33466-5 During Cryogenic Endurance Testing	351
319	Mixture Ratio Valve Instrumentation Schematic (B-22 Stand).	352
320	Rotary Shaft Seal Test Rig Schematic for B-22 Stand.	353
321	Flow Divider Valve Rig Pressure Drop vs Percent Thrust.	355
322	Flow Divider Valve Rig Design Requirements for Operation from 10 to 100% Thrust.	356
323	Flow Divider Valve Primary Flow Rate vs Percent Thrust.	357
324	Flow Divider Valve, Pintle-Orifice Candidate. . . .	358
325	Preburner Flow Divider Valve Required Area.	359
326	Flow Divider Valve Required Contour	359
327	Percent Error in Area vs Percent Error in Stroke for Preburner Flow Divider Valve.	360
328	Noncompensated Force Balance vs Percent Thrust (Preburner Flow Divider Valve)	361

ILLUSTRATIONS (Continued)

FIGURE		PAGE
329	Flow Divider Valve, Pintle-Venturi Candidate.	362
330	Pintle Venturi Flow Area vs Percent Thrust (Flow Divider Valve).	363
331	Pressure Recovery vs Percent Thrust (Flow Divider Valve).	363
332	Pintle Position vs Percent Thrust (Flow Divider Valve).	364
333	Pintle Face Force vs Percent Thrust (Flow Divider Valve).	365
334	Flow Divider Valve Net Pintle Force vs Percent Thrust (Noncompensated)	365
335	Flow Divider Valve Net Pintle Force vs Percent Thrust (Compensated).	366
336	Flow Divider Valve, Ball and Rotating Sleeve Candidate.	368
337	Development of Sleeve Valve with Three Constant Percentage Contour Ports	368
338	Geometric Inlet Area of Ball Valve vs Angle of Rotation for 1.5-inch Inlet Diameter	369
339	Effective Area of Inlet to Ball Valve vs Angular Position for 1.5-inch Diameter.	369
340	K-Factor for Ball Valve vs Angular Opening (Flow Divider Valve).	370
341	Pressure Drop Across Ball Valve vs Percent Thrust . .	370
342	Geometric Area of Contoured Port vs Percent Thrust (Flow Divider Valve)	371
343	Flow Area of Contoured Port vs Angular Opening of Sleeve Port Valve.	372
344	Angular Opening of Sleeve vs Percent Thrust (Flow Divider Valve).	372
345	Maximum Port Width vs Line Diameter (Flow Divider Valve).	373
346	Percent Area Error vs Percent Position Error (Flow Divider Valve).	373
347	Flow Divider Valve, Rotary Sleeve Candidate	374
348	Required Increase in Pressure Upstream of Flow Divider Sleeve Valve vs Percent Thrust.	375
349	Flow Divider Valve, Translating Sleeve Candidate. . .	377

ILLUSTRATIONS (Continued)

FIGURE		PAGE
350	Effective Area of Secondary Valve vs Percent Thrust (Preburner Flow Divider Valve). . . .	377
351	Maximum Required Port Width vs Valve Stroke.	378
352	Stroke vs Diameter for Translating Sleeve Valve (Preburner Flow Divider Valve)	378
353	Port Contour of Constant Area Error Port Based on 5 Equal Ports	379
354	Flow Divider Valve Port Contour (10 Ports Required).	379
355	Valve Force (Noncompensated) vs Percent Thrust (Preburner Flow Divider Valve)	380
356	Flow Forces vs Percent Thrust (Preburner Flow Divider Valve)	381
357	Flow Divider Valve with Oxidizer Side of Preburner Injector	383
358	Flow Divider Valve Parts	384
359	Rig and Demonstrator Flow Divider Valve.	386
360	Cross Section of Primary Ports	387
361	Cross Section of Secondary Ports	387
362	Secondary Metering Piston Ring and Shutoff Seal. . .	388
363	Upper Piston Ring Seal	388
364	High-Pressure Spool Valve Seal Package	389
365	Nitrogen Dam Seal Package.	389
366	Servoactuator Mount.	390
367	Preburner Oxidizer Flow Divider Valve (Predicted Effective Area vs Stroke)	391
368	Revised Flow Divider Valve Locktab Design.	392
369	Exploded View of Piston Seal Test Rig.	392
370	Effective Area vs Pressure Drop for Primary Circuit.	394
371	Effective Area vs Pressure Drop for Secondary Circuit.	394
372	Flow Divider Valve Effective Area vs Stroke - Rig F-33469.	395
373	Preburner Oxidizer Flow Divider Valve Effective Area vs Stroke - Rig F-33458-2	395

ILLUSTRATIONS (Continued)

FIGURE		PAGE
374	Flow Nomograph.	396
375	Bode Plot for Flow Divider Valve Actuator Rig F-33465-1	397
376	B-22 Test Stand Flow Divider Valve Actuator Controls.	398
377	Nonlinearity vs Percent Valve Stroke for Flow Divider Valve Actuator Rig F-33465-1 (Fixed Step Increments).	400
378	Hysteresis vs Percent Valve Stroke for Flow Divider Valve Actuator Rig F-33465-1 (Fixed Step Increments).	401
379	Nonlinearity vs Percent Valve Stroke for Flow Divider Valve Actuator Rig F-33465-1 (Increasing Step Increments).	402
380	Hysteresis vs Percent Valve Stroke for Flow Divider Valve Actuator Rig F-33465-1 (Increasing Step Increments).	403
381	Actuator Breakaway Force vs Cycles for Flow Divider Valve Rig F-33458-4	404
382	Teflon Shutoff Seal Leakage vs Cycles for Flow Divider Valve Rig F-33458-4	405
383	Pretest and Post-Test Condition of Shutoff Mechanical Stop Surface	406
384	Post-Test Condition of Secondary Sleeve Sealing Edge.	406
385	Secondary Seal Ring Leakage vs Cycles for Flow Divider Valve Rig F-33458-4.	408
386	Effects of Pressure Loading	409
387	Flow Divider Valve Housing Prior to Testing	409
388	Pretest and Post-Test Condition of Upper Secondary Piston Ring and Secondary Post Area in the Valve Housing	410
389	Pretest and Post-Test Condition of Lower Secondary Piston Ring	410
390	Pretest and Post-Test Condition of Primary Spool. .	411
391	Pretest and Post-Test Condition of Housing Primary Spool Bore Area	411
392	Post-Test Condition of Primary Spool Shaft Surface	412

ILLUSTRATIONS (Continued)

FIGURE		PAGE
393	Flow Divider Valve Effective Area vs Stroke - Rig F-33458.	412
394	Pretest and Post-Test Condition of the Secondary Valve Housing Showing the Effects of Piston Ring Differential Pressure	413
395	Pretest and Post-Test Condition of Secondary Port Area on the Valve Housing	413
396	Flow Divider Valve Piston Ring Leakage vs Cycles - Rig F-33458-6	415
397	Pretest and Post-Test Condition of Upper Secondary Piston Ring.	416
398	Pretest and Post-Test Condition of Lower Secondary Piston Ring.	416
399	Piston Seal Ring Leakage vs Differential Pressure.	417
400	Flow Divider Valve Effective Area vs Stroke Rig F-33458-6.	418
401	Flow Divider Valve Maximum Power Requirements for Full Stroke of 2.25 in.	418
402	Piston Seal Test Rig and Seal Candidates	423
403	Piston Seal Test Rig Leakage vs Cycles for Rig F-33435-1.	425
404	Bal-Seal After Test.	425
405	Omniseal After Test.	426
406	Piston Bal-Seal After Test	426
407	Primary Omniseal After Test.	427
408	Piston Seal Test Rig Leakage vs Cycles for Rig F-33435-3.	427
409	Teflon Piston Bal-Seal After Test.	428
410	Piston Bal-Seal After Test, Rig F-33435-4.	428
411	Piston Seal Test Rig Leakage vs Cycles for Rig F-33435-5.	429
412	Piston Seal Test Rig Leakage vs Cycles for Rig F-33435-6.	429
413	Piston Seal Test Rig Leakage vs Cycles for Rig F-33435-6A	430
414	Piston Seal Test Rig Leakage vs Cycles for Rig F-33435-7.	430
415	Piston Seal Test Rig Leakage vs Cycles for Rig F-33435-8.	431

ILLUSTRATIONS (Continued)

FIGURE		PAGE
416	Piston Seal Rig Leakage, Rig F-33435-9.	432
417	Post-Test Condition of Shaft.	433
418	Seals from Rig F-33435-9.	433
419	Polishing Techniques.	435
420	B-21 Control Calibration Facility	436
421	B-22 Cryogenic Static Cycle Stand	437
422	Flow Divider Valve Mounted on B-21 Stand.	437
423	Schematic of Flow Divide. Valve Mounted on B-21 Stand.	438
424	Flow Divider Valve Mounted on Test Block for Cryogenic Endurance Test.	438
425	Schematic of Flow Divider Valve Test Stand Installation.	439
426	Piston Seal Test Rig.	439
427	Translating Seal Rig As Installed in B-22 Stand . . .	440
428	Thrust Control Valve Requirements for Operation . . .	442
429	Thrust Control Translating Sleeve-Inverted Pintle Valve Candidate.	443
430	Thrust Control Translating Sleeve-Port Contoured. . .	445
431	Geometric Flow Area Required vs Percent Thrust (Thrust Control Valve).	444
432	Percent Error in Area vs Percent Error in Stroke (Thrust Control Valve).	446
433	Maximum Port Width Required for a Constant Percentage Sleeve Valve as a Function of Total Stroke (Thrust Control Valve)	447
434	Diameter Required vs Total Stroke (Thrust Control Valve).	448
435	Sleeve Valve Port Contour and Post Effective Area vs Axial Valve Stroke (3.0-inch Stroke) (Thrust Control Valve).	448
436	Sleeve Valve Port Contour and Port Effective Area vs Axial Valve Stroke (2.5-inch Stroke) (Thrust Control Valve).	449
437	Sleeve Valve Port Contour and Port Effective Area vs Axial Valve Stroke (2.0-inch Stroke) (Thrust Control Valve).	449

ILLUSTRATIONS (Continued)

FIGURE		PAGE
438	Axial Dynamic Flow Forces vs Percent Thrust at r = 5 (Thrust Control Valve)	451
439	Horsepower Required to Overcome Flow Force vs Percent Thrust at r = 5 (Thrust Control Valve)	451
440	Thrust Control Pintle Orifice Valve Candidate	453
441	Geometric Flow Area vs Percent Thrust (Thrust Control Valve)	453
442	Percent Recovery Factor vs Percent Thrust (Thrust Control Valve)	454
443	Pintle Axial Face Force vs Percent Thrust (Thrust Control Valve)	454
444	Pintle Net Axial Force vs Percent Thrust (Thrust Control Valve)	455
445	Axial Pintle Position vs Percent Thrust (Thrust Control Valve)	455
446	Thrust Control Pintle Venturi Valve Candidate	457
447	Throat Pressure vs Percent Thrust Defining Region of Noncavitation (Thrust Control Valve)	457
448	Throat Pressure Required to Meter Scheduled Flow and ΔP Loss Across Venturi vs Percent Thrust	458
449	Thrust Control Rotating Plate Valve Candidate	459
450	Thrust Control Butterfly Valve Candidate	460
451	Butterfly Angular Position (Min + Max) vs Butterfly Inlet Dia (Thrust Control Valve)	460
452	Butterfly Angular Opening vs Percent Thrust (Thrust Control Valve)	461
453	Butterfly Effective Area vs Butterfly Angular Opening (Thrust Control Valve)	462
454	Area Error Per Degree Angular Error vs Butterfly Angular Position (Thrust Control Valve)	462
455	Dynamic Torque vs Percent Thrust (Thrust Control Valve)	464
456	Butterfly Actuator Horsepower vs Frequency of Actuation at Max Torque Point of Operation (Thrust Control Valve)	464
457	Thrust Control Valve	465
458	Thrust Control Valve Line	466
459	Thrust Control Valve Floating Seal Retainer	466

ILLUSTRATIONS (Continued)

FIGURE		PAGE
460	Thrust Control Valve Pressure Drop vs Percent Thrust	467
461	Thrust Control Valve Effective Area vs Flapper Angle	468
462	Noncavitating Chamber Coolant Valve Effective Area vs Thrust	469
463	Noncavitating Chamber Coolant Valve (Flange-to-Flange) Pressure Drop vs Thrust	469
464	Chamber Coolant Valve Flow vs Total Pressure Drop	470
465	Cavitating Chamber Coolant Valve Operating Requirements	470
466	Chamber Coolant Valve	472
467	Shutoff Seal	472
468	Flow Path Dimensions	473
469	Shaft Seal	473
470	Operating Margin	476
471	Pintle Breakaway Force vs Percent Thrust	476
472	Pintle Dynamic Force vs Percent Thrust	477
473	Area Error vs Error in Stroke	477
474	Effective Flow Area vs Percent Thrust	478
475	Inlet Pressure vs Percent Thrust	478
476	Inlet Temperature vs Percent Thrust	479
477	Flow Rate vs Percent Thrust	479
478	Chamber Coolant Valve Seal Test Rig	480
479	Seal Test Rig Configuration	481
480	Seal Test Rig Parts	482
481	Seal Test Rig Parts	482
482	Chamber Coolant Valve Seal Test Rig Schematic	483
483	Translating Shaft Seal Rig Mounted in G-6 Stand	483
484	Translating Shaft Seal Rig During Test	484
485	Ignition System Schematic	489
486	Preburner Igniter Assembly	490
487	Preburner Igniter Assembly	490

(This page is Unclassified)

ILLUSTRATIONS (Continued)

FIGURE		PAGE
488	Details of Preburner Igniter Assembly.	491
489	Preburner Igniter Cooling Flow Schematic	491
490	Preburner Igniter Spark Plug	492
491	Main Chamber Igniter Assembly.	492
492	Main Chamber Igniter Assembly.	493
493	Igniter Combustion Chamber	494
494	Main Chamber Igniter Spark Plug.	494
495	250K Preburner Test Rig Milestones - 1967.	498
496	Propellant Flow Schematic.	499
497	Preburner Injector Final Configuration	499
498	Preburner Instrumentation Installation	500
499	Fuel Element Temperature Profile	501
500	Preburner Injector Configuration After Testing . . .	503
501	Stability Liner Showing Erosion After Testing With Intermediate Injector	503
502	Temperature Profile for Test No. 51.	504
503	Primary Manifold Configuration	505
504	Cross Section of Secondary Manifold.	505
505	Variation in Velocity With Thrust.	506
506	Oxidizer Primary-To-Total Flow Split vs Percent Thrust	507
507	Variation in Velocity With Thrust Dual Orifice . . .	507
508	Correlation of Injector and Combustion Chamber Parameters vs Temperature Profile.	509
509	Momentum Ratio vs Percent Thrust	510
510	Preburner Injector Initial Configuration	510
511	Variable Fuel Element Gear Arrangement	511
512	Preburner Injector Face Schematic.	511
513	Injector Housing Assembly.	512
514	Primary and Secondary Oxidizer Supply Passages . . .	512
515	Cross Section of Welded Preburner Injector Main Housing	513
516	Adjustable Fuel Arrangement.	514

(This page is Unclassified)

ILLUSTRATIONS (Continued)

FIGURE		PAGE
517	Variable Area Drive and Seal Package.	516
518	Faceplate Assembly.	517
519	Preburner Injector Transpiration Cooled Faceplate	517
520	Preburner Combustion Chamber Instrumentation.	518
521	Preburner Chamber Cooling Liner Combustion Section. .	519
522	Preburner Chamber Acoustic Liner.	520
523	Pulse Gun and Kistler Probe Configuration	521
524	Pulse Gun and Kistler Probe Installation.	521
525	Preburner Pulse Gun Details	522
526	Temperature Probe Installation.	522
527	Preburner Flow Divider Valve Housing.	523
528	Preburner Combustion Rig Configuration.	524
529	Facility Thrust Structure Attachment for Preburner Combustion Rig.	524
530	Back Pressure Nozzle Plate.	525
531	Preburner Igniter Assembly.	526
532	Details of Preburner Igniter Assembly	527
533	Preburner Igniter Cooling Flow Schematic.	527
534	Ignition System Schematic	528
535	Preburner Igniter Spark Plug.	529
536	250K Preburner Mixture Ratio Profile - Run 46 (Transient from 7% to 80% Rated Flows).	531
537	Preburner Igniter Installation With Dual Electrical Exciter Units.	532
538	250K Preburner Igniter Test Stand Schematic (Rig F-35100R).	533
539	Variable Length Thermocouple Location and Temperature Recorded.	534
540	Test Data from Test 250I54PB.	534
541	Preburner Mixture Ratio vs Percent Vacuum Thrust ADP Demonstration Engine	566
542	Alternative Secondary Slot Configuration.	567
543	250K Preburner Test Rig Assembled for Test.	567
544	250K Preburner Test Rig Installed in Test Facility. .	568

ILLUSTRATIONS (Continued)

FIGURE		PAGE
545	250K Torch Igniter Start Transient on Preburner Test Rig (Run 22)	569
546	250K Preburner Test Rig (Run 6)	569
547	250K Preburner Injector - View Showing Burn Damage to Dual-Orifice Oxidizer Nozzles in Plane of Transfer and Entry Slots	570
548	Schematic of 250K Preburner Injector Showing Method of Removal of Damaged Dual-Orifice Oxidizer Nozzle	570
549	250K Preburner Injector - View Showing the Injector from Test Rig F-33447-1 After Replacement of Five Damaged Dual-Orifice Oxidizer Nozzles, View 1	571
550	250K Preburner Injector - View showing the Injector from Test Rig F-33447-1 After Replacement of Five Damaged Dual-Orifice Oxidizer Nozzles, View 2	571
551	250K Preburner Injector Dual-Orifice Oxidizer Nozzle View Showing a Nozzle Unit With Damaged Slot Section Removed	572
552	Schematic of 250K Preburner Injector Dual-Orifice Nozzle Assembly Showing the Replacement of Damaged Entry Slot Section	572
553	Revised 250K Preburner Injector Oxidizer Purge Schematic	573
554	Modified Purge Systems for 250K Preburner Testing (Effective Run 32)	574
555	Temperature Profile for Run 46	574
556	Preburner Injector Fuel Drive System	576
557	Preburner Injector Modification	576
558	Preburner Dual-Orifice Oxidizer Element Water Flow Test at 300 psid	577
559	Temperature Profile Comparison of the Three Preburner Injectors Tested During Phase I	578
560	Preburner Temperature Profile Comparison of Three Injector Configurations	578
561	Preburner Test at 100% Level	579
562	250K Preburner Dome Housings - View Showing Comparison of Revised Dome Housing to Original Design	580

ILLUSTRATIONS (Continued)

FIGURE		PAGE
563	Data from Run 19 (Rig F-33463-2A) Describing Power Level Ramp to 20% Thrust.	583
564	250K Preburner Test Rig (Run 19).	583
565	250K Preburner Test Rig (Run 22).	584
566	Data from Run 24 (Rig F-33463-2A) Describin Power Level Ramp to 50% Thrust.	585
567	250K Preburner Dynamic Stability Data - Run 64 (100% Flow).	588
568	250K Preburner Dynamic Stability Data - Run 65 (20% Flow)	588
569	E-8 High Pressure Test Facility	600
570	Preburner Control Block Diagram	601
571	250K Preburner Test Sequence.	602
572	Staged-Combustion Rig Configuration	605
573	Main Burner	606
574	Main Injector Cor iguration	607
575	Main Injector Spraybar Cross-Section.	608
576	Main Injector Assembly.	608
577	Main Chamber Configuration.	610
578	Cross Section of Typical Photoengraved Wafer. . . .	610
579	Photoengraved Spiral Groove Average Widths for 250K Chamber Plates	611
580	Photoengraved Spiral Groove Average Depths for 250K Chamber Plates	612
581	Photoengraved Spiral Groove Average Areas for 250K Chamber Plates	613
582	Relative Coolant Flux vs Average Wafer Flow Area	614
583	250K Translating Nozzle Showing Drive Mechanism	614
584	250K Translating Nozzle Showing Primary and Sheetmetal Secondary.	615
585	Main Chamber Pulse Gun Installation	616
586	Main Chamber Pressure Transducer Installation.	616
587	250K Main Chamber Pulse Testing Configuration	617

ILLUSTRATIONS (Continued)

FIGURE		PAGE
588	Staged-Combustion Rig Installed in Test Stand.	618
589	Throttled Vacuum Performance, Area Ratio = 20	620
590	Demonstration of Cooled Thrust Chamber Thermal Strain Relief.	622
591	Effect of Strain on Wafer Low Cycle Fatigue Life . . .	622
592	Two-Directional Thermal Strain Reliefs	623
593	Grooved Wafer Thermal Relief	623
594	Vacuum Performance at 100% Thrust-Area Ratio = 60	624
595	Sea Level Performance at 100% Thrust, Area Ratio = 60.	625
596	Throttled Sea Level Performance, Area Ratio = 20	626
597	Main Injector History, Cooling Optimization and Performance Test Series.	629
598	Main Chamber History, Cooling Optimization and Performance Test Series	630
599	Test No. 15 Preburner Temperature and Pressure	631
600	250K Staged-Combustion Test Sequence - Test No. 250SC3C.	632
601	250K Staged-Combustion Rig Operating at 100% Thrust.	633
602	Zone 16 Estimated Surface Temperature vs Zone Coolant Flow	634
603	Coolant Mass Flow.	634
604	Main Chamber Surface Temperature Pattern (Tests 250SC7C Through 250SC11C)	635
605	Main Chamber Wall Temperature Profiles	636
606	Post-Test Condition of Preburner Injector.	636
607	Typical 250K Translating Nozzle Test Data - Test No. 250SC9C	638
608	Typical 250K Translating Nozzle Test Data - Test No. 250SC11C.	639
609	250K Two-Position Nozzle Tests	640
610	Wall Static Pressures of 250K Translating Nozzle Tests	640

ILLUSTRATIONS (Continued)

FIGURE		PAGE
611	250K Staged-Combustion Rig Configuration.	641
612	Test 250CP1C Dynamic Pressure Data (20% Thrust, r_{inj} = 5.9, r_o = 5.1).	642
613	Test 250CP2C Dynamic Pressure Data (100% Thrust, r_{inj} = 6.70, r_o = 5.43)	642
614	Test 250CP3C Dynamic Pressure Data (100% Thrust, r_{inj} = 8.46, r_o = 6.48)	643
615	Test 250CP1C Dynamic Pressure Data (20% Thrust, r_{inj} = 5.87, r_o = 5.11)	643
616	Pretest Condition of Main Chamber	644
617	Post-Test Condition of Main Chamber (250CP3C)	644
618	E-8 High Pressure Test Facility	646
619	E-8 Test Stand Flow Schematic	647
620	Staged-Combustion Control Block Diagram	649
621	Operating or Nonoperating Engine Acceleration Requirements.	651
622	Demonstrator Engine Control System.	657
623	Operational Envelope.	661
624	Transpiration Cooling Flow vs Thrust and Mixture Ratio	661
625	Main Fuel Pump Design Suction Capability.	662
626	Main Oxidizer Pump Design Suction Capability. . . .	662
627	Engine Section Diagram.	663
628	Fuel Low-Speed Inducer and Flowmeter Analog Section.	665
629	Fuel Low-Speed Inducer Characteristics Curve (Sheet 1)	666
630	Fuel Low-Speed Inducer Characteristics Curve (Sheet 2)	666
631	Main Fuel Pump and Turbine Characteristics Curve (Sheet 1)	670
632	Main Fuel Pump and Turbine Characteristics Curve (Sheet 2)	670
633	Oxidizer Low-Speed Inducer Characteristics Curve (Sheet 1)	681
634	Oxidizer Low-Speed Inducer Characteristics Curve (Sheet 2)	681

ILLUSTRATIONS (Continued)

FIGURE		PAGE
635	Main Oxidizer Pump and Preburner Injector Characteristics Curve (Sheet 1)	684
636	Main Oxidizer Pump and Preburner Injector Characteristics Curve (Sheet 2)	684
637	Logic Diagram Used for Analog Simulation	693
638	Vacuum Specific Impulse vs Thrust With Base Contour Two-Position Nozzle (r = 5.0)	720
639	Vacuum Specific Impulse vs Thrust With Base Contour Two-Position Nozzle (r = 5.5)	720
640	Vacuum Specific Impulse vs Thrust With Base Contour Two-Position Nozzle (r = 6.0)	721
641	Vacuum Specific Impulse vs Thrust With Base Contour Two-Position Nozzle (r = 6.5)	721
642	Vacuum Specific Impulse vs Thrust With Base Contour Two-Position Nozzle (r = 7.0)	722
643	Vacuum Specific Impulse vs Thrust With Maximum Performance Contour Two-Position Nozzle (r = 5.0)	722
644	Vacuum Specific Impulse vs Thrust With Maximum Performance Contour Two-Position Nozzle (r = 5.5)	723
645	Vacuum Specific Impulse vs Thrust With Maximum Performance Contour Two-Position Nozzle (r = 6.0)	723
646	Vacuum Specific Impulse vs Thrust With Maximum Performance Contour Two-Position Nozzle (r = 6.5)	724
647	Vacuum Specific Impulse vs Thrust With Maximum Performance Contour Two-Position Nozzle (r = 7.0)	724
648	Vacuum Specific Impulse vs Thrust With Minimum Surface Area Contour Two-Position Nozzle (r = 5.0)	725
649	Vacuum Specific Impulse vs Thrust With Minimum Surface Area Contour Two-Position Nozzle (r = 5.5)	725
650	Vacuum Specific Impulse vs Thrust With Minimum Surface Area Contour Two-Position Nozzle (r = 6.0)	726
651	Vacuum Specific Impulse vs Thrust With Minimum Surface Area Contour Two-Position Nozzle (r = 6.5)	726

ILLUSTRATIONS (Continued)

FIGURE		PAGE
652	Vacuum Specific Impulse vs Thrust With Minimum Surface Area Contour Two-Position Nozzle (r = 7.0)	727
653	Vacuum Specific Impulse vs Chamber Pressure (100,000-lb Thrust)	727
654	Vacuum Specific Impulse vs Chamber Pressure (150,000-lb Thrust)	728
655	Vacuum Specific Impulse vs Chamber Pressure (200,000-lb Thrust)	728
656	Vacuum Specific Impulse vs Chamber Pressure (250,000-lb Thrust)	729
657	Vacuum Specific Impulse vs Chamber Pressure (300,000-lb Thrust)	729
658	Vacuum Specific Impulse vs Chamber Pressure (350,000-lb Thrust)	730
659	Altitude Performance With Base Contour Two-Position Nozzle (r = 5.0)	731
660	Altitude Performance With Base Contour Two-Position Nozzle (r = 6.0)	732
661	Altitude Performance With Base Contour Two-Position Nozzle (r = 7.0)	733
662	Altitude Performance With Maximum Performance Contour Two-Position Nozzle (r = 5.0)	734
663	Altitude Performance With Maximum Performance Contour Two-Position Nozzle (r = 6.0)	735
664	Altitude Performance With Maximum Performance Contour Two-Position Nozzle (r = 7.0)	736
665	Altitude Performance With Minimum Surface Area Contour Two-Position Nozzle (r = 5.0)	737
666	Altitude Performance With Minimum Surface Area Contour Two-Position Nozzle (r = 6.0)	738
667	Altitude Performance With Minimum Surface Area Contour Two-Position Nozzle (r = 7.0)	739
668	Altitude Performance With Base Contour Nozzle, 100,000-lb Thrust, r = 5.0	740
669	Altitude Performance With Base Contour Nozzle, 250,000-lb Thrust, r = 5.0	740
670	Altitude Performance With Base Contour Nozzle, 350,000-lb Thrust, r = 5.0	741

ILLUSTRATIONS (Continued)

FIGURE		PAGE
671	Altitude Performance With Base Contour Nozzle, 100,000-lb Thrust, r = 6.0	741
672	Altitude Performance With Base Contour Nozzle, 250,000-lb Thrust, r = 6.0	742
673	Altitude Performance With Base Contour Nozzle, 350,000-lb Thrust, r = 6.0	742
674	Altitude Performance With Base Contour Nozzle, 100,000-lb Thrust, r = 7.0	743
675	Altitude Performance With Base Contour Nozzle, 250,000-lb Thrust, r = 7.0	743
676	Altitude Performance With Base Contour Nozzle, 350,000-lb Thrust, r = 7.0	744
677	Altitude Performance With Maximum Performance Contour Nozzle, 100,000-lb Thrust, r = 5.0	744
678	Altitude Performance With Maximum Performance Contour Nozzle, 250,000-lb Thrust, r = 5.0	745
679	Altitude Performance With Maximum Performance Contour Nozzle, 350,000-lb Thrust, r = 5.0	745
680	Altitude Performance With Maximum Performance Contour Nozzle, 100,000-lb Thrust, r = 6.0	746
681	Altitude Performance With Maximum Performance Contour Nozzle, 250,000-lb Thrust, r = 6.0	746
682	Altitude Performance With Maximum Performance Contour Nozzle, 350,000-lb Thrust, r = 6.0	747
683	Altitude Performance With Maximum Performance Contour Nozzle, 100,000-lb Thrust, r = 7.0	747
684	Altitude Performance With Maximum Performance Contour Nozzle, 250,000-lb Thrust, r = 7.0	748
685	Altitude Performance With Maximum Performance Contour Nozzle, 350,000-lb Thrust, r = 7.0	748
686	Altitude Performance With Minimum Surface Area Contour Nozzle, 100,000-lb Thrust, r = 6.0, P_c = 2000 psia	749
687	Altitude Performance With Minimum Surface Area Contour Nozzle, 250,000-lb Thrust, r = 6.0, P_c = 2000 psia	749
688	Altitude Performance With Minimum Surface Area Contour Nozzle, 350,000-lb Thrust, r = 6.0, P_c = 2000 psia	750

ILLUSTRATIONS (Continued)

FIGURE		PAGE
689	Altitude Performance With Minimum Surface Area Contour Nozzle, 100,000-lb Thrust, r = 6.0, P_c = 2500 psia.	750
690	Altitude Performance With Minimum Surface Area Contour Nozzle, 250,000-lb Thrust, r = 6.0, P_c = 2500 psia.	751
691	Altitude Performance With Minimum Surface Area Contour Nozzle, 350,000-lb Thrust, r = 6.0, P_c = 2500 psia.	751
692	Altitude Performance With Minimum Surface Area Contour Nozzle, 100,000-lb Thrust, r = 6.0, P_c = 3000 psia.	752
693	Altitude Performance With Minimum Surface Area Contour Nozzle, 250,000-lb Thrust, r = 6.0, P_c = 3000 psia.	752
694	Altitude Performance With Minimum Surface Area Contour Nozzle, 350,000-lb Thrust, r = 6.0, P_c = 3000 psia.	753
695	Altitude Performance With Minimum Surface Area Contour Nozzle, 100,000-lb Thrust, r = 6.0, P_c = 3000 psia.	753
696	Altitude Performance With Minimum Surface Area Contour Nozzle, 250,000-lb Thrust, r = 6.0 P_c = 3000 psia.	754
697	Altitude Performance With Minimum Surface Area Contour Nozzle, 350,000-lb Thrust, r = 6.0, P_c = 3000 psia.	754
698	Altitude Performance With Minimum Surface Area Contour Nozzle, 100,000-lb Thrust, r = 7.0, P_c = 3000 psia.	755
699	Altitude Performance With Minimum Surface Area Contour Nozzle, 250,000-lb Thrust, r = 7.0, P_c = 3000 psia.	755
700	Altitude Performance With Minimum Surface Area Contour Nozzle, 350,000-lb Thrust, r = 7.0, P_c = 3000 psia.	756
701	Altitude Performance With Minimum Surface Area Contour Nozzle, 100,000-lb Thrust, r = 6.6, P_c = 3500 psia.	756
702	Altitude Performance With Minimum Surface Area Contour Nozzle, 250,000-lb Thrust. r = 6.0, P_c = 3500 psia.	757

ILLUSTRATIONS (Continued)

FIGURE		PAGE
703	Altitude Performance With Minimum Surface Area Contour Nozzle, 350,000-lb Thrust, r = 6.0, P_c = 3500 psia.	757
704	Total Engine Weight vs Vacuum Thrust for Engine With Base Contour Two-Position Nozzle (ϵ_p 35)	758
705	Total Engine Weight vs Vacuum Thrust for Engine With Maximum Performance Contour Two-Position Nozzle (ϵ_p = 35).	758
706	Total Engine Weight vs Vacuum Thrust for Engine With Minimum Surface Area Contour Two-Position Nozzle (ϵ_p = 35).	759
707	Total Engine Weight vs Vacuum Thrust for Engine With Base Contour Two-Position Nozzle (ϵ_p = Minimum).	759
708	Total Engine Weight vs Vacuum Thrust for Engine With Maximum Performance Contour Two-Position Nozzle (ϵ_p = Minimum)	760
709	Total Engine Weight vs Vacuum Thrust for Engine With Minimum Surface Area Contour Two-Position Nozzle (ϵ_p = Minimum)	760
710	Total Engine Weight vs Chamber Pressure for 100,000-lb Thrust Engine (ϵ_p = 35)	761
711	Total Engine Weight vs Chamber Pressure for 150,000-lb Thrust Engine (ϵ_p = 35)	761
712	Total Engine Weight vs Chamber Pressure for 200,000-lb Thrust Engine (ϵ_p = 35)	762
713	Total Engine Weight vs Chamber Pressure for 250,000-lb Thrust Engine (ϵ_p = 35)	762
714	Total Engine Weight vs Chamber Pressure for 300,000-lb Thrust Engine (ϵ_p = 35)	763
715	Total Engine Weight vs Chamber Pressure for 350,000-lb Thrust Engine (ϵ_p = 35)	763
716	Total Engine Weight vs Chamber Pressure for 100,000-lb Thrust Engine (ϵ_p = Minimum).	764
717	Total Engine Weight vs Chamber Pressure for 150,000-lb Thrust Engine (ϵ_p = Minimum).	764
718	Total Engine Weight vs Chamber Pressure for 200,000-lb Thrust Engine (ϵ_p = Minimum).	765
719	Total Engine Weight vs Chamber Pressure for 250,000-lb Thrust Engine (ϵ_p = Minimum).	765

ILLUSTRATIONS (Continued)

FIGURE		PAGE
720	Total Engine Weight vs Chamber Pressure for 300,000-lb Thrust Engine (ϵ_p = Minimum)	766
721	Total Engine Weight vs Chamber Pressure for 350,000-lb Thrust Engine (ϵ_p = Minimum)	766
722	Engine Configuration With Two-Position Nozzle	767
723	Stowed Length vs Vacuum Thrust for Engine With Base Contour Two-Position Nozzle (ϵ_p = 33)	767
724	Stowed Length vs Vacuum Thrust for Engine With Maximum Performance Contour Two-Position Nozzle (ϵ_p = 35)	768
725	Stowed Length vs Vacuum Thrust for Engines With Maximum Surface Area Contour Two-Position Nozzle (ϵ_p = 35)	768
726	Minimum Stowed Length vs Vacuum Thrust for Engine With Base Contour Two-Position Nozzle	769
727	Minimum Stowed Length vs Vacuum Thrust for Engine With Maximum Performance Contour Two-Position Nozzle	769
728	Minimum Stowed Length vs Vacuum Thrust for Engine With Minimum Surface Area Contour Two-Position Nozzle	770
729	Stowed Length vs Chamber Pressure for 100,000-lb Thrust Engine (ϵ_p = 35)	770
	Stowed Length vs Chamber Pressure for 150,000-lb Thrust Engine (ϵ_p = 35)	771
731	Stowed Length vs Chamber Pressure for 200,000-lb Thrust Engine (ϵ_p = 35)	771
732	Stowed Length vs Chamber Pressure for 250,000-lb Thrust Engine (ϵ_p = 35)	772
733	Stowed Length vs Chamber Pressure for 300,000-lb Thrust Engine (ϵ_p = 35)	772
734	Stowed Length vs Chamber Pressure for 350,000-lb Thrust Engine (ϵ_p = 35)	773
735	Minimum Stowed Length vs Chamber Pressure for 100,000-lb Thrust Engine	773
736	Minimum Stowed Length vs Chamber Pressure for 150,000-lb Thrust Engine	774
737	Minimum Stowed Length vs Chamber Pressure for 200,000-lb Thrust Engine	774

ILLUSTRATIONS (Continued)

FIGURE		PAGE
738	Maximum Stowed Length vs Chamber Pressure for 250,000-lb Thrust Engine	775
739	Minimum Stowed Length vs Chamber Pressure for 300,000-lb Thrust Engine	775
740	Minimum Stowed Length vs Chamber Pressure for 350,000-lb Thrust Engine	776
741	Overall Length vs Vacuum Thrust With Base Nozzle Contour	776
742	Overall Length vs Vacuum Thrust With Maximum Performance Nozzle Contour	777
743	Overall Length vs Vacuum Thrust With Minimum Surface Area Nozzle Contour	777
744	Overall Length vs Chamber Pressure for 100,000-lb Thrust Engine	778
745	Overall Length vs Chamber Pressure for 150,000-lb Thrust Engine	778
746	Overall Length vs Chamber Pressure for 200,000-lb Thrust Engine	779
747	Overall Length vs Chamber Pressure for 250,000-lb Thrust Engine	779
748	Overall Length vs Chamber Pressure for 300,000-lb Thrust Engine	780
749	Overall Length vs Chamber Pressure for 350,000-lb Thrust Engine	780
750	Overall Exit Diameter vs Vacuum Thrust	781
751	Overall Exit Diameter vs Chamber Pressure For 100,000-lb Thrust Engine	781
752	Overall Exit Diameter vs Chamber Pressure for 150,000-lb Thrust Engine	782
753	Overall Exit Diameter vs Chamber Pressure for 200,000-lb Thrust Engine	782
754	Overall Exit Diameter vs Chamber Pressure for 250,000-lb Thrust Engine	783
755	Overall Exit Diameter vs Chamber Pressure for 300,000-lb Thrust Engine	783
756	Overall Exit Diameter vs Chamber Pressure for 350,000-lb Thrust Engine	784

ILLUSTRATIONS (Continued)

FIGURE		PAGE
757	Nozzle Throat Evaluation.	786
758	Discharge Coefficient vs Chamber Geometry	786
759	Typical P_c Tracer Showing Base for Firing Duration and Data Period.	792
760	Mixture Ratio Profile	798
761	$\Sigma (\Delta L/D)$ vs Area Ratio.	799
762	Nozzle Recovery Factor.	800
763	Mixture Ratio Profile Predicted by Combustion Gas Profile Model for r_{in} = 6.5 and P_c = 3000 psi . .	801
764	Rocket Exhaust Gas Sampling Probe	802
765	Rocket Exhaust Combustion Gas Sampling System	803
766	Exhaust Gas Sampling System Installed in Test Stand.	803
767	Probe Tap Locations	804
768	250K Exhaust Gas Analysis	805
769	Percent Free Hydrogen (Captured by Sampling Probe) vs Radial Distance From Centerline at Nozzle Exit.	806
770	Percent Oxygen (Captured by Sampling Probe) vs Radial Distance From Centerline at Nozzle Exit	806
771	Post-Test Condition of Exhaust Gas Sampling Probe . .	807

TABLES

TABLE		PAGE
I	Demonstrator Engine Characteristics.	1
II	Estimated Engine Performance, Weight, and Dimensions	13
III	Comparison of Engine Characteristics and Requirements	14
IV	Changes in Pump Discharge Pressures Indicated by Turbopump Optimization Study Results (Maximum Turbine Inlet Temperature = 2335°R)	21
V	Summary of Fuel Turbine Configurations	24
VI	Oxidizer Preburner Injector Volumes.	26
VII	Operating Condition to Maintain Thrust	31
VIII	Maintaining Component Limits	34
IX	Estimated Demonstrator Engine Operating Characteristics, Upper Stage Nozzle Extended (Cycle AF-1107)	44
X	Weight Breakdown by Components for Demonstrator Engine (250,000-lb Thrust, 100 in. Dia)	54
XI	Operating Characteristics of Oxidizer Low-Speed Inducer.	56
XII	Operating Characteristics of Fuel Low-Speed Inducer.	59
XIII	Operating Characteristics of Oxidizer Turbopump.	61
XIV	Operating Characteristics of Fuel Turbopump.	64
XV	Flight Engine Development Parameters	95
XVI	Estimated Flight Engine Operating Characteristics, Upper Stage Nozzle Extended (Cycle AF-1107)	96
XVII	Demonstrator and Flight Engine Estimated Weight	102
XVIII	Performance Index Summary (250K Study)	120
XIX	Performance Index Summary (350K Study)	121
XX	Preburner Injector Characteristics	129
XXI	Injector Characteristics.	136
XXII	Summary of Measured Data for the 50K Staged-Combustion Test Series.	151
XXIII	Summary of Calculated Performance for the 50K Staged-Combustion Test Series.	154

TABLE . (Continued)

TABLE		PAGE
XXIV	Potential Thermal Barrier and Temperature Sensitive Materials Test Evaluation (Test No. 50SC5), ...	161
XXV	Grooved Wafer Relative Cooling Requirements for Selected Materials.	184
XXVI	Wafer and Rigimesh Properties	187
XXVII	Wafer Rigimesh Material Evaluation.	188
XXVIII	Cage Material Spin Test Summary	216
XXIX	LH$_2$ Roller Bearing Test Summary	218
XXX	Quantitative Valve Summary Comparison	274
XXXI	Qualitative Valve Summary Comparison.	275
XXXII	Allowable Mixture Ratio Control Valve Loads and Stresses.	281
XXXIII	Test Summary, Mixture Ratio Valve F-33406	285
XXXIV	Test Summary, Mixture Ratio Valve F-35106	317
XXXV	Test Summary, Rotary Shaft Seal Test Rig F-33443. .	325
XXXVI	Flow Divider Valve Candidates	381
XXXVII	Flow Divider Valve F-33455.	419
XXXVIII	Flow Divider Valve F-33464.	421
XXXIX	Flow Divider Valve F-33469.	422
XL	Translating Seal Rig Test Summary	424
XLI	Chamber Coolant Valve Parts Stress Margins.	474
XLII	Allowable Chamber Coolant Valve Loads	475
XLIII	Translating Seal Test Rigs.	487
XLIV	350K Preburner Igniter Tests.	539
XLV	350K Preburner Test Summary	541
XLVI	Summary of Measured Parameters for Preburner Tests	591
XLVII	Summary of Calculated Performance for Preburner Tests	593
XLVIII	Summary of Measured Parameters for Preburner During Staged-Combustion Tests.	595
XLIX	Summary of Calculated Performance for Preburner During Staged Combustion Tests.	597

TABLES (Continued)

TABLE		PAGE
L	Summary of Measured Data for 250K Staged-Combustion Test Series, ...	624
LI	Summary of Preliminary Calculated Performance for 250K Staged-Combustion Test Series, ...	627
LII	Pulse Test Data Tabulation, ...	641
LIII	Allowable ε Load (10 hr), ...	652
LIV	f_{14} (KOFHT) as a Function of (OFC), ...	667
LV	$f_6\left\|W\sqrt{T}/(AP)\right\|$ as a Function of (PHDC/PAMB), ...	668
LVI	f_{49} (WTC) as a Function of (PFPD)	671
LVII	$f_{15}\left\|W\sqrt{T}/(AP)\right\|$ as a Function of (PHX1/PTRA)	674
LVIII	$f_{17}\left(\sqrt{1-(PTRA/PHX1)^{\gamma-1/\gamma}}\right)$ as a Function of (PTRA/PHX1)	674
LIX	f_{43}(KOFTT) as a Function of (OFC)	676
LX	f_{50}(KOFTF) as a Function of (OFC)	677
LXI	$f_{24}\left\|W\sqrt{T}/AP)\right\|$ as a Function of (PHX2/PB)	679
LXII	f_{31}(RB · TB) as a Function of (OFB)	686
LXIII	$f_{32}\left(1/\sqrt{RB \cdot TB}\right)$ as a Function of (OFB), ...	686
LXIV	$f_{33}\left\|W\sqrt{RT}/(AP)\right\|$ as a Function of (PB/PMIJ), ...	686
LXV	$f_{34}\left(\sqrt{CPB \cdot TB}\right)$ as a Function of (OFB)	687
LXVI	$f_{35}\left(\sqrt{1-(PMIJ/PB)^{\gamma-1/\gamma}}\right)$ as a Function of (PMIJ/PB)	687
LXVII	f_{39}(RC · FC) as a Function of (OFC)	689
LXVIII	$f_{40}\left\|1/(\eta_c^* \cdot C^*)\right\|$ as a Function of (OFC), ...	689
LXIX	$f_{38}\left\|W\sqrt{RT}/(AP)\right\|$ as a Function of (PMIJ/PC), ...	689
LXX	Engine Initial Conditions at Engine Mixture Ratio of 6 and Thrust Levels of 20, 50, and 100 Percent	703

LIST OF ABBREVIATIONS AND SYMBOLS

Item	Definition
A	Effective area
A^*	Throat area
ΔA^*	Change in throat area
A_c	Combustion chamber area
A_{cd}	Effective flow area
A_e	Nozzle exit area
A_f	Fairing area
A_g	Groove cross section at area
A_i	Interstage area
A_m	Maximum port area
A_{th}^*	Pretest throat area
A_p	Port area
A_s	Nozzle area at diffuser seal
A_x^*	Throat area at time X
ADP	Accessory drive pad
AFBI	Fuel preburner injector area
AFLW	Fuel low-speed inducer turbine bypass area
AFV	Main fuel venturi area
AJPP	Primary jet pump area
ALBI	Oxidizer preburner flow divider valve area
ALBT	Oxidizer low-speed inducer turbine area
AMRC	Mixture ratio control area
ATC	Turbine, dome, and igniter
ATHC	Thrust control area
ATRV	Transpiration cooling flow valve area
c^*	Characteristic velocity
c^{*}_{th}	Theoretical characteristic velocity
C_d	Discharge coefficient
C_f	Thrust coefficient
$C_{F_{vac}}$	Vacuum thrust coefficient
$C_{F_{vac}}$	Delivered vacuum thrust coefficient

(This page is Unclassified)

LIST OF ABBREVIATIONS AND SYMBOLS (Continued)

Item	Definition
C_n	Nozzle contour type correction factor
C_p	Coolant specific heat
C_v	Velocity coefficients
D_H	Hydraulic diameter
D_v	Valve diameter
e	Nozzle exit
f	Fuel
f_{actual}	Plate friction factor
f_s	Smooth tube friction factor
F	Thrust
F_{vac}	Vacuum thrust
g	Gravitational constant
h	Turbine inlet enthalpy
h_g	Chamber heat transfer coefficient
I_s	Specific impulse
I_{sa}	Specific impulse without nozzle heat loss
I_{vac}	Vacuum specific impulse
I'_{vac}	Theoretical vacuum specific impulse
I_{sl}	Sea level specific impulse
J	$778 \frac{ft\ lb_f}{Btu}$
K	Experimentally determined value
L	Groove angle
L^*	Characteristic thrust chamber length
L_t	Instrumental groove length
L/D	Length to diameter ratio
MR	Momentum ratio
MRI	Mixture ratio input
NPSH	Net positive suction head
Nu	Nusselt No.
o	Oxidizer
O/F	Oxidizer/fuel
P	Static pressure

LIST OF ABBREVIATIONS AND SYMBOLS (Continued)

Item	Definition
P_a	Ambient pressure
P_c	Chamber pressure
P_{inj}	Static pressure at the injector face
P_{cn}	Static pressure at nozzle entrance
P_e	Nozzle exit pressure
P_x	Diffuser pressure at nozzle exit
P_{sl}	Standard pressure at sea level
ΔP	Pressure drop
P_D	Venturi discharge pressure (total)
ΔP_i	Incremental pressure drop
$(\Delta P_i)_s$	Incremental pressure drop for a smooth tube
P_{in}	Venturi inlet pressure (total)
P_L	Pressure loss
P_o	Total pressure
ΔP_p	Primary pressure drop
P_t	Throat pressure
PLA	Power lever angle
q_x	Heat loss at section X
r	Mixture ratio
r_{inj}	Injector mixture ratio
r_{oa}	Overall mixture ratio
R	Gas constant
r_c (req)	Chamber mixture ratio request
Re	Reynolds Number
R_f	Recovery factor
r_{im}	Pioneer mixture ratio
r_t	Throat mixture ratio
r_{pv}	Preburner mixture ratio
r_{pb} (max)	Maximum preburner mixture ratio
r_{pb} (req)	Preburner mixture ratio request
r_{pb} (req)	Preburner mixture ratio request (limited)
s	Laplace operator

LIST OF ABBREVIATIONS AND SYMBOLS (Continued)

Item	Definition
S	Number of grooves per plate
SITVC	Secondary fluid injection thrust vector control
T	Total temperature
T_{exit}	Temperature at nozzle exit
T_{adw}	Adiabatic wall temperature
T_o	Coolant ambient (reservoir) temperature
T_w	Wall hot side temperature
T_x	Temperature at location X
TBO	Time between overhaul
TVC	Thrust vector control
v, V	Velocity
V_c	Combustion chamber volume
VR	Injection velocity ratio
$\dot{w}$	Mass flow rate
$\dot{w}/A_s$	Coolant mass flux
$\dot{w}_c$	Cooling flow
$\dot{w}/A_x$	Coolant flow per groove cross-sectional area
W_{ic}	Corrected burnout weight
$\dot{w}_{cc}$	Chamber cooling flow
W_e	Installed engine weight
$\dot{w}_f$	Total fuel flow
$\dot{w}_f$(meas)	Flowmeter total fuel flow
$\dot{w}_{fp}$	Ireburner fuel flow
$\dot{w}_{fpb}$	Control preburner fuel flow
$\dot{w}_o$	Total oxidizer flow
$\dot{w}_o$(meas)	Flowmeter total oxidizer flow
$\dot{w}_{o_{(corr)}}$	Chamber oxidizer flow corrected
$\dot{w}_{o_{(req)}}$	Fuel-rich oxidizer flow request
$\dot{w}_{o_{(sec)}}$	Main injector secondary flow
$\dot{w}_{o_{(sec)}}$	Injector secondary flow
$\dot{w}_{o_{(sec)}}$(corr)	Fuel-rich oxidizer flow corrected

LIST OF ABBREVIATIONS AND SYMBOLS (Cont'd)

Item	Definition
$\dot{w}_{cp}$ (corr)	Turbine flow at corrected flow
$\dot{w}_{cp}$ (req)	Engine corrected flow request
$\dot{w}_f$	Fuel flow
$\dot{w}_f$	Flow rate
$\dot{w}_v$	Secondary flow
$\dot{w}_t$	Total engine flow ($\dot{w}_f + \dot{w}_a$)
$\dot{w}_t$ (act)	Total actual gas propellant flow
$\dot{w}_t$ (corr)	Total propellant flow corr
$\dot{w}_{cp}$ (req)	Corr. engine flow request
$\dot{w}_{fb}$ (corr)	Elements of computation of corr flow effect
$\dot{w}_{fg}$ (corr)	Fuel control computation corr flow
$\dot{w}_{fs}$ (corr)	Steady-state computation corr flow
W_f	Fuel number index
w/f	Air ratio to stoich ratio
$\dot{w}_t$	Total propellant flow rate through an engine
WCV	Engine, duct, and turbine cooling flow
ρ	Water total flow reference conditions
χ	Max throttle angle position
γ	Max throttle angle position
Δ	Angle between the projections of the
ζ	Actuator indicates thrust condition
β	Coolant entrance angle
γ	Ratio of specific heat
ϕ	Nozzle area ratio
ϵ	Correction factor
ϕ_n	Nozzle area ratio
η	Coefficient for control
η_{cp}	Engine corrected
η_{cp}	Engine corrected
η_t	Turbine efficiency

LIST OF ABBREVIATIONS AND SYMBOLS (Continued)

Item	Definition
$(\dot{m}_f)$	Fuel factor
θ	Angle
ρ_w	Heat exchanger wall reflectance
μ	Drop size (microns)
ρ	Density
ρ_1	Density of radiation 1
τ	Time constant

AD 385 910

AUTHORITY: AFRPL
ltr. 5 Feb 86



SECTION I
INTRODUCTION

(U) Phase I of the Advanced Development Program for an Advanced Cryogenic Rocket Engine was a 19-month program starting 1 March 1966 and ending 30 September 1967. Phase I was an evaluation of the critical technology associated with the staged-combustion two-position ball-nozzle engine concept in the areas of the preburner, main chamber, nozzle, turbopump bearings, controls, and a preliminary design of the demonstrator engine system. The program was oriented toward a demonstrator engine module having the characteristics outlined in table I.

(C) Table I. Demonstrator Engine Characteristics

Nominal Vacuum Thrust	250,000 lb
Minimum Delivered I_s	96% of theoretical shifting I_s at rated thrust
	95% of theoretical shifting I_s during throttling
Overall Mixture Ratio	Engine to operate from 5 through 7 with a nominal of 6
Throttling Range	Continuous down to 20% of rated thrust
Expansion Ratio	Low Area Ratio: approximately 60:1 High Area Ratio: approximately 100 in nozzle exit diameter
Durability	Engine design to be based on a 10-hour time between overhauls (TBO) life criterion, 100 reuses, and 300 starts
TVC Capability	± 7 degree equivalent angle at 30°/sec
Ignition	Multiple starts with restart at altitude
NPSH	LH_2: 60 ft LO_2: 16 ft

(U) Phase I of the program consisted of two major tasks and specific subtasks as follows:

Task I - Analysis and Design

a. Module Design
b. Applications Study

Task II - Fabrication and Test

c. Cooling Investigation
d. Turbopump Components Evaluation
e. Module Control System Investigation
f. Preburner Demonstration
g. 250K Staged-Combustion Demonstration

(U) The Module Design subtask had as its objectives the accomplishment of the following engine system studies and analyses: a system cycle balance, steady-state off-design analyses, transient analyses, component and system design studies, a weight study, and a parametric engine study. The module design studies were conducted to integrate the component technology data into an engine system with the required performance, weight, simplicity, reliability, life and versatility.

(U) The Application Study subtask included generation of engine/vehicle installation designs, parametric equations for installation equipment weight and size for both 250K and 350K sized engine systems, engine/vehicle performance, and an evaluation of alternative methods of thrust vector control.

(U) The Cooling Investigation subtask included design, fabrication, and test of a 50K main injector, and uncooled and cooled main chambers to evaluate cooling requirements, new materials and fabrication techniques, performance, and chamber geometry. The objective of this program was to demonstrate a high impulse efficiency, and to demonstrate the feasibility of a two-position translating nozzle.

(C) The Turbopump Components subtask included design, fabrication, and testing of turbopump bearings at high DN values to demonstrate durability and long life under the predicted operating conditions. Life and durability were based on the criteria of 10 hours time between overhauls (TBO), 100 reuses, and 300 starts.

(U) The Module Control System subtask included design, fabrication, and testing to demonstrate the feasibility of the critical control components associated with a variable-thrust, high-pressure, staged-combustion, liquid rocket engine. The critical control components included the oxidizer flow divider valve for the preburner, the mixture ratio valve, and the ignition systems.

(U) The Preburner Demonstration subtask objectives included design, fabrication, and testing to demonstrate the satisfactory operation of a full-scale 250K preburner over the required operating range

(U) The 250K Staged-Combustion subtask included design, fabrication, and testing to demonstrate the satisfactory operation and performance of a full-scale 250K preburner, main burner, and two-position nozzle as a combined staged-combustion rig.

(C) Under the Module Design subtask, the major accomplishment was the definition of the demonstrator engine system for the Phase II program. The engine configuration uses a staged-combustion cycle and [illegible] a lightweight two-position bell nozzle. The overall engine performance and operating characteristics were determined by combining the individual component technologies that have been demonstrated on the USAF, NASA, and company programs. Component performance data were integrated with engine cycle balance studies to optimize the engine configuration. These cycle balance data were also used to define the component requirements for hardware designs and to supply the basis for dynamic system simulations used in transient and stability analyses. Steady-state performance analysis over the thrust and mixture ratio operating ranges, and steady-state off-design analyses were completed. A control system analysis was conducted to establish the engine dynamics and to estimate the control system requirements. Detailed weight studies were also conducted. The flight engine data were derived using projected improvements in turbopump efficiencies, reduced main chamber coolant flow, and flightweight designs that could result from an engineering development program. The flight engine data were used to establish the base points for the parametric analysis of engine performance and envelope. These parametric data were used in the Applications Study.

(U) Under the Applications Study subtask, engine/vehicle installations, parametric equations for installation equipment for both 250K and 330K sized engine system, engine/vehicle performance, and an evaluation of alternative methods of thrust vector control were conducted and completed. These studies are presented in a separate final report, AFAPL-TR-67-270, "Applications Study for a High Performance Cryogenic Staged-Combustion Rocket Engine."

(C) Under the Cooling Investigation subtask, 14 successful 50K staged-combustion tests were conducted. Five of the tests were made with the uncooled chambers to evaluate performance at chamber contraction ratios of three and five and chamber lengths from 8.5 to 13 inches. Nine of the tests were made with a cooled copper wafer liner to optimize the main chamber cooling flow at design chamber pressure and determine the effect of cooling on performance. The last three cooled tests evaluated the two-position nozzle. Studies were also conducted to evaluate various materials and configurations for possible use in an advanced cooled chamber. Hardware that was designed and manufactured for this cooling investigation included one cooled chamber, nine uncooled chamber graphite nets, one film-cooled copper chamber liner, one main injector, and one two-position sheet metal nozzle skirt.

(C) Under the Turbopump Components subtask, the fuel turbopump bearing configuration and principle requirements that were established for the preliminary 250K turbopump design were as follows: (1) a 55mm ID roller bearing, (2) a design speed of 46,000 rpm, (3) a maximum radial load of 1700 lb, and (4) a 10-hour bearing life. Eight spin tests were conducted

to provide a relative ranking of mechanical integrity of candidate cages. Armalon and Polyimide SP-1 were the only materials that exceeded the design speed (approximately 25,000 rpm) without external armor and these materials were selected for evaluation in the bearing rig tests. Eleven tests were conducted for cage and bearing geometry screening tests. As a result of these tests, the bearing configuration selected for endurance testing consisted of AISI 440C material rollers and races, and an outer-race-piloted Armalon cage, with 0.040-inch total roller end to inner race flange clearance. Negative internal radial clearance was used to provide roller preload. A total of 12 hours and 33 minutes of endurance was accumulated on the second roller bearing tested in the reaction position (85% load) of the test rig. This bearing remained in excellent condition with roller end wear less than 0.001 inch. The first reaction bearing failed, due to roller skewing, at 1 hour and 32 minutes. Four bearings were tested in the load ring position and these failed, due to roller skewing, at 7 hours and 26 minutes, 1 hour and 19 minutes, and 3 hours and 50 minutes, respectively, during this endurance testing.

(C) Under the Module Control System subtask, the critical control components associated with a variable-thrust, high-pressure, staged-combustion, liquid rocket engine were designed, fabricated, and tested. These control components were the preburner oxidizer flow divider valve, the mixture ratio valve, and the ignition systems. Testing of these control components has demonstrated the basic design concepts although further seal development is necessary. A comprehensive valve selection study was conducted to determine the best valve type for the chamber coolant valve, mixture ratio valve, thrust control, and preburner oxidizer flow divider valve, based on the functional and mechanical requirements of each. A translating seal rig was designed and fabricated, and nine endurance tests were conducted to evaluate candidate seal configurations. These translating seal rig endurance tests demonstrated acceptable leakage characteristics; less than 10 scim of vent seal leakage for the selected seal package configuration. A rotary shaft seal test program was also conducted to develop a laminated plastic lip seal, which demonstrated overboard leakage and endurance better than the target values.

(C) Under the Preburner Demonstration subtask, a full-scale 250K preburner was designed, manufactured, and tested. A dual-orifice oxidizer and variable-area fuel preburner injector configuration was selected for Phase I. The most significant achievements of the preburner test program were the resolution of test stand operational problems and the development of a preburner injector adequate for staged-combustion testing. The initial injector configuration did not provide a satisfactory temperature profile. Modifications to the fuel elements, provided a temperature profile of approximately 500°R at an average temperature of 2000°R. Further development is necessary to provide a temperature profile of 150°R or less at an average temperature of 2325°R, which is required for the demonstrator engine. The pulsing tests conducted on the preburner demonstrated dynamic stability. Pressure disturbance at 20% and 100% flow conditions, with approximately 110°R fuel temperature, damped to within 0.5% of nominal operating pressure within 30 milliseconds. The preburner torch igniters accumulated more than 250 firing tests, including rig tests, preburner pressure check firings, and preburner tests. This torch

igniter design has demonstrated excellent ignition characteristics. The primary use operated for time running in staged-combustion tests. Twelve of the preburner performance tests obtained all test objectives. 24 tests were classified as partially successful, 20 tests were classified as facility checkout runs, and 10 tests were aborted before useful data were obtained.

(C) Under the 250n staged-combustion subtask, a full-scale preburner, with burner, and two-position [redacted] was combined into a 250K staged-combustion rig was designed, manufactured, and tested with satisfactory results. Fourteen successful staged-combustion tests were conducted. Six tests were conducted to establish operating procedures and to optimize the chamber coolant flow rate. Five tests were conducted with the optimum coolant flow to demonstrate performance. Three pulsing with the optimum coolant flow to demonstrate performance. Three pulsing tests were conducted by firing 40 and 80 grain charges into the main chamber, and these tests did demonstrate dynamic combustion stability. On eight tests the two-position nozzle was translated. Four of these tests incorporated the regeneratively cooled primary nozzle.

CONFIDENTIAL

SECTION III
CONCLUSIONS AND RECOMMENDATIONS

(U) Studies conducted during this program resulted in the conclusions and recommendations listed for each of the major subtasks.

A. MODULE DESIGN STUDIES

(U) 1. Detailed analytical and design studies conducted to evaluate the benefits provided by dual, fuel-rich preburners showed that increased control complexity is required and only a small reduction in the fuel pump pressure is possible. It was concluded that the dual preburner cycle does not warrant further consideration.

(C) 2. Detailed analytical and design studies were conducted for several combinations of variable-area and dual-orifice injectors that might be used in the preburner. Analytical studies comparing ignition, start , and steady-state performance, temperature profile, feasibility, weight, and manufacturing complexity of the two principal injector configurations were made. It was concluded that an injector configuration using dual-orifice oxidizer and variable-area fuel elements was best for the preburner.

(U) 3. It was concluded that by detailed component optimization the engine module can provide the full mixture ratio range at rated thrust with significantly lower turbopump pressures than earlier module designs.

(U) 4. It was concluded that a variable turbine inlet area was required for the oxidizer low-speed inducer because at low flows (low thrust levels) there is not sufficient power to drive the oxidizer inducer with a constant turbine inlet area.

(C) 5. Based on the start transient analysis, it was concluded that the present areas of the fuel shutoff valve and the preburner flow divider valve (also a shutoff valve) will provide a positive means of safe transients with simple valve action.

(C) 6. Based on the shutdown transient analysis of the demonstrator engine, a basic sequencing procedure has been established for accomplishing a satisfactory shutdown from any thrust level.

(U) 7. It was concluded that the advantages of the lightweight (dump cooled) two-position nozzle compared with the conventional regeneratively cooled fixed bell nozzle are: lighter engine weight, improved sea level and low altitude performance, and better packaging.

(U) 8. A basic control system concept, which satisfied the static and dynamic engine requirements, was identified.

(U) 9. It is recommended that the demonstrator engine system for the Phase II program be based on demonstrated component performance levels, incorporate a lightweight two-position nozzle and be designed to operate at 2740-psia nominal chamber pressure.

(U) 10. Based on the weight analysis, weights of 3450 lb and 2680 lb have been established for the 100-inch diameter 250K demonstrator and flight engines, respectively.

B. APPLICATIONS STUDIES[1]

(U) 1. It was concluded that the mechanically gimbaled thrust vector control system provides better performance for all the ADP cases than hot-gas, secondary-injection systems. Therefore, the mechanically gimbaled TVC system has been selected for the demonstrator module.

(U) 2. It was concluded that one of the major advantages of the staged-combustion engine module is that the ability to stage-match the nozzle area ratio to the same power package adds greatly to the versatility of the engine to achieve high vehicle performance for all cases studied.

C. COOLING INVESTIGATION

(C) 1. Based on the 50K cooled staged-combustion tests, it was concluded that the transpiration coolant flow could be reduced to 1% of total flow for the 250K chamber; subsequent 250K staged-combustion tests confirmed this conclusion.

(C) 2. Based on the final performance analysis of the 50K staged-combustion tests, it was concluded that 96% of the theoretical shifting specific impulse at rated thrust up to an overall mixture ratio of 6.0 can be attained.

(C) 3. The 50K two-position nozzle tests demonstrated that this concept can provide the desired flow stabilization over the 5:1 throttling range with small exhaust gas-side loads.

D. TURBOPUMP COMPONENTS

(U) 1. It was concluded that 55mm x 100mm AISI 4400 roller bearings will provide the best design characteristics for the fuel turbopumps.

---

[1] The Applications Study subtask is discussed in detail in a separate final report, AFRPL-TR-67-270, "Applications Study for a High Performance Cryogenic Staged-Combustion Rocket Engine."

CONFIDENTIAL

(U) 2. Based on the spin tests and bearing R.S evaluation tests of candidate cage materials, Armalon is the best material.

(C) 3. Based on the turbopump components investigation, it was concluded that a roller bearing life of 10 hours with a radial load of 1700 lb at 48,000 rpm is feasible but additional development is needed to solve the roller skewing problem.

E. CONTROL SYSTEM

(C) 1. A comparison was made of alternative engine control systems that use chamber pressure as an indication of thrust level and that use direct measurement of the fuel and oxidizer flow rate. It was concluded that a major advantage in accuracy and repeatability results from using the flowmeter control system as compared with the pressure measurement control system.

(U) 2. Based on a detailed valve selection study, it was concluded that butterfly valves were best for both the mixture ratio and thrust control valves, a cavitating venturi was best for the chamber coolant valve, and a sleeve valve was best for the flow divider valve.

(U) 3. Based on calibration and hot firing tests, both the flow divider valve and mixture ratio valve have satisfactorily demonstrated basic component operating characteristics. Further development is needed to meet static and dynamic leakage limits.

(U) 4. A Kapton F and PTFE Teflon lip seal will meet the overboard leakage targets.

F. PREBURNER

(C) 1. Water flow tests were conducted on four single-element and one six-element, dual-orifice preburner oxidizer injector configurations to determine the best atomizing and performing configuration at 10%, 30%, and 100% flow conditions. It was concluded that the dual-orifice element with a straight-through primary, a tangential slot secondary, and a 15-degree convergence angle was best for the 230% preburner injector oxidizer element.

(C) 2. Water flow tests were conducted on a six-element, dual-orifice configuration that represented the cross section of the preburner injector. These tests were conducted to investigate the filling characteristics of the secondary passage and to investigate the effect of hydrostatic head on mixture ratio and temperature profile. These tests indicated that, below 12% thrust, the hydrostatic head

across the injector face from top to bottom could produce a temperature profile distortion of approximately 900°R. It was concluded that increasing the injector pressure drop to 325 psid at nominal thrust would eliminate the distortion caused by the hydrostatic effect.

(U) 3. It was concluded that preburner ignition was consistent and combustion was dynamically stable based on pulse tests. It was also concluded that redesign of the preburner dome flange to allow rated pressure operation and redesign of the preburner injector to provide a more uniform temperature profile is required.

C. STAGED COMBUSTION

(C) 1. Full-scale staged-combustion performance test data indicate the 96% specific impulse efficiency goal over the 5 to 7 mixture ratio range is attainable. Tests at 100% thrust have exceeded 96% of theoretical shifting specific impulse at overall mixture ratios between 5 and 6.3. Additional development will be required to attain the 96% efficiency level between mixture ratios of 6.3 and 7 and to achieve the 95% efficiency during throttling.

(C) 2. Based on the 250K staged-combustion tests, feasibility of the full-scale tandem-combustion concept was demonstrated by operation between 20% and 100% thrust with steady-state data points taken at 20%, 50%, 70%, and 100% of thrust.

(U) 3. These 250K tests indicate that the fundamental design of the 250K staged-combustion rig is sound.

(U) 4. Based on the 50K and 250K two-position nozzle tests, feasibility of this concept was demonstrated.

(U) 5. Based on the 250K main chamber pulsing tests, it was concluded that the main chamber and injector are dynamically stable in their present configuration.

SECTION IV
MODULE DESIGN

A. INTRODUCTION 11
B. SUMMARY 11
C. CONFIGURATION ANALYSIS 13
1. Demonstrator Engine Analysis 13
2. Flight Engine and Parametric Performance Data 92
3. Dual-Preburner Cycle Study 104

SECTION IV
MODULE DESIGN

A. INTRODUCTION

(U) The module design studies were conducted to combine the component technology data into an engine system with the required performance, weight, simplicity, reliability, life, and versatility.

(U) Component performance data were integrated with engine cycle balance studies to optimize the engine configuration. These cycle balance data were used to define the component requirements for hardware designs and to supply the basis for dynamic system simulations used in transient and stability analyses.

(U) Parametric engine performance data for wide ranges of thrust, chamber pressure, area ratio, and nozzle contour were generated.

B. SUMMARY

(U) The major accomplishment of the module systems analysis task was the definition of the demonstrator engine system for the Phase II program. The recommended engine configuration uses a staged-combustion cycle and incorporates a lightweight two-position bell nozzle. The overall engine performance was determined by combining the individual component technologies that have been demonstrated during USAF, NASA, and company programs.

(U) The engine propellant flow paths and relative locations of the major components are illustrated in figure 1.

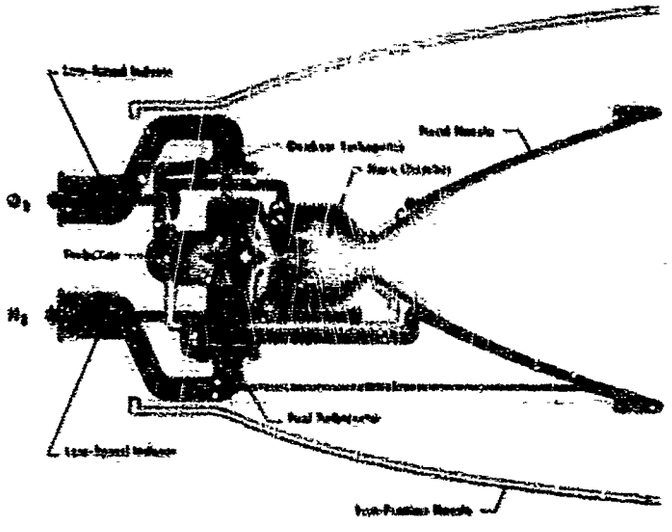


Figure 1. Propellant Flow Schematic FD 21001

(U) The turbopumps, preburner, main combustion chamber, and controls are integrated at the upper end of the engine envelope. This assembly is the "power package." This arrangement provides a system where the nozzle skirts can be interchanged without modifying the power package, except for retimming of control settings. Engine driven low-speed inducers provide low NPSH capability for the fuel and oxidizer systems. The physical orientation of components is shown in figure 2.

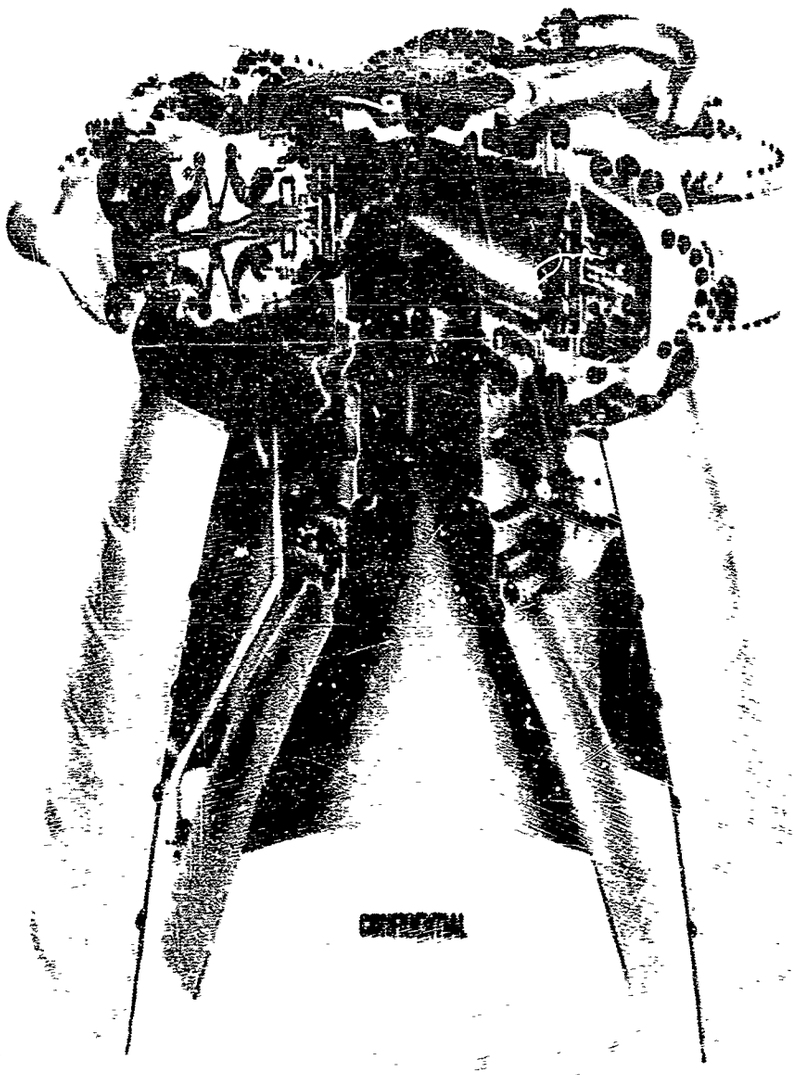


Figure 2. 250K Engine Component Arrangement FD 21027A

(U) Estimated demonstrator and flight engine characteristics are compared in table II. The flight engine data were derived using projected improvements in turbopump efficiencies, reduced main chamber coolant flow, and flightweight designs.

THIS PAGE CONTAINS SUBJECT MATTER COVERED BY A SECRECY ORDER WITH A MODIFYING "SECURITY REQUIREMENTS PERMIT" ISSUED BY U.S. COMMISSIONER OF PATENTS

(C) Table II. Estimated Engine Performance, Weight, and Dimensions

Parameter	Demonstrator	Flight
Vacuum Thrust, lb	250,000	250,000
Nominal Chamber Pressure, psia	2740	3000
Nozzle Area Ratio		
Extended	166	184
Retracted	80	80
NPSH (Required), ft		
Fuel	60	60
Oxidizer	16	16
Vacuum Specific Impulse, sec		
r = 5	462	465
r = 6	460	463
r = 7	450	456
Dry Weight, lb	3450	2680
Overall Diameter, in.	100	100
Length, in.		
Nozzle Extended	170	166
Nozzle Retracted	101	90
Thrust Range	20% to 100%	20% to 100%
Mixture Ratio Range	5 to 7	5 to 7

(U) The flight engine data were used to establish the base points for the parametric analysis of engine performance and envelope. These parametric data were used in the Applications Study portion of this program.

(U) The above engine configurations were defined as a result of a continuous process of cycle and component investigations and analyses. Prediction of steady-state performance over the thrust and mixture ratio operating ranges was completed and transient analyses were conducted. A control system analysis was conducted to establish the engine dynamics and to estimate the control system requirements.

C. CONFIGURATION ANALYSIS

1. Demonstrator Engine Analysis

a. General

(C) The primary purpose of the demonstrator engine analysis was to define a lightweight, high performance rocket engine configuration that would have the characteristics outlined in table III. Results from individual related component technology programs and advanced engine design studies were used to determine the overall engine performance. A steady-state cycle balance was evolved that provided 5:1 continuous throttling

capability and full mixture ratio range (5 to 7) at all operating thrust levels. The engine component designs were optimized to provide the mixture ratio range capability with minimal turbopump speed and pressure requirements. Technology limits were set at the state-of-the-art levels demonstrated in the high pressure component technology programs conducted under contract for the Air Force and NASA, or by PWA under independent programs.

(C) Table III. Comparison of Engine Characteristics and Requirements

Item	Requirement	Demonstrator Engine	Flight Engine
Vacuum Thrust	250,000 lb @ nominal mixture ratio.	250,000 lb @ nominal mixture ratio.	250,000 lb @ nominal mixture ratio.
Sea Level Thrust	Not specified.	200,000 lb @ nominal mixture ratio.	211,000 lb @ nominal mixture ratio.
Minimum Delivered Specific Impulse	90% of theoretical shifting I_s @ rated thrust. 95% of theoretical shifting I_s during throttling.	99.0% of theoretical shifting I_s @ full thrust and r = 5. 99.2% of theoretical shifting I_s @ rated thrust and r = 6. 99.2% of theoretical shifting I_s @ full thrust and r = 7. 99.4% of theoretical shifting I_s @ 70% thrust and r = 6.	99.4% of theoretical shifting I_s @ full thrust and r = 5. 99.0% of theoretical shifting I_s @ rated thrust and r = 6. 99.2% of theoretical shifting I_s @ full thrust and r = 7. 99.0% of theoretical shifting I_s @ 70% thrust and r = 6.
Throttling Range	Continuous down to 70% of rated thrust.	Continuous down to 70% of rated thrust.	Continuous down to 60% of rated thrust.
Weight	Not specified.	3650 pounds with upper stage area ratio. 3350 pounds with booster stage area ratio.	3500 pounds with upper stage area ratio. 3250 pounds with booster stage area ratio.
Mixture Ratio Range	Engine operation from 5.0 to 7.0. Nominal design point 6.0.	Engine operation from 5.0 to 7.0 at any thrust between 105% and 70% of rated thrust. Nominal design point 6.0.	Engine operation from 5.0 to 7.0 at any thrust between 105% and 65% of rated thrust. Nominal design point 6.0.
Area Ratio	Area ratio(s) representative of booster and upper stage applications. Overall nozzle exit diameter will not exceed 100 inches.	Upper stage area ratio of 164, nozzle diameter of 100 inches. Booster stage area ratio of 75, nozzle diameter of 68 inches.	The engine can accept interchangeable nozzle skirts to optimize the area ratio for any of the vehicles defined in the applications study.
Propellant Conditions at Engine Inlet	LO_2: 15 ft at NPSH from one (1) atmosphere boiling temperature (162.3°R) to 190°R. LH_2: 40 ft NPSH from one (1) atmosphere boiling temperature (36.3°R) to 41°R.	LO_2: 15 ft NPSH from one (1) atmosphere boiling temperature to 190°R. LH_2: 40 ft NPSH from one (1) atmosphere boiling temperature to 41°R.	LO_2: 15 ft at NPSH from one (1) atmosphere boiling temperature (162.3°R) to 190°R. LH_2: 40 ft NPSH from one (1) atmosphere boiling temperature (36.3°R) to 41°R.
Environmental Conditions	Sea level to vacuum conditions. Combined accelerations: 10g axial with 2g's transverse, 6.5g axial with 3g's transverse, 3g axial with 6g's transverse.	Sea level to vacuum conditions. Combined accelerations: 10g axial with 2g's transverse, 6.5g axial with 3g's transverse, 3g axial with 6g's transverse.	Sea level to vacuum conditions. Combined accelerations: 10g axial with 2g's transverse, 6.5g axial with 3g's transverse, 3g axial with 6g's transverse.
Engine/Vehicle Interface Conditions	The engine will receive no external power, with the exception of normal electrical power and 3000 psig helium from the vehicle.	The engine will receive no external power, with the exception of normal electrical power and 3000 psig helium from the vehicle.	The engine will receive no external power, with the exception of normal electrical power and 3000 psig helium from the vehicle.
Durability	10-hour time between overhauls, 100 reuses, 200 starts, 300 thermal cycles, 10,000 valve cycles.	10-hour time between overhauls, 100 reuses, 200 starts, 300 thermal cycles, 10,000 valve cycles.	10-hour time between overhauls, 100 reuses, 200 starts, 300 thermal cycles, 10,000 valve cycles.
Single Continuous Run Duration	Capability from 10 sec to 600 sec.	Capability from 10 sec to 600 sec.	Capability from 10 sec to 600 sec.
Engine Starts	Multiple restart at sea level or altitude.	Multiple restart at sea level or altitude.	Multiple restart at sea level or altitude.
TVC	Amplitude: 2°, Rate: 20°/sec, Acceleration: 30 rad/sec².	Amplitude: 2°, Rate: 20°/sec, Acceleration: 30 rad/sec².	Amplitude: 2°, Rate: 20°/sec, Acceleration: 30 rad/sec²
Control Capability	±3% accuracy in thrust and mixture ratio at rated thrust. Excursion from extreme to extreme in thrust or mixture ratio within 3 sec.	±3% accuracy in thrust and mixture ratio at rated thrust. Excursion from extreme to extreme in thrust or mixture ratio within 3 sec.	±3% accuracy in thrust and mixture ratio at rated thrust. Excursion from extreme to extreme in thrust or mixture ratio within 3 sec.

(U) Preliminary engine cycle balances using estimated component performance defined the operating conditions of the major engine components. Based on the cycle requirements, hardware was designed for rig-testing. Results of these tests can be used in designing the hardware for a demonstrator engine.

(C) Steady-state analyses conducted defined the operating characteristics, performance, and weight, as well as the control system, for the demonstrator engine. Transient analyses investigated the problems of and defined the control system requirements for safe start and shutdown operation. Ramp times and the resulting operating characteristics were defined for accelerations and decelerations between 20% and 100% thrust. System dynamics using both digital and analog engine simulations, were conducted to investigate fuel system stability and to provide a tool for the evaluation of the controls system transient operation and fuel side stability.

b. Cycle Analysis

(1) General

(U) The steady-state analyses were conducted to generate engine cycle data that would define the configuration, system characteristics, and the component operating requirements of a Phase II demonstrator engine. Cycle data generated early in Phase I of the program were used to define the operating requirements of hardware designed for testing during Phase I.

(U) Initial steady-state cycle studies were performed using analytically-derived turbopump performance and results from other sub-scale component tests. A continuous iteration took place between cycle and mechanical requirements. Component performance obtained from technology program tests was included as it became available. A control system derived from the controls study for a high pressure engine conducted under Contract NAS8-11427 (Advanced Engine Design Study, Bell) was used in these cycle studies. Preliminary designs for major components for the Phase II demonstrator engine were generated based on these initial cycle requirements. Alternative component designs for the preburner and main injectors, as well as the turbines, were also evaluated. Optimization of engine cycles was accomplished by matching the main fuel and oxidizer turbine areas and designing the turbopumps at the appropriate extremes of operating conditions.

(C) Oxidizer and fuel pump efficiency levels demonstrated during component technology programs were used for the candidate Phase II demonstrator engine cycle balances. An engine cycle balance was generated that provided full mixture ratio range capability at a nominal chamber pressure of 2740 psia. This cycle balance was selected for the Phase II demonstrator engine. The operating region for the selected demonstrator engine configuration is illustrated in figure 3.

(C) An alternative 3000-psia nominal chamber pressure cycle balance was generated for a demonstrator engine. However, the mixture ratio range at rated thrust was limited to ± 0.52 from the nominal mixture ratio of 6.

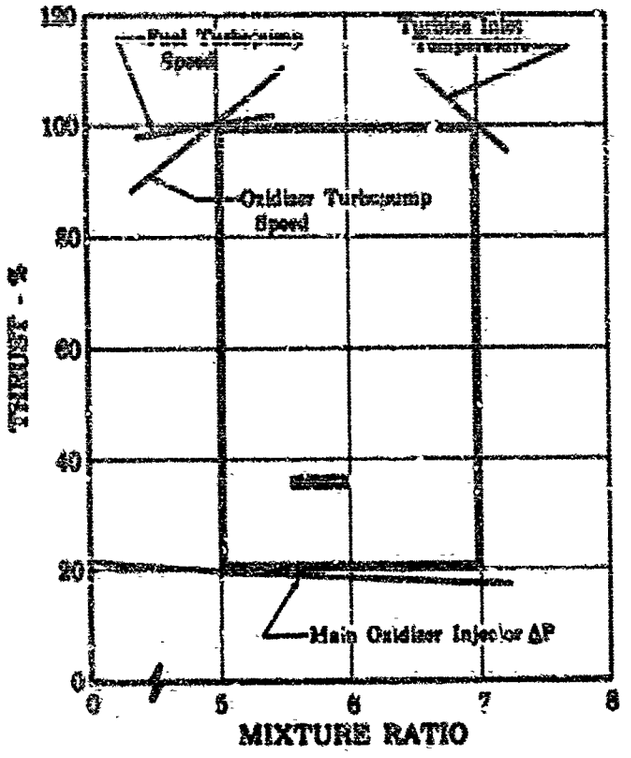


Figure 3. Demonstrator Engine Operating Range FD 21083B

(2) Optimization Techniques

(U) Two techniques were developed for optimizing engine cycles when a wide mixture ratio range capability is required. The first technique concerns the operating point at which the pumps are designed and the second is the matching of the fuel and oxidizer turbine areas. The turbine areas are arranged in parallel. The use of these techniques, which are described in the following paragraphs, reduce the pump pressure and speed requirements at the nominal operating point.

(U) Off-design operating requirements impose power and pressure restrictions on the 100% thrust and nominal mixture ratio operating point. Increased power and pressure must be provided at the nominal operating point to accomplish off-design mixture ratio excursions. This problem is compounded by the normal decrease in component performance at off-design operating conditions. The design approach taken in the cycle studies to obtain a wide mixture ratio operating range was to consider the extremes of the mixture ratio range as the design points. This method was used rather than taking the nominal operating point as the component design point and providing sufficient bias to reach the extremes.

(U) The fuel pressure requirement controls the power balance at the lowest mixture ratio, and the oxidizer pressure requirement controls the balance at the highest mixture ratio. In addition, the minimum available turbine

power results at the highest mixture ratio where the fuel flow is a minimum. At an extreme mixture ratio where one pump controls the power match, the other pump is in an "overspeed" condition. "Overspeed" means that excess pressure over the pressure required to satisfy the flow conditions is provided.

(C) A reduction in efficiency results when a centrifugal pump is operated at flow rates and rotor speeds other than the pump design point. By selecting the design point of the main pumps at their respective minimum flow conditions, two advantages are obtained. First, the best efficiency point of the pump coincides with the engine operating point where the respective pump is controlling the power balance; second, the reduced efficiency at the low flow condition (i.e., the other extreme mixture ratio point) tends to minimize overspeed and to minimize the control system corrections required. Thus, the fuel pump is designed for a mixture ratio of 5.0 and rated thrust and the oxidizer pump is designed for a mixture ratio of 7.0 and rated thrust. Use of this cycle optimization technique results in appreciably reduced pump pressure and speed requirements.

(D) The technique of turbine inlet area matching was also developed for cycle optimization. The basic variable was the total turbine area (the sum of the oxidizer and fuel turbine areas). At a particular value of total combined turbine areas, the ratio of fuel turbine area to oxidizer turbine area was established to balance turbopump speeds and the turbine inlet temperatures to the design values. This was accomplished by varying the pump diameter in addition to the ratio of the turbine areas. This procedure establishes the pump diameter and turbine area matching at the mixture ratio extremes and power-limits both turbopumps. The highest mixture ratio mainly controls the area ratio, while the required pump diameters are chiefly a function of the low mixture ratio requirement. The effect of the total turbine area on the fuel pump design is shown in figures 4 and 5. Large turbine areas reduce the fuel pump requirements, particularly at the high mixture ratio design point. However, the large turbine areas require increased oxidizer-to-fuel turbine area ratio to satisfy the high mixture ratio (i.e., maximum inlet temperature) design point. (See figure 6.) This has an adverse effect on the oxidizer "overspeed" condition at the low mixture ratio point. (See figures 7 and 8.) The maximum oxidizer turbopump speed occurs at the lowest mixture ratio point.

(3) Components

(U) The designs of the major components were dependent on the ability of the component to meet the requirements in terms of cycle flow rate, pressure, and estimated stresses as well as durability and serviceability requirements. Also considered was the component weight and complexity. The final component design was the result of an iterative procedure involving preliminary design cycle requirements, preliminary hardware designs, cycle optimization studies, and component test results. The component designs in the Module Design studies provided for a wide range of operation in mixture ratio and thrust. Durability requirements and acceleration stresses were also considered in the component designs. (See Appendix I.) Performance characteristics and technology levels used for the components in the demonstrator engine cycle studies were based on the results of hardware designed, procured, and tested during the program, as well as the results from related technology programs.

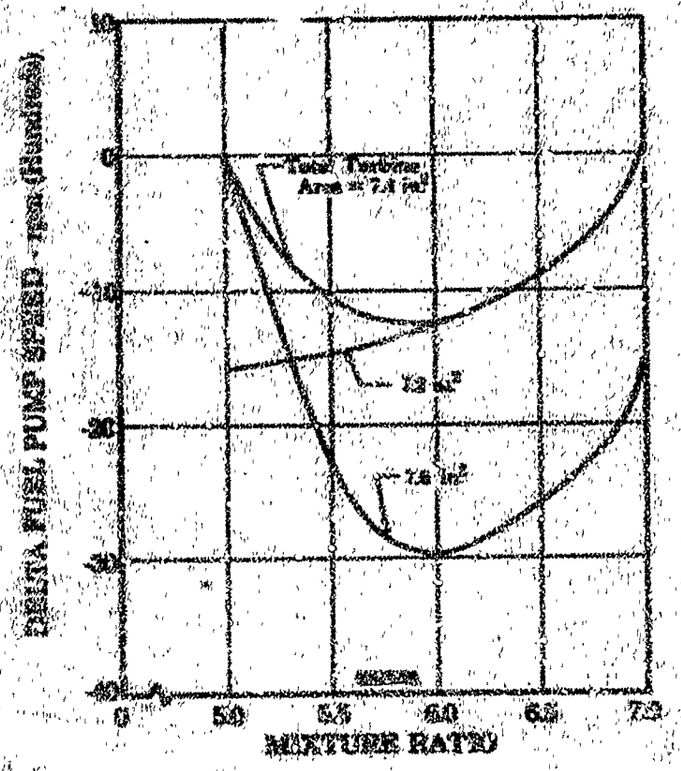


Figure 4. Effect of Turbine Area on Fuel Pump Speed

FD 17941

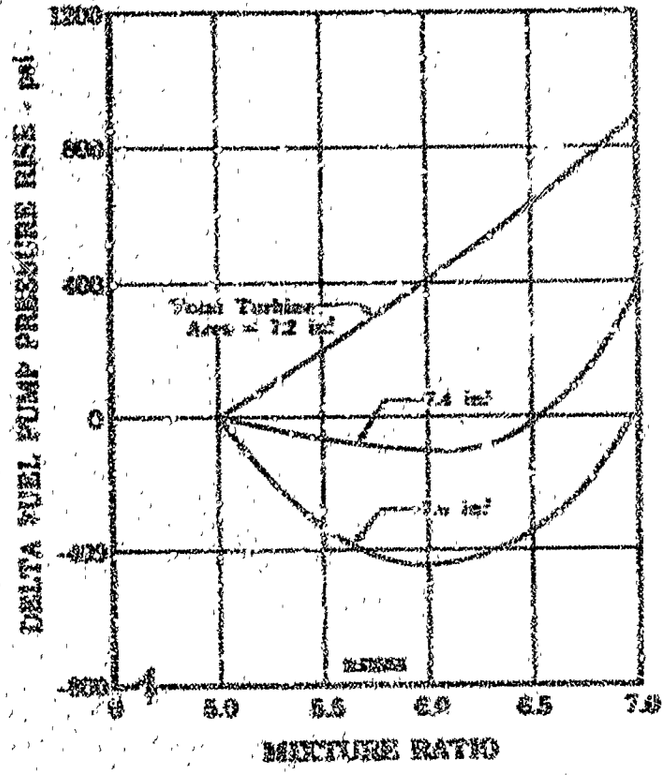


Figure 5. Effect of Turbine Area on Fuel Pump Pressure Rise

FD 17936

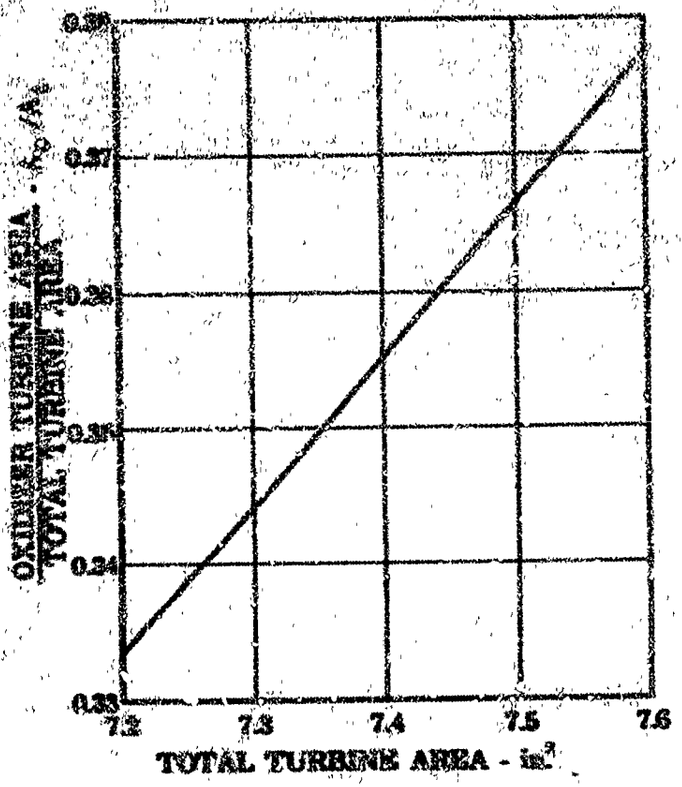


Figure 6. Effect of Total Turbine Area on Turbine Area Ratio

FD 18239

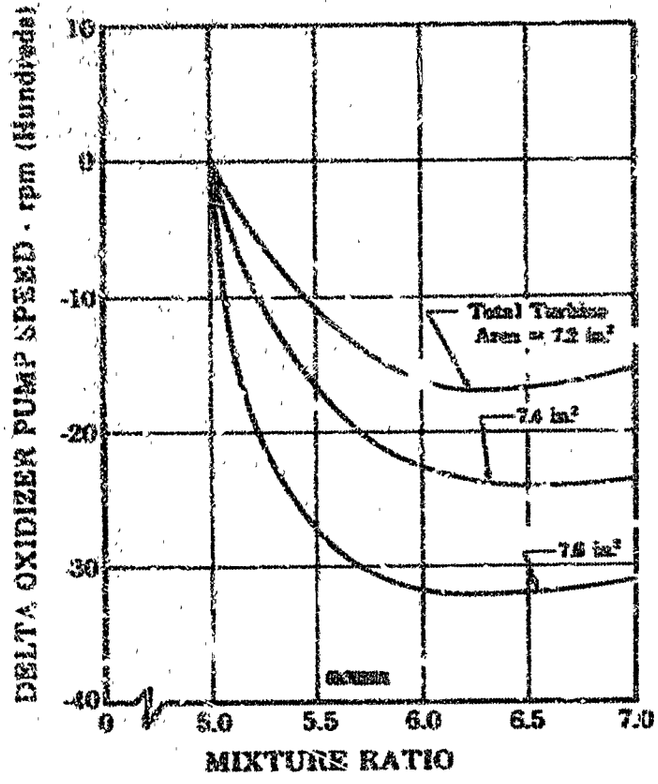


Figure 7. Effect of Turbine Area on Oxidizer Pump Speed

FD 17948

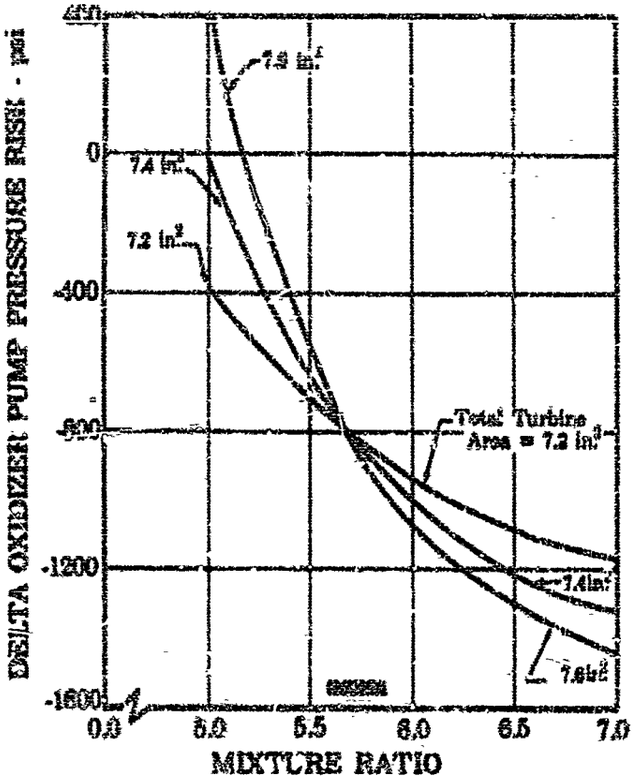


Figure 8. Effect of Turbine Area on Oxidizer Pump Pressure Rise — FD 17937

(U) The following paragraphs present a brief description of the major components, details of component design optimization studies where applicable.

(a) Main Turbopumps

(C) Fuel Pump: The fuel pump is a single shaft unit with two back-to-back, centrifugal stages driven by a two-stage pressure-compounded turbine. A double acting thrust balance piston system is incorporated in the pump design to compensate for axial thrust unbalance. The fuel pump was designed for the operating conditions at an engine mixture ratio of 5.0. The pump efficiency of 64% at the design point was established on the basis of results from 350K fuel pump tests conducted under Contract NAS8-11714.

(C) Oxidizer Pump: The oxidizer pump is a single shaft unit with a single, shrouded centrifugal stage driven by a two-stage pressure-compounded turbine. A single-acting thrust balance piston absorbs axial thrust unbalance. The oxidizer pump was designed for the maximum oxidizer operating flow condition (engine mixture ratio of 7). Pump efficiency at the design point was set at 69% based on the results of 350K oxidizer pump tests conducted under Contract NAS8-20540. The effect of designing the pumps at the maximum flow conditions on pump discharge pressures is illustrated in table IV.

(C) Table IV. Changes in Pump Discharge Pressures Indicated by Turbopump Optimization Study Results (Maximum Turbine Inlet Temperature = 2325°R)

	Fuel Pump			Oxidizer Pump		
	r = 5.0	r = 6.0	r = 7.0	r = 5.0	r = 6.0	r = 7.0
Design Main Turbopumps at Nominal Mixture Ratio, psia	6010	5640	6640	7630	5830	5770
Design Main Turbopumps at Maximum Flow Conditions, psia	5855	5612	6314	7420	5947	5804
Two-Stage Oxidizer Turbine, psia	5590	5280	5880	6920	5610	5480

(U) Turbines: The main fuel and oxidizer turbines are two-stage, pressure compounded turbines designed to operate with low mixture ratio preburner combustion products. Considerations involved in the selection of the number of turbine stages, blade type (integral or attached) and blade material are presented in the following paragraphs.

(U) A study of possible improvements in the oxidizer turbine performance was completed. The oxidizer turbopump was not critical-speed-limited, and therefore, the same rotor speed could be retained for either the single or two-stage configuration. Further, space limitations prevent using a large turbine diameter, which is desirable for a single-stage design. A turbine efficiency gain of approximately 14 points can be realized with the use of a two-stage design. This is illustrated in figure 9. However, turbine disk cooling flow cannot be used for turbine work. Also, leakage of 1st-stage cooling flow imposes a minor efficiency penalty on the 2nd-stage turbine efficiency. The net result of a two-stage oxidizer turbine on the system is shown in table IV and is of sufficient magnitude to justify the choice of a two-stage design. Design studies indicated that the two-stage turbine would not violate the engine envelope limitations. Figure 10 illustrates preliminary designs of the single-stage and two-stage turbines.

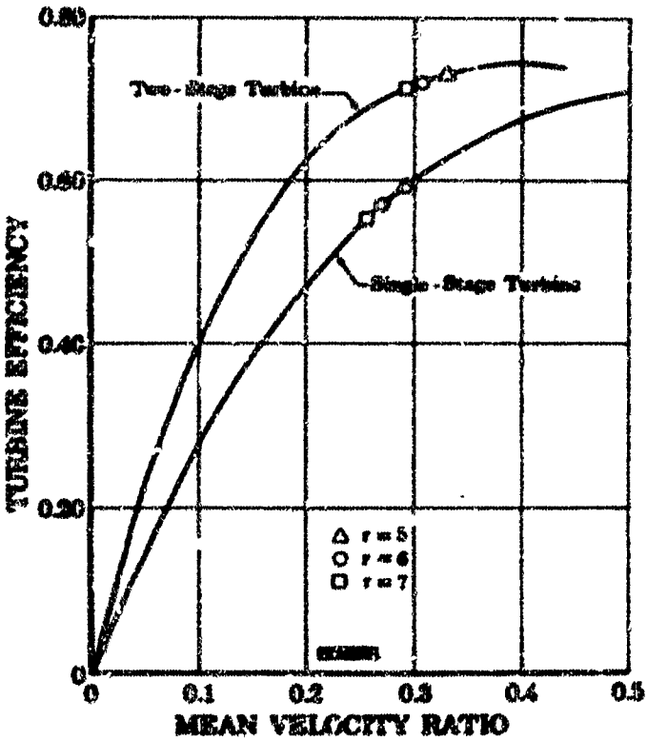


Figure 9. Main Oxidizer Turbine Efficiency vs Mean Velocity Ratio

FD 18247A

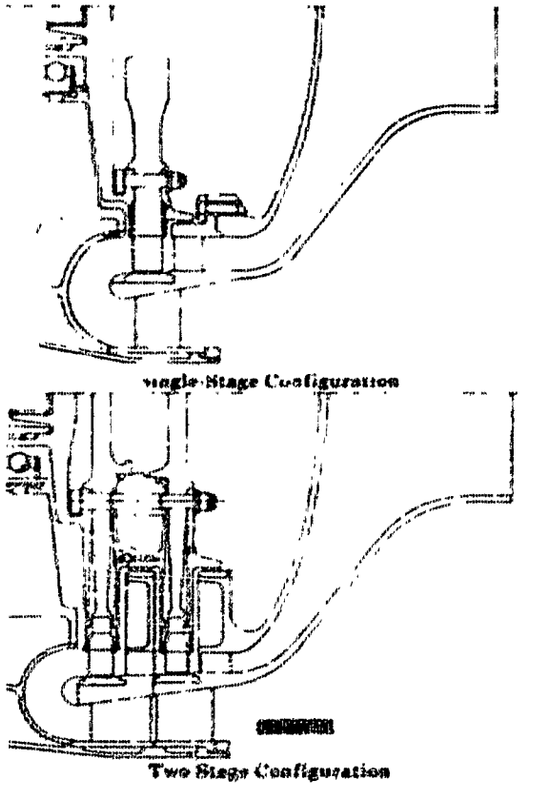


Figure 10. Comparison of Oxidizer Turbine Assemblies

FD 18106

(U) Turbine inlet temperature limitations were also studied because an increase in this temperature offers increased mixture ratio range and/or reduced system pressures. The turbine blade material limits the turbine inlet temperature. Because the fuel turbine operates at a higher mean wheel speed than the oxidizer turbine, the fuel turbine blade material limits the turbine inlet temperature. A blade material study was combined with the fuel turbine configuration analysis. Both integral and attached blades were considered in order to increase the range of materials selection and to permit evaluation of advanced blade materials that are not normally satisfactory disk materials.

(U) The fuel turbine design directly affects the allowable rotor speed because the turbopump is critical-speed-limited. The use of a two-stage turbine offers increased turbine efficiencies as shown in figure 11, but the critical speed is decreased, which reduces the fuel pump efficiency. Two-stage turbines also require an increase in turbine cooling flow, which reduces system power. In addition, the wheel speed limit of each turbine configuration and blade type must be determined because the possible efficiency may be limited. Therefore, the alternative turbine configurations were evaluated considering their effect on fuel pump efficiency, turbine efficiency, turbine disk cooling flow, and allowable turbine inlet temperature.

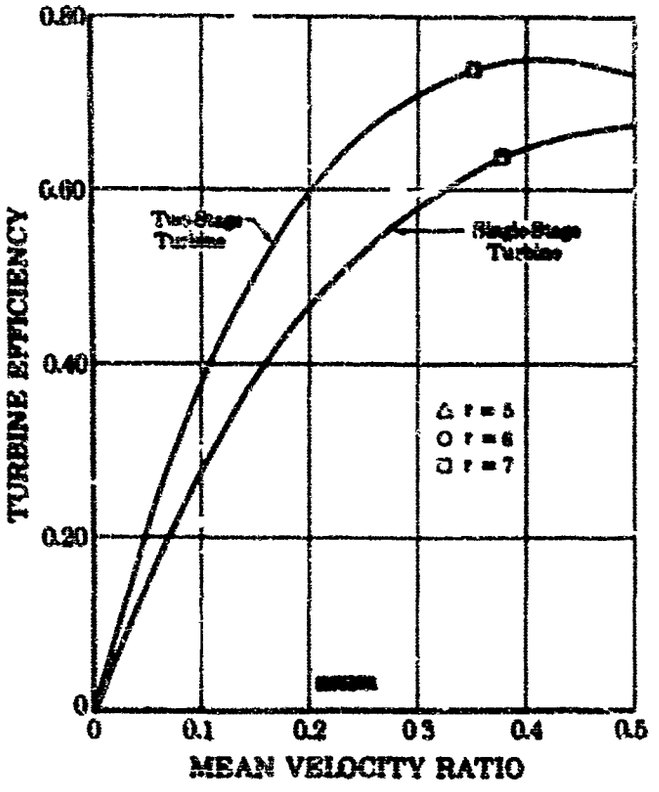


Figure 11. Main Fuel Turbine Efficiency vs Mean Velocity Ratio FD 18240B

(U) One-stage and two-stage turbines were considered with both integral and attached blades. PWA 689 (forged Udimet 700) was considered for the integral configuration because of properties that make it a suitable disk material, in addition to being a good high-temperature blade material. Because attached blades allow the use of special blade materials, directionally solidified PWA 664 material was selected for the attached blade configurations.

(U) Critical speed was established for each turbine configuration. For the two-stage turbine configurations, it was determined that the critical speed could be improved approximately 15% by locating the front bearing between two stages of the fuel pump instead of placing the bearing in front of the first stage. The wheel speed limit of each configuration was determined based on blade and disk material strength. High wheel speeds are desirable because of the resulting increased efficiencies. The turbine inlet temperature limit was established for each candidate configuration. The temperature limit is a function of the blading centrifugal stress and the blade material properties. An iteration is required between the allowable wheel speed and operating temperature.

(U) A disk and blade vibration analysis was completed for the attached blade configurations. The results of this analysis indicated sufficiently high frequencies for the unshrouded blade designs. Therefore, the candidate configurations with shrouded blades were eliminated from consideration. The increased centrifugal stress of a shrouded blade decreases the allowable wheel speed and operating temperature.

(U) By taking the various limits of the candidate turbine configurations, the resulting net performance effect on the system was determined in terms of pump discharge pressure. A summary of the four basic configurations is provided in table V. The two-stage turbine with PWA 664 blades results in the most efficient system.

(C) Table V. Summary of Fuel Turbine Configurations

Turbine Configuration	1	2	3	4
Number of Stages	1	1	2	2
Blade Material	PWA 689	PWA 664	PWA 689	PWA 664
Maximum Design Speed, rpm	55,600	55,600	50,000	48,000
Maximum Wheel Speed, fps	1700	1700	1500	1500
Maximum Turbine Inlet Temperature, °R	2200	2315	2310	2325
Change in Fuel Pump Discharge Pressure, psi (r = 5.0)	-340	-556	-355	-735
Change in Oxidizer Pump Discharge Pressure, psi (r = 5.0)	-360	-650	-350	-860

(U) In optimizing the turbopump to reduce the required fuel pump discharge pressure, one additional parameter considered was the main fuel turbine vane exit angle. The vane exit angle affects turbine efficiency and turbine blade stress and, therefore, the required pump discharge pressure.

(U) As vane exit angle increases, less of the velocity is directed tangentially; therefore, less of the pressure ratio goes into work and the turbine efficiency is reduced. However, increasing the vane exit angle reduces the blade height and therefore reduces the blade stress. Because the allowable turbine inlet temperature is controlled by the stress level, increasing the vane angle allows higher turbine inlet temperatures.

(U) By establishing the relationship between the vane exit angle, turbine efficiency, turbine inlet temperature, and fuel pump discharge pressure, the optimum vane angle was selected. As the vane angle is increased, the power gain made by increased turbine inlet temperature overcomes the power loss made by reduced efficiency. However, when the angle is increased past a certain point, the loss of efficiency overcomes the gain made by increased temperature, and the required fuel pump discharge pressure is increased. Figure 12 shows the estimated effect of the fuel vane exit angle on pump discharge pressures.

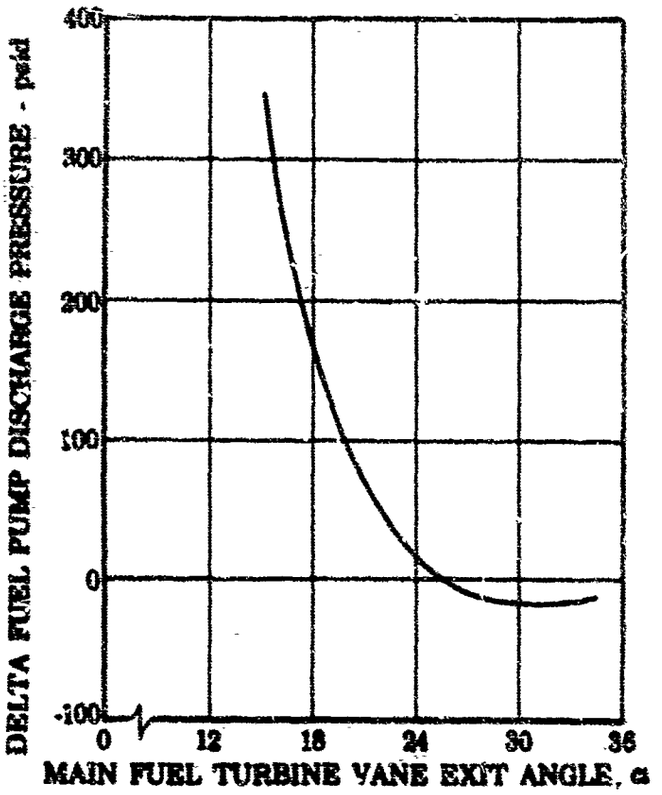


Figure 12. Effect of Turbine Vane Exit Angle on Fuel Pump Discharge Pressure FD 17983

(This page is Unclassified)

(U) Because the main oxidizer turbine is not stress-limited, the allowable turbine inlet temperature is not controlled by the oxidizer turbine vane exit angle. Therefore, on the oxidizer turbine it is desirable to run the smallest vane angle mechanically possible to obtain high efficiency.

(b) Low-Speed Inducers

(C) Oxidizer Low-Speed Inducer: The oxidizer low-speed inducer is a single-shaft unit with a high specific speed, axial-flow inducer driven by a variable inlet area, single-stage, liquid oxygen turbine. Turbine operation is controlled by varying the inlet area, which can be adjusted between 5% and 50% of the total annular area. The oxidizer low-speed inducer was designed at a mixture ratio of 7 with an analytically determined efficiency of 78.5%.

(C) Fuel Low-Speed Inducer: The fuel low-speed inducer is a single-shaft unit with a high specific speed, axial-flow inducer driven by a partial admission, single-stage hydrogen turbine, which uses the transpiration coolant supply as the working fluid. The fuel low-speed inducer was designed at a mixture ratio of 5 with an analytically determined efficiency of 79.9%. Analysis indicated that a variable turbine control was not necessary; a simple, fixed-area turbine bypass provides the desired control function.

(c) Preburner

(U) A detailed comparison of alternative preburner configurations was made. Variable-area and dual-orifice configurations were studied for the oxidizer side, and fixed-area, variable-area, and dual-element configurations were studied for the fuel side. From start transient analyses, it was concluded that either oxidizer injector configuration could meet the transient requirements. Because an internal shutoff could be incorporated into either configuration, the desired low manifold volume (2 to 10 $in.^3$) could be obtained. While the total manifold volume for an external shutoff of a dual-orifice configuration is less than that of the variable-area configuration (table VI), both volumes are too large for acceptable filling times.

(U) Table VI. Oxidizer Preburner Injector Volumes

	Volumes - $in.^3$	
	External Shutoff	Internal Shutoff
Dual-Orifice		
Primary	15	4
Secondary	110	10
Variable-Area	200	2 to 10

(C) The oxidizer preburner injector system requirements were made the same for both configurations; i.e., the pressure drop provided by the oxidizer preburner injector was the same for both the dual-orifice and variable-area configurations and was equal to 4.5% of the preburner pressure at any operating condition. This minimum pressure drop was set to maintain system stability. Using the above criteria the effect of either of these oxidizer preburner injector designs on the engine system is the same and the preburner combustion performance is a function of the detailed mechanical design of the injector.

(C) The use of either the variable-area fuel injector or fixed fuel area has a direct effect on the engine system and the fuel pump pressure requirements. For the fuel injector, a 4.5% minimum injector pressure drop was set to maintain system stability. With a fixed-area, the minimum drop will occur at the highest mixture ratio because the effect of increased fuel temperature from the heat exchanger is not sufficient to compensate for the decreased fuel flow. Figure 13 shows the percent drop as a function of thrust and mixture ratio for a fixed-area fuel injector. At 100% thrust, the highest drop occurs at a mixture ratio of 5.0, where the fuel pump operating conditions are most severe. With a variable-area configuration, the pressure drop can be adjusted to maintain a 4.5% pressure drop at a mixture ratio of 5.0 and reduce the fuel pressure required. Further, at a mixture ratio of 7.0 the excess fuel pressure available in the cycle can be used in the preburner injector to provide high injection velocity for improved combustion performance where the turbine temperature is the highest. The pressure drop for the variable-area configuration is shown in figure 14.

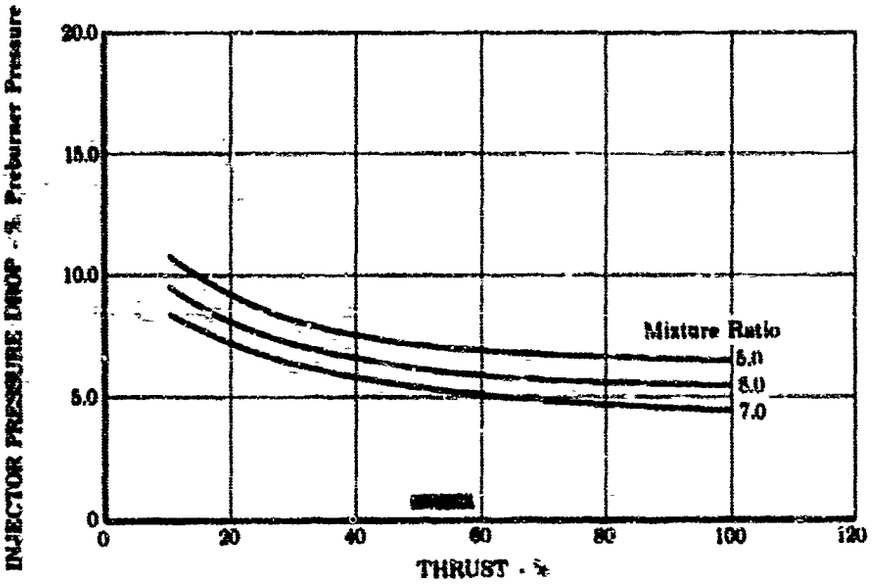


Figure 13. Preburner Fuel Injector Pressure Drop for Fixed Fuel Area FD 15975

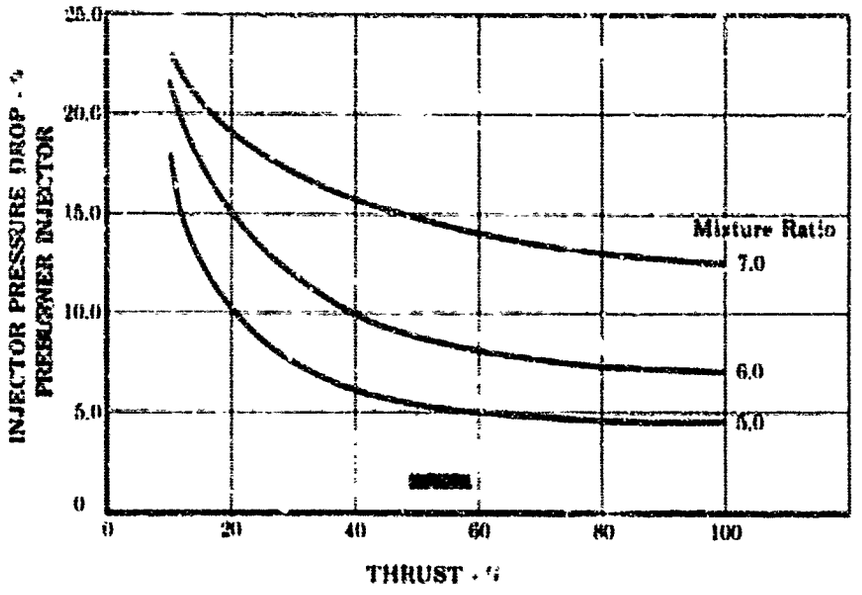


Figure 14. Preburner Fuel Injector Pressure Drop - Variable Fuel Area FD 15970

(U) Another important function provided by the variable-area fuel preburner injector is the ability of this configuration to compensate for changes in fuel inlet temperature to the preburner. This function makes it feasible to use different regenerative nozzle skirt assemblies that can more closely match the engine area ratio to the needs of a particular vehicle and mission. When different nozzle skirts are used, the surface area of the nozzle varies, which results in a proportional change in the coolant exit temperature. This coolant flow establishes the preburner fuel temperature, which directly affects the injector drop for a fixed area. This drop, in turn, establishes the fuel pump pressure rise requirements.

(C) Because of the complicated heat transfer process in the regeneratively cooled nozzle skirt assemblies, some prediction error must be assumed in addition to the known variations due to area ratio changes. Based on past engine experience, a ± 20% prediction error is possible with a subsequent ± 5 to 10% scatter band for a developed configuration. A ± 10% variation in heat transfer produces a ± 2% variation from the nominal required preburner fuel injector area. A 1% required change in area is equivalent to 120 psi in fuel pump pressure. Consequently, the variable-area fuel injector can provide for changes in nozzle area ratio from 184 to 60 with a fuel pump designed for 720 psi less pressure rise, assuming nominal heat transfer. The probable errors in heat transfer amplify this effect. Therefore, a variable fuel preburner area is desirable for an optimum modular engine.

(U) Dump-cooled nozzle usage in booster and upper stage applications for a range of nozzle expansion ratios produces a variation in the preburner fuel injector area requirements. Even though the regeneratively cooled nozzle section may terminate at a specific area ratio, the nozzle contour (and thus the hot-side surface area of the tubed heat exchanger) will

vary with the overall nozzle expansion ratio. The surface area effects the heat transfer of the heat exchangers. This, in turn, causes a change in the preburner fuel inlet temperature which may make it desirable to adjust the preburner fuel injector area to maintain propellant-combustion system stability or minimize pump pressure rise requirements. The effects of nozzle expansion ratio (for dump cooled nozzles) on preburner fuel injector area are shown in figure 15 for booster and upper stage engine configurations.

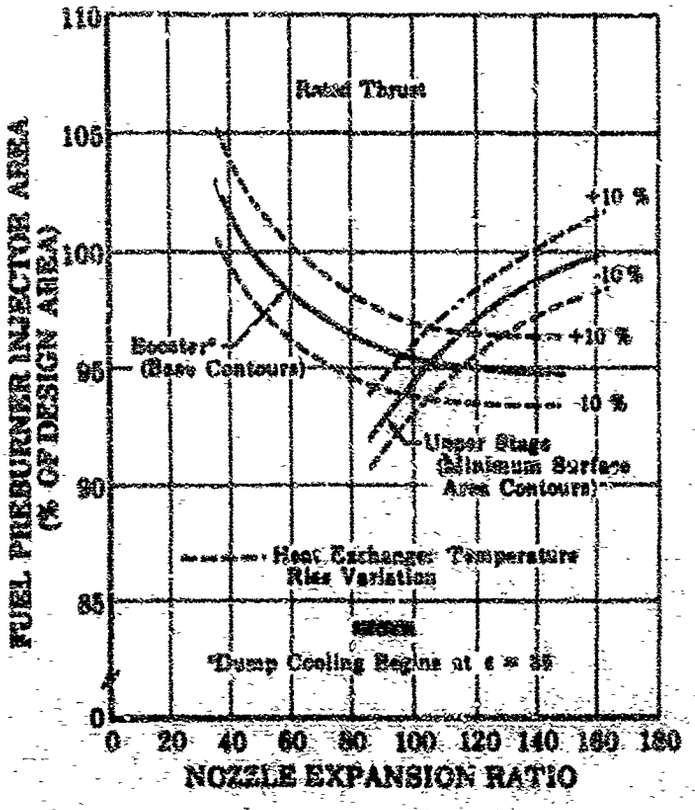


Figure 15. Required Fuel Preburner Injector Area vs Expansion Ratio FD 23417

(d) Other Components

(U) The designs of the main injector and combustion chamber were based on the 50K staged-combustion program hardware designs, which demonstrated their durability and high performance capabilities. The main injector configuration uses fixed-area oxidizer injection elements arranged in a radial spraybar pattern. The oxidizer injector area was sized to provide a minimum pressure loss of 4-1/2% to ensure combustion stability. The bulk of the hot, fuel-rich, turbine exhaust gas is injected adjacent to the oxidizer injection elements to provide direct impingement and mixing with the oxidizer; the remainder of the fuel-rich gas flows through a porous Rigimesh faceplate to prevent burning or excessive temperatures at the injector face.

(U) The main combustion chamber uses slotted wafers to provide passages for the transpiration coolant flow in the region of high heat flux. An outer shell serves as the main chamber pressure vessel and as a structural member for the support of the exhaust nozzle. The cylindrical combustion chamber was sized to provide sufficient length to ensure good combustion and high performance. The exhaust nozzle selected for the high pressure engine is a lightweight two-position, ball nozzle. The use of this nozzle improves packaging, provides increased performance, and reduces engine weight. The nozzle weight is decreased by low pressure dump cooling a large portion of the nozzle skirt. The area ratio of the nozzle may be easily changed to match the particular application. Descriptions and design details of the main injector, main chamber, and exhaust nozzle are provided in Section IX.

(4) Error Analysis

(U) An error analysis was performed to determine the effect of component performance variations on the engine system. This analysis assumed the component designs were fixed, and the performance variations were evaluated in terms of their effect on engine parameters such as turbopump speeds, turbine inlet temperature, and system pressures.

(U) The performance variables (errors) investigated included pump and turbine efficiencies, turbine area, coolant flows, and nozzle cooling jacket pressure loss and temperature rise.

(U) The analysis was conducted on a fixed hardware basis, which is the equivalent to an initial test of the engine where performance variations of components would be trimmed by adjusting control valve areas. Values of performance for each component were changed individually. The largest magnitude of component variation was considerably greater than the expected engine-to-engine variation. The effects of the variations on engine parameters were determined and evaluated by two methods. The first method involved determining the required levels of component operating conditions to maintain 100% thrust over the complete mixture ratio operating range. The control valve areas were adjusted to obtain these operating conditions, and an analysis of control areas indicate that the required area settings for all conditions were within the design operating ranges of the valves. The effects of variations in the engine component performance on the critical parameters using the first method are summarized in table VII. Engine performance effects are given for varying degrees of component performance changes. The range and number of points for parametric variation were selected to define the nonlinear characteristics.

(U) The second method presents the performance effects in terms of the allowable mixture ratio range at full thrust and the thrust level obtained at the extreme mixture ratio operating points if the turbopump speeds and/or turbine inlet temperature are limited to their respective nominal design maximum values. The results using the second method are shown in table VIII.

(C) Table VII. Operating Condition to Maintain Thrust

Component	Variation	Percent Change Oxidizer Pump Speed			Percent Change Fuel Pump Speed			Preburner Temperature Change, °R		
		r = 5	r = 6	r = 7	r = 5	r = 6	r = 7	r = 5	r = 6	r = 7
Maximum Increase Allowable		0	8.67	9.25	0	2.95	0	545	347	0
Fuel Pump Efficiency	+2%	-2.15	-0.79	0	-0.93	0.08	0.98	- 38	- 17	1
	-5%	5.64	4.75	0.54	2.69	1.95	-1.83	98	91	14
	-10%	12.49	10.47	5.97	6.16	4.36	0.56	219	198	132
Oxidizer Pump Efficiency	+2%	1.20	1.15	-0.50	0	0	-1.41	0	0	-31
	-5%	-2.93	0.56	1.45	0	3.38	4.80	0	69	110
	-10%	-4.96	2.24	3.16	1.0	8.53	9.96	18	174	230
Fuel Turbine Efficiency	+2%	-1.55	-0.77	0.01	-0.27	0.44	1.36	- 26	- 14	0
	-5%	4.43	3.53	-0.08	0.77	0	-3.11	75	66	0
Oxidizer Turbine Efficiency	+2%	1.34	1.32	-0.47	0	0	-1.70	0	0	-41
	-5%	-3.34	0.13	1.02	0	3.49	4.80	0	72	110
Fuel Turbine Area	+5%	-3.44	-0.66	0.15	-0.56	1.74	2.92	6	60	95
	-5%	3.39	3.0	-0.13	0.56	0	-2.71	- 13	- 20	-90
Oxidizer Turbine Area	+5%	1.68	1.02	-0.46	-0.01	0	-1.96	34	40	- 2
	-5%	-2.16	-0.38	0.44	-0.06	1.38	2.52	- 41	- 12	12
Fuel Cooling Flows	+2 lb/sec	-0.50	-0.40	0.10	-0.10	0	0.46	51	70	110
	-4 lb/sec	-0.83	-0.53	0.26	-0.15	0.08	1.06	109	151	229
Total Turbine Area	+5%	-1.73	-0.95	-0.11	-0.50	0.01	0.89	43	62	93
	-5%	1.60	1.04	0.28	0.60	0.01	-0.49	-47	-60	-82

CONFIDENTIAL

(C) Table VII. Operating Condition to Maintain Thrust (Continued)

Component	Variation	Percent Change Oxidizer Pump Speed			Percent Change Fuel Pump Speed			Preburner Temperature Change, °R		
		r = 5	r = 6	r = 7	r = 5	r = 6	r = 7	r = 5	r = 6	r = 7
Maximum Increase Allowable		0	8.67	9.25	0	2.95	0	545	347	0
Temperature Rise	-2%	0.52	2.08	-0.08	0.53	1.88	-0.28	8.6	37.7	- 4.9
Transmission Heat Exchanger	-20%	0	0	0	0.09	-0.12	0	-0.4	- 2.3	0
Pressure Loss	+20%	0	1.02	0	0	0.68	-0.13	0.6	13.7	- 0.5
Recuperator Heat Exchanger	-20%	0	0	0	0	-0.06	0	-0.4	- 0.3	- 0.5
Temperature Rise Main Heat Exchanger	+20%	0.17	0	-0.05	0.12	0	0.01	9.0	5.9	8.2
	-20%	-0.18	0.07	0.05	-0.13	0	-0.01	-8.8	- 5.8	- 8.3
Pressure Loss Main Heat Exchanger	+20%	0	0	0	0.14	0	0	0.1	0	0
	-20%	0	0	0	-0.06	0	0	0.1	0	0
Overall Impulse Efficiency	+ 1%	-0.72	0.09	-0.71	-0.64	-0.17	-0.81	-5.6	7.8	- 5.2
	- 1%	0.74	0.68	0.66	0.68	0.52	0.68	6.1	2.9	3.2
Preburner Combustion Efficiency	+ 1%	-0.03	0.20	-0.14	-0.05	0	-0.20	8.4	12.9	8.0
	- 1%	-0.02	0.23	0.04	0.05	0	-0.05	-9.0	- 7.1	-13.9
Fuel Pump Head Coefficient	+ 5%	0.11	-0.16	0	-1.95	-2.16	-2.25	1.1	- 0.6	2.0
	- 5%	-0.36	0.028	0.004	2.03	2.32	2.36	-7.2	0.1	3.1

(C) Table . Operating Condition to Maintain Thrust (Continued)

Component	Variation	Percent Change Oxidizer Pump Speed			Percent Change Fuel Pump Speed			Preburner Temperature Change, °R		
		r = 5	r = 6	r = 7	r = 5	r = 6	r = 7	r = 5	r = 6	r = 7
Oxidizer Pump Head Coefficient	+ 5%	-2.16	-2.31	-1.92	0.002	0	0.71	0.1	-0.4	16.1
	- 5%	2.43	2.47	2.08	0.002	0	-0.28	0.1	-0.4	-4.1
Main Heat Exchanger Flow	+ 3	0.42	0.040	-0.041	0.31	0	0.077	10.6	5.6	10.3
	- 3	-0.27	0.089	0.004	-0.25	0.075	0.052	-9.9	-4.2	-2.9
Fuel Low-Speed Inducer Turbine Efficiency	+ 5%	0	0	0	0.02	-0.06	0	0	0	0
	- 5%	0	0.16	0	0.09	0.13	0	0	0	0

(C) Table VIII. Maintaining Component Limits

Component	Variation	Mixture Ratio Range at 100% Thrust		Percent Thrust Change			Limit		
		r_{min}	r_{max}	r = 5	r = 6	r = 7	r = 5	r = 6	r = 7
Nominal Case		5.0	7.0	0	5.7	0	NF	NF	TB
Fuel Pump Efficiency	+2%	5.0	6.77	1.4	4.3	-1.2	NF	NF	NF
	-5%	5.54	6.95	-7.8	1.9	-0.9	NL	NF	TB
	-10%			-15.6	-3.0	-21.0	NL	NF	TB
Oxidizer Pump Efficiency	+2%	5.11	7.0	-1.9	0	0	NL	NF	NF
	-5%	5.0	5.9	0	-0.5	-9.2	NF	NF	TB
	-10%			-1.6	-7.0	-18.7	NF	NF	TB
Fuel Turbine Efficiency	+2%	5.0	6.7	0.4	2.4	-1.9	NF	NF	NF
	-5%	5.39	7.0	-3.2	5.9	0.5	NL	NF	TB
Oxidizer Turbine Efficiency	+2%	5.12	7.0	-2.1	5.9	2.6	NL	NF	NF
	-5%	5.0	5.83	0	-0.8	-9.2	NF	NF	TB
Fuel Turbine Area	+5%	5.0	6.31	0.9	1.5	-8.0	NF	NF	TB
	-5%	5.32	7.0	-4.9	5.9	4.3	NL	NF	NF
Oxidizer Turbine Area	+5%	5.16	7.0	-2.5	5.9	0.7	NL	NF	TB
	-5%	5.0	6.43	0.1	2.1	-3.4	NF	NF	NF
Fuel Cooling Flows	+2 lb/sec	5.0	6.75	0.2	5.7	-9.2	NF	NF	TB
	+4 lb/sec	5.0	6.51	0.3	4.0	-18.8	NF	NF	TB
Total Turbine Area	+5%	5.0	6.76	0.8	4.3	-7.9	NF	NF	TB
	-5%	5.16	7.0	-2.4	5.7	0.7	NL	NF	NF
Temperature Rise Transpiration Heat Exchangers	+20%	5.15	7.0	-0.8	3.3	0.3	NF	NF	TB
	-20%	5.0	7.0	0	6.0	0	NF	NF	TB

TB = Preburner Temperature
NF = Fuel Pump Speed
NL = Oxidizer Pump Speed

CONFIDENTIAL

CONFIDENTIAL

(C) Table VIII. Maintaining Component Limits (Continued)

Component	Variation	Mixture Ratio Range at 100% Thrust		Percent Thrust Change			Limit		
		r_{min}	r_{max}	r = 5	r = 6	r = 7	r = 5	r = 6	r = 7
Pressure Loss	+20%	5.0	7.0	0	4.5	0	NL & NF	NF	TB
Transpiration	-20%	5.0	7.0	0	5.9	0	NL & NF	NF	NF & TB
Heat Exchangers									
Temperature	+20%	5.02	6.97	-0.3	5.7	-0.9	NL	NF	TB
Rise Main Heat	-20%	5.0	7.0	0.2	5.7	0	NL	NF	NF
Exchanger									
Pressure Rise	+20%	5.02	7.0	-0.1	5.7	0	NF	NF	TB & NF
Main Heat	-20%	5.0	7.0	0	5.7	0	NL	NF	NF & TB
Exchanger									
Overall	+1%	5.0	7.0	1.1	6.3	0.5	NL & NF	NF	TB
Impulse	-1%	5.1	6.84	-1.2	3.9	-1.0	NL	NF	NF
Efficiency									
Preburner	+1%	5.0	6.97	0	6.1	-0.8	NL	NF	TB
Efficiency	-1%	5.01	7.0	-0.1	5.9	0	NF	NF	NF
Fuel Pump	+5%	5.01	7.0	-0.1	10.3	0	NL	NF	TB
Head	-5%	5.58	6.46	-3.1	1.2	-3.1	NF	NF	NF
Coefficient									
Oxidizer Pump	+5%	5.0	6.84	0	5.7	-1.1	NF	NF	TB
Head Coefficient	-5%	5.24	7.0	-3.6	5.9	0.4	NL	NF	NF
Main Heat	+3	5.06	6.97	-0.7	5.7	-0.6	NL	NF	TB
Exchanger Flow	-3	5.0	7.0	0.3	5.7	0	NL	NF	NF
Fuel Low-Speed	+5%	5.0	7.0	0	5.7	0	NL & NF	NF	NF & TB
Inducer Turbine	-5%	5.0	7.0	0	5.7	0	NL & NF	NF	NF & TB
Efficiency									

TB = Preburner Temperature
NF = Fuel Pump Speed
NL = Oxidizer Pump Speed

(U) Main turbine nozzle area changes can be varied to counteract an error in component performance to (1) reduce the required operating levels of the critical parameters, and/or (2) increase the thrust operating range.

(U) The results presented in Tables VII and VIII indicate that oxidizer turbopump efficiencies are as important as fuel turbopump efficiencies because of the flat fuel speed characteristic with mixture ratio. The oxidizer turbopump efficiencies are less critical if turbine nozzle area variations are permitted, and this adjustment would be made for large variations in component performance.

(C) The analysis was extended to the 30% thrust level; however, no limits in engine operating range at this thrust level were indicated from the results.

(5) Controls

(U) The objective of the controls study was to define the simplest system that would provide the desired control of mixture ratio and thrust within the specified operating regime. This study included the selection of the control and sense points.

(U) The basis for the control system selection was a detailed controls study performed under Contract NAS8-11427.[2] This study evaluated several control systems and 17 control points for an advanced high pressure rocket engine system using a preburner cycle. The following description of the analysis and resultant data for the selected control point system was taken from this study. Four-valve, three-valve, and two-valve systems were analyzed to compare the operating range and engine performance. The engine cycle blanace used in this comparison was derived from the fixed nozzle skirt demonstrator engine configuration. This cycle balance was subsequently revised to the recommended Phase II demonstrator cycle balance, which provides full mixture ratio range at rated thrust.

(C) The allowable engine operating envelope for the four-valve system is illustrated in figure 16. The excursion of mixture ratio at 100% thrust is limited between 5.4 and 6.8 by oxidizer pump speed and turbine inlet temperature. The system was more limited at high thrusts than the previous systems due primarily to the requirement for higher pump pressures inherent with load controls. No lower thrust restriction was encountered.

(U) The area schedules for the four control points are also illustrated in figure 16. A complex area schedule was required for the preburner fuel supply control to satisfy the three control functions provided by this valve. The three-valve functions were (1) coolant control, (2) injector stability control, and (3) load control. A smooth area schedule can be derived that would result in a slight increase in pump pressure at reduced thrust.

---

[2] "Advanced Engine Design Study, Bell (ARB), Control System Study," FR-2488, Pratt & Whitney Aircraft, 31 July 1967.

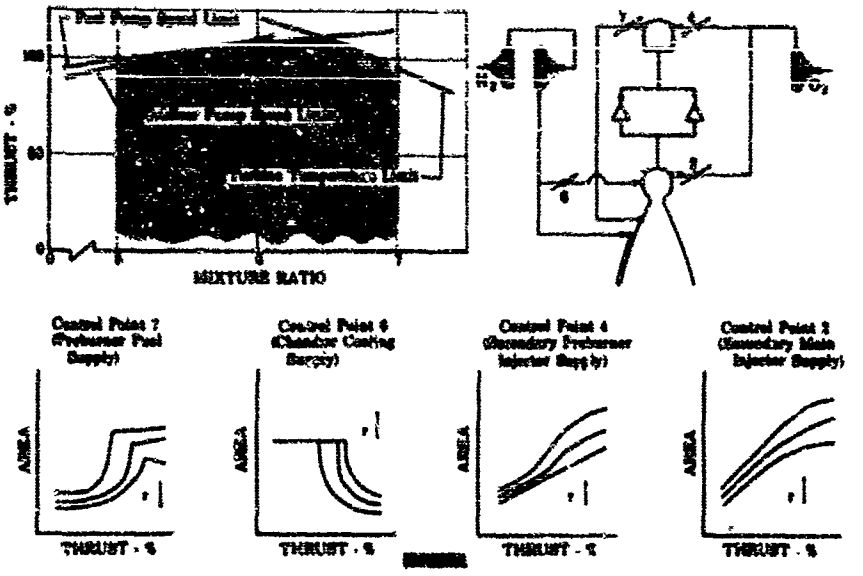


Figure 16. Load Control System (4-Valve Configuration) Operating Region and Control Areas FD 20663

(C) A three-valve combination was derived by eliminating the chamber cooling supply control. To select the coolant orifice area, two coolant control areas required by the four-valve system at 100% thrust at mixture ratios of 5 and 7 were analyzed. With the orifice sized at 100% thrust and r = 7.0, and with the preburner fuel supply control scheduled to maintain minimum chamber coolant flow, a significant portion of the operating region was lost because of the preburner injector stability limit. (See figure 17.) This limit was encountered because the fuel side control was scheduled to maintain the minimum required chamber coolant flow. If the control had been scheduled to provide injector stability, excessive chamber cooling could have resulted.

(C) With the orifice sized at 100% thrust and r = 5.0, and with the preburner fuel supply control scheduled to maintain minimum chamber coolant flow, there was an envelope reduction at high mixture ratio. This reduction was the result of additional turbine power requirements necessary with this smaller orifice. (See figure 18.)

(C) With the orifice sized at 100% thrust and r = 7.0, and with the preburner fuel supply control scheduled to maintain injector stability, an operating envelope nearly equal to that of the four-valve system was obtained. (See figure 19.) This method differs from the first two in that overcooling of the chamber was permitted to occur while maintaining injector stability. A specific impulse penalty of 0.1 second results from the excess coolant flow. The control schedules are illustrated in figure 19.

(U) No two-valve system could be established that permitted a reasonable operating envelope. Operation was limited to a small range of thrust and mixture ratio near rated thrust by a chamber cooling limit, a turbine temperature limit, and a maximum fuel turbopump speed limit. (See figure 20.) Rematching of the orifices in the two-valve system would shift the operating envelope but would not significantly alter its size.

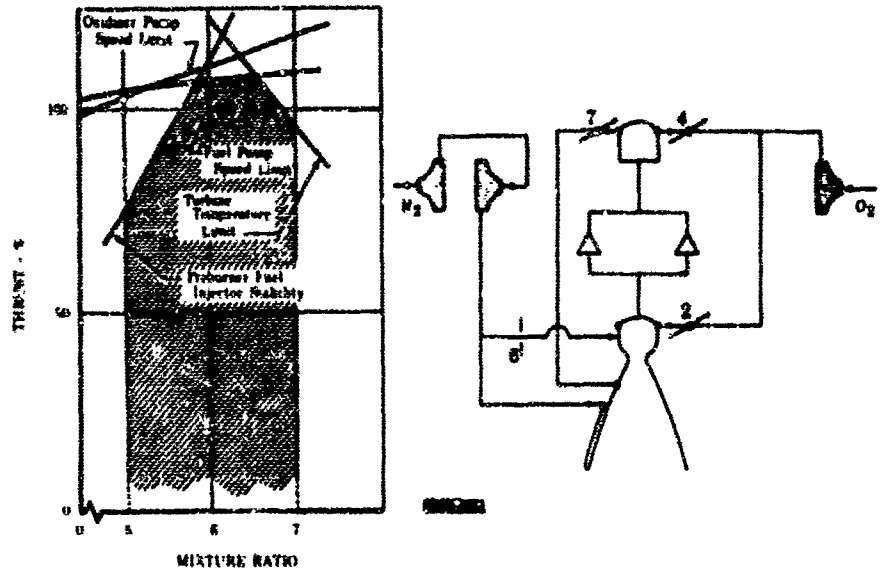


Figure 17. Load Control System (3-Valve Configuration) Operating Region (Control Point 7 Scheduled for Minimum Chamber Cooling Flow) FD 20672

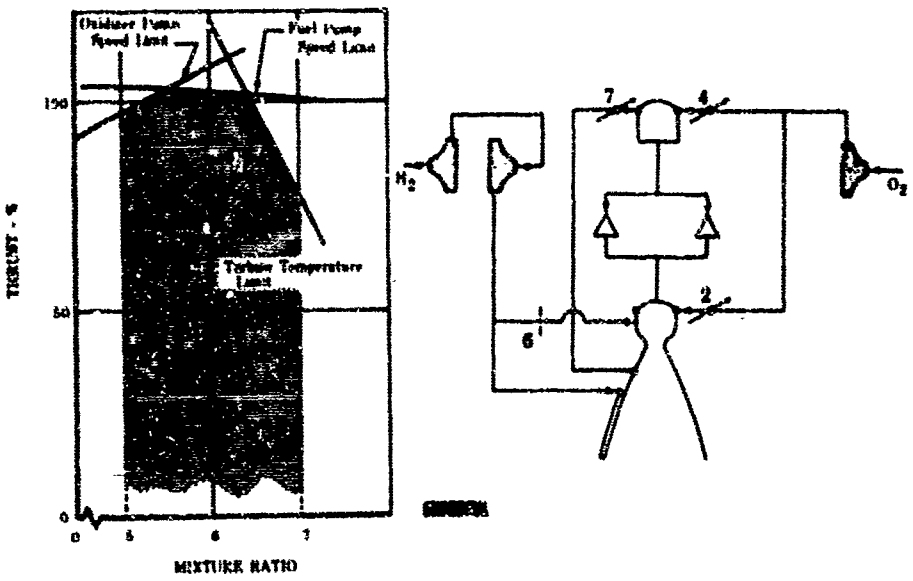


Figure 18. Load Control System (3-Valve Configuration) Operating Region (Control Point 6 Orifice Area Too Small) FD 20676

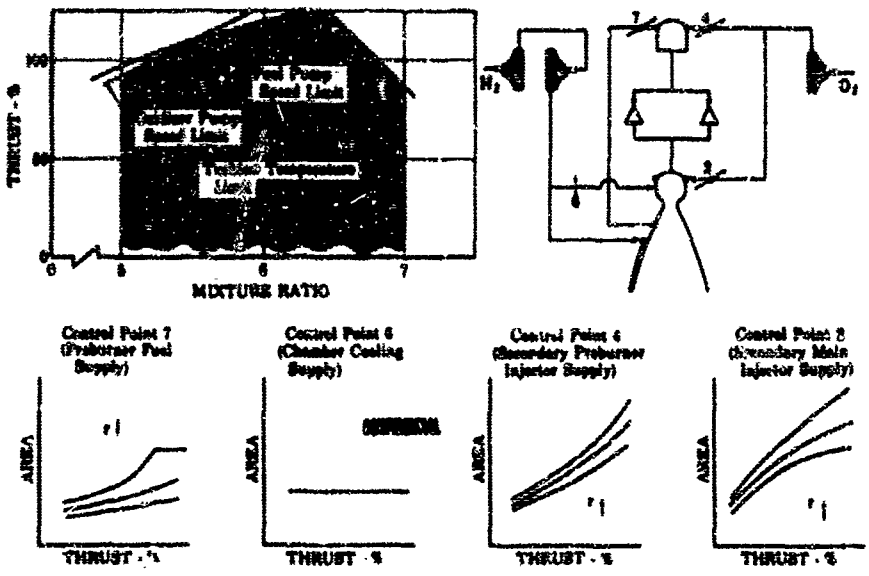


Figure 19. Load Control System (3-Valve Configuration) Operating Region and Control Areas (Control Point 7 Scheduled for Injector Stability) FD 20661

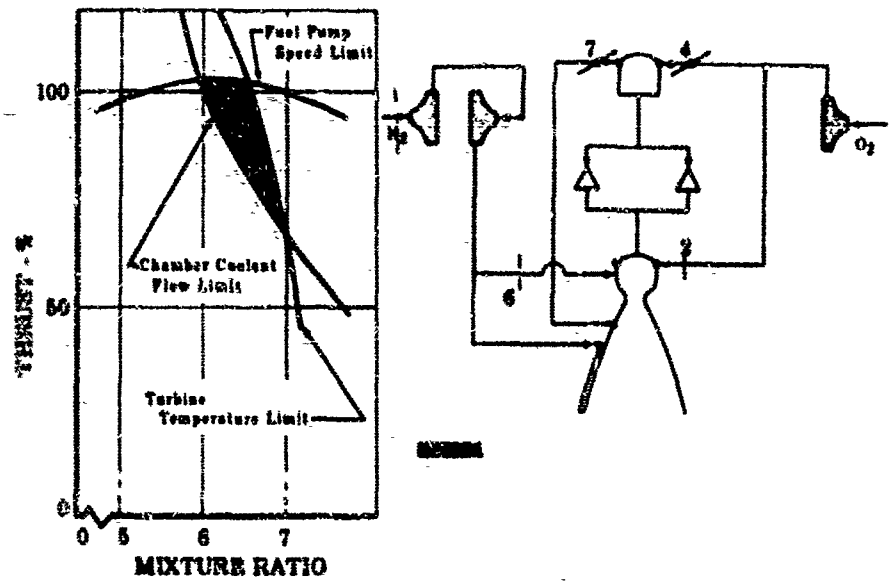


Figure 20. Load Control System (2-Valve Configuration) Operating Region FD 20678A

(U) The control system selected for the demonstrator engine was a three-valve system. This system allows the excess turbine power available at throttled conditions to increase the pump speeds and pressures at the desired flow rates and then throttles the pressures to the levels required by the engine system. The three primary control functions are provided by the preburner variable-area fuel injector, the preburner oxidizer flow divider valve and the main chamber oxidizer flow control valve. The primary control valves are in easily accessible locations on the engine. A demonstrator engine control system schematic showing the control valves, propellant shutoff valves, and propellant flowmeters is presented in figure 21.

CONFIDENTIAL
(This page is Unclassified)

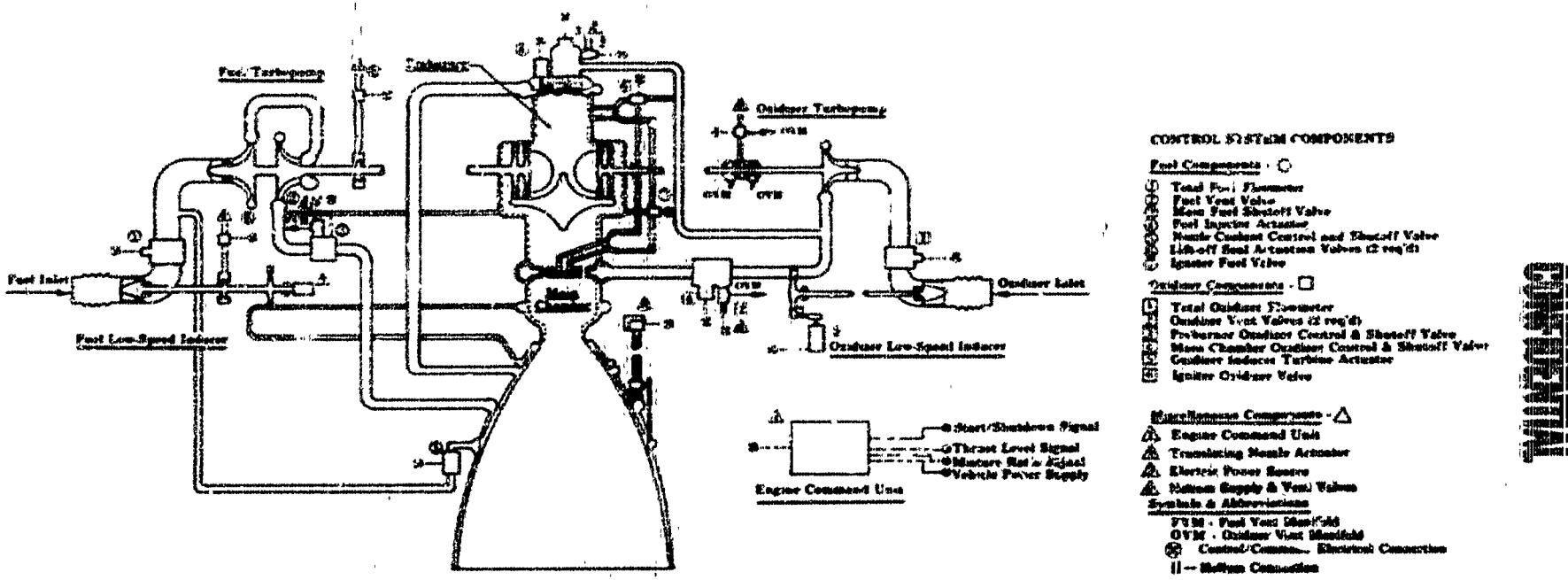


Figure 21. Demonstrator Engine Control System

FD 21006B

(U) The primary functions of the preburner fuel control are to throttle excess fuel system pressure and maintain stable preburner injector performance at reduced thrust operation. In addition, the preburner control will provide the proper fuel system resistance so that adequate transpiration cooling flow is supplied to the main chamber throughout the operating regime. The preburner oxidizer control throttles excess oxidizer system pressure, regulates the preburner combustion temperature, preburner oxidizer flow, and maintains stable preburner combustion during throttled operation. The main chamber oxidizer flow control regulates the oxidizer flow split between the preburner and the main chamber, and serves as an oxidizer system load control in conjunction with the preburner oxidizer control to regulate engine mixture ratio when there is excess oxidizer side pressure.

(U) An analysis of the control system was performed using known instrumentation accuracy and precision factors to compare the accuracies of a system using pressures as the primary control inputs and one using directly measured engine flow rates.

(U) In the pressure control system, preburner pressure and chamber pressure were the primary control inputs. These pressure measurements were used in combination with oxidizer metering valves in both the preburner and main chamber flow paths to determine the engine mixture ratio and thrust. This indirectly measured engine flow was then compared to the desired flow by computer. The values are compared and an error signal is fed back from the computer to the regulator portion of the valves. The accuracy of this system is shown in figure 22. The large error at low thrust levels is caused mainly by the dependence of the system on the pressure transducer measurement precision, which is expressed as a percent of the full-scale reading. Therefore, the system error increases as the absolute pressure level is reduced at low thrusts.

(C) In the second system, the fuel and oxidizer flows are measured directly. Flowmeter errors are proportional to the flow and, therefore, the turndown in flow at low thrust does not magnify the errors as in the case where pressure transducers are used. The gain in overall system accuracy is also shown in figure 22.

(C) The precision of the flow measurement control system at the 100% and 20% thrust levels is presented in figure 23. The mixture ratio and thrust precisions for the nominal and minimum thrust levels is ±2.5% and 0.8%, respectively, at mixture ratios of 5, 6, and 7. The above precision values reflect only the capability of the flow measurement system and do not include the effects of the control system computer, control actuator precision, etc.; however, all other effects can be controlled to the extent that the measurement system inprecision is the primary factor. The overall thrust and mixture ratio control capability will then be, approximately, equal to the measurement system capability and will meet the specific requirement of ±3% at rated thrust.

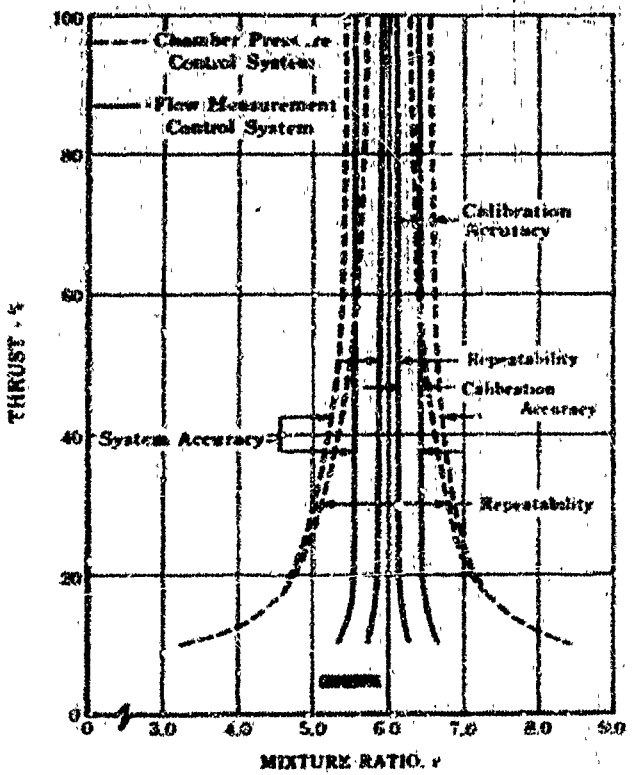


Figure 22. Control System Accuracy Comparison FD 15654C

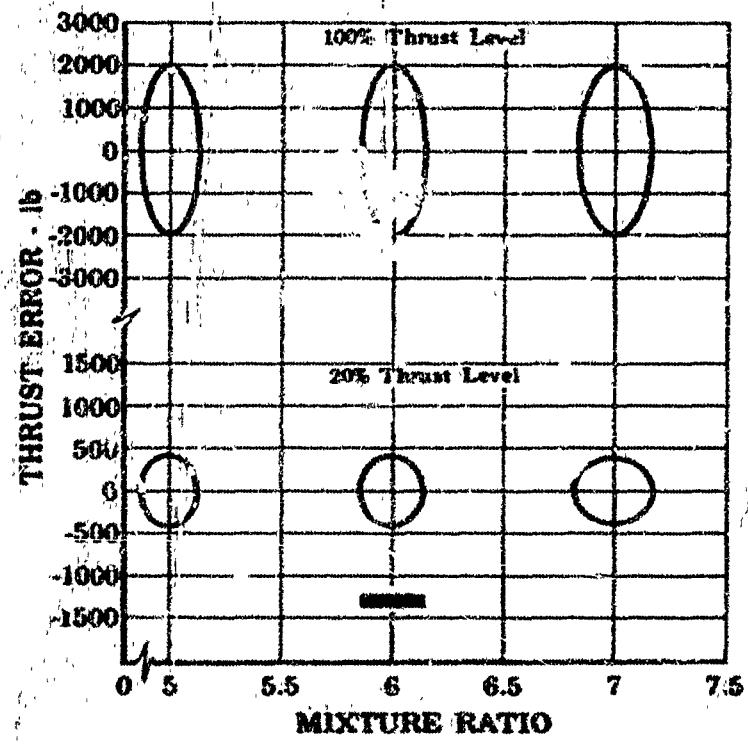


Figure 23. Flow Measurement Control System Precision FD 23403

(C) Locating the flowmeters between the low-speed inducers and the pumps increases the oxidizer and fuel inducer horsepower requirements by 15% and 30%, respectively, at the highest flow rates to provide for the meter pressure loss. However, there is sufficient excess power available in both inducers to allow placing the meters in this location.

(C) The selected principal control inputs were the fuel and oxidizer flowmeter signals. The flowmeter readings are compared to the desired input and differences between the actual and desired flows are used as error signal inputs to the engine control system.

(6) Demonstrator Engine Configuration

(a) Operating Characteristics

(C) The demonstrator engine cycle balance was derived using conservative estimates of component efficiencies, system pressure levels, and coolant requirements determined during the component technology programs to date. The estimated operating characteristics of this engine at rated and 20% thrust for mixture ratios of 5, 6, and 7 are presented in table IX. Vacuum specific impulse during throttled operation for the upper stage configuration is presented in figure 24. Performance as a function of altitude for the booster application is shown in figure 25.

(C) A 3000-psia nominal chamber pressure cycle balance was generated using the same pump efficiency levels as cited above. The specific impulse for this cycle was less than 1 second greater than that achieved with the selected configuration. However, the mixture ratio range at rated thrust was limited to ±0.52 from the nominal mixture ratio of 6, and it was therefore dropped from consideration for the demonstrator engine configuration.

(C) The recommended demonstrator engine configuration has a relatively small fuel system volume because of the use of the two-position nozzle. A small fuel system volume tends to reduce the likelihood of the occurrence of fuel instability. However, an alternative cycle balance was generated for an engine with a variable-area fuel pump discharge valve to provide additional fuel stability if it is required. In addition to providing a variable fuel system pressure loss, this control also serves as the fuel shutoff valve. The availability of sufficient excess fuel system pressure at off-design conditions permits the use of a variable-area fuel pump discharge valve without appreciably affecting turbopump operation or causing a degradation of engine performance. The nominal chamber pressure was reduced only 10 psi to 2730 psia. The fuel system pressure losses were distributed between the fuel pump discharge valve and the preburner fuel injector. A univariant area schedule was selected for the fuel pump discharge valve (controlled as a function of thrust only). The remainder of the fuel side pressure loss, which provides the control functions for injector stability and transpiration coolant flow, is in the variable preburner fuel injector.

(C) Table IX. Estimated Demonstrator Engine Operating Characteristics, Upper Stage: Nozzle Extended (Cycle AF-1107)

	100% Thrust r = 5.0	100% Thrust r = 6.0	100% Thrust r = 7.0	20% Thrust r = 5.0	20% Thrust r = 6.0	20% Thrust r = 7.0
Configuration						
Thrust, lb	250,000	250,000	250,000	50,000	50,000	50,000
Specific Impulse, sec	462	460	450	461	457	446
Envelope:						
Diameter, in.	100	100	100	100	100	100
Length: Nozzle Extended/Retracted, in.	170/101	170/101	170/101	170/101	170/101	170/101
Nozzle Area Ratio: Extended/Retracted	166/80	166/80	166/80	166/80	166/80	166/80
Fuel Flow, lb/sec	90.3	77.7	69.5	18.1	15.6	14.1
Oxidizer Flow, lb/sec	451.2	466.2	486.6	90.4	93.9	98.4
Total Propellant Flow, lb/sec	541.5	543.9	556.1	108.5	109.5	112.5
Main Combustion Chamber						
Throat Total Pressure, psia	2826	3140	2672	561	648	527
Mixture Ratio (injector)	5.92	6.48	7.65	5.39	6.59	7.78
Specific Impulse Efficiency, %	97	96.5	95.1	96.4	96.2	94.4
Fuel Injector Pressure Loss, psi	193	173	160	21	21	20
Oxidizer Injector Pressure Loss, psi	645	700	775	30	32	35
Chamber Pressure Loss, psi	108	105	102	21	21	20
Transpiration Coolant Flow, lb/sec	4.35	4.82	4.71	1.07	1.16	1.19
Throat Diameter, in.	7.7	7.7	7.7	7.7	7.7	7.7
Preburner Combustion Chamber						
Total Pressure, psia	4867	4563	4334	769	765	721
Mixture Ratio (preburner injector)	1.01	1.15	1.39	0.85	0.82	0.98
Maximum Pressure Loss, psi	41	38	35	6	6	5
Temperature, °R	1870	2096	2329	1268	1384	1810
Fuel Injector Pressure Loss, psi	223	777	1034	457	551	570
Oxidizer Injector and Control Valve Pressure Loss, psi	1795	1197	807	582	594	546
Total Propellant Flow, lb/sec	158	163	151	24.1	22.5	20.6
Combustion Efficiency, %	98.3	98.3	98.3	98.3	98.3	98.3
Thrust Nozzle						
Regenerative Section:						
Coolant Flow, lb/sec	83	71	62	15	13	12
Coolant Inlet Pressure, psia	5686	5658	5603	1261	1326	1316
Coolant Inlet Temperature, °R	128	131	135	71	76	81
Coolant Pressure Loss, psi	186	137	107	15	15	9
Coolant Temperature Rise, °R	71	72	86	88	99	101
Dump Section:						
Coolant Flow, lb/sec	1.3	1.3	1.2	0.3	0.3	0.25
Thrust, lb	587	562	512	130	125	114
Specific Impulse, sec	441	441	441	459	459	459

CONFIDENTIAL
CONFIDENTIAL

(C) Table IX. Estimated Demonstrator Engine Operating Characteristics, Upper Stage: Nozzle Extended (Cycle AF-1107) (Continued)

	100% Thrust r = 5.0	100% Thrust r = 5.5	100% Thrust r = 7.0	20% Thrust r = 5.0	20% Thrust r = 6.0	20% Thrust r = 7.0
Fuel Turbopump						
Pump:						
Number of Pump Stages	2	2	3	3	3	4
Speed, rpm	47,980	47,680	46,840	22,050	23,090	23,131
Pressure Rise, psi	5496	5624	5677	1211	1273	1281
Overall Efficiency, %	64.0	63.5	62.5	49.7	45.8	43.1
Impeller Tip Velocity (rms), ft/sec	2390	2360	2340	1100	1,30	1150
Temperature Rise, °R	84	39	48	29	35	34
Flow Rate, lb/sec	89.6	90.4	88.2	17.8	15.9	13.9
Turbine:						
Number of Stages	2	2	3	3	3	3
Pressure Ratio	1.44	1.38	1.34	1.30	1.31	1.30
Inlet Temperature, °R	1870	2096	1978	1268	1366	1893
Inlet Pressure, psia	4646	4564	4419	766	967	719
Temperature Drop, °R	114	170	114	54	51	48
Mean Wheel Velocity, ft/sec	1641	1612	1591	769	784	742
Efficiency, %	73.2	73.1	73.1	65.7	64.6	64.2
Flow Rate, lb/sec	108	91.6	89.8	16.5	15.1	14.0
Oxidizer Turbopump						
Pump						
Number of Stages	1	1	1	1	1	1
Speed, rpm	29,750	24,050	20,510	15,47	10,470	10,470
Pressure Rise, psi	6540	5670	4868	1268	1258	1190
Efficiency, %	67.3	68.7	69.0	66.8	47.9	45.9
Impeller Tip Velocity, ft/sec	905	845	795	484	583	573
Temperature Rise, °R	64	36	30	4	15	17
Flow Rate, lb/sec	491.2	466.2	486.6	93.4	93.9	90.4
Turbine						
Number of Stages	2	2	2	2	3	3
Pressure Ratio	1.49	1.45	1.42	1.24	1.26	1.25
Flow Rate, lb/sec	49.8	45.7	41.4	7.0	7.0	6.6
Inlet Temperature, °R	1687	1896	1787	1267	1366	1433
Inlet Pressure, psia	4821	4521	4294	767	739	716
Temperature Drop, °R	129	130	130	67	69	57
Mean Wheel Velocity, ft/sec	1121	1050	980	475	473	460
Efficiency, %	64.3	68.0	68.6	56.6	56.3	52

CONFIDENTIAL

(C) Table IX. Estimated Demonstrator Engine Operating Characteristics, Upper Stage: Nozzle Extended (Cycle AF-1107) (Continued)

	1.0 Thrust r = 1.0	94% Thrust r = 0.8	100% Thrust r = 1.0	20% Thrust r = 5.0	10% Thrust r = 6.0	10% Thrust r = 7.0
Low-Speed Inducer						
Fuel Inducer						
Flow Rate, lb/sec	97.3	77.7	69.5	18.1	11.6	8.1
Speed, rpm	19,8[illegible]	18,360	17,350	6020	4140	4201
Pressure Rise, psi	14	92	88	20	25	24
NPSH, ft	60	60	60	60	60	60
Efficiency, %	76.0	79.0	77.2	47.2	41.4	37.5
Oxidizer Inducer						
Flow Rate, lb/sec	451.2	406.2	486.6	99.4	95.9	98.6
Speed, rpm	6335	5961	5154	3952	3840	3826
Pressure Rise, psi	252	220	191	48	58	49
NPSH, ft	16	16	16	16	16	35
Efficiency, %	80.1	80.2	76.5	54.6	42.0	43.6
Fuel Low-Speed Inducer Turbine						
Pressure Ratio	1.37	1.41	1.43	1.55	1.49	1.50
Flow Rate, lb/sec	6.2	6.4	6.7	1.7	1.3	1.3
Speed, rpm	19,8[illegible]	18,360	17,350	6020	4140	4187
Efficiency, %	53.7	49.3	48.7	21.7	20.7	20.5
Oxidizer Low-Speed Inducer Turbine						
Pressure Drop, psi	710	833	946	452	436	320
Flow Rate, lb/sec	370	388	420	80.8	63.1	67.6
Speed, rpm	5739	5141	5143	1435	1040	1025
Efficiency, %	51.9	51.7	50.7	34.9	34.0	34.5

CONFIDENTIAL

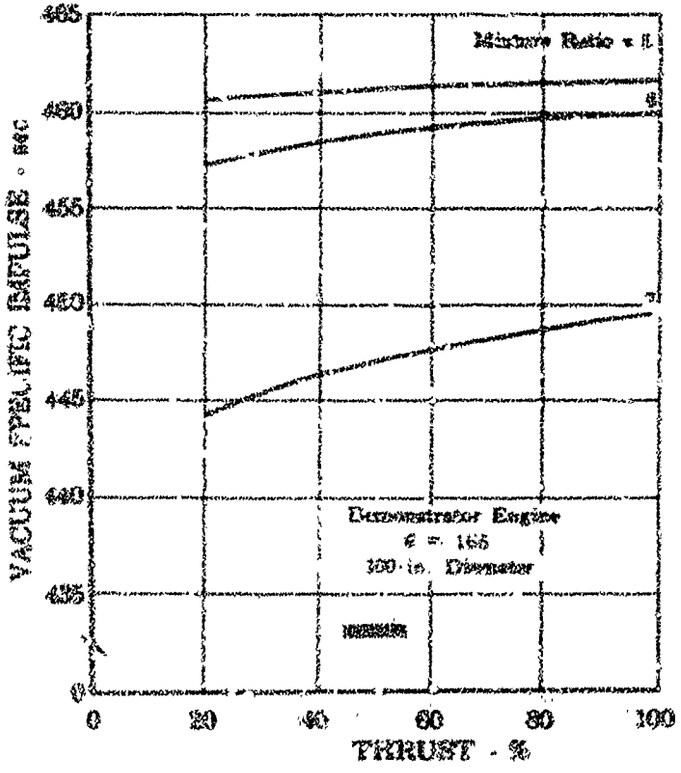


Figure 24. Vacuum Specific Impulse vs Thrust (Upper Stage)

FD 21059

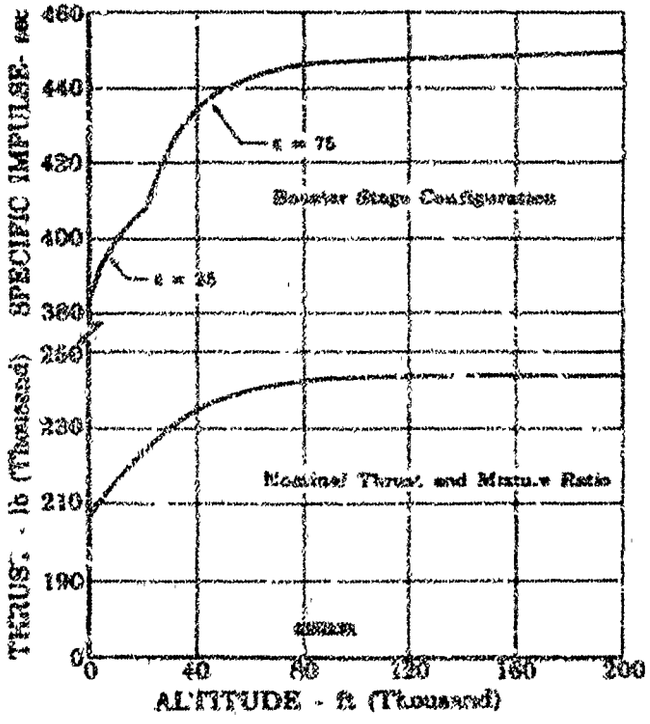


Figure 25. Altitude Performance for Booster Application

FD 21219

(U) The preliminary results using the current analog computer simulation indicated the pressure drop may be required. The pump discharge pressure drop schedule, however, will be affected by the control system dynamics as well as the engine system dynamics. Because the control system dynamics are not completely defined, a conservative estimate was made to assure stability in a demonstrator engine fuel system.

(C) The available pressure loss at a mixture ratio of 7.0 from the alternative cycle balance is compared to the estimated requirement in figure 26. The shape of the available loss curve results from the smooth univariant valve area schedule selected at a mixture ratio of 5 to minimize the effect on cycle power and control system complexity.

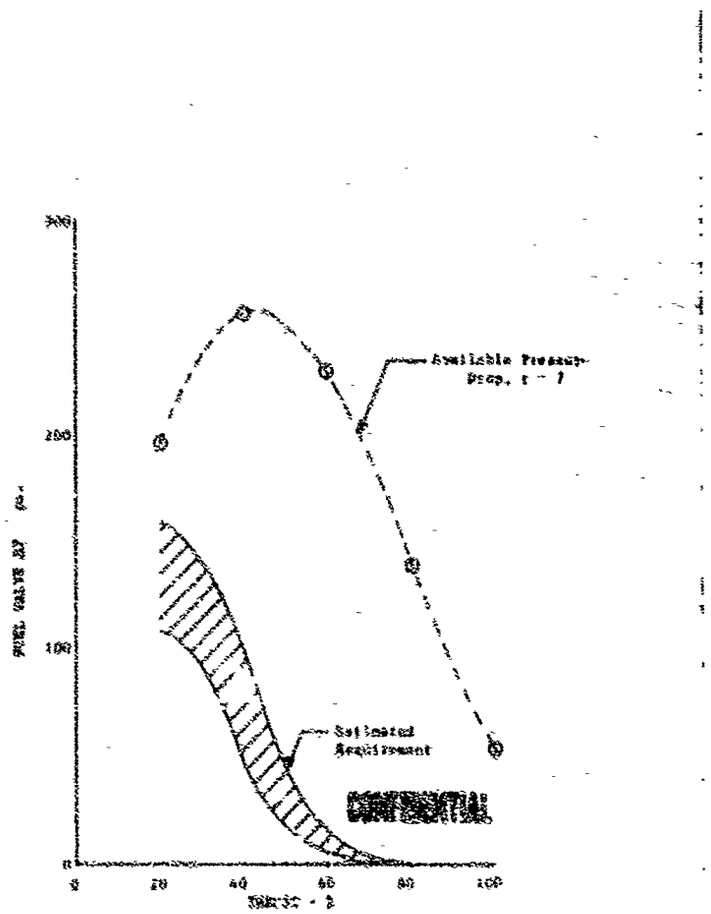


Figure 26. Fuel Valve Pressure Drop Schedule

DF 59056

(U) More detailed studies are needed using a revised analog computer simulation of the AF-1107 cycle balance to determine whether the fuel system will require a stability valve at the main pump discharge.

(b) Engine Description

(U) A propellant flow schematic illustrating the principal flow paths of this engine is shown in figure 27. Hydrogen and oxygen enter at the engine-driven low-speed inducers. The low-speed inducers are used to minimize vehicle tank pressure requirements while maintaining high speed main propellant pumps for high turbopump efficiencies. The low-speed fuel inducer is a single shaft unit with an axial-flow inducer driven by a partial-admission, single-stage, hydrogen turbine. The low-speed oxidizer inducer is also a single shaft unit with an axial-flow inducer driven by a partial-admission, single-stage liquid oxygen turbine.

(U) The main fuel turbopump is a single-shaft unit with two back-to-back centrifugal pump stages driven by a two-stage, pressure-compounded turbine. A double-acting thrust balance piston is provided between the pump and turbine.

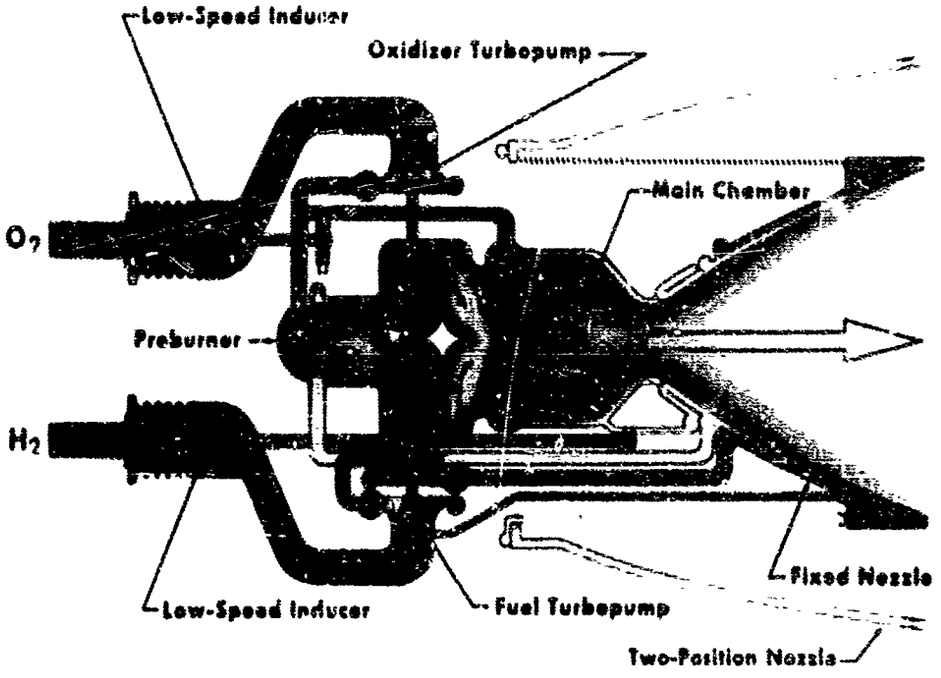


Figure 27. Propellant Flow Schematic FD 21002A

(U) The oxidizer turbopump is a single-shaft unit with a single, shrouded centrifugal pump stage driven by a two-stage, pressure-compounded turbine. A single-acting thrust balance piston is provided between the pump and turbine.

(U) The preburner injector consists of dual-orifice tangential-swirler oxidizer injection elements and variable-area fuel injection elements. A flow divider valve is incorporated to vary the total oxidizer flow rate for turbine inlet temperature control and to adjust the relative flow of the primary and secondary elements. The preburner combustion

chamber is an integral part of the transition case, which contains the turbine drive gas ducts and a cooled outer-shell. The main turbopumps are mounted to the transition case with a plug-in arrangement of the turbines to facilitate maintainability.

(U) The main chamber injector consists of fixed-area, tangential-swirler oxygen injection elements arranged in radial spraybars. The fuel injector is a fixed-area design that directs fuel-rich turbine exhaust gas around each row of oxidizer injection points. A small portion of the fuel-rich gas flows through a porous face to provide cooling. The combustion chamber wall is composed of a hydrogen cooled liner extending from the injector face through the throat region to a point immediately downstream of the throat.

(U) The nozzle, which attaches immediately downstream of the throat, is composed of a regeneratively cooled section and a low pressure dump cooled section. The forward portion, which is in the higher heat flux region, is regeneratively cooled with conventional tubular heat exchangers.

(U) The main hydrogen flow is pumped to the system operating pressure level by the main fuel pump. The hydrogen is then ducted to cool the regenerative section of the nozzle. The rearward portion of the fixed regeneratively cooled nozzle section is cooled with the total hydrogen flow from the main fuel pump in a single pass, counter-flow heat exchanger. Most of this flow exits the nozzle at a point downstream of the transpiration cooled chamber and is ducted to the preburner. The remainder, a small portion of the hydrogen, is used to regeneratively cool the smaller forward section of the regeneratively cooled nozzle and is subsequently used as a working fluid to power the low-speed fuel inducer drive turbine. This flow is then used in the transpiration cooled main chamber walls. A small amount of hydrogen is used at low supply pressure to cool the nozzle skirt downstream of the regeneratively cooled nozzle section. This hydrogen is heated to high temperature in the skirt and expelled overboard through small nozzles at the end of the skirt, providing a specific impulse approximately that of the main gas stream.

(U) The low pressure nozzle skirt cooling flow is ducted from the discharge of the fuel low-speed inducer. A quick disconnect fitting is provided to stop the flow when the secondary nozzle is retracted.

(U) After being pumped to system operating pressure levels, the oxygen is divided between the preburner and the main chamber. The smaller portion of the flow is ducted to the preburner where it is burned with the hydrogen. The resulting combustion products provide the working fluid for the main turbines, which are arranged with their flows in parallel. The individual turbine exhaust gases are recombined and directed to the main injector.

(U) The main chamber oxidizer flow provides the oxidizer low-speed inducer turbine working fluid and uses the available pressure drop between the main oxidizer pump discharge pressure and the main chamber for turbine power. The oxidizer flow is then injected into the main combustion chamber where it mixes and burns with the fuel-rich turbine exhaust gases. The resulting combustion gas is then expanded through the bell nozzle.

(U) The primary engine thrust and mixture ratio controls are located in the liquid oxygen supply lines to the preburner and the main chamber and in the variable-area fuel side of the preburner injector.

(U) A preliminary demonstrator engine installation drawing of the booster and upper stage applications are provided as figures 28 and 29, respectively

(c) Engine Weight

(U) The demonstrator engine weight is based upon lightweight construction. Lightweight construction results in heavier than flightweight components because additional design margins are used to ensure the structural integrity commensurate with the objectives of the demonstrator engine program. These designs, however, are not boilerplate type and the elements are functionally the same as flight-type designs.

(C) The weight of the demonstrator engine as defined by cycle balance AF-1107 was estimated to be 3450 lb. This is considerably less than earlier configuration weights. The major part of the weight reduction resulted from the use of a two-position lightweight nozzle skirt. Additional significant weight reductions were obtained by modifying the designs of the main injector and combustion chamber, preburner assembly, transition case, and other components. A component weight breakdown is given in table X.

(C) The lightweight two-position nozzle reduced the weight of the nozzle assembly 715 lb. This reduction in the nozzle skirt weight is obtained by dump cooling with a low coolant pressure instead of regenerative cooling at high pressure. Dump cooling permits the use of lightweight expanded sheet metal construction rather than the conventional brazed tube assembly. This reduces the weight per unit of nozzle surface area from approximately 4 lb/ft^2 to 1 lb/ft^2.

(U) The demonstrator engine weights were estimated on the basis of "lightweight" construction. The component designs were made with internal mechanisms and characteristics representative of a flightweight engine. However, the demonstrator engine components were designed to minimize cost of fabrication by not removing excess materials from locations that are difficult to machine, and by not scalloping flanges.

(U) The stress margins applied during component design directly affect the material thickness and weight. These margins are determined from the design requirements of life and duty cycles, and are based on previous material tests and engine component experience.

(d) Preliminary Component Design

(U) Preliminary turbomachinery and transition case designs were prepared to provide the necessary envelope, weight, and component requirements for overall engine system evaluation. The remaining components associated with the staged-combustion test rig were not included under the Module Design Task, but were studied under their respective component programs. The low-speed inducers, main turbopumps and transition case preliminary designs are described below.

CONFIDENTIAL
(This page is Unclassified)

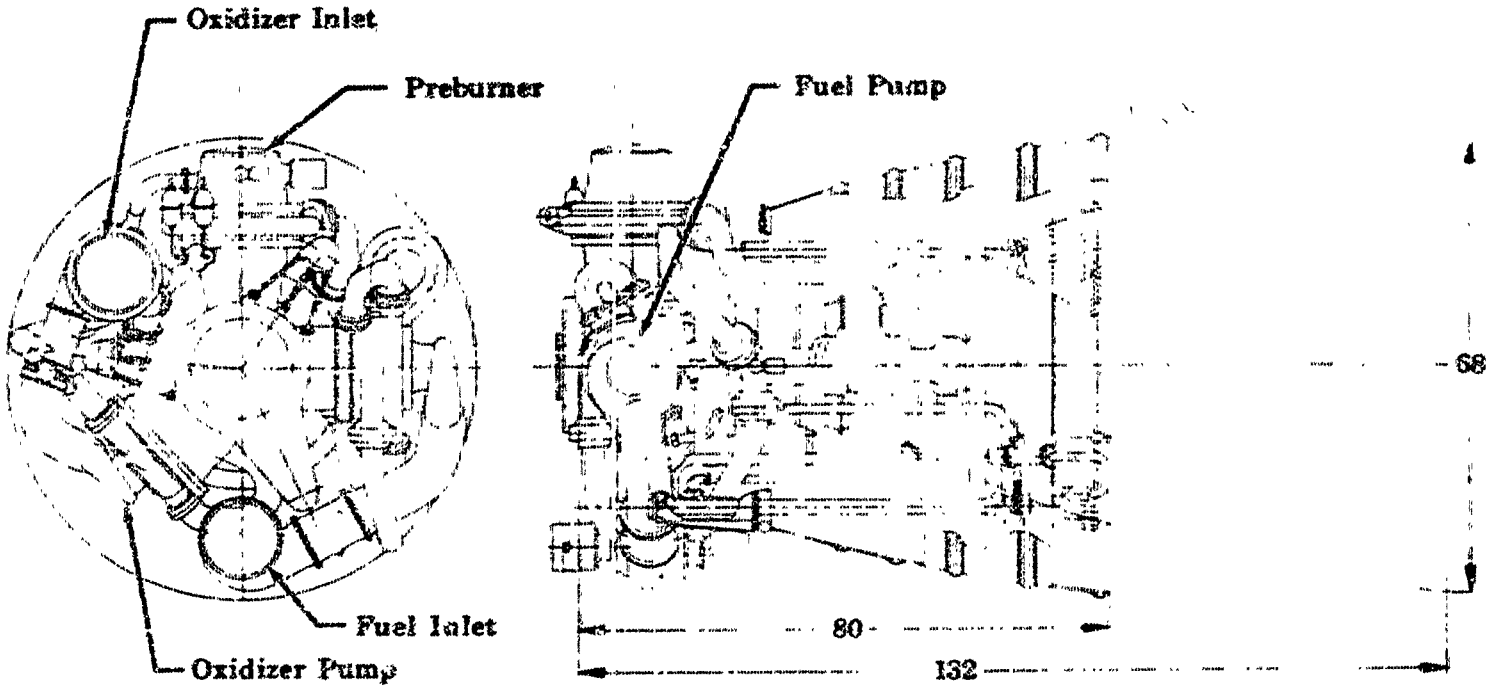


Figure 28. Demonstrator Engine Preliminary Installation Drawing (Booster Application)

FD 23353

CONFIDENTIAL

CONFIDENTIAL

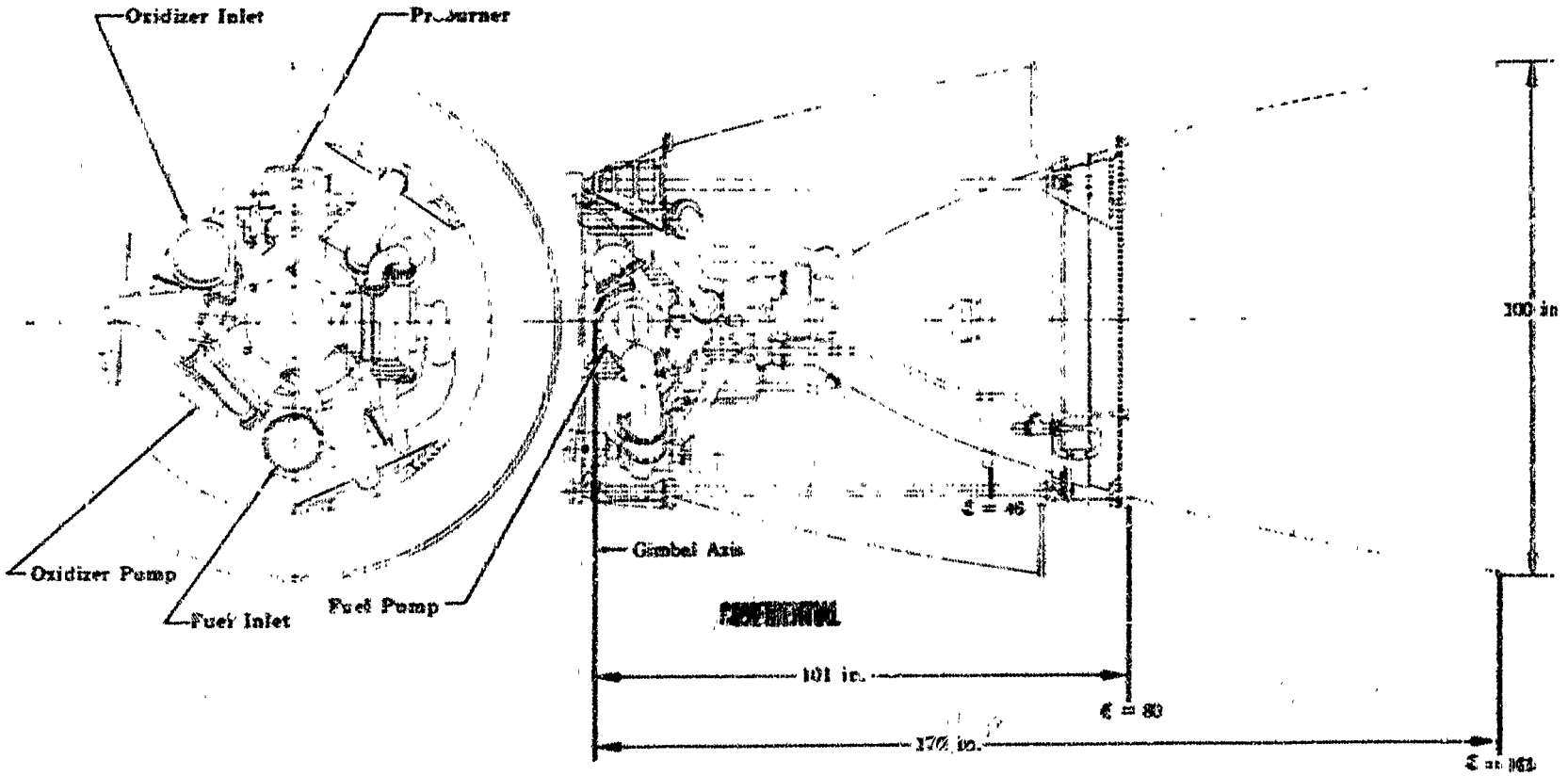


Figure 29. Demonstrator Engine Preliminary Installation Drawing (Upper Stage)

FD 210124

CONFIDENTIAL

(C) Table X. Weight Breakdown by Components for Demonstrator Engine (250,000-lb Thrust, 100-in. Dia)

	Demonstrator Engine (AF-1107)
Preburner	320
Transition Case	360
Main Injector	135
Main Chamber	445
Nozzle and Actuators	555
Fuel Turbopump	355
Oxidizer Turbopump	280
Low-Speed Inducers	215
Controls (Less Actuators and ECU)	380
Plumbing	310
Miscellaneous	75
Total	3450 lb

(1) Oxidizer Low-Speed Inducer

(U) The oxidizer low-speed inducer, shown in figure 30, is a single-shaft unit with a high specific speed, axial-flow inducer driven by a variable inlet area, single-stage, liquid oxygen turbine. The inducer is designed to supply the main oxidizer turbopump with sufficient liquid oxygen inlet pressure to prevent cavitation.

(C) The inducer has a constant tip diameter and a 2-degree blade camber to obtain the required head rise and maintain maximum suction capability. The volute is a constant velocity design with a single discharge. Axial thrust unbalance is absorbed through the front bearing and bearing support.

(C) The liquid oxygen powered turbine has a variable inlet control that enables the turbine inlet arc-of-admission to be varied between 5% and 50%.

(U) Aluminum (AMS 4130) was selected as the material for the inducer and turbine housings. The inducer housing accommodates both front and rear bearing supports and the variable turbine inlet valve shaft. The Inconel 718 (AMS 5664) inducer has three blades and is attached to an Inconel 718 (AMS 5664) drive shaft. The shaft is supported by a fixed front bearing and a floating rear bearing. The material for the single-stage, shrouded turbine and stator vanes is Inconel 718 (AMS 5664) and the stator vanes are a part of the rear bearing support.

CONFIDENTIAL

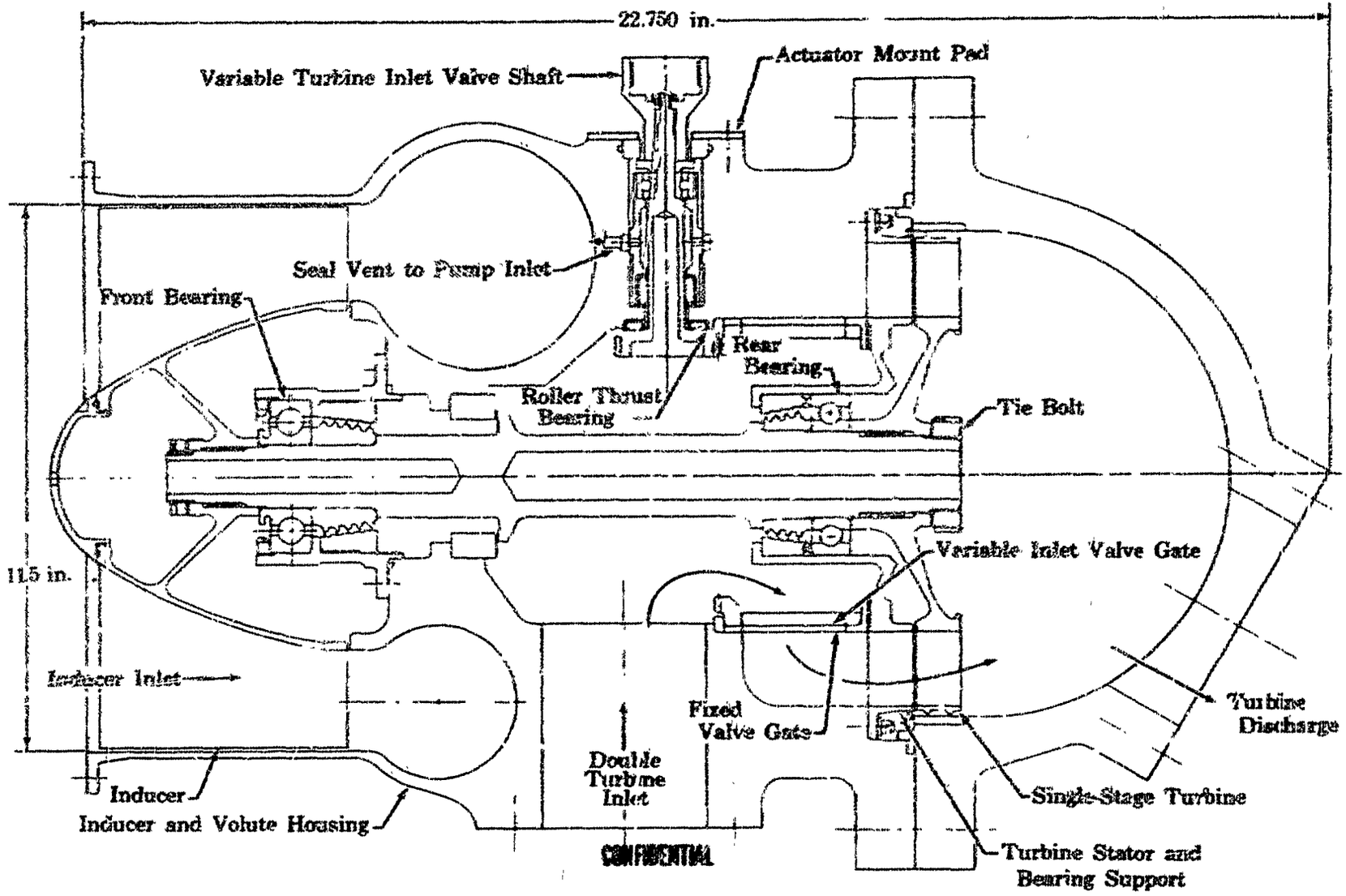


Figure 30. Oxidizer Low-Speed Inducer

FD 18906D

CONFIDENTIAL

(C) The turbine driving fluid enters the housing cavity through two inlets. The inlet control gate valve permits the fluid to flow from the housing cavity through the exposed housing passages, stator vanes, rotor, and out the turbine discharge housing. The turbine inlet area is varied by rotating a cylindrical gate valve past the ports in the inducer housing. The gate valve was designed and located so the pressure drop will be small and the resulting radial loads will be transmitted into the housing. The front edge of the gate contains a face gear that mates with the control shaft piston gear.

(U) The operating characteristics of the oxidizer low-speed inducer are presented in table XI.

(C) Table XI. Operating Characteristics of Oxidizer Low-Speed Inducer

Pump	
Engine Operating Point for Component Design:	
Mixture Ratio	7
Thrust, %	100
Speed, rpm	5140
Tip Speed, ft/sec	251
Diameter, in.	11.4
Blade Entrance Angle, deg	6
Number of Blades	3
Blade Height Inlet, in.	3.5
Blade Height Exit, in.	1.75
Blade Thickness, in.	0.068
Flow Coefficient	0.119
Head Coefficient	0.212
Suction Specific Speed	40,000
Specific Speed	3700
NPSH (Required), ft	14
NPSP (Required), psi	6.70
Flow Rate, gpm	3140
Flow Rate, lb/sec	485
Head Rise, ft	410
Pressure Rise, psi	201
Inlet Density, lb/ft^3	69.1
Exit Density, lb/ft^3	69.1
Horsepower	471
Efficiency, %	78.5
Turbine	
Engine Operating Point for Component Design:	
Mixture Ratio	7
Thrust, %	100
Speed, rpm	5140
Mean Wheel Velocity, ft/sec	158
Mean Diameter, in.	7
Vane Height, in.	1.35
Percent Admission	42.5
Velocity Ratio	0.63

(U) Table XI. Operating Characteristics of Oxidizer Low-Speed Inducer (Continued)

Turbine (Continued)	
Flow Area, $in.^2$	3.04
Vane Angle, deg	15
Flow Rate, lb/sec	410
Inlet Pressure, psia	4093
Inlet Temperature, °R	206
Pressure Ratio	1.14
Efficiency, %	50.7
Horsepower	471
Number of Stages	1

(2) Fuel Low-Speed Inducer

(U) The fuel low-speed inducer shown in figure 31 is a single-shaft unit with a high specific speed, axial-flow inducer driven by a partial-admission, single-stage, hydrogen expander turbine. The inducer is designed to supply the main fuel turbopump with sufficient liquid hydrogen pressure to prevent cavitation.

(U) The inducer is helical with a constant tip diameter and is designed to obtain the required head rise and maintain maximum suction capability. The volute is a constant velocity design with a single discharge. Axial thrust unbalance is absorbed through the bearing supports.

(U) The single-stage, partial-admission turbine is driven by high-pressure gaseous hydrogen. An orificed turbine bypass path is provided to trim the turbine flow for the most adverse power condition. No adjustment is required during engine operation.

(U) The inducer housing is made of aluminum (AMS 4130) and contains the volute and provisions for both bearing supports. The Inconel 718 (AMS 5664) drive shaft and turbine assembly. The turbine inlet and turbine discharge are on the same housing interface. Prior to start, the inducer lift-off seal prevents fuel flow through the transpiration cooled main combustion chamber wall. During the start transient, as main fuel pump discharge pressure becomes higher than inducer discharge pressure, the seal is lifted off and high-pressure fuel is introduced to cool both the front and rear bearings. An accessory drive mount pad is provided on the turbine end of the shaft.

(U) The operating characteristics of the fuel low-speed inducer are presented in table XII.

CONFIDENTIAL

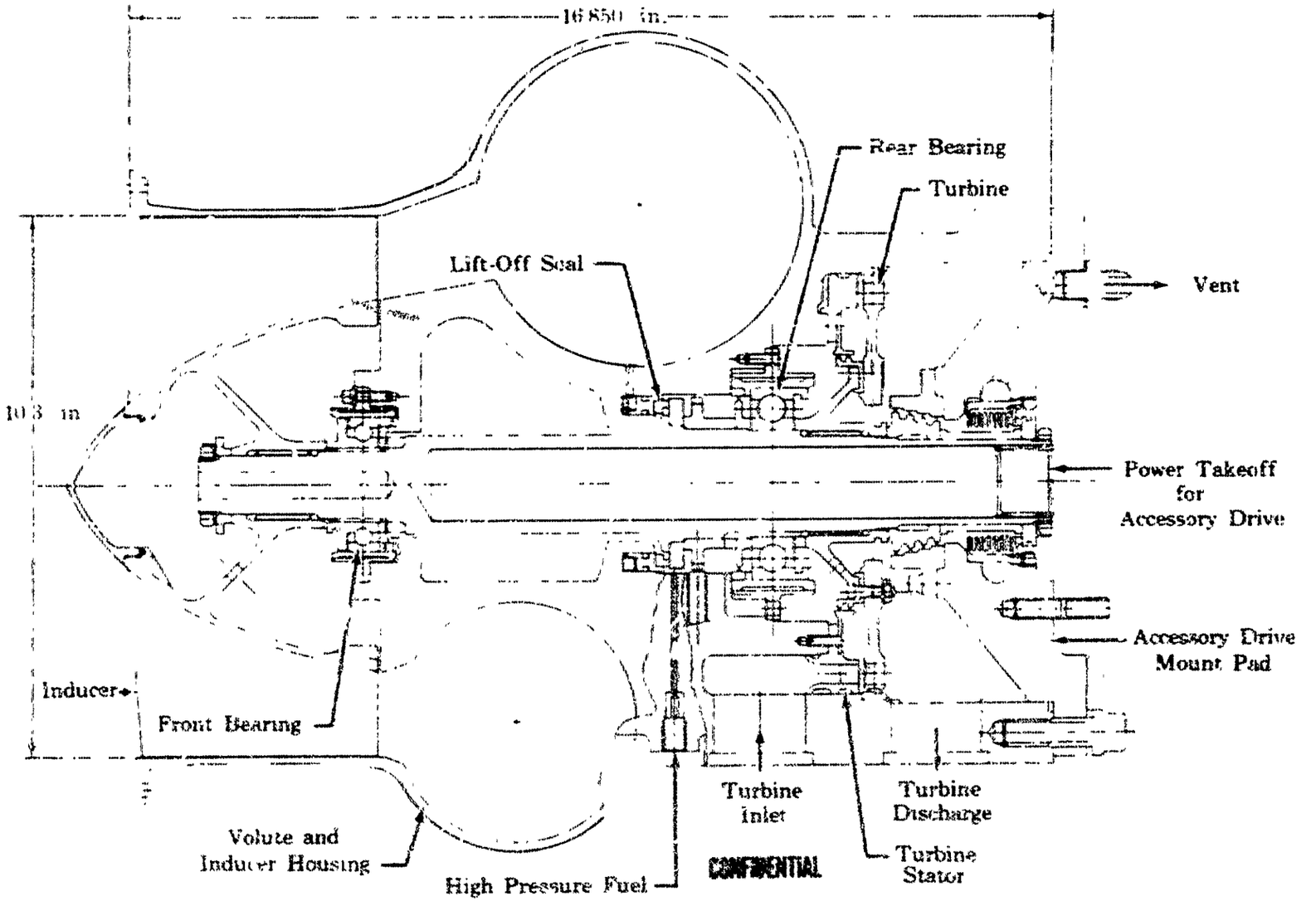


Figure 31. Two-Speed Inducer

FD 16885L

CONFIDENTIAL

(C) Table XII. Operating Characteristics of Fuel Low-Speed Inducer

Pump	
Engine Operating Point for Component Design:	
Mixture Ratio	5
Thrust, %	100
Speed, rpm	20,000
Tip Speed, ft/sec	890
Diameter, in.	10.[illegible]
Blade Entrance Angle, deg	6
Number of Blades	3
Blade Height Inlet, in.	3.47
Blade Height Exit, in.	1.5[illegible]
Blade Thickness, in.	0.051
Flow Coefficient	0.104
Head Coefficient	0.1
Suction Specific Speed (Water Reference)	46,790
Specific Speed	7150
NPSH (Required), ft	54.3
NPSH (Required), psi	3.96
Flow Rate, gpm	9570
Flow Rate, ft³/sec	90.0
Head Rise, ft	2440
Pressure Rise, psi	71.3
Inlet Density, lb/ft³	4.22
Exit Density, lb/ft³	4.22
Horsepower	500
Efficiency, %	79.9
Turbine	
Engine Operating Point for Component Design:	
Mixture Ratio	5
Thrust, %	100
Speed, rpm	20,000
Mean Wheel Velocity, ft/sec	700
Mean Diameter, in.	8.0
Vane Height, in.	0.35
Percent Admission	7.[illegible]
Velocity Ratio	0.249
Flow Area, in²	0.166
Vane Angle, deg	15
Flow Rate, lb/sec	4.25
Inlet Pressure, psia	451[illegible]
Inlet Temperature, °R	503
Pressure Ratio	1.37
Efficiency, %	53.[illegible]
[illegible]	[illegible]
Number of Stages	1

(5) Oxidizer Turbopump

(U) The preliminary oxidizer turbopump design shown in figure 32 is a single shaft unit with a single, shrouded, centrifugal pump stage driven by a two-stage, pressure-compounded turbine. The pump supplies the preburner and main burner with oxidizer at the required pressure and is mounted in the transition case between the preburner and main burner. The preburner combustion products provide the working fluid for the two-stage turbine.

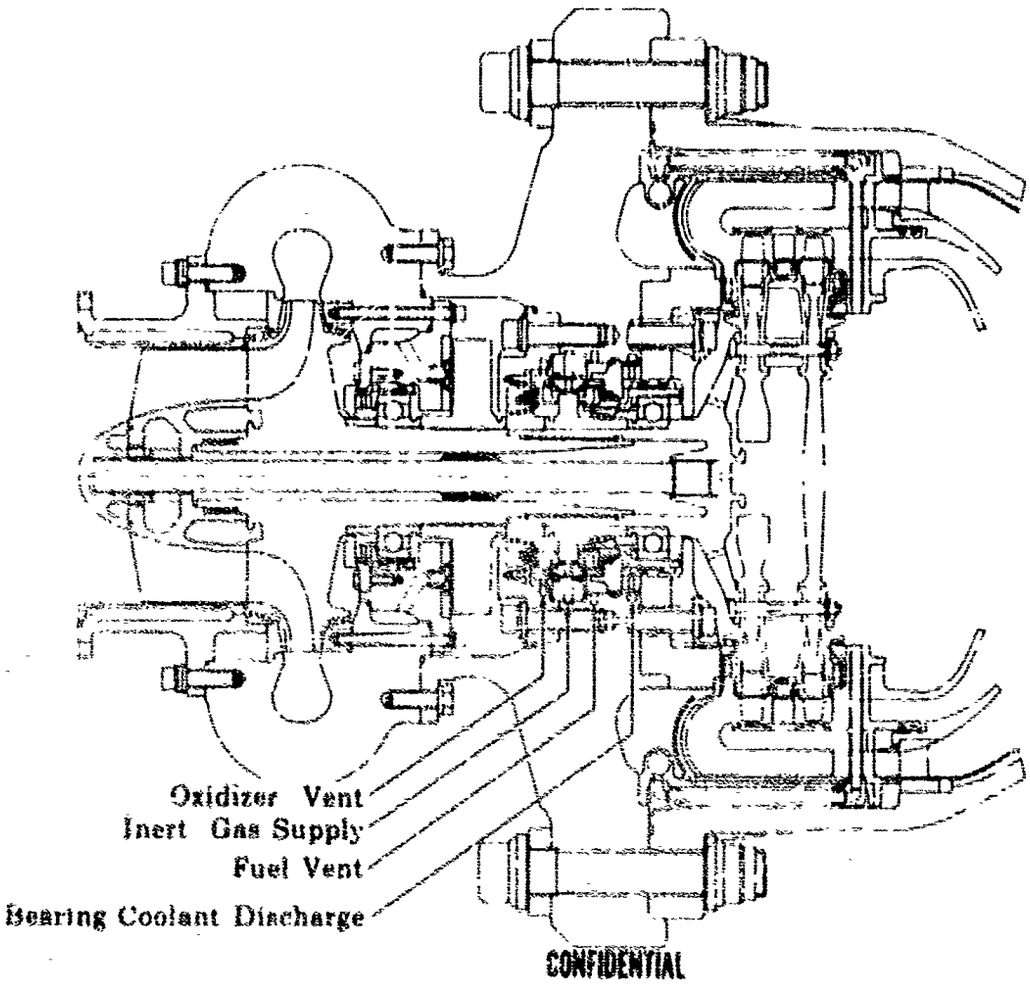


Figure 32. Oxidizer Turbopump Fb 21270

(6) The oxidizer pump has a constant velocity, deep, volute diffuser collector system, and a single-acting thrust balance piston to absorb [illegible] used to introduce oxidizer flow from the thrust piston and impeller near labyrinth seal back into the pump inlet.

(U) Aluminum (AMS 4130) was selected for the inducer housing, volute housing, and rear housing, and stainless steel was selected for the inducer, impeller, and thrust balance piston. The rotor assembly, composed of the Inconel 718 (AMS 5664) shaft tie bolt, inducer, impeller, and turbine, is supported by two axially preloaded bearings and the single-acting thrust balance piston. High-pressure oxidizer is supplied to the pump side of the thrust balance piston to prevent impeller axial movement resulting from turbine axial loading.

(U) The turbine disks are made of Titanium and the stators of Udimet 700. The turbine blades are made of PWA 664, a columnar cast, high-temperature material, and are attached to the disks with a conventional fir-tree design.

(U) The operating characteristics of the oxidizer turbopump are presented in table XIII.

(C) Table XIII. Operating Characteristics of Oxidizer Turbopump

Pump	
Engine Operating Point for Component Design:	
Mixture Ratio	7
Thrust, %	100
Speed, rpm	22,500
Tip Speed, ft/sec	790
Diameter, in.	8.05
Blade Exit Angle, deg	25
Number of Blades	12
Blade Height, in.	518
Blade Thickness, in.	0.06
Flow Coefficient	0.106
Head Coefficient	0.528
Suction Specific Speed	20,000
Specific Speed	1230
NPSH (Required), ft	225
NPSP (Required), psia	122
Flow Rate, gpm	3170
Flow Rate, lb/sec	485.2
Head Rise, ft	10,210
Pressure Rise, psi	4867
Inlet Pressure, psia	170.6
Discharge Pressure, psia	5037
Inlet Density, lb/ft^3	69.2
Exit Density, lb/ft^3	68.6
Horsepower	13,058
Efficiency, %	69.0
Inlet Temperature, °R	176.2
Discharge Temperature, °R	206.2

(C) Table XIII. Operating Characteristics of Oxidizer Turbopump (Continued)

Turbine	
Engine Operating Point for Component Design:	
Mixture Ratio	7
Thrust, %	100
Mean Wheel Velocity, ft/sec	980
Mean Diameter, in.	10
First Vane Height	0.453
Percent Admission	100
Velocity Ratio	0.34
Flow Area, in^2	2.30
Vane Angle, deg	17.7
Flow Rate, lb/sec	41.4
Inlet Temperature, R	2325
Inlet Pressure, psia	4293
Pressure Ratio	1.42
Efficiency, %	67.0
Horsepower	13,058
Cooling Flow, lb/sec	2.31
Number of Stages	1
Hub-to-Tip Diameter Ratio	0.905

(4) Fuel Turbopump

(C) The preliminary fuel turbopump design shown in figure 33 is a single-shaft unit with two back-to-back, unshrouded, centrifugal-pump stages driven by a two-stage, pressure-compounded turbine. The pump supplies the preburner and main burner with fuel at the required pressure and is mounted on the transition case between the preburner and main burner. The preburner combustion products provide the working fluid for the full-admission turbine.

(U) Both stages of the fuel pump have constant-velocity, dual, volute-diffuser collector systems with the 1st-stage discharge entering the second stage through radial inlets in the rear housing. A double-acting thrust balance piston system is incorporated in the pump design to compensate for axial thrust unbalance.

(U) Aluminum (AMS 4130) was selected for the inducer, first stage, intermediate, and rear housings; and titanium was selected for the inducer and impellers. The double-acting thrust balance piston and thrust piston housing are made of Inconel 718 (AMS 5664). The rotor assembly, composed of the Inconel 718 (AMS 5664) shaft tie bolt, inducer, impellers, and turbine, is supported by the bearings and the double-acting thrust balance piston. The thrust balance piston system works on the principle of a hydrostatic bearing.

Fig. 33. Fuel Turbopump

ED 21075

(U) Prior to start, a liftoff seal separates the turbine cavity from the rear bearing cavity and prevents fuel from leaking into the main combustion chamber. During the start transient, the pressure differential across the seal is reversed and the seal surfaces separate, the leakage is then controlled by a close tolerance labyrinth seal.

(U) The turbine disks are made of titanium and the stators of Udimet 700. The turbine blades are made of PWA 664, a columnar cast, high-temperature material, and are attached to the disks with a conventional fir-tree design.

(U) The operating characteristics of the fuel turbopump are presented in table XIV.

(C) Table XIV. Operating Characteristics of Fuel Turbopump

	First Stage	Second Stage
Pump		
Engine Operating Point for Component Design:		
Mixture Ratio	5	5
Thrust, %	100	100
Speed, rpm	48,000	48,000
Tip Speed, ft/sec	2270	2500
Diameter, in.	10.6	11.95
Blade Exit Angle, deg	25	25
Number of Blades	24	24
Blade Height, in.	0.49	0.435
Blade Thickness, in.	0.10	0.10
Flow Coefficient	0.0939	0.0857
Head Coefficient	0.525	0.332
Suction Specific Speed	20,000	—
Specific Speed	910	808
NPSH (Required), ft	1423	—
NPSP (Required), psia	41.7	—
Exit Flow Rate, gpm	9350	9230
Flow Rate, lb/sec	88.5	88.5
Head Rise, ft	83,925	102,436
Inlet Pressure, psia	71.6	2504
Pressure Rise, psi	2482	3068
Discharge Pressure, psia	2554	5572
Inlet Density, lb/ft^3	4.22	4.26
Exit Density, lb/ft^3	4.26	4.31
Horsepower	20,935	25,550
Efficiency, %	64	64
Inlet Temperature, °R	41.3	80.4
Discharge Temperature, °R	80.4	128

(C) Table XIV. Operating Characteristics of Fuel Turbopump (Continued)

	First Stage	Second Stage
Turbine		
Engine Operating Point for Component Design:		
Mixture Ratio	7	
Thrust, %	100	
Mean Wheel Velocity, ft/sec	1630	
Mean Diameter, in.	7.8	
First Vane Height, in.	0.56	0.62
Number of Blades	86	80
Percent Admission	100	100
Velocity Ratio (Overall)	0.503	
Flow Area, in^2	4.99	
Vane Angle, deg	25.9	26.2
Flow Rate, lb/sec	108	
Inlet Temperature, °R	1859	
Inlet Pressure, psia	4845	
Pressure Ratio (Overall)	1.64	
Efficiency, %	73.2	
Horsepower	47,083	
Cooling Flow, lb/sec	2.1	
Number of Stages	2	
Hub-to-Tip Diameter Ratio	0.865	

(U) The transition case assembly consists of that portion of the engine between the main combustion chamber injector forward (or upper) flange and the vehicle/engine thrust interface. With the incorporation of the preburner and turbomachinery components, the transition case is a self-contained "power head" capable of supplying the main chamber and nozzle with the high pressure propellants necessary to produce the required design thrust. It serves as the primary stage for the proposed staged-combustion cycle. Conventional external "hot" ducting of turbopump turbine flow gases is elminated by the use of a unique component plug-in concept permitting the design of internal flow passages confined within the basic transition case assembly. Providing thin, convectively cooled liners between the hot gas flow and external transition case walls permits optimum use of structural material to assure a minimum weight design of the geometrically complex transition case.

(U) Figure 24 depicts the general component arrangement and configuration of the transition case. The primary structure is essentially a non-symmetric pressure vessel consisting of three large diameter cylinders whose centerlines intersect the centerline of a fourth, and larger diameter cylinder, at right angles. The centerline of this larger cylinder, which serves as a collecting manifold for the turbine exhaust gases, coincides with the engine thrust axis. For optimum weight and manufacturing simplicity, the basic case structure is made from a series of forgings welded together using conventional fabrication techniques.

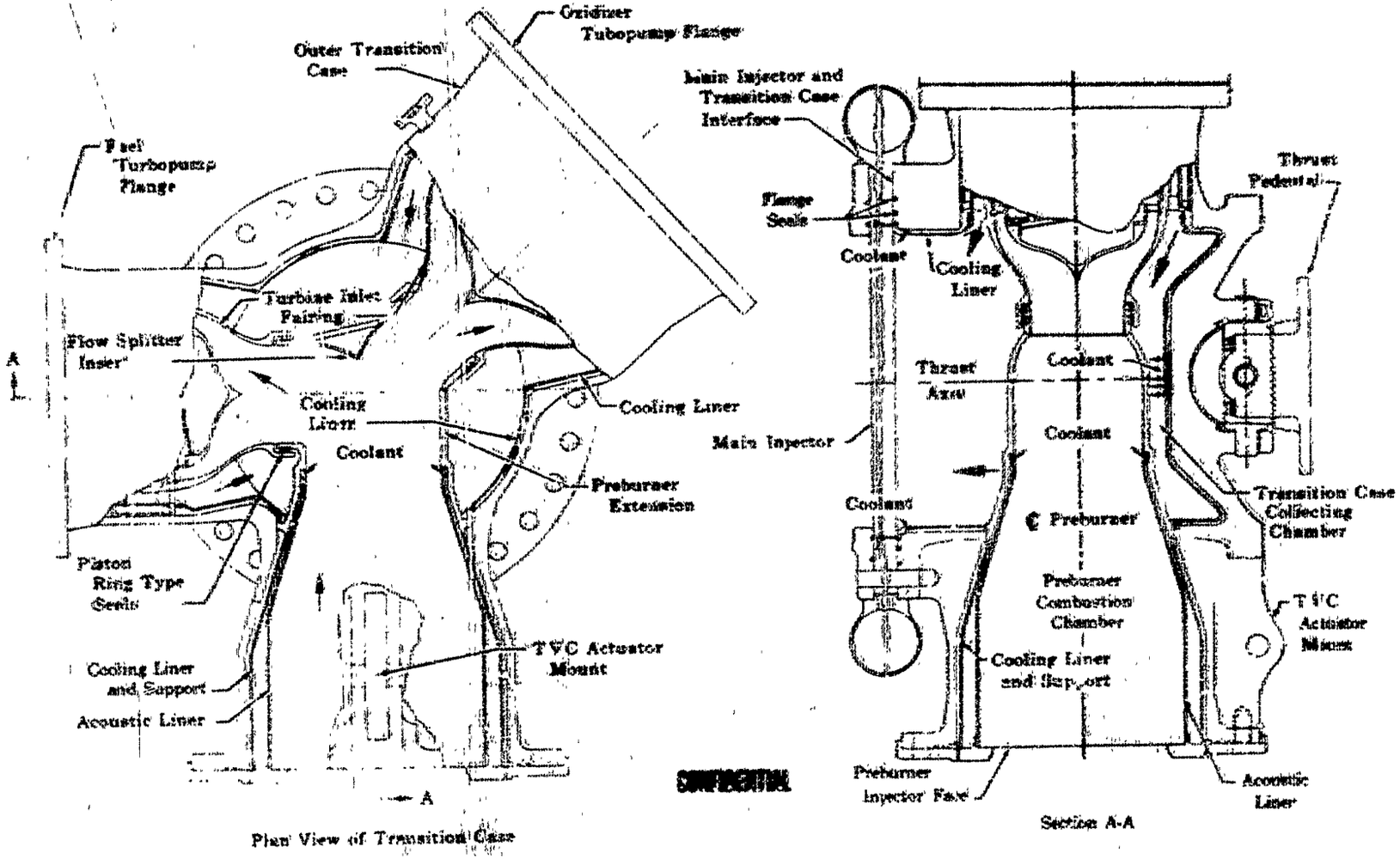


Figure 34. Transition Case Component and Cooling Liner Arrangement

FD 23404

(U) Although not integral parts of the transition case structure, the cooling liners and preburner discharge gas flow ducts are essential elements to the overall concept. Therefore, consideration is given herein to specific design aspects of these components and their influence in establishing the ultimate configuration of the transition case assembly.

(U) The main oxidizer and fuel turbopumps, as well as the preburner injector and combustion chamber assembly, are mounted on flanged cylinders that form an integral part of the transition case. Machined bosses for installing both the preburner and main chamber igniters, as well as the main chamber injector coolant supply lines are also located on the transition case.

(U) The gimbal-ball spherical seat (socket) and retainer on the upper dome end, is machined integrally with the basic case forging.

(U) The aft, or lower, portion of the transition case is flanged to provide a mating interface with the main injector and combustion chamber.

c. Transient Analysis

(1) General

(U) Detailed transient analyses, which included start, throttling, shutdown and stability analysis, were conducted to further evaluate and refine the overall system. Complete engine digital computer simulations were used for each operating mode of start, throttling, and shutdown. An electronic analog computer model of the complete engine was developed for further stability and throttling analysis.

(2) Start Transient Analysis

(C) A detailed start transient analysis was conducted to determine the ignition and acceleration characteristics of the engine during the time interval from the start signal until the idle-thrust level (20% of rated thrust) is achieved. During this time period, the propellants fill the fuel and oxidizer system volumes, ignition in the preburner and main chamber occurs, and the acceleration of the turbopumps takes place. A start transient to 20% thrust (idle-thrust level) was simulated for the selected demonstrator engine configuration in which the control valves were preset to their respective idle-thrust settings. This operational method represents the simplest possible starting procedure. The resulting transient simulation of the Phase II demonstrator configuration had an acceleration time slightly less than 1 second to 90% of idle thrust and exhibited safe and satisfactory characteristics.

(U) The start transient analyses were conducted using detailed digital computer programs to simulate the system dynamics, such as transient flow filling system volumes and inertia of the turbopump rotors. The programs contain the normal thermodynamic relationships used to define torque, horsepower, flows, pressures, and temperatures in time derivative form. Two-phase calculation procedures are incorporated in the filling

and flow relationships. Transient heat transfer analyses are used for the "warm" components in the engine as well as transient heat transfer in the regeneratively and dump cooled sections of the nozzle skirt. Heat input to the main injector spraybars, which are filled from a relatively cold injector manifold, is also considered.

(U) An important aspect of the start transient is the filling and ignition characteristics of the preburner. Because of the oxidizer phase change from gas to two-phase to liquid, the oxidizer flow characteristic to the preburner is important. Low flow results in an unburnable mixture ratio and high flow results in excessive temperatures. The phase change in the oxidizer flow characteristic results in a relatively rapid change in the preburner combustion temperature. The preburner combustion temperature exhibits a spike at the time when the oxidizer manifold and element volume fills completely with liquid. This is caused by the rapid increase in manifold pressure due to density changes, which increases the oxidizer flow into the preburner. The increased preburner pressure causes a momentary reduction in fuel flow. The temperature spike is the bulk temperature calculated from the various core or front temperatures. From this analysis two important dependent variables were established: (1) the temperature spike, and (2) the fill time. The temperature spike is important because transition case, turbine, and main injector parts may be damaged if the temperature remains high for extended durations. Long filling times are undesirable because this would extend the engine starting time. The dual-orifice elements of the oxidizer side result in two temperature spikes during the acceleration. However, the secondary volume is large relative to the primary and this volume fills later because of the lower secondary pressure drop. Long filling times of the oxidizer preburner were indicated unless the manifold volume is very small. Therefore, it is highly desirable to incorporate the liquid shutoff feature very close to the preburner injector face.

(U) The establishment of fuel flow to the preburner is also important in limiting the level of the preburner spike. Reduced fuel side volume aid in rapid build-up of the preburner fuel flow. The simulation for the demonstrator engine is currently programmed to have a cooldown prior to the engine start signal. The fuel system is cooled from the engine inlet to the fuel pump discharge. The oxidizer plumbing is cooled from the engine inlet to the main chamber oxidizer flow control valve in the main chamber line and to the preburner flow divider valve located within the preburner dome.

(U) The amount of excess torque available is also an important aspect of the start transient. Results of the analysis indicated that the engine "bootstraps" satisfactorily on tank pressure to idle thrust conditions.

(U) It was desirable to determine a valve or control sequence that was as simple as possible but yet resulted in safe transients. The basic approach then was to open the shutoff valves to preset conditions. The areas are held constant during the start transient. Analyses were conducted to determine the effect of opening the shutoff valves to various preset but constant values. These analyses indicated several significant conclusions.

(This page is Unclassified)

As the idle thrust setting is increased, the preburner flow divider valve is opened to larger areas according to the steady-state throttling schedule. This has the effect of filling the secondary preburner volume at a faster rate, and the time of achieving liquid flow out of the secondary volume approaches the time of obtaining primary volume liquid conditions. This effect can result in a preburner temperature spike caused by the secondary flow, in addition (i.e., approaching the same time) to the temperature spike from the primary flow, which results in excessive temperature. As noted, the attainment of liquid oxidizer flow in either the primary or secondary preburner injector volume results in a rapid increase in oxidizer preburner flow and preburner pressure. This in turn momentarily decreases the fuel flow.

(U) The time required to establish fuel flow also has a significant effect on the transient. One method of greatly reducing the temperature spike is to achieve relatively high flow conditions before the preburner secondary oxidizer injector volume attains liquid conditions. The significance of achieving fuel liquid flow conditions is that a higher fuel flow rate is available to the preburner when the oxidizer attains complete liquid flow. Therefore, the effect of the rapid rate of oxidizer flow into the preburner is diminished because of the higher and accelerating fuel flow rate. This fuel filling time is controlled mainly by the preset area of the fuel shutoff valve. Increasing the area reduces the filling time and also reduces the overall mixture ratio. This allows conditions where the preburner primary is flowing liquid early in the transient but with a fuel flow at a higher rate when complete oxidizer liquid flow is obtained.

(C) It was concluded that the preset areas of the fuel shutoff valve and the preburner flow divider valve (also a shutoff valve) are very important control points for the start transient and will provide a means of safe transients with simple valve action. It also was concluded that the relative valve settings are more important than the actual idle thrust level. This indicates that satisfactory start transients can be achieved for levels of idle thrust up to 20%. The basic requirements are low mixture ratio, and a valve sequence or area setting that produces the high fuel flow rate when the oxidizer secondary volume obtains liquid flow into the preburner, or a definite time interval between the primary and secondary volumes attaining liquid conditions. Therefore, the exact idle thrust condition need not be selected only from the start transient analysis.

(C) The idle conditions for the demonstrator engine is 20% thrust with a mixture ratio of 5 to 7. The simulation of the start transient to idle condition for the recommended demonstrator engine configuration is shown in figure 35. The acceleration time to 90% of idle thrust was 0.98 second. In this simulation, the shutoff valves are opened to their idle thrust and mixture ratio of 5.0 setting. The opening time for all of the valves is 50 milliseconds. A valve sequence is shown in figure 36. The remaining control areas are preset to their idle thrust value prior to the start signal. No further control setting changes are required during the start transient until the point of thrust control takeover.

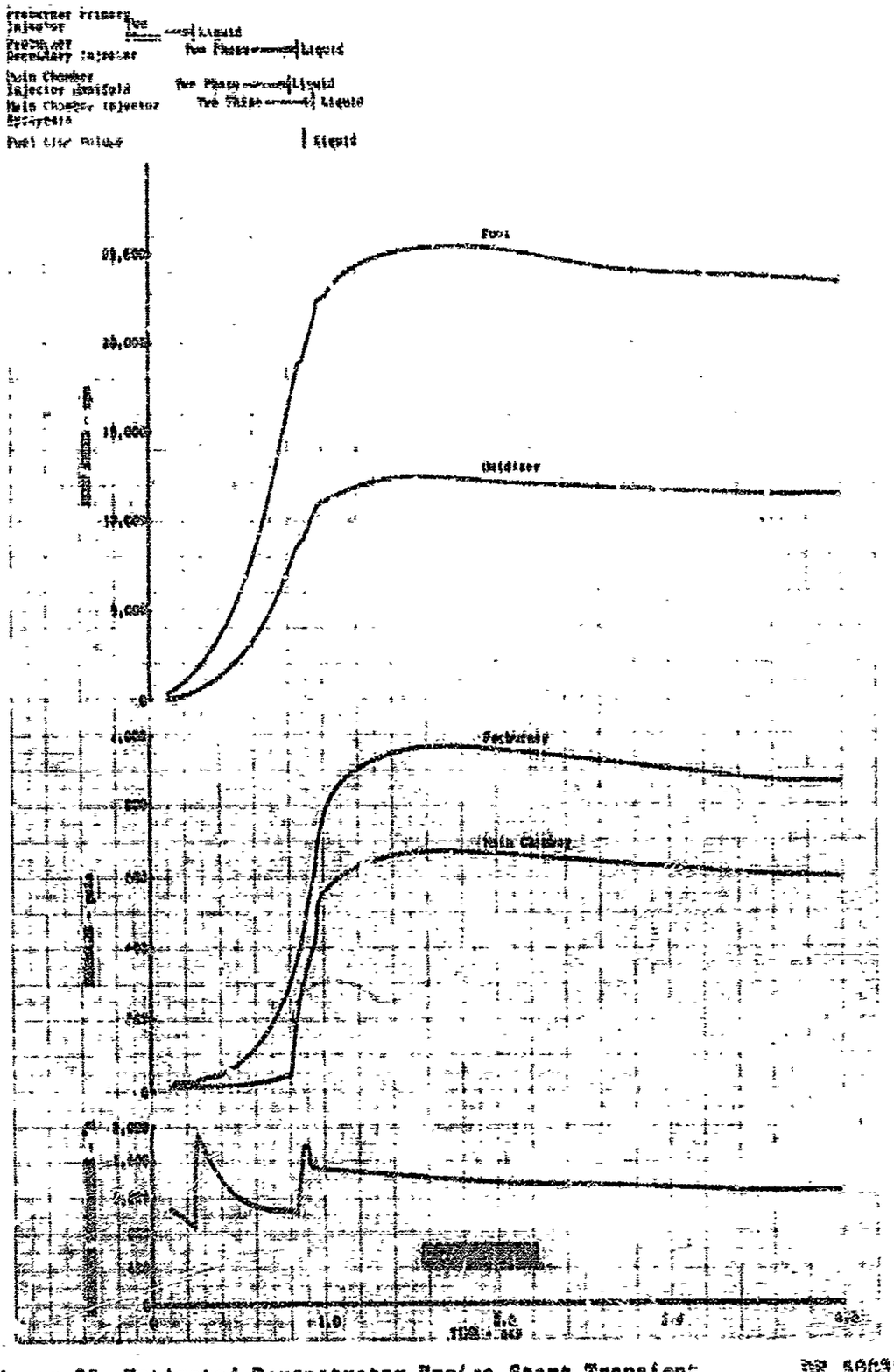


Figure 35. Estimated Demonstrator Engine Start Transient to 20% Thrust, r = 5

59632

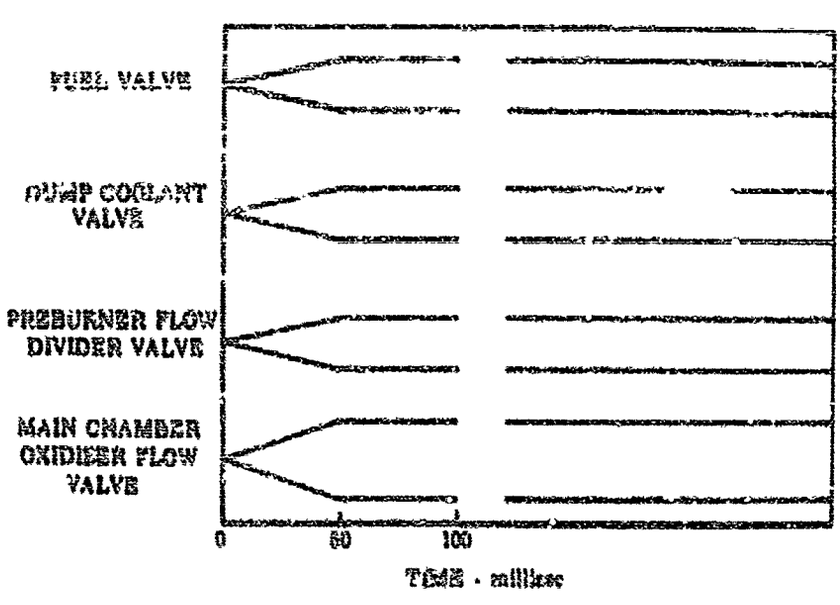


Figure 36. Valve Sequence for Start Transient FD 20024A

(C) Earlier start transient simulations required a lower mixture ratio control area setting (4.1 to 4.5) to prevent excessive preburner temperatures. In this latest start transient, the maximum preburner temperature was 1,124°R. While somewhat higher than noted in low mixture ratio simulations for earlier configurations, the maximum temperature was well within acceptable limits.

(C) The use of the dump cooled nozzle concept reduces the fuel system volume between the pump and preburner. In this start transient simulation, shown in figure 35, the relatively rapid filling of the fuel side caused by the decreased heat exchanger volume tends to reduce the preburner temperature spikes that occur when the preburner primary and secondary injector flows become liquid. It also increases the total preburner flow in the early portion of the transient (first half-second) when chamber pressure is low. The available turbine power is also enhanced by the comparatively low chamber pressure, which sharply increases the turbine pressure ratio during this time period. The comparatively long period of low chamber pressure resulted from the increased main injector filling time. The increased turbine power, in turn, causes a faster rise in turbopump speeds. This produces, in effect, a bootstrapping of the system that culminates in the filling of the main injector manifold and the resultant sharp rise in main chamber oxidizer flow. The increased oxidizer flow rate to the main chamber produces a rapid rise in chamber pressure, which reduces the turbine pressure ratio and available turbine power. The reduced turbine power slows the acceleration of the main pumps. For the particular case simulated, an overshoot characteristic exists because the control system is inoperative. When starting to the idle thrust level, this degree of overshoot is not detrimental to engine safety or operation; however, the overshoot can be reduced or eliminated by several control techniques, if desired.

(3) Throttling Transient Analysis

(U) The objective of the transient analysis was to establish control requirements that achieve safe and satisfactory engine response during throttling between idle and rated thrust. A complete nonlinear engine simulation is used to predict engine system performance during the acceleration and deceleration transients.

(C) Accelerations and decelerations between 20% and 100% thrust were simulated by ramping simultaneously all the control valves from one steady-state thrust level setting to the other. Several ramp rates were investigated for accelerations and decelerations before acceptable transients were simulated. A ramp rate of 3 seconds resulted in a satisfactory acceleration between 20% and 100% thrust while a 1 second ramp produced an acceptable deceleration between the same two thrust levels. Operating characteristics for the acceleration and deceleration are presented in figures 37 and 38, respectively. Complex transient control scheduling was not required because the engine response to throttling ramps was sufficiently rapid to eliminate significant thrust overshoot and turbopump overspeed during acceleration.

(U) Analysis of the throttle transient was also conducted using the analog computer engine simulation studies and is discussed later in this section.

(4) Shutdown Transient Analysis

(C) A shutdown transient analysis of the demonstrator engine was completed. The objective of the shutdown analysis was to investigate the problem areas and to determine the proper valve sequence to obtain a rapid thrust decay within the constraints of safe component operating characteristics. The basic shutdown procedure considered was from idle thrust conditions. A shutdown procedure from any thrust level between 20% and 100% was also established. A valve sequencing was determined that will ensure a rapid, safe shutdown. The shutdown is accomplished from idle conditions by using only the shutoff valves. An acceptable and rapid shutdown was simulated by first terminating the oxidizer flow to the preburner and then to the main injector, and finally the fuel side flow.

(C) Several shutdown transients from idle condition were simulated with varying shutoff valve sequencing. Analysis indicated that the most desirable valve sequence is a rapid closure (in approximately 50 milliseconds) of the preburner oxidizer shutoff valve, which results in rapid decreases in the turbopump speeds and pressures. The main chamber oxidizer valve and fuel valve are closed after a slight delay and, therefore, at lower thrust and pressure levels. The criterion used to establish the valve sequence was to reduce turbine power (and thereby reduce speeds, pressures, and flows), while maintaining thrust balance capability, adequate cooling flows, and fuel system stability. The selected valve sequence is illustrated in figure 39. Shutdown transients from the 20% idle condition for the demonstrator configuration using this valve sequence are shown in figure 39. A deceleration to 0.5% thrust in approximately 1 second was predicted. This shutdown procedure provides a smooth deceleration of the pumps and a rapid cessation of thrust.

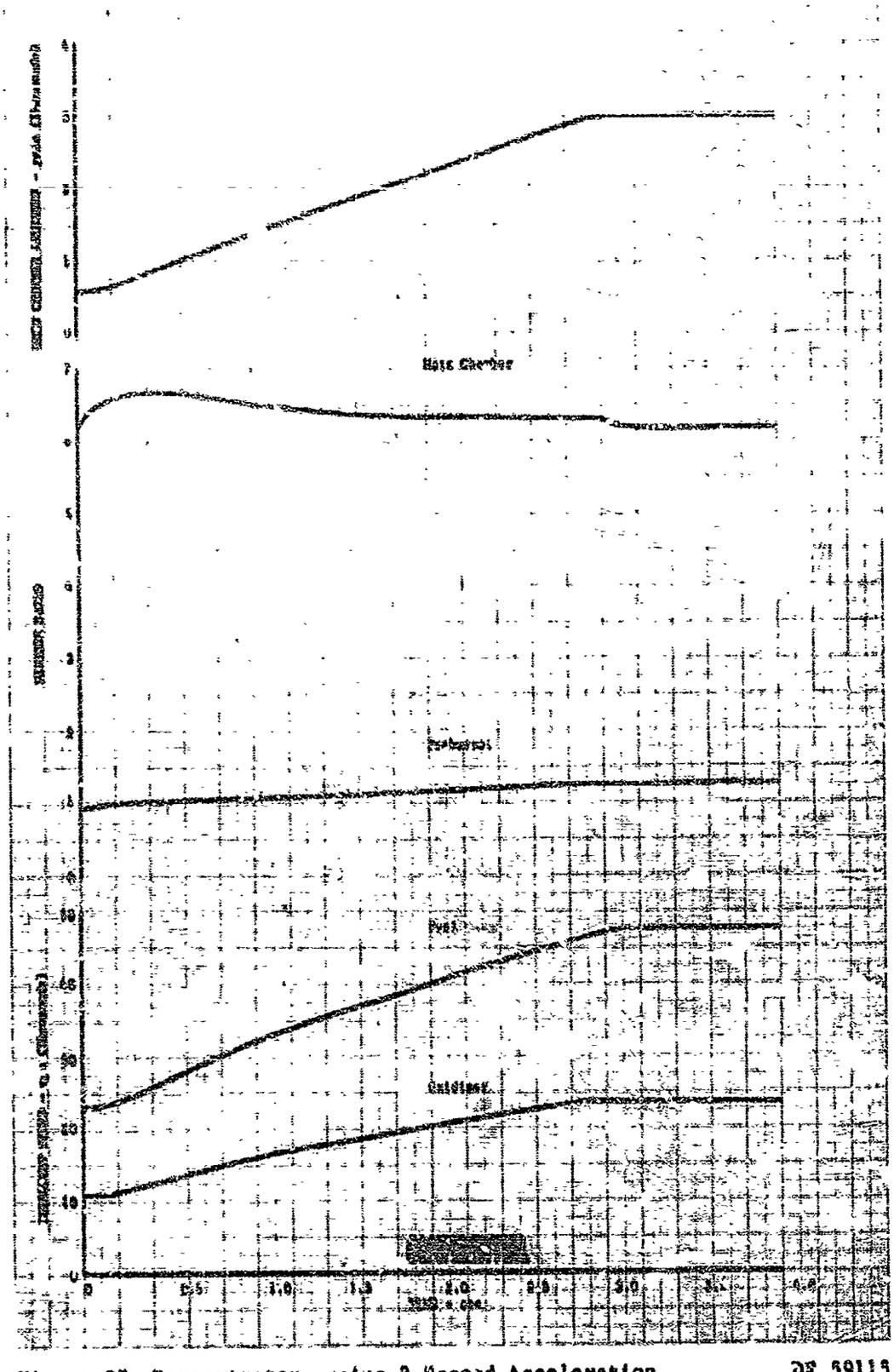


Figure 37. Demonstrator Engine 3-Second Acceleration 20% to 100% Thrust DF 59113

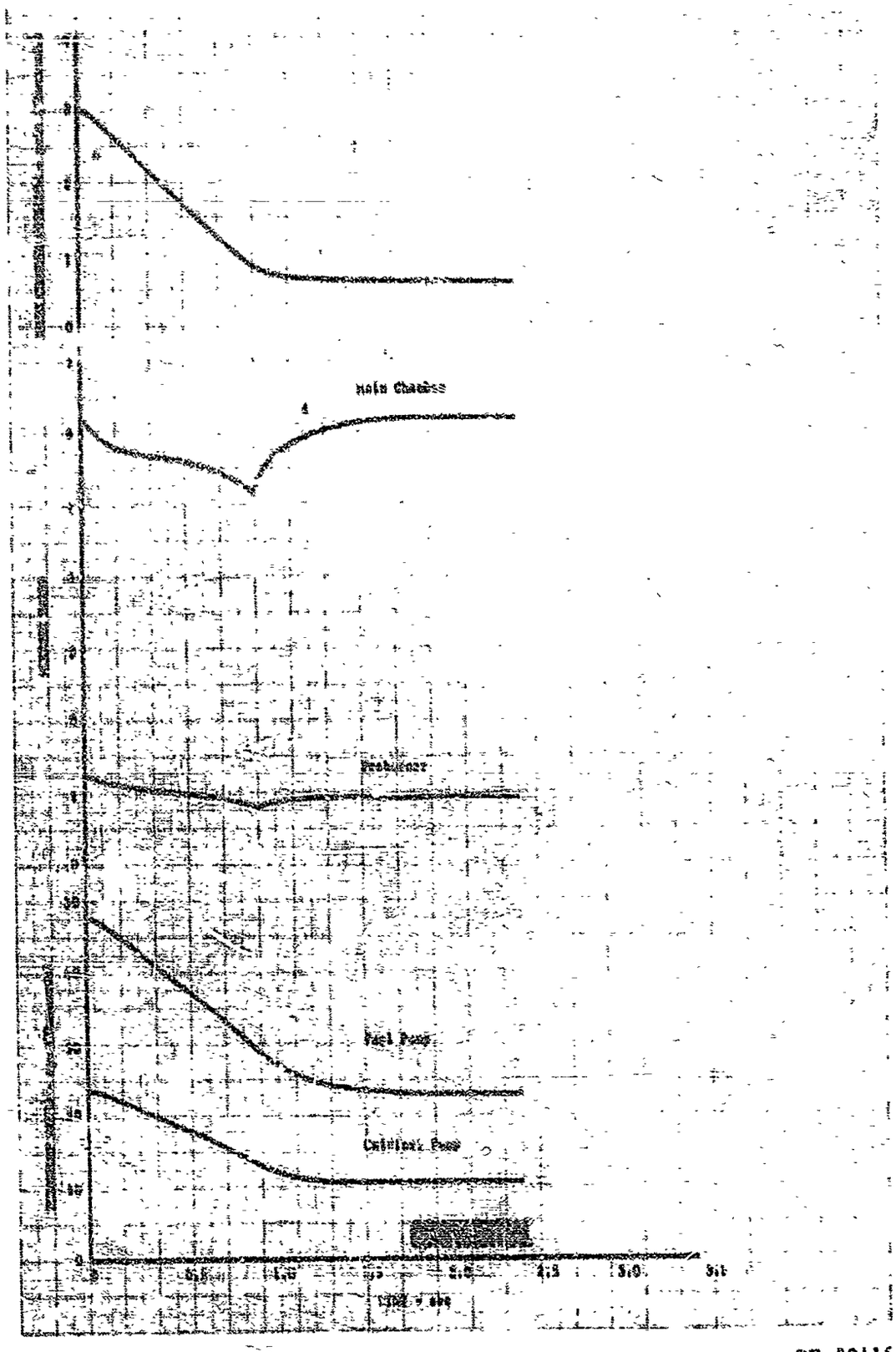


Figure 38. Demonstrator Engine 1-Second Deceleration 100% to 20% Thrust

DF 99116

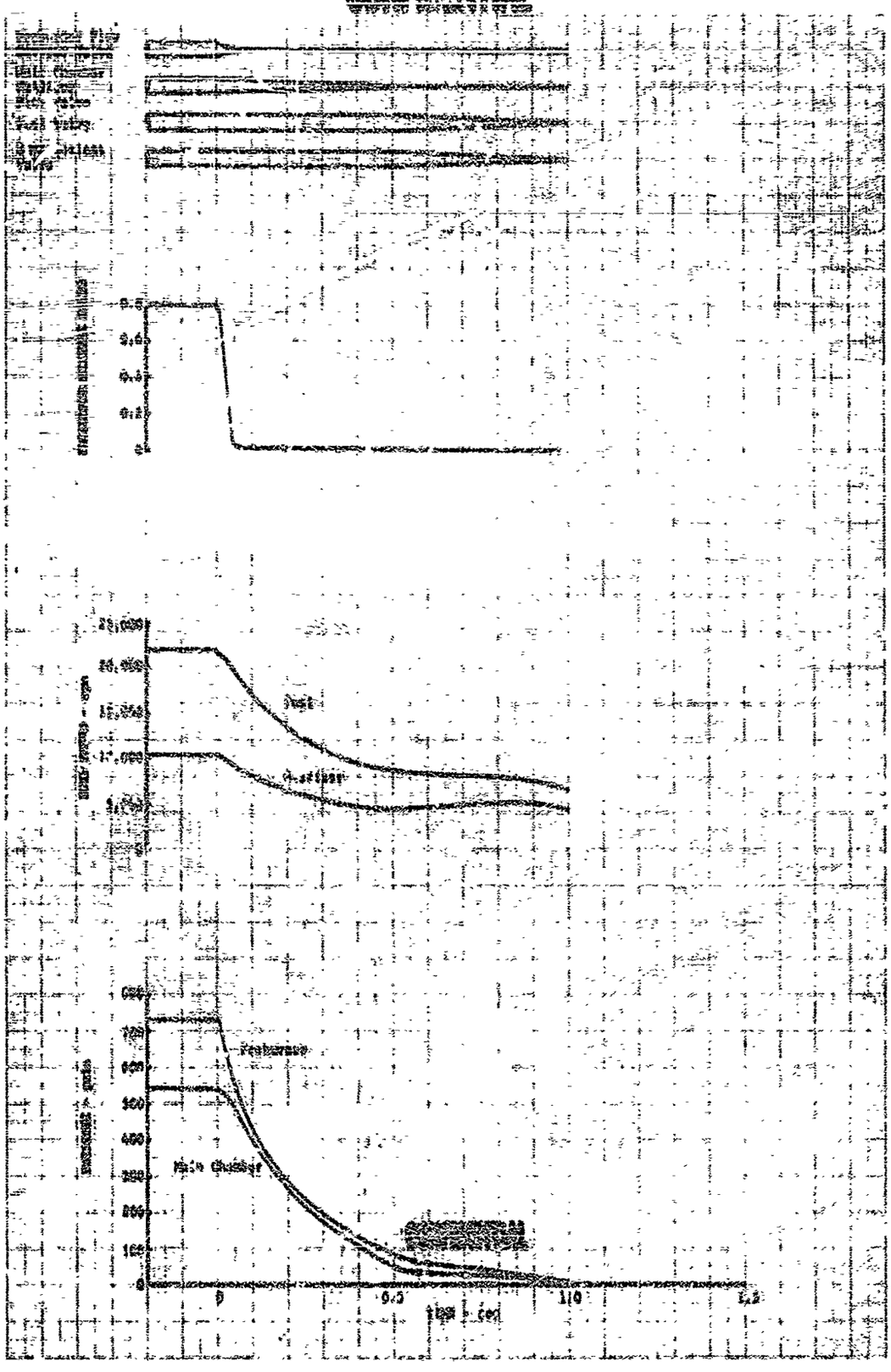


Figure 39. Estimated Demonstrator Engine Shutdown Transient from 20% Thrust, r = 6.0 DF 59033 Sheet 1 of 2

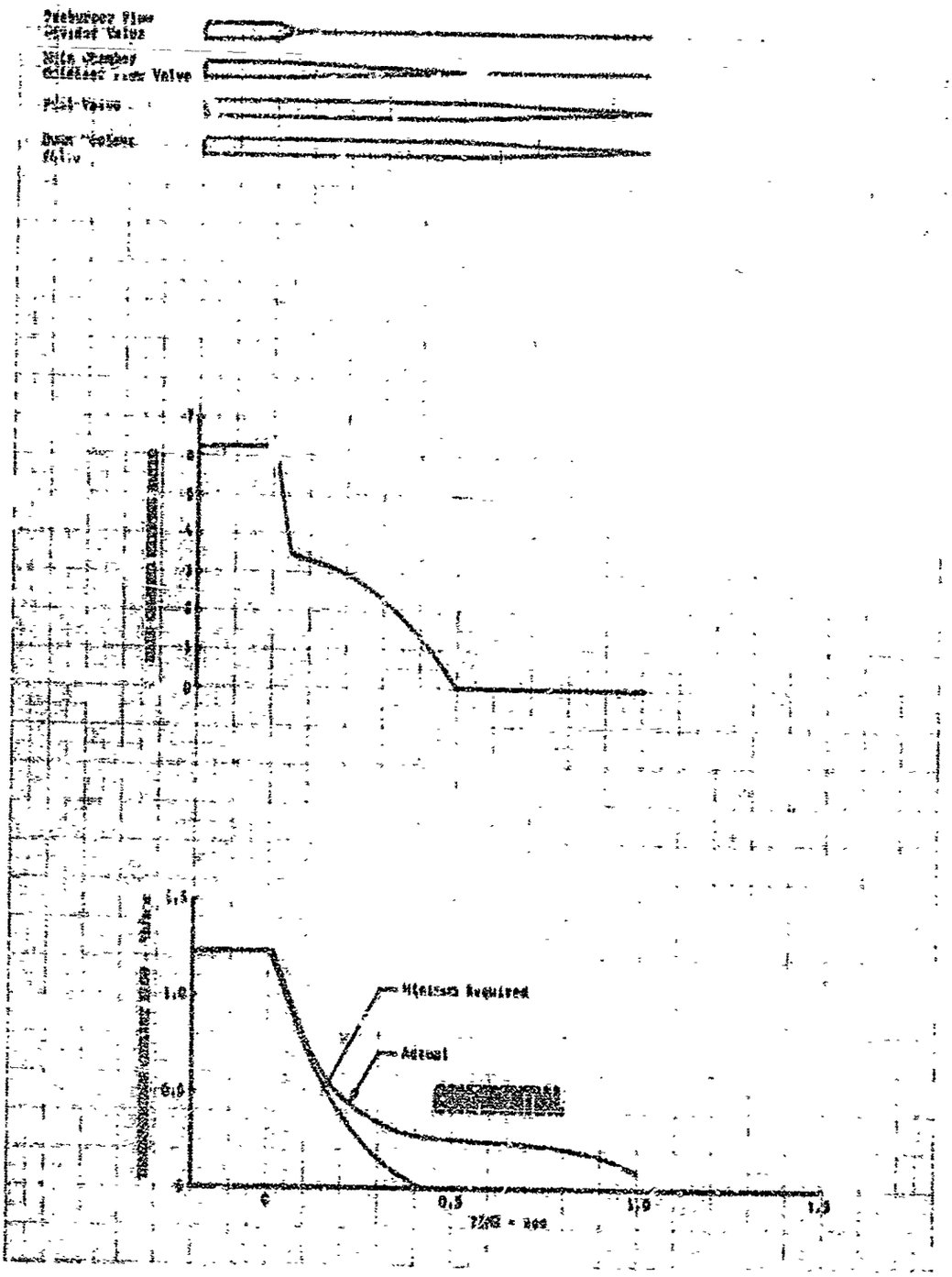


Figure 39. Estimated Demonstrator Engine Shutdown Transient from 20% Thrust, r = 6.0 (Concluded)

DF 59033
Sheet 2 of 2

(U) The rapid closing of the preburner flow divider valve in 50 milliseconds terminates oxidizer flow to the preburner and causes a sharp decline in the preburner mixture ratio. The declining turbine inlet temperatures, caused by reduced preburner mixture ratio, and the reduced turbine flow rates result in a rapid decrease in turbopump speeds and pump discharge pressures. The turbopump deceleration produces an initial sharp decay in main chamber pressure, but the decline becomes less rapid until the main chamber oxidizer flow is terminated 0.50 seconds after shutdown is initiated. Main chamber pressure then decreases slowly as fuel flow decreases because of the closing of the fuel valve. Main chamber pressure attains essentially ambient level shortly after the cessation of fuel flow to the preburner at approximately 1 second after shutdown was initiated.

(U) Shutdowns from higher thrust levels can be achieved by a rapid throttle transient followed by the shutdown valve sequence established for the idle thrust conditions. The chamber pressure and turbopump speed deceleration characteristics for a shutdown from 100% thrust using this procedure are shown in figure 40. For this particular simulation only the preburner oxidizer valve was closed.

(C) The sequence of events assumed for shutdown from a thrust level above idle thrust would be as follows:

1. Shutdown signal is given by vehicle system
2. Control system logic test is activated to compare actual thrust level to permissive thrust level for shutdown. If thrust is greater than 25%, a thrust selector over-ride is activated to reduce thrust at a rate of 200,000 lb/sec.
3. The thrust level is rapidly reduced by the automatic throttle over-ride
4. When the engine thrust level is reduced to 25%, the logic circuit gives a permissive signal to initiate the shutdown sequence of valve closures
5. The preburner oxidizer flow is terminated
6. The main chamber oxidizer flow is terminated
7. The fuel flow is terminated.

(C) The relative timing of the shutoff valve closures during shutdown effects both the chamber pressure and speed decay. Figure 41 shows several chamber pressure and fuel turbopump speed transients for various shutoff valve times. These data are shown for shutdown transients from 10% thrust; however, the results are typical for other idle thrust levels. Only the fuel turbopump speed trace is shown because the oxidizer turbopump deceleration is similar. The shutdown valve sequence is initiated by stopping the oxidizer flow to the preburner, thus reducing available power. This shutoff valve is closed in 0.050 seconds. If the other valves are not closed, the engine decelerates to a low thrust level. Trace 1 in figure 41

shows the early portion of this type of shutdown. The closing of the other valves results in the final flow cessation. As the relative timing between the oxidizer preburner shutoff valve and main chamber valve is reduced, the chamber pressure decays at a more rapid rate. However, the more rapid chamber pressure decay increases the turbine pressure ratio and delays deceleration of the turbopumps.

(U) This can be seen from comparison of traces 2, 3, 4, and 5 in figure 41. It is desirable, but not essential, to maintain a smooth deceleration of the turbopumps. The fuel shutoff valves are sequenced slightly later to ensure more than adequate transpiration cooling flow. The timing of these valves has little effect on chamber pressure and speed deceleration, as illustrated in figure 41 (traces 3, 4, and 5).

(5) Stability Analysis

(U) The frequency response characteristics of the engine system were determined for control area changes in the preburner and main chamber oxidizer supply lines. Variations in the principal parameters affecting the engine response, the fuel system volume and the oxidizer turbopump inertia, were investigated as well as the effect of thrust and mixture ratio variations. The thrust response characteristics were similar to a first order system with the corner frequency varying directly with thrust. Mixture ratio response was essentially flat within the range of interest (0 to 100 cps), and was not appreciably affected by thrust level.

(C) The engine system response to a change in the preburner oxidizer control area at 100% thrust and a mixture ratio of 7 exhibited a resonance at approximately 3 cps. Figure 42 illustrates the resonance, and compares the response at mixture ratios of 5, 6, and 7. The same phenomenon is present in the engine mixture ratio response to a change in the main chamber oxidizer control area as shown in figure 43. This resonance will be taken into consideration in setting the gain of the control system at the corner frequency or in determining a compensation network to modify the overall control-engine gain to assure stability.

(C) Two primary factors that establish the frequency response characteristics of the engine system are the polar moment of inertia of the oxidizer turbopump rotor and the volume of the coolant passages of the regeneratively cooled nozzle skirt. Both of these parameters were arbitrarily varied to determine their effect on the engine response. Reasonably wide variations in the coolant passage volume can be tolerated without major changes in the engine corner frequency or gain, as shown in figure 44. A reduction in volume to 10% of nominal, or an increase to 200% of nominal, varies the gain approximately 3 db. Figure 45 shows a similar trend for the polar moment of inertia of the oxidizer pump. A 50% reduction in the inertia increases the gain about 7 db. A 50% increase in inertia reduces the gain approximately 3 db. These variables are important because they determine the first corner frequency of the two propellant systems. The coolant volume is the "slowest" or lowest frequency unit in the fuel system, and the oxidizer turbopump polar moment of inertia is the slowest unit in the oxidizer system. The results of the stability analysis discussed above indicate reasonable variations in these parameters can be tolerated without large effects on the overall engine response.

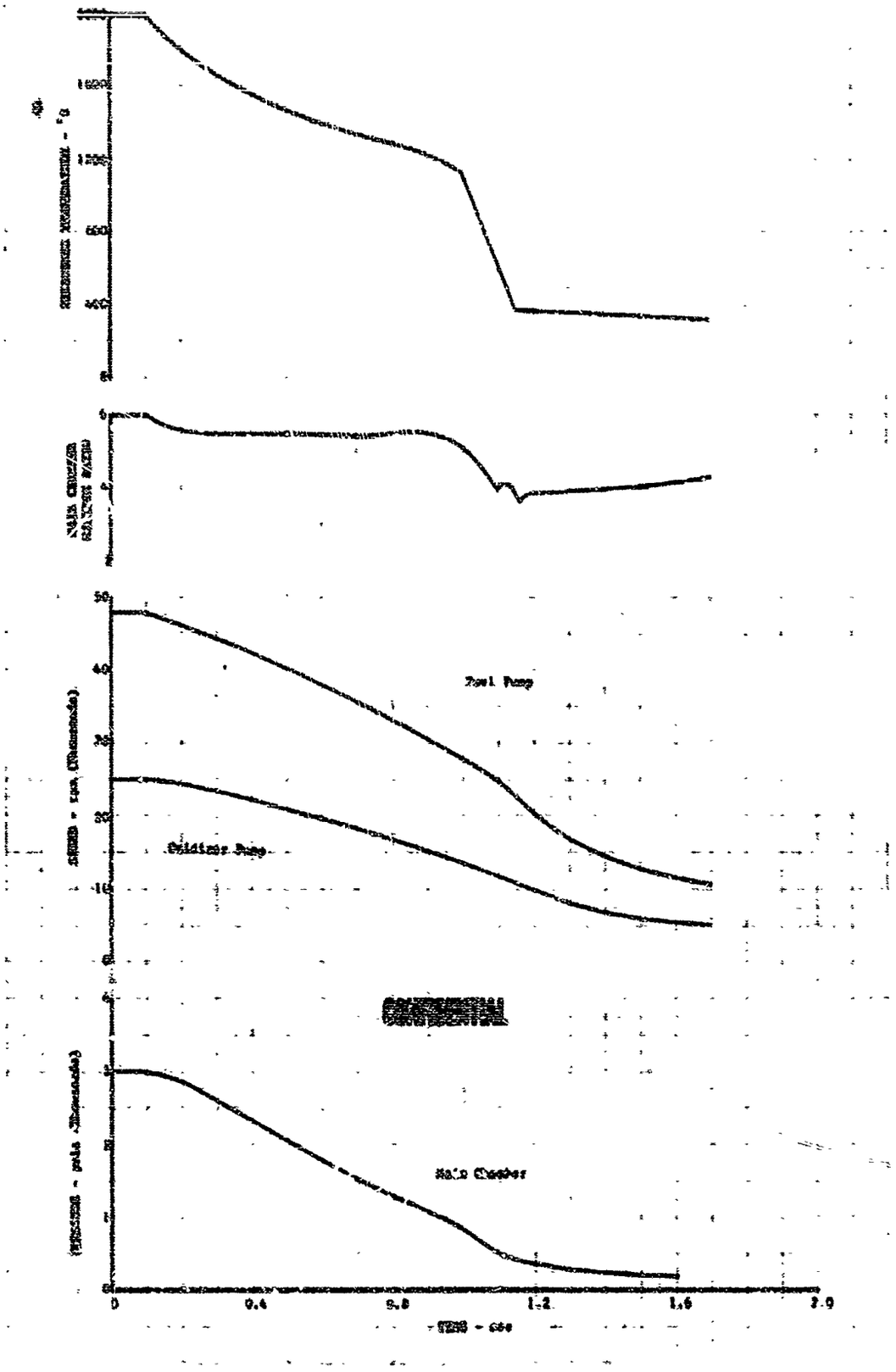


Figure 40. Estimated Shutdown Transient from Rated Thrust DF 57059

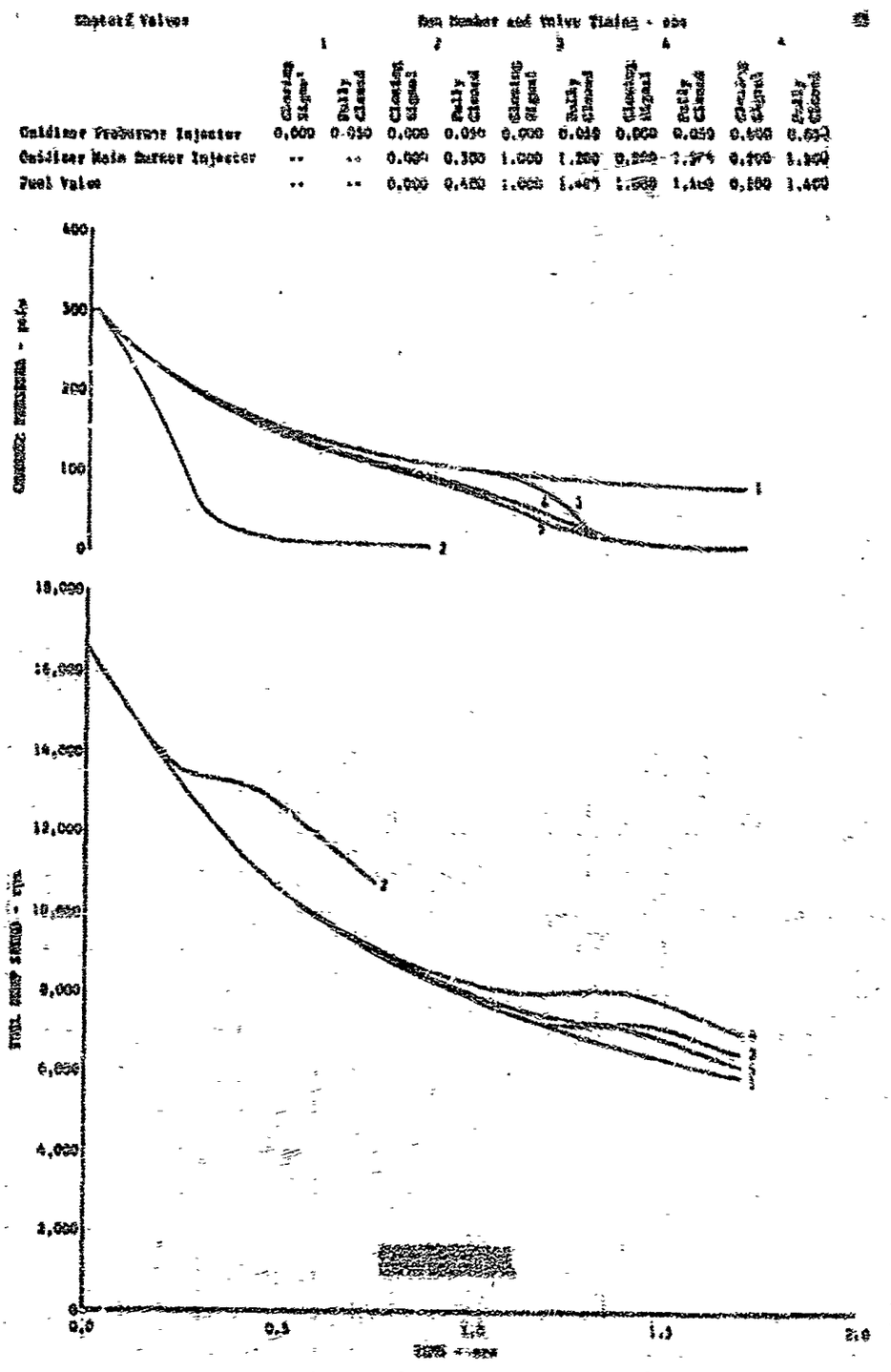


Figure 41. Effect of Shutoff Valve Timing on Shutdown Characteristics

DF 59338

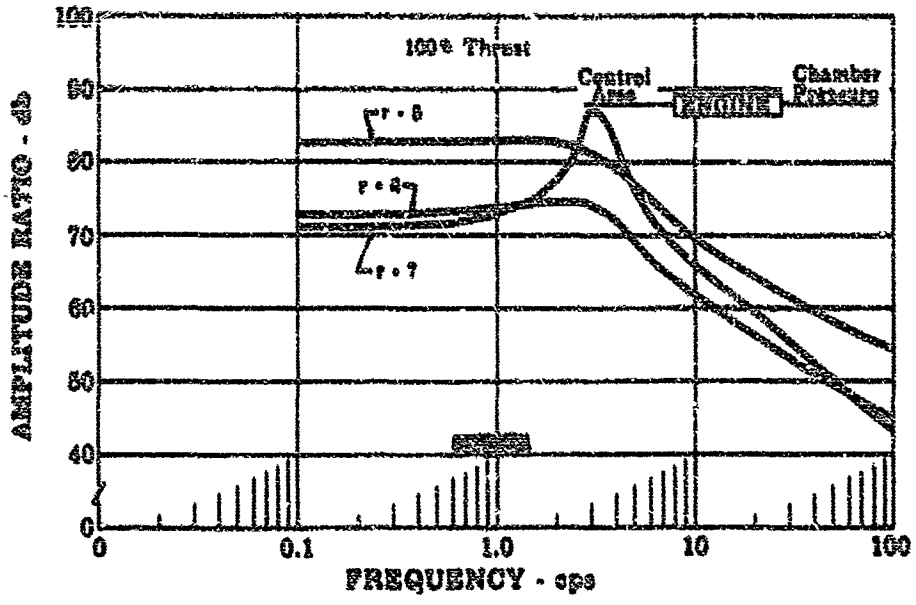


Figure 42. Response of Chamber Pressure to Preburner Oxidiser Control Area — FD 17954A

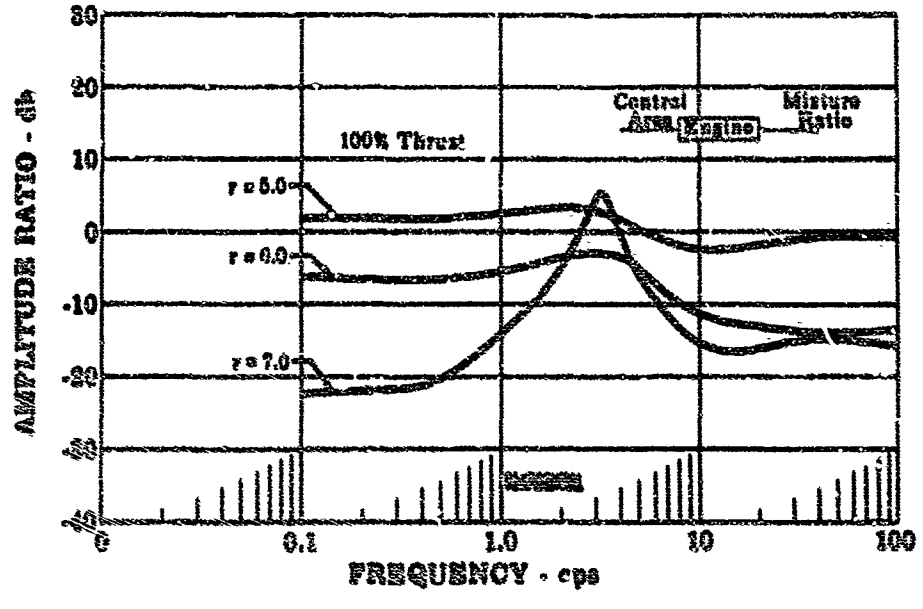


Figure 43. Response of Chamber Mixture Ratio to Main Chamber Oxidiser Control Area — FD 17967A

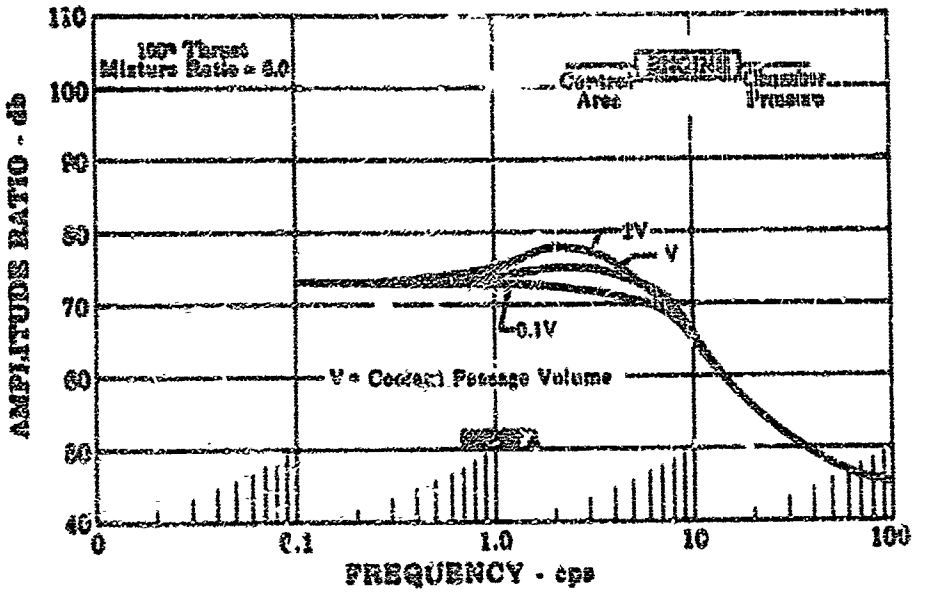


Figure 44. Response of Chamber Pressure With Varying Coolant Passage Volume FD 18102A

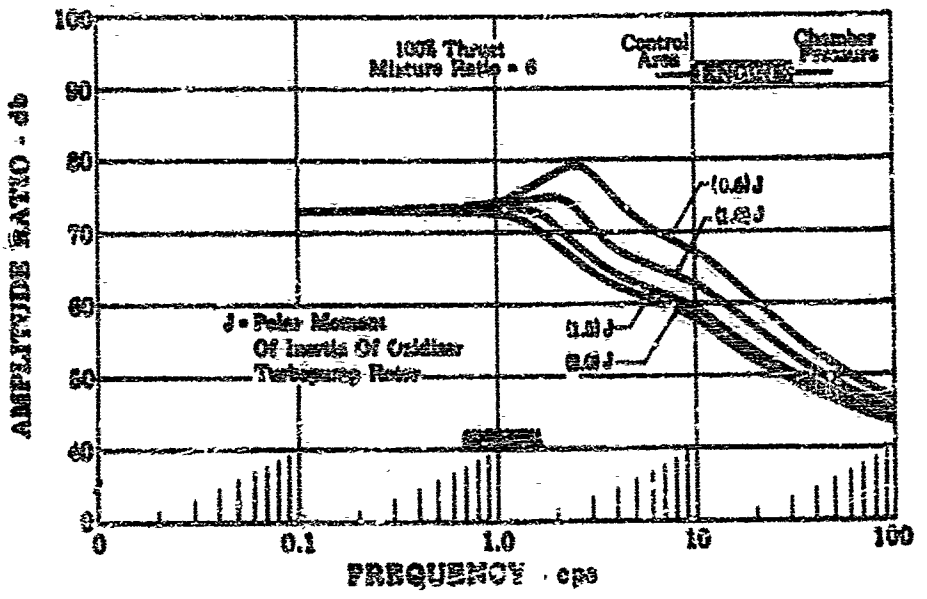


Figure 45. Response of Chamber Pressure With Varying Oxidizer Turbopump Inertia FD 18369A

(C) Frequency response data were also generated at 10% thrust for both thrust and mixture ratio. These data, as shown in figures 46 and 47, exhibit no resonances for the thrust control input, and the mixture ratio response does not vary as widely as the high thrust data.

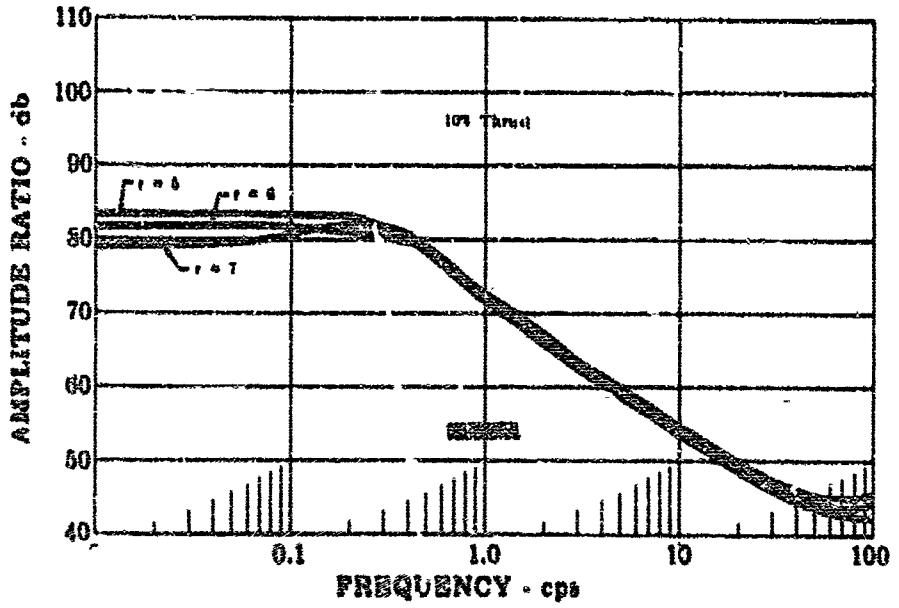


Figure 46. Response of Chamber Pressure to Preburner Oxidizer Control Area FD 18113

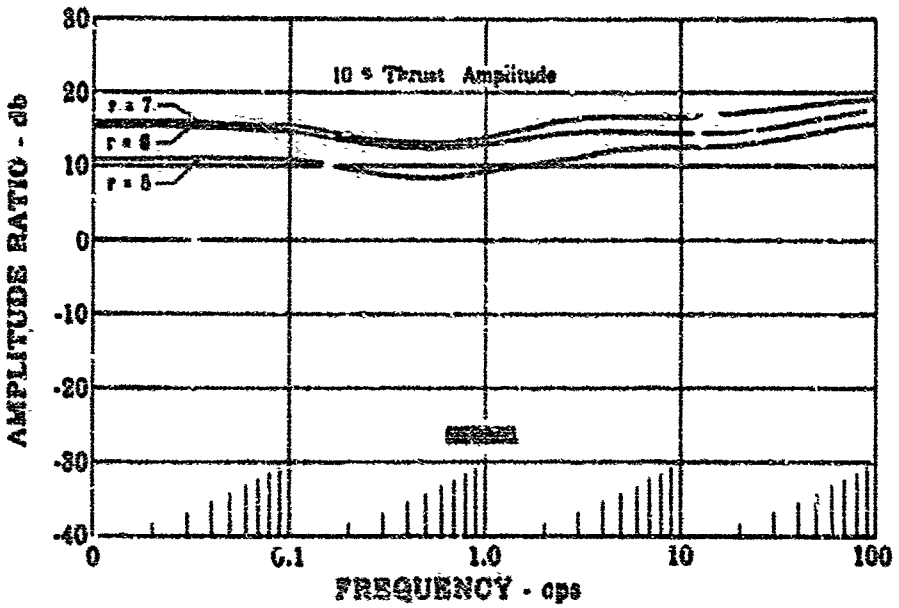


Figure 47. Response of Chamber Mixture Ratio to Main Chamber Oxidizer Control Area FD 18096

(U) The thrust response of the engine system throughout the 20% to 100% thrust range will have a corner frequency that is proportional to thrust level. The frequency response of the engine system at 20% thrust would have characteristics similar to the 10% thrust data but would have a thrust response corner frequency of approximately 0.6 cps. The mixture ratio response would be essentially the same at 10% and 20% thrust. The gain levels of both thrust and mixture ratio will vary directly with thrust level.

(U) These analyses were completed utilizing the demonstrator engine system with a fixed, regeneratively cooled nozzle skirt. The modifications to this engine system to derive the recommended demonstrator engine included a reduction in the fuel system volume and an increase in the oxidizer turbopump rotor inertia. As illustrated by figures 44 and 45, both of these modifications tend to reduce the peak gain at the resonant frequency and effectively increase the system damping coefficient.

(U) Complete engine and control system dynamic analysis utilizing the nonlinear analog simulation of the recommended demonstrator engine configuration is required.

(6) Dynamic Engine Simulation (Analog Computer)

(U) Control system studies and the associated engine dynamics may be more conveniently investigated with an analog computer simulation than with a digital computer simulation. An engine simulation was completed during Phase I and has been updated to this revised demonstrator engine configuration with a variable area pump discharge valve. The updated simulation is presented and discussed in Appendix II.

(U) Several studies using the analog engine simulation were completed deriving basic information on both the static and dynamic behavior of the engine system. The studies are summarized in the following paragraphs.

(C) The analog engine simulation was used to investigate the response of the fuel feed system to torque and inlet pressure disturbances. The simulation was trimmed to a 30% thrust operating condition. Figure 48 illustrates the approximate operating lines of the engine on a fuel pump map. The fuel pump speed was just above 25,000 rpm for this study

(C) Torque disturbances were arbitrarily input to the fuel pump with two levels of pressure loss (95 and 160 psi) at the pump discharge, and with a cavitating venturi at the pump discharge. Both plus and minus step inputs were used, but the minus inputs were more severe because the fuel pump is driven toward lower flow rates for this condition. Figure 49 compares the results of the minus step inputs for the three different pump discharge configurations. The step input in torque was made excessively large (approximately 30%) to ensure significant reaction levels. The cavitating venturi case was completely stable, even though the pump flow was significantly reduced and mixture ratio was driven to 8.5. The 160 psi loss case provided a stable reaction where the fuel flow exhibited small fluctuations, but settled out in approximately 0.250 seconds. The 95 psi pressure loss case reacted in an unstable manner to the step input, even

though it was stable before the step. Figure 50 shows the 95 psi pressure loss case reaction to a smaller torque change. The minus step resulted in gradually increasing flow oscillations, finally resulting in high amplitude flow excursions until the torque was returned to the nominal value. A positive step, shown on the first section of the trace, was stable.

(U) A similar procedure was followed with main fuel pump inlet pressure step input changes. Again, a large variation (± 30 psi) was used to obtain significant reaction levels. The fuel pump discharge configurations were repeated and the results were similar, as shown in figure 51 (e.g., the cavitating venturi and the 160 psi loss cases were stable, and the 95 psi loss case was unstable). The overall engine mixture ratio and flow reactions were smaller because the mean levels are little affected by the 30 psi pump inlet pressure change.

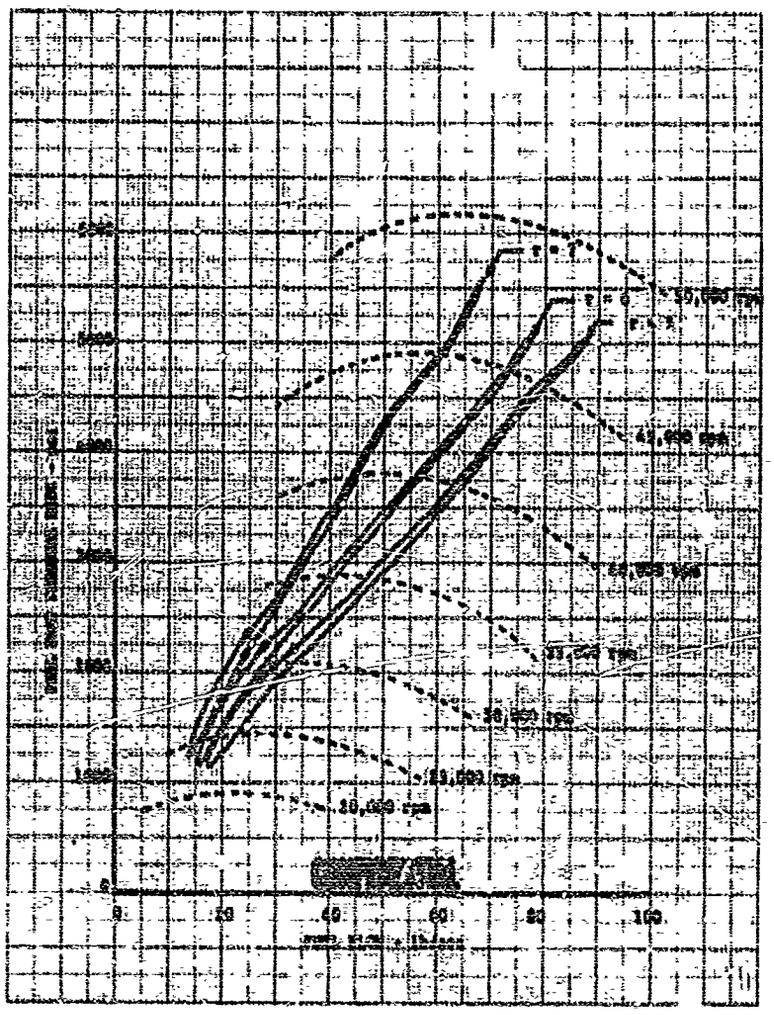


Figure 48. Fuel Pump Performance During 10-Second Ramp Between 20% and 100% Thrust (Open-Loop Control System) DF 59577

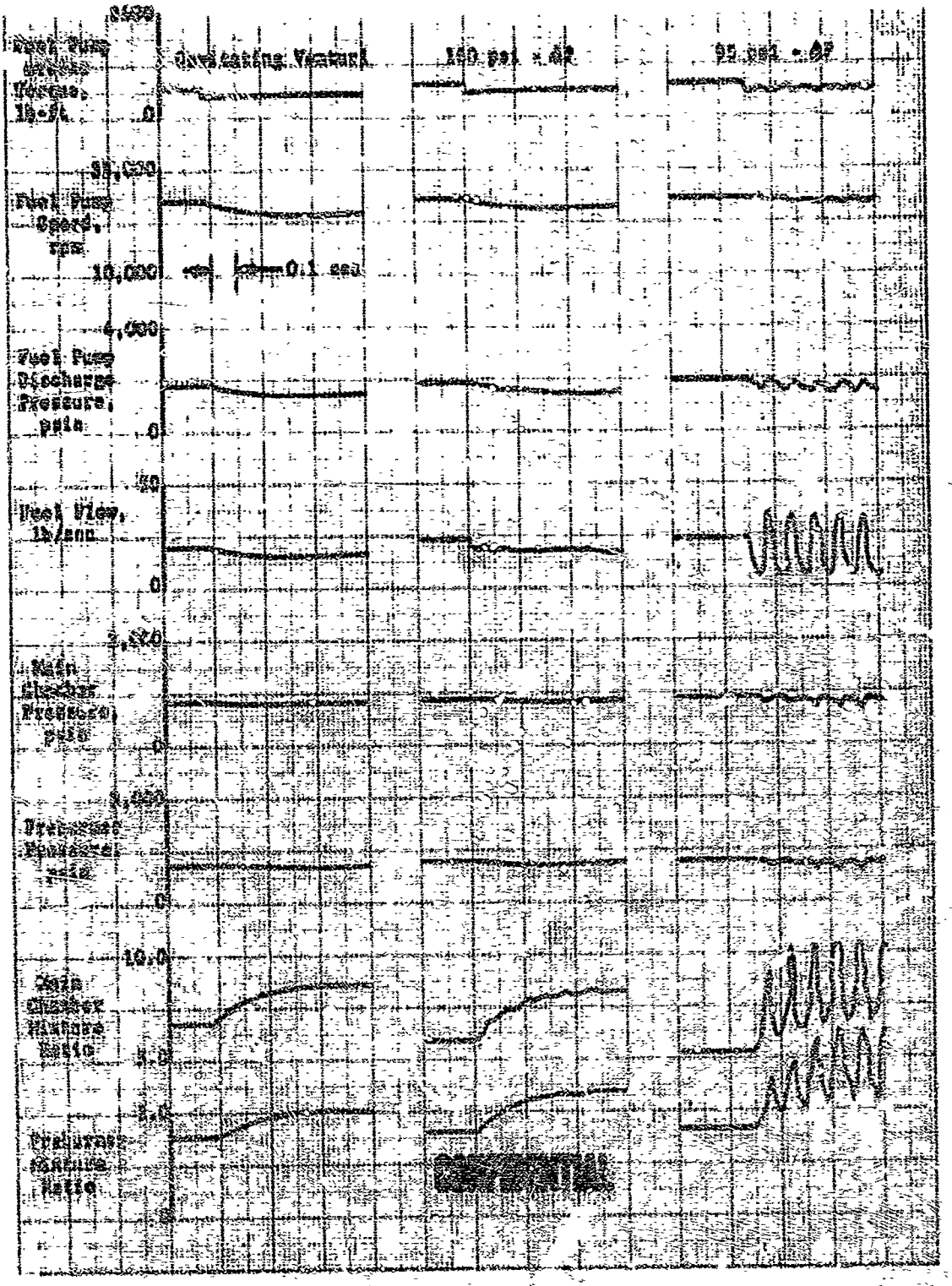


Figure 49. ADF Analog Simulation, Effects of Fuel Turbopump Torque Disturbance

DF 59579

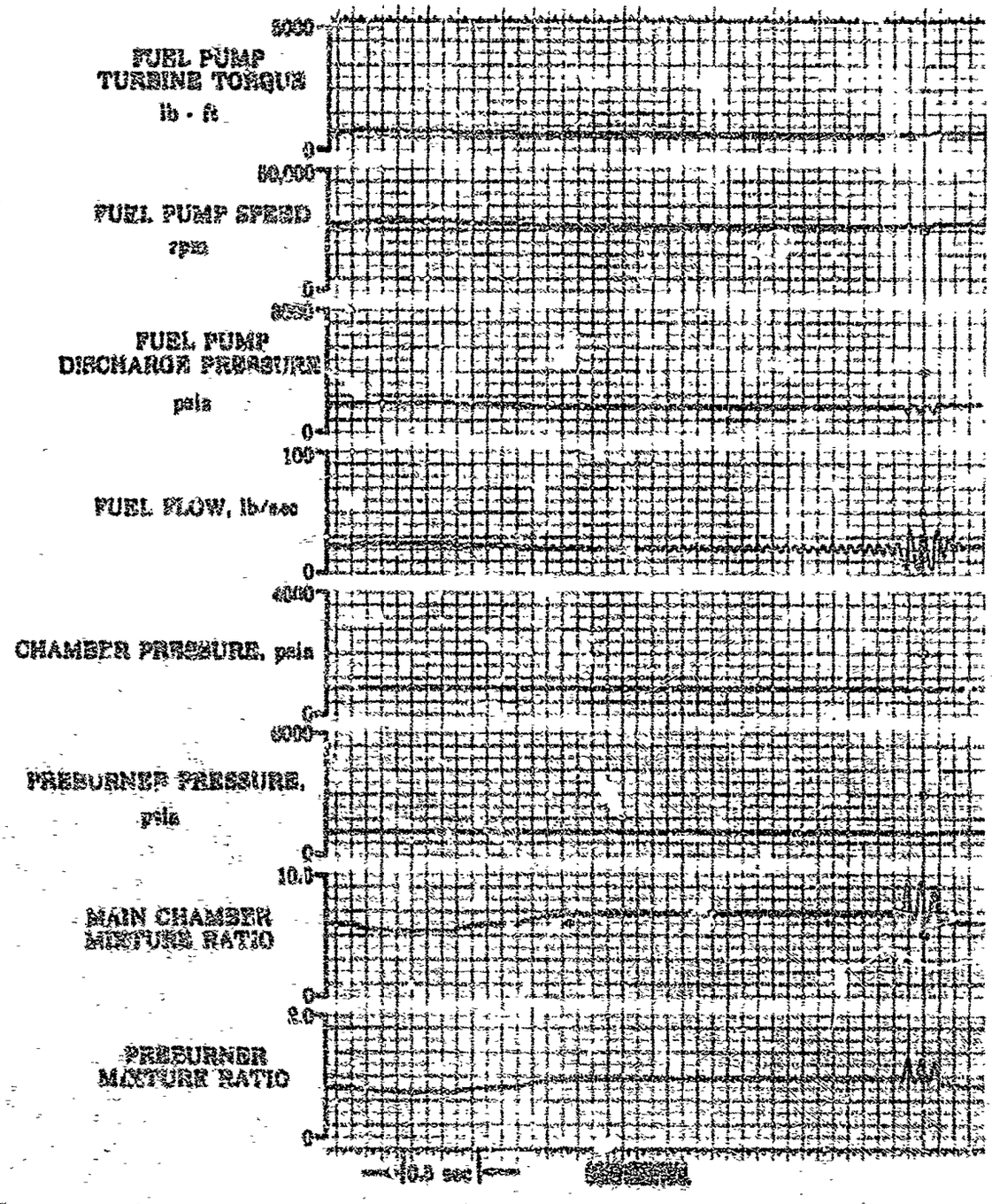


Figure 50. ASP Analog Simulation, 93 psi Pressure Loss Case Results FD 23061

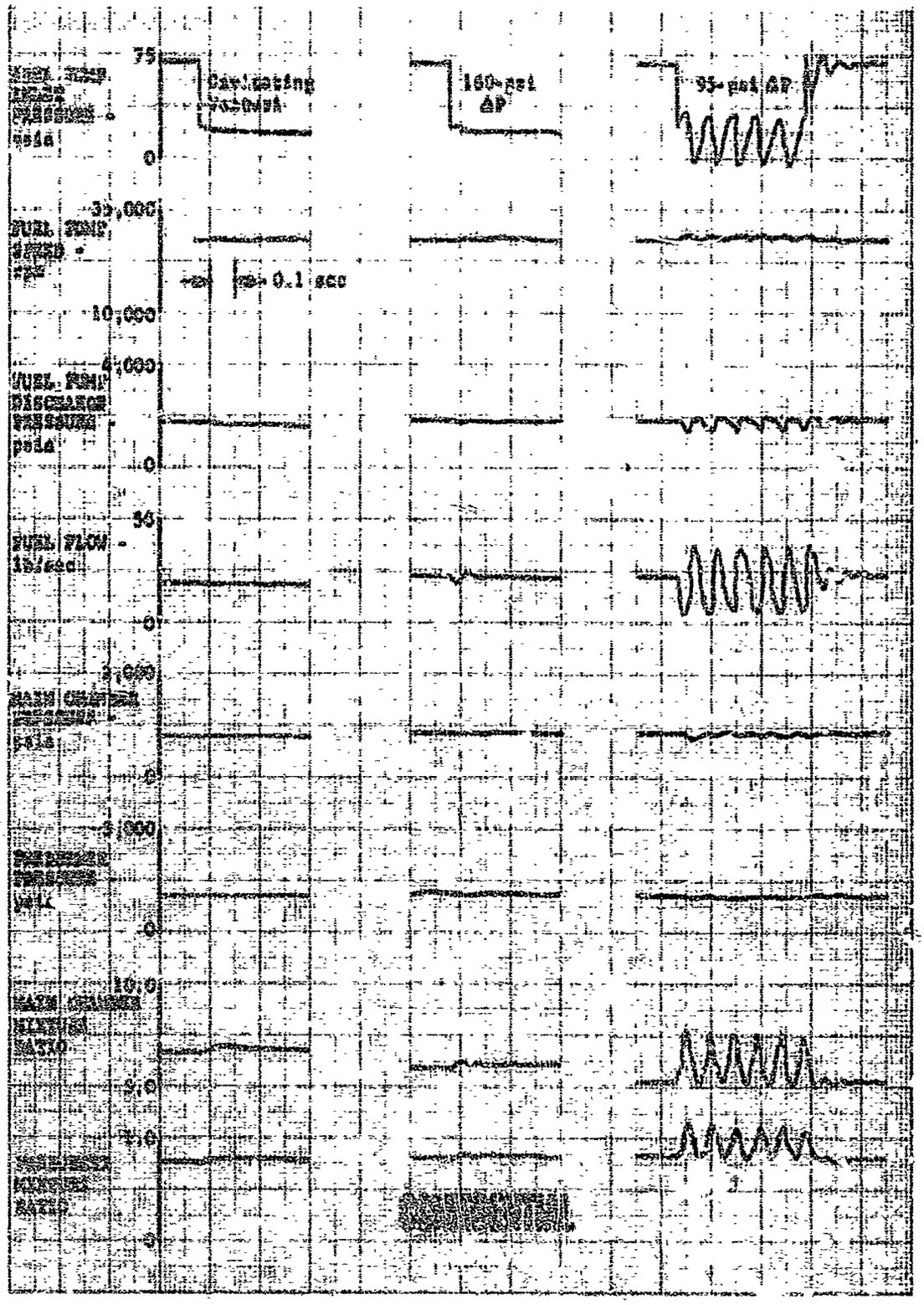


Figure 51. ADP Analog Simulation, Effects of Fuel Pump Inlet Pressure Disturbance DF 59378

(U) These data were generated with fixed control areas to illustrate the response of the basic engine system. Closed-loop controls should improve the dynamic response; however, if a stabilization device is required, the fuel shutoff valve may be scheduled in the low thrust range to provide the small pressure drop.

(C) Information regarding the influence of potential control area locations upon engine performance was developed. Setting the open-loop controlled engine analog at one of a series of nominally designated thrust levels (30, 60, and 90%) and mixture ratios (5, 6, and 7), a single control area was incrementally varied in each of the three main propellant lines.

1. Fuel preburner line (AVEN)
2. Oxidizer preburner line (ATC + ALB)
3. Oxidizer main chamber line (AMBC + ALBT + ALIJ).

(U) Values for thrust, mixture ratio, and control area were recorded for several area values that were set about each nominal point.

(U) The results of this investigation are shown in figures 52 through 54. A control area (AVEN) in the fuel line to the preburner has a high gain with mixture ratio with very little effect upon thrust. A control area (ATC + ALB) in the preburner oxidizer line has high thrust gain with a small mixture ratio gain. However, a control in the main chamber oxidizer line has significant influence in both thrust and mixture ratio. The thrust level influence results from the back pressure produced on the main turbines by oxidizer flow into the main chamber, which directly affects chamber pressure. These results indicate a fuel side mixture ratio control (AVEN or AFB) will have less closed-loop interaction with the thrust control (ATC) than will oxidizer side mixture ratio control (AMBC).

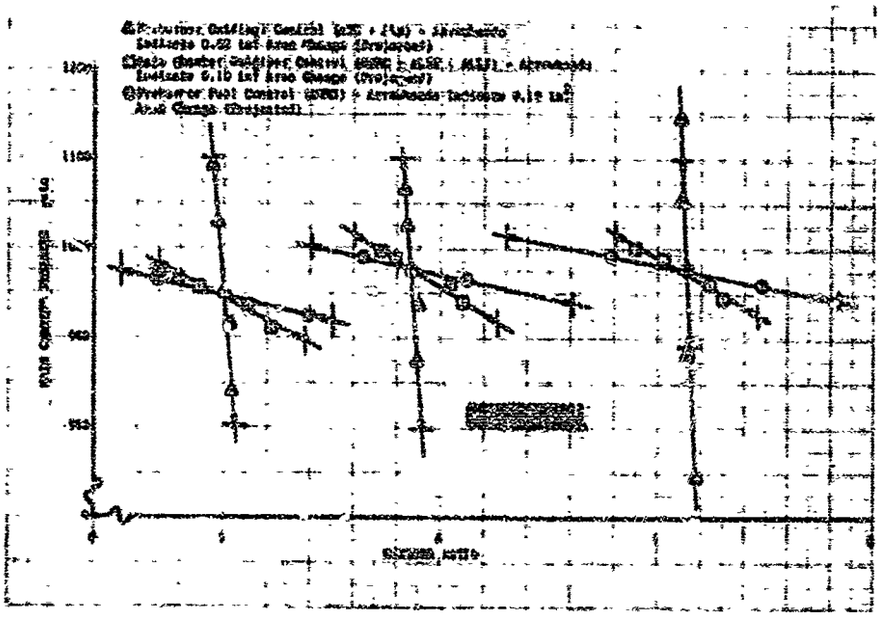


Figure 52. Control Area Influence at 30% Thrust DF 57077

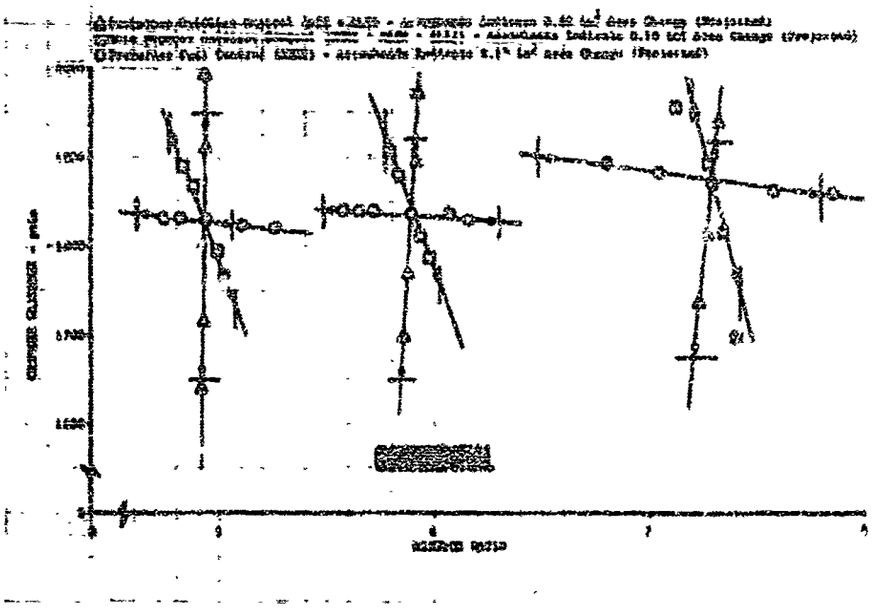


Figure 53. Control Area Influence at 60% Thrust DF 57078

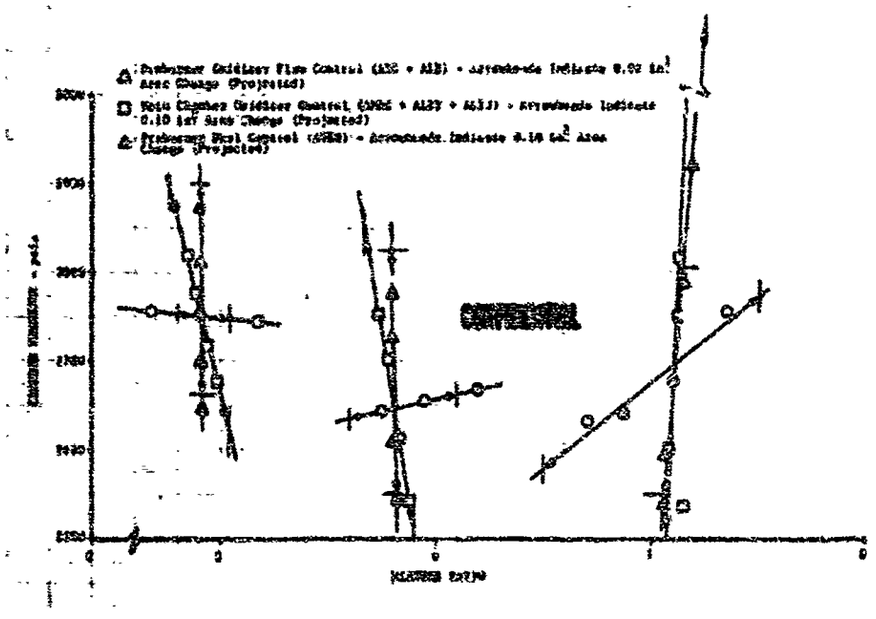


Figure 54. Control Area Influence at 90% Thrust DF 57079

(C) System stability was evaluated with both integral and proportional control gains. A schematic of the control logic used for the thrust and mixture ratio controls is shown in figure 55. During these investigations, the scheduled valves were controlled directly by the power lever angle, which produces the desired thrust input to the control system. Only the thrust and mixture ratio controls received feedback information from the engine systems. Figure 56 illustrates, the recovery dynamics of the

engine and control system to a large step input disturbance. The input disturbance was obtained by retarding the power lever to a thrust below 20%, allowing the system to settle and then instantaneously advancing the power lever to the 20% thrust level. This results in a step change in all the scheduled valve areas and a step change in the error signals to the thrust control. Although the control gains are not optimized, these results illustrate the rapid response (approximately 0.2 second for chamber pressure to reach the desired level) and the stable recovery of all parameters without oscillations. Most parameters have reached equilibrium in 0.5 second and the entire system has settled in slightly more than 1.0 seconds.

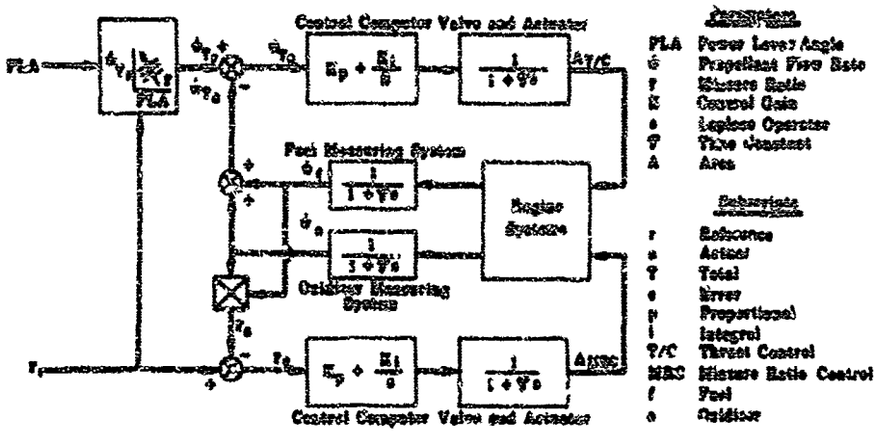


Figure 55. Control System Logic Diagram FD 20047

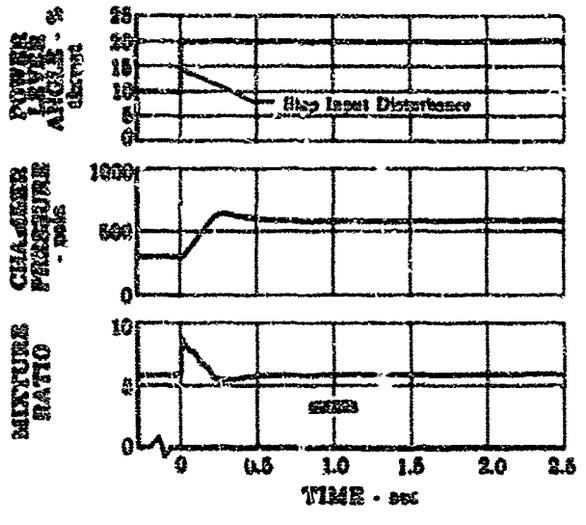


Figure 56. Stability Analysis Data FD 20025

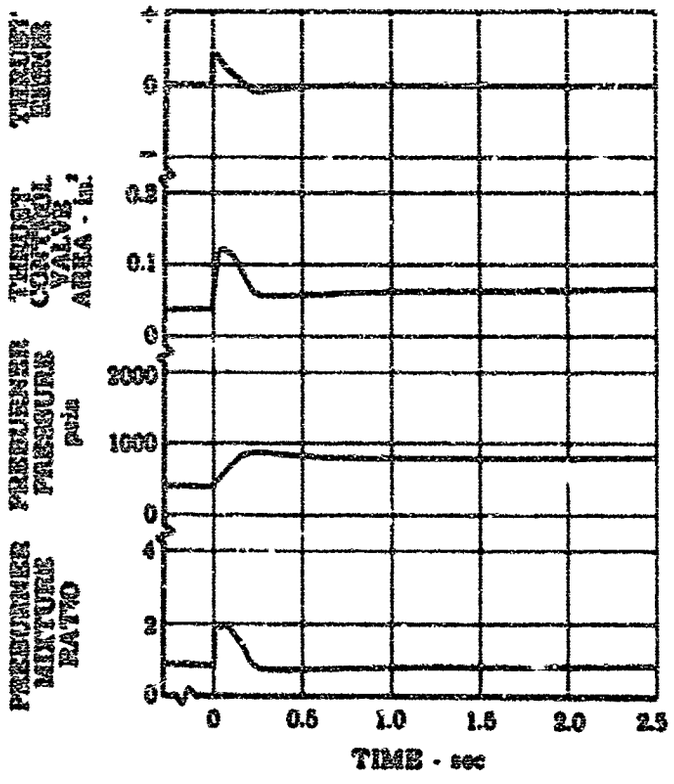


Figure 56. Stability Analysis Data (Concluded) FD 20049

(C) The analog computer engine simulation was used to determine the transient characteristics of the engine system using closed-loop thrust and mixture ratio controls with flow feedback. Figures 57 through 59 show engine performance during accelerations and decelerations using a closed-loop thrust control located in the preburner oxidizer line and a closed-loop mixture ratio control located in the preburner fuel line. The accelerations and decelerations (between 20% and 100% thrust) were simulated by 4-second power lever ramp inputs, which is 20% faster than the nominal requirement of 5 seconds. Both preburner and engine mixture ratio variations from the nominal values during the transients were small except at low thrust levels as shown in figures 57 and 58. No significant overshoot or undershoot was observed in the simulations as shown in figure 59.

2. Flight Engine and Parametric Performance Data

a. General

(U) The objectives of this task were to define a 250,000-lb thrust flight engine configuration and to generate parametric engine performance data for use in the Applications Study.

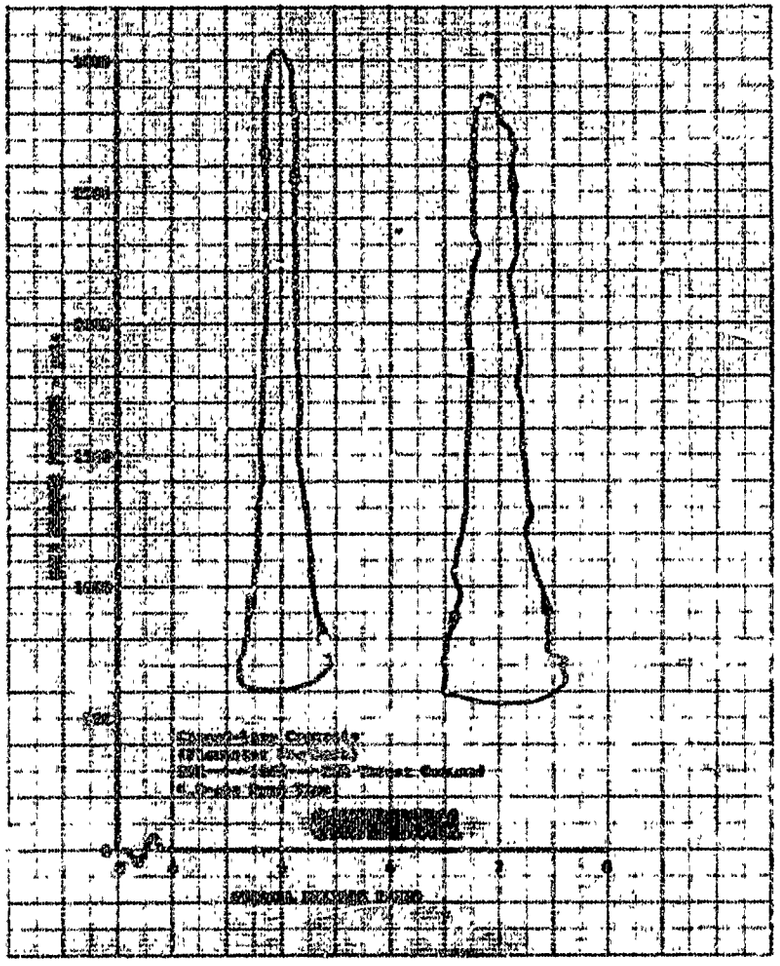


Figure 57. Main Chamber Pressure vs Mixture Ratio - Analog Simulation DF 59117

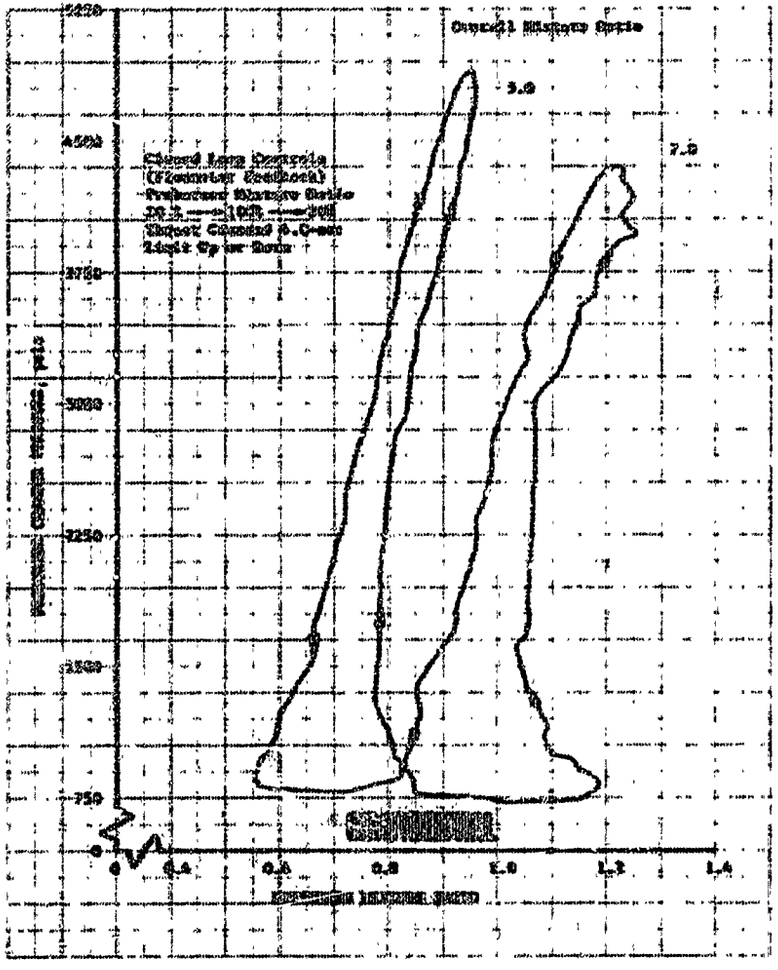


Figure 58. Preburner Chamber Pressure vs Mixture Ratio - Analog Simulation DF 59118

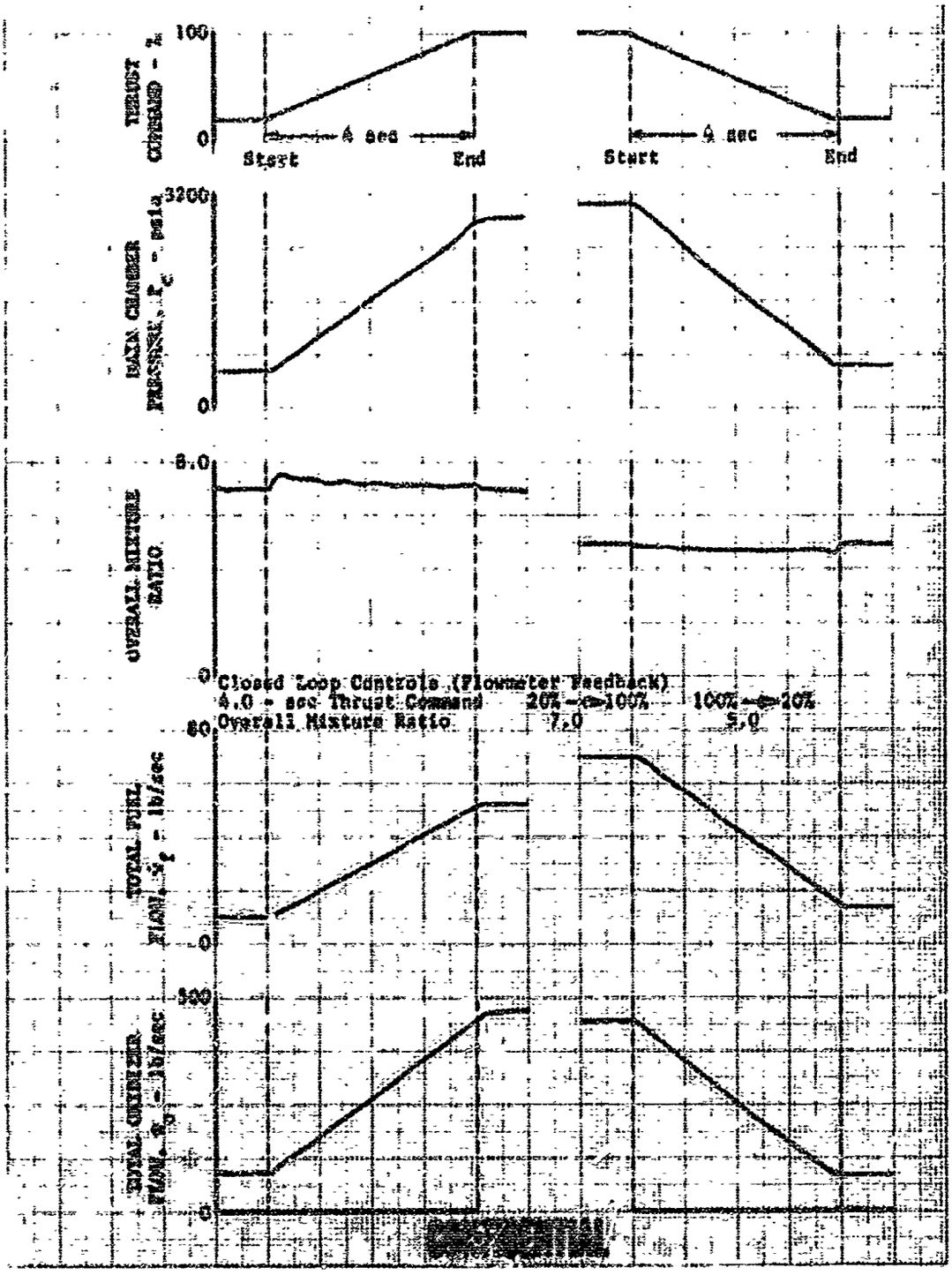


Figure 59. Acceleration and Deceleration Transient Simulation

DF 59119

(U) The requirements and the resultant operational capabilities of the high pressure demonstrator and flight engines are the same. (Refer to table III.) The flight and demonstrator engines differ in that the flight engine has assumed higher turbopump efficiencies and lower transpiration coolant flows which reflect anticipated improvements resulting from hardware development and refinement of analytical techniques; demonstrator engine components used lightweight designs while the flight engines were flightweight. Engine cycle optimization techniques used in the flight engine analysis were similar to those employed in the demonstrator engine analysis. The weight analysis of the flight engine was completed assuming a mid-1973 time constraint for technology and materials development.

(U) The flight engine configuration was used as the base-point for the parametric data analysis. The engine was scaled to provide engine performance data for a wide range of thrusts, chamber pressures, nozzle area ratios, and nozzle contours. The operational capabilities are the same as for the flight and demonstrator engines. The parametric performance data are presented in Appendix III.

b. Flight Engine Configuration

(1) Cycle Balance

(U) Relatively high performance was achieved for the demonstrator engine and very modest improvements in technology were assumed for the flight engine. Table XV presents the estimate of these technology improvements and following sections describe the development steps required to provide the flight engine technology.

(C) Table XV. Flight Engine Development Parameters

Parameter	Demonstrator Engine	Flight Engine	Development Steps
Fuel Pump Efficiency, %	64	72	Shrouding of impellers
Oxidizer Pump Efficiency, %	69	73	Hydraulic development, increased bearing DN
Overall Specific Impulse Efficiency at r = 6	96.5	96.9	Refinement in cooling techniques, improved injector performance
Weight (Upper Stage Application)	3450	2680	"Flight" criteria rather than "light" criteria

(C) Applying the above improvements, cycle balance data were generated for an upper stage flight engine for 100% and 20% thrust at mixture ratios of 5, 6, and 7. These estimated operating characteristics are presented in table XVI.

(C) Table XVI. Estimated Flight Engine Operating Characteristics, Upper Stage: Nozzle Extended (Cycle AF-1104)

	100% Thrust r = 5.0	100% Thrust r = 6.0	100% Thrust r = 7.0	20% Thrust r = 5.0	20% Thrust r = 6.0	20% Thrust r = 7.0
Configuration						
Thrust, lb	250,000	250,000	250,000	50,000	50,000	50,000
Specific Impulse, sec	445	461	456	464	461	459
Mixture Ratio (overall)	5.0	6.0	7.0	5.0	6.0	7.0
Envelope:						
Diameter, in.	100	100	100	100	100	100
Length: Nozzle Extended/Retracted, in.	166/90	166/90	166/90	164/90	164/90	164/90
Nozzle Area Ratio: Extended/Retracted	285/80	184/80	184/80	184/80	184/80	184/80
Fuel Flow, lb/sec	89.6	77.2	68.5	18.0	15.5	13.8
Oxidizer Flow, lb/sec	448.1	463.0	479.4	89.8	93.0	95.8
Total Propellant Flow, lb/sec	537.9	540.2	547.9	107.8	108.5	110.4
Main Combustion Chamber						
Throat Total Pressure, psia	3063	3000	2926	615	593	577
Mixture Ratio (injector)	5.29	6.41	7.55	5.33	6.49	7.64
Specific Impulse Efficiency, %	97.4	96.9	96.1	97.4	96.8	96.0
Fuel Injector Pressure Loss, psi	173	156	143	18	19	18
Oxidizer Injector Pressure Loss, psi	422	422	761	29	31	33
Momentum Pressure Loss, psi	118	115	112	24	23	22
Transpiration Coolant Flow, lb/sec	2.3	2.5	2.6	0.6	0.6	0.7
Throat Diameter, in.	7.3	7.3	7.3	7.3	7.3	7.3
Preburner Combustion Chamber						
Total Pressure, psia	4994	4709	4463	813	787	762
Mixture Ratio (preburner injector)	1.02	1.18	1.33	0.67	0.86	1.03
Momentum Pressure Loss, psi	42	39	37	6	6	6
Temperature, °R	1846	2193	2334	1269	1589	1841
Fuel Injector Pressure Loss, psi	222	819	949	435	542	553
Oxidizer Injector Pressure Loss, psi	1900	1177	605	430	452	603
Total Propellant Flow, lb/sec	194	148	127	24.0	21.9	20.2
Combustion Efficiency, %	98.3	98.3	98.3	98.3	98.3	98.3
Thrust Nozzle						
Regeneration Section:						
Exit Diameter, in.	43	43	43	43	43	43
Coolant Flow, lb/sec	81.2	69.3	59.5	15.3	12.9	11.1
Coolant Inlet Pressure, psia	5305	5764	5582	1271	1367	1329
Coolant Inlet Temperature, °R	106	119	111	64	72	73
Coolant Pressure Loss, psi	105	78	65	7	5	24
Coolant Temperature Rise, °R	48	52	56	55	62	60
Dump Section:						
Exit Diameter, in.	99.0	99.0	99.0	99.0	99.0	99.0
Coolant Flow, lb/sec	2.6	2.5	2.4	0.6	0.5	0.5
Thrust, lb	1345	1100	1050	257	248	234
Specific Impulse, sec	448	440	440	438	439	439

(C) Table XVI. Estimated Flight Engine Operating Characteristics, Upper Stage: Nozzle Extended (Cycle AF-1104) (Continued)

	100% Thrust r = 5.0	105% Thrust r = 6.0	100% Thrust r = 7.0	20% Thrust r = 5.0	2% Thrust r = 6.0	2% Thrust r = 7.0
Fuel Turbopump						
Pump:						
Number of Pump Stages	2	2	2	2	2	2
Speed, rpm	49,000	47,700	46,700	22,600	23,600	23,700
Pressure Rise, psi	5322	5217	5340	1227	1299	1282
Overall Efficiency, %	71.8	71.0	70.0	54.2	51.1	48.0
Impeller Tip Velocity (rms), ft/sec	2300	2265	2239	1083	1130	1130
Temperature Rise, °R	64	68	68	24	30	33
Flow Rate, lb/sec	87.0	74.7	66.1	17.4	15.0	13.9
Turbine:						
Number of Stages	2	2	2	2	2	2
Pressure Ratio	1.53	1.49	1.44	1.36	1.34	1.25
Inlet Temperature, °R	1864	2109	2324	1269	1589	1241
Inlet Pressure, psia	4976	4892	4448	811	705	759
Temperature Drop, °R	166	150	132	54	64	71
Mean Wheel Velocity, ft/sec	1633	1623	1589	769	802	806
Efficiency, %	74.2	70.2	66.1	68.2	67.6	67.2
Flow Rate, lb/sec	102	91	83	15.7	14.3	13.2
Oxidizer Turbopump						
Pump:						
Number of Stages	1	1	1	1	1	1
Speed, rpm	27,100	25,600	23,900	11,770	11,756	11,430
Pressure Rise, psi	6750	5951	5050	1382	1379	1365
Efficiency, %	72.2	72.8	73.4	49.6	50.7	52.7
Impeller Tip Velocity, ft/sec	923	870	813	401	400	389
Temperature Rise, °R	42	34	28	13	13	12
Flow Rate, lb/sec	448.1	463.0	479.4	89.8	93.0	96.6
Turbine:						
Number of Stages	2	2	2	2	2	2
Pressure Ratio	1.41	1.38	1.35	1.20	1.21	1.20
Flow Rate, lb/sec	54	49	45	8.3	7.8	7.0
Inlet Temperature, °R	1844	2109	2322	1269	1589	1241
Inlet Pressure, psia	4962	4661	4419	807	781	735
Temperature Drop, °R	115	119	119	60	47	50
Mean Wheel Velocity, ft/sec	1257	1285	1107	546	565	550
Efficiency, %	72.0	71.5	70.7	62.2	60.1	58.7

(C) Table XVI. Estimated Flight Engine Operating Characteristics, Upper Stage: Nozzle Extended (Cycle AF-1104) (Continued)

	100% Thrust r = 5.0	120% Thrust r = 6.0	102% Thrust r = 7.0	24% Thrust r = 4.0	30% Thrust r = 5.0	28% Thrust r = 7.0
Low-Speed Inducer						
Fuel Inducer:						
Flow Rate, lb/sec	89.4	77.2	68.5	18.0	15.2	13.8
Speed, rpm	20,300	19,300	18,290	6340	6700	6290
Pressure Rise, psi	51	68	68	10	19	19
NPSH, ft	60	60	60	6*	60	60
Efficiency, %	79.2	77.8	75.4	47.3	48.7	37.9
Oxidizer Inducer:						
Flow Rate, lb/sec	448.2	463.8	479.4	99.8	93.0	96.4
Speed, rpm	3480	3480	3420	1573	1563	1230
Pressure Rise, psi	175	168	152	34	33	30
NPSH, ft	16	16	16	16	16	16
Efficiency, %	79.1	80.5	80.6	38.6	40.0	42.5
Fuel Low-Speed Inducer Turbine						
Pressure Ratio	1.26	1.32	1.30	1.31	1.29	1.36
Flow Rate, lb/sec	4.3	5.0	4.9	1.3	1.3	1.3
Speed, rpm	20,450	19,393	17,810	6543	6700	6290
Efficiency, %	51.1	49.6	49.7	19.3	12.4	19.1
Oxidizer Low-Speed Inducer Turbine						
Pressure Drop, psi	578	553	536	243	225	277
Flow Rate, lb/sec	369	387	406	69.2	82.9	82.4
Speed, rpm	2480	3041	3420	1573	1965	1883
Efficiency, %	45.7	44.3	43.3	40.6	41.6	44.0

(a) Fuel Pump Efficiency

(U) The flight fuel pump efficiency is obtained by shrouding the impellers. Shrouded impellers produce a higher head coefficient that permits reduced impeller and housing diameters, which reduces turbopump weight and size. Tests conducted with the 350K fuel pump and the RL10 fuel pump have shown this hydraulic performance improvement can be achieved. Mechanical development is currently being pursued under an independent program to demonstrate shroud attachment.

(b) Oxidizer Pump Efficiency

(U) Hydraulic development of the oxidizer pump and increased rotor speed will increase the oxidizer pump efficiency. The 350K oxidizer pump test results have determined the areas where hydraulic development is required. These areas are in the high-speed inducer/impeller matching and in impeller blade and passage geometry.

(C) Further improvement is possible by increasing the maximum rotor speed from 25,800 rpm to 27,000 rpm. This requires increased bearing DN capability from 1.29 to 1.35 x 10^6 mm-rpm (about 4%). Increased speed improves pump efficiency through higher specific speed. These modest development steps will improve the oxidizer pump efficiency from 69%, as used in the demonstrator engine, to the 73% level estimated for the flight engine.

(c) Oxidizer Turbine Efficiency

(C) The improved turbine efficiency of the flight turbopump is based on the increased rotor speed described above and the decreased turbine power as a result of the improved pump efficiency. Turbine aerodynamic development is not required. The oxidizer turbine wheel speed will increase to approximately 1200 ft/sec, which is 70% of the demonstrator engine fuel turbine wheel speed.

(d) Overall Specific Impulse Efficiency

(U) Reduced transpiration coolant flow through the application of advanced cooling techniques will provide a two-fold improvement in impulse efficiency. First, the lower coolant flow increases the propellant flow available to the main injector and reduces the injector mixture ratio for any engine operating mixture ratio. This increases the specific impulse of the main propellant stream. Secondly, the amount of propellant expanded at low mixture ratio near the nozzle wall is reduced.

(U) Injector development will result in a more uniform combustion profile. A uniform profile improves both the combustion efficiency and the efficiency of the nozzle expansion process.

(2) Engine Description

(U) The 250,000-lb thrust, staged-combustion high-pressure rocket engine with a two-position bell nozzle is a versatile, compact, high-performance propulsion system for use in both upper and lower stages of advanced vehicles. Nozzle interchangeability and the two-position nozzle concept

permit operation of the same engine system with optimum nozzle area ratios for improving the performance of the lower stages within the atmosphere and provides high performance in upper stages by using high area ratio nozzles. This interchangeability is achieved by using a common turbomachinery power package and attaching the desired nozzle skirt for the various application requirements.

(U) The flow paths and the components of the flight and demonstrator engine are identical except for the following items:

1. Flight engine fuel impellers are shrouded.

2. A part of the flight engine fuel low-speed inducer turbine flow is ducted back into the main turbine discharge because it is not required for cooling the main chamber.

3. Dump cooling starts at an area ratio of 35.

(U) A preliminary installation drawing of the engine is presented in figure 60.

(3) Flight Engine Weight

(C) The flight engine estimated weight is 2680 lb for a 250,000-lb thrust engine with a nozzle area ratio of 184. This weight is achieved by straight forward engineering refinement and does not require technology advances. A comparison of the component weight breakdown for the demonstrator engine and for the flight engine is shown in table XVII.

(U) The basic ground rules used in the flight engine weight analysis were:

1. Engine preliminary flight rating test (PFRT) development program has been completed (target PFRT dated mid-1973).

2. Component technology and materials that can be developed by mid-1973 were considered.

3. Control actuators were not included in the demonstrator engine weight. However, the flight engine weight summary includes the complete control system.

(a) Preburner

(U) The weight of the demonstrator engine preburner injector assembly will be reduced 45 pounds by using a tapered fuel manifold and by reducing the volume enclosed by the outboard housing. The housing volume reduction is permitted because the facility actuator mounting used on the demonstrator assembly is eliminated, thereby eliminating the seal package.

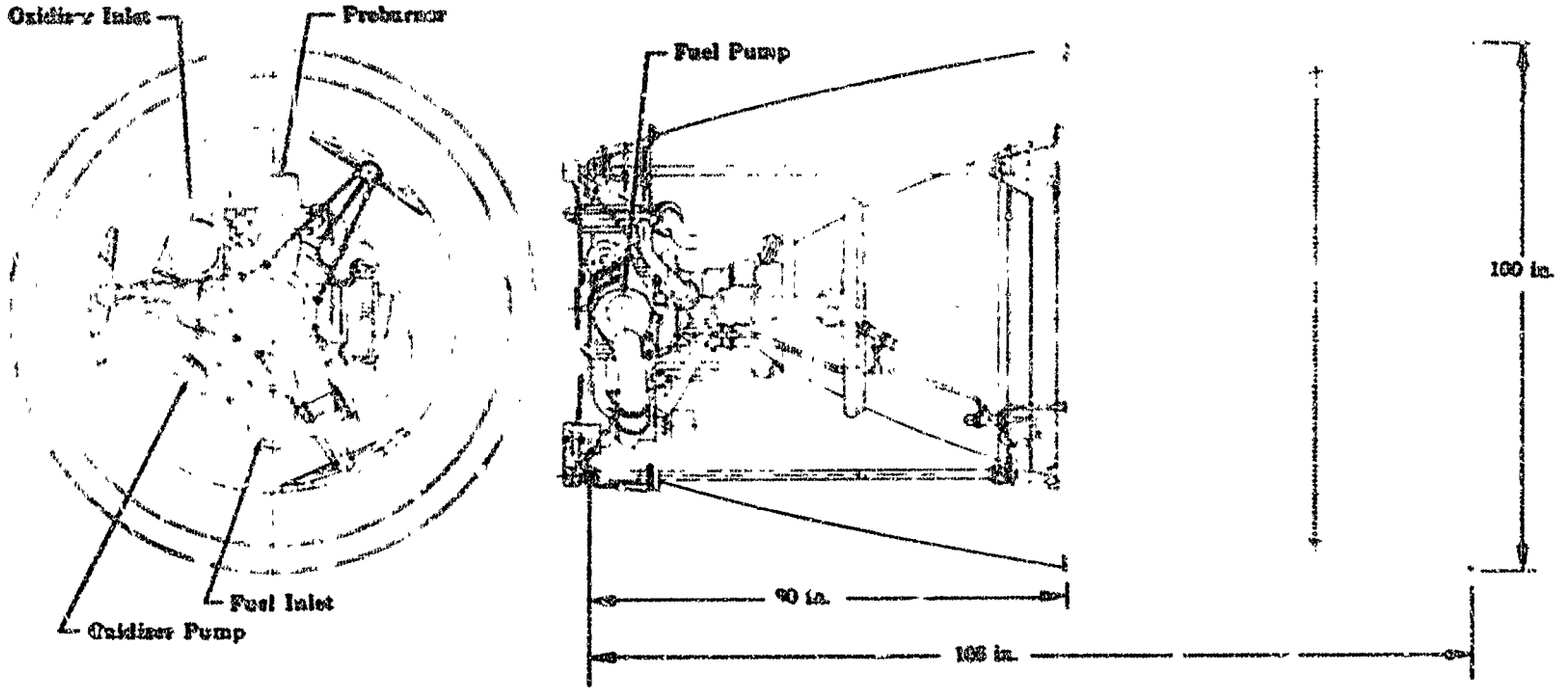


Figure 60. Preliminary Flight Engine Installation Drawing

FD 21969C

(C) Table XVII. Demonstrator and Flight Engine Estimated Weight

Component Assembly	Demonstrator Engine	Flight Engine
Preburner	320	275
Transition Case	380	316
Main Injector	135	126
Main Chamber	445	272
Two-Position Nozzle and Actuators	555	446
Fuel Turbopump	355	274
Oxidizer Turbopump	280	250
Low-Speed Inducers	215	213
Controls (Less Actuators and ECU)	380	342
Plumbing	310	112
Miscellaneous	75	74
Total	3450	2680

(b) Transition Case

(U) The demonstrator engine transition case design is based on conservative design margins pending model tests and completion of a detailed design. Fabrication of the flight engine transition case from boron filament reinforced Inconel 718 rather than an Inconel 718 forging provides the 64-pound weight reduction.

(c) Main Injector

(U) The 9-pound weight reduction in the main injector is derived from reduced main chamber diameter made possible by thinner transpiration wall thickness.

(d) Main Chamber

(U) Elimination of replaceable metering orifices in the copper wafers and material changes made possible by application of advanced cooling concepts permit a reduction in the chamber wall thickness, with a resultant reduction in the outer structural shell diameter. A 2-inch reduction in chamber length and a reduction in the transpiration cooled area downstream of the throat was also incorporated in the flight engine weight estimates. These modifications produce an estimated weight reduction of 173 pounds.

(e) Two-Position Nozzle and Actuators

(U) The flight engine nozzle configuration was assumed to be dump cooled from an expansion ratio of 35 rather than from an area ratio of 80 used in the demonstrator engine. The use of the lightweight dump cooled nozzle construction in place of the tubular regenerative heat exchanger reduces the weight of the fixed nozzle skirt. Actuation system weights are reduced through the use of hollow foam-filled formed steel jack screws. A sheet metal seal at the junction of the translating and fixed nozzle sections replaces the ring seals used in the demonstrator configuration. The weight is reduced 109 pounds by these changes.

(f) Fuel Turbopump

(C) Shrouded impellers to provide an increase in pump efficiency from 64 to 72% reduce the flight engine impeller diameters and permit a reduction in housing weights. The fuel turbopump weight is reduced 81 pounds by the diameter changes and machining away excess housing material.

(g) Oxidizer Turbopump

(C) Higher rotor speed, 27,000 vs 25,800 rpm, increases the pump and turbine efficiencies of the oxidizer turbopump and permits a reduction in the impeller and housing diameters. The weight reduction (30 pounds) is primarily from the reduced housing weights.

(h) Low-Speed Inducers

(U) The demonstrator engine fuel and oxidizer low-speed inducer turbopumps are essentially flightweight designs. Scalloping flanges and excess material removal result in a 2-pound weight savings.

(i) Controls

(U) A comparison of the control system weights given in table XVII must consider the facility-type equipment that will be used during the demonstrator program. The controls system computer and valve actuators for the demonstrator engine controls are facility equipment and are not included in the weight estimate. The demonstrator engine control valves and flowmeters weigh 340 pounds. Comparable flight engine valves and flowmeters weigh 232 pounds. This reduction is accomplished through reduced housing thickness and the elimination of actuator mounting provisions to accept both flight and facility-type actuators. The actuators included in the demonstrator controls weigh 40 pounds. Flight-type actuators for all controls are estimated to weigh 65 pounds. A computer (no comparable weight included in the demonstrator controls) weighing 25 pounds is included in the flight engine controls weight.

(j) Plumbing

(U) Boron filament wound plumbing using an aluminum binder was assumed for the flight engine. This fabrication technique provides a weight reduction of 198 pounds. This weight reduction was based on a strength-to-density ratio of 2×10^6 in. With continued development of boron filament technology, strength to density ratios of 4×10^6 in. are expected in the 1970's.

c. Parametric Performance Data

(U) The objective of the parametric data analysis was to establish the effect of thrust level, mixture ratio, chamber pressure, nozzle area ratio, and nozzle contour on specific impulse, engine envelope, and weight. These parametric data are presented in Appendix III.

(C) The ranges of engine parameters included in the parametric data are:

1. Vacuum thrust - 100,000 to 350,000 lb
2. Chamber pressure - 2000 to 3500 psia
3. Overall engine mixture ratio - 5 to 7
4. Overall expansion ratio - 50 to 400
5. Nozzle contour - maximum performance, baseline, and minimum surface area
6. Primary expansion ratio - 35 and those required for minimum stowed length.

(U) Values of specific impulse are given for an altitude range from sea level to vacuum conditions. Engine weight, overall diameter, and length are given. Both the overall length for the nozzle fully extended and the stowed length for the fully retracted nozzle are shown. The 230,000-lb thrust flight engine served as the base-point engine for the parametric performance data.

3. Dual-Preburner Cycle Study

(U) An alternative engine cycle using a dual-preburner system was evaluated. The purpose of the study was to determine if the dual-preburner system afforded an appreciable advantage over a single-preburner system in terms of fuel and oxidizer pump discharge pressures. It was concluded from this study that a dual-preburner system does not allow a sufficient reduction in fuel pump discharge pressure to warrant the increased system and control complexity that results from its use.

(U) This study was undertaken before the cycle optimization techniques used in later cycle studies were developed and thus the absolute values of parameters presented in the text and accompanying figures are not necessarily applicable when making a direct comparison of the dual and single preburner systems. However, the relative levels of parameters are realistic and the conclusions drawn from the study remain valid.

(U) Detailed analytical studies were conducted to establish the design point cycle balance and off-design performance characteristics of a dual-preburner engine system. Preliminary design layouts to define the component arrangements for the dual-preburner system were also completed.

(U) A flow schematic of the dual-preburner system is shown in figure 61. For comparison purposes, a flow schematic of a single-preburner system is provided in figure 62. There are several possible combinations of flow paths; however, all would have the same basic performance characteristics. The flow required to cool the nozzle is included in the fuel line to the oxidizer preburner. Because the fuel turbopump has the largest horsepower requirements, this path provides the most efficient fuel system. Including the cooling flow in the oxidizer preburner line

eliminates the need for a mixing valve. The oxidizer flow system of thrust and mixture ratio control was assumed with the use of the flow sensing controls. The oxidizer pump discharge flow is divided to supply the two preburners and each branch required a control. Additional flow measurements will also be required in the propellant lines to the fuel preburner.

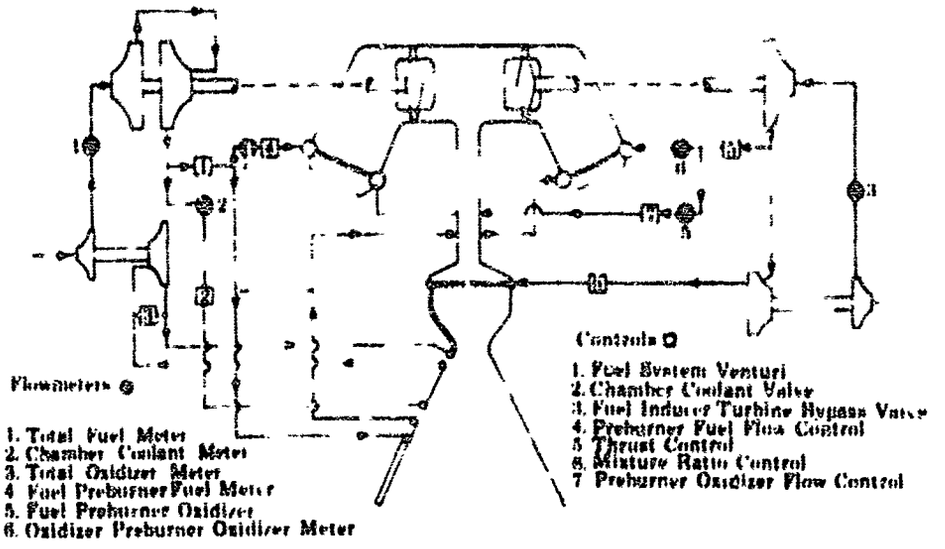


Figure 61. Dual-Preburner Cycle Control Schematic FD 13998

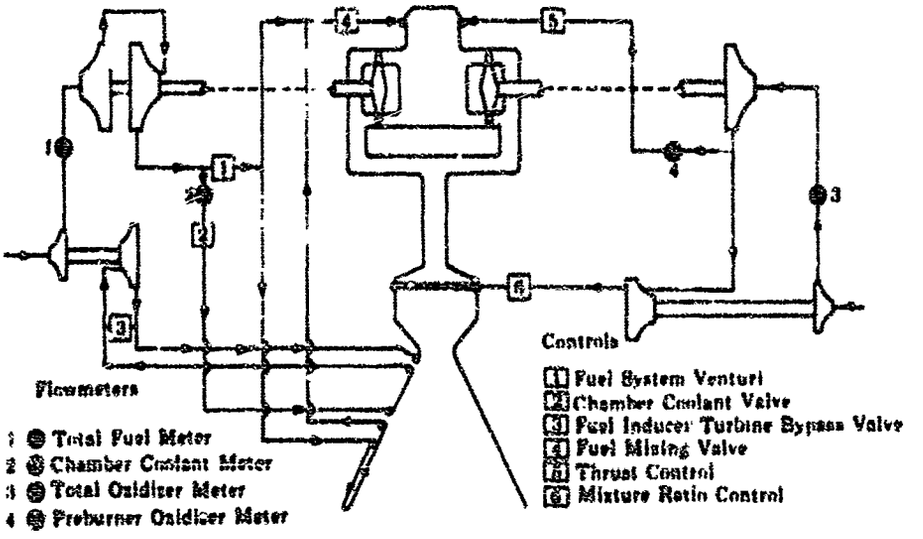


Figure 62. Single Preburner Cycle Propellant Flow Schematic FD 15344

(C) The fuel and oxidizer pump requirements (as a function of mixture ratio at full thrust) are given in figures 63 through 65. For comparison purposes, the single-preburner cycle operating at full thrust and the variable turbine vane area system are also shown. The fuel pump requirements are superimposed on the fuel pump performance curve in figure 66. The results indicate that the maximum fuel pump discharge pressure at the highest flow condition (r = 5.0) would be reduced approximately 150 psia with the dual-preburner system.

(C) In a preburner cycle, the pump power requirements are provided by turbines that derive their power from the preburner flow, energy level, and pressure ratio.

$$\text{Turbine horsepower} = \frac{Wh}{C}\left[1 - \left(\frac{P}{P_o}\right)^{\frac{\gamma-1}{\gamma}}\right] \qquad (1)$$

where:

W = Turbine weight flow
h = Turbine inlet enthalpy
P_o = Turbine inlet total pressure
P = Turbine discharge static pressure
γ = Ratio of specific heats
C = Conversion factor

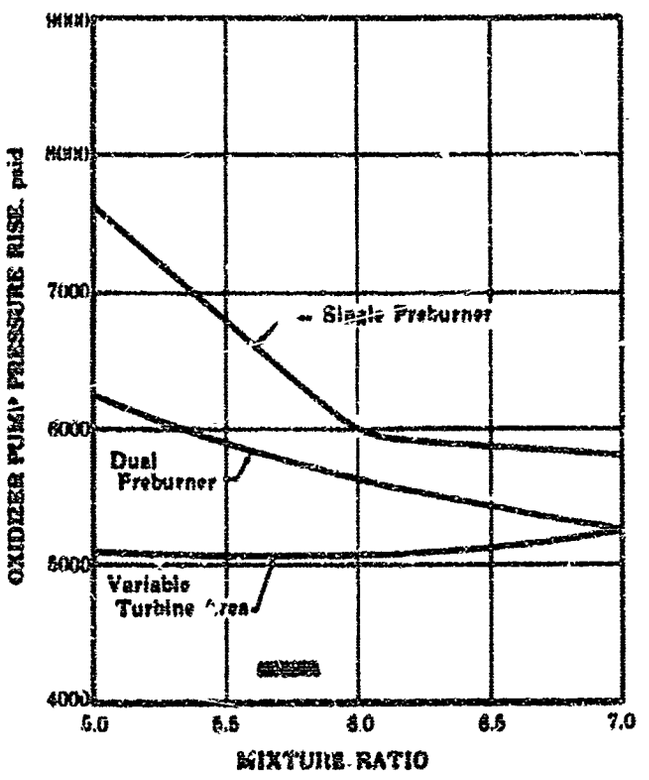


Figure 63. Oxidizer Pump Pressure Rise vs Mixture Ratio

ED 15945

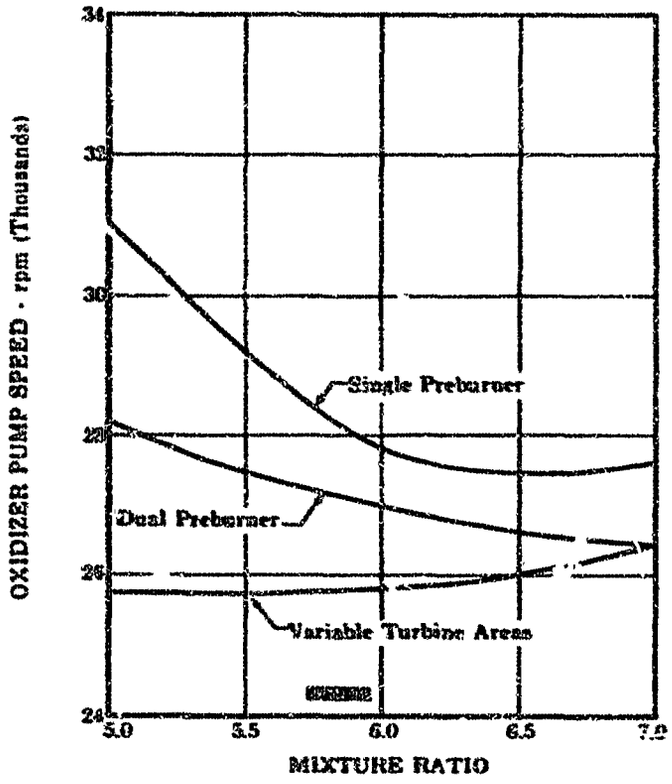


Figure 64. Oxidizer Pump Speed vs Mixture Ratio FD 15973

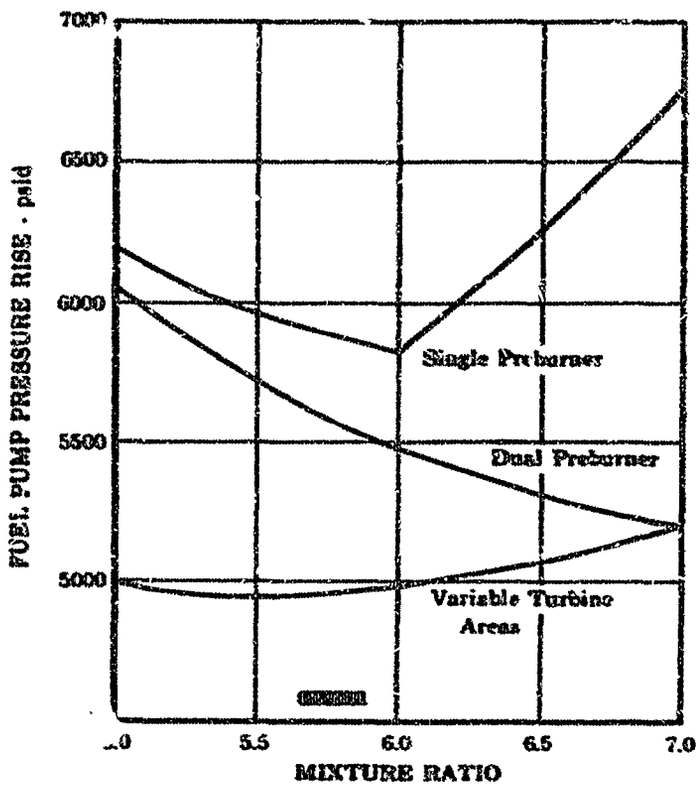


Figure 65. Fuel Pump Pressure Rise vs Mixture Ratio FD 15987

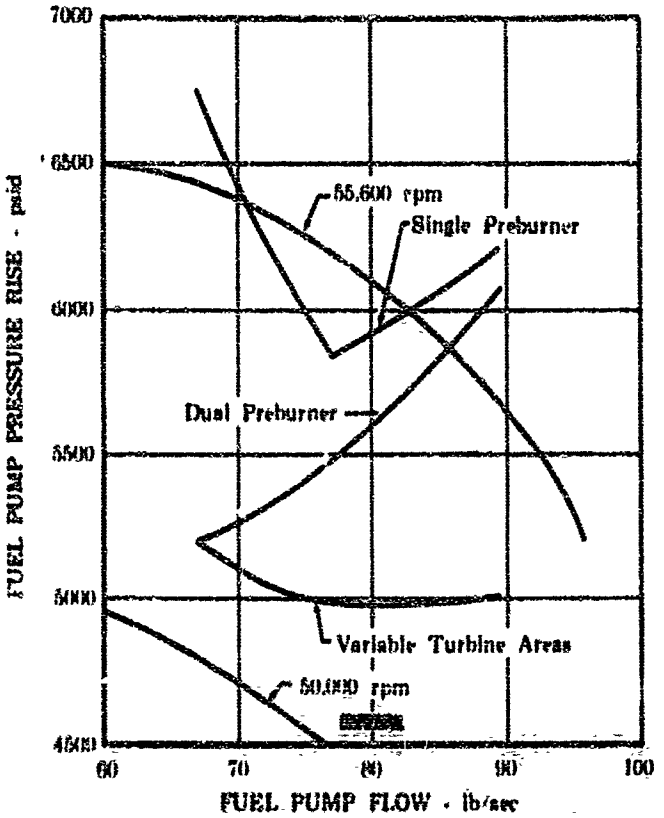


Figure 66. Fuel Pump Pressure Rise vs Fuel Pump Flow FD 15992

(U) The maximum turbine power is provided with maximum fuel and oxidizer flow to the preburner and burning at maximum allowable temperature.

(U) All of the fuel, except the transpiration coolant, flows to the preburner, which is limited in maximum temperature and thus in mixture ratio. The available turbine flow, therefore, decreases with increasing mixture ratio as shown in Figure 67.

(U) Operation at the highest mixture ratio point is the limiting case from an available turbine power standpoint for both the single- and dual-preburner configuration. The pump horsepower characteristics, as a function of mixture ratio, result in a net decrease in required power as mixture ratio increases (figure 68); however the decrease does not offset the reduced available turbine power.

(U) The power balance must involve using the available flow and enthalpy to establish the required pressure ratio to satisfy the pump power requirements.

(U) The relationship of flow, temperature, inlet pressure, area and pressure ratio must also be satisfied. The equation for gases is expressed as:

$$\frac{\dot{w}\sqrt{T}}{AP} = \left[\frac{2\gamma}{R(\gamma-1)}\right]^{1/2}\left[\frac{P}{P_o}\right]^{\frac{1}{\gamma}}\left[1-\left(\frac{P}{P_o}\right)^{\frac{\gamma-1}{\gamma}}\right]^{1/2} \qquad (2)$$

where:

$\dot{w}$ = Mass flow rate
A = Effective area
T = Total temperature
P_o = Inlet total pressure
P = Exit static pressure
γ = Ratio of specific heats
R = Gas constant

If the inlet pressure and pressure ratio are determined by the power requirements, the area must be set to satisfy the flow requirements.

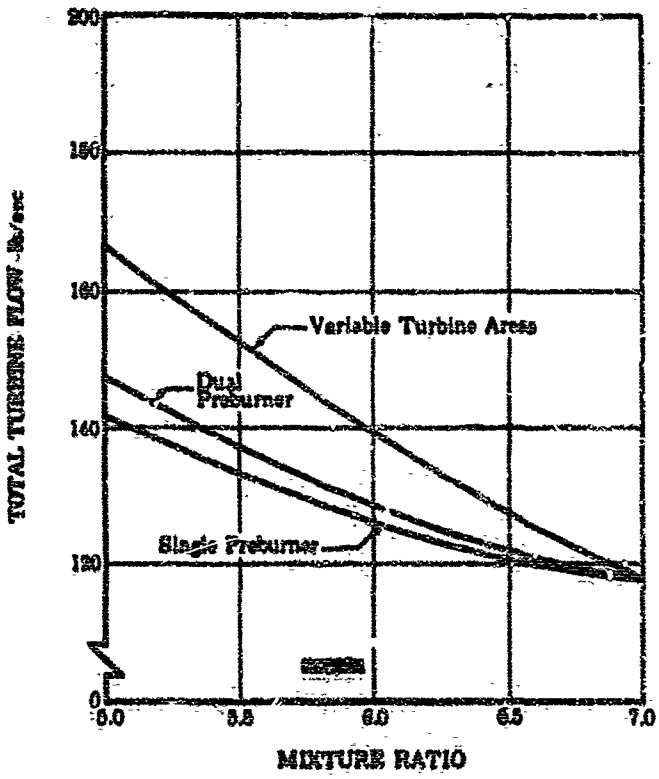
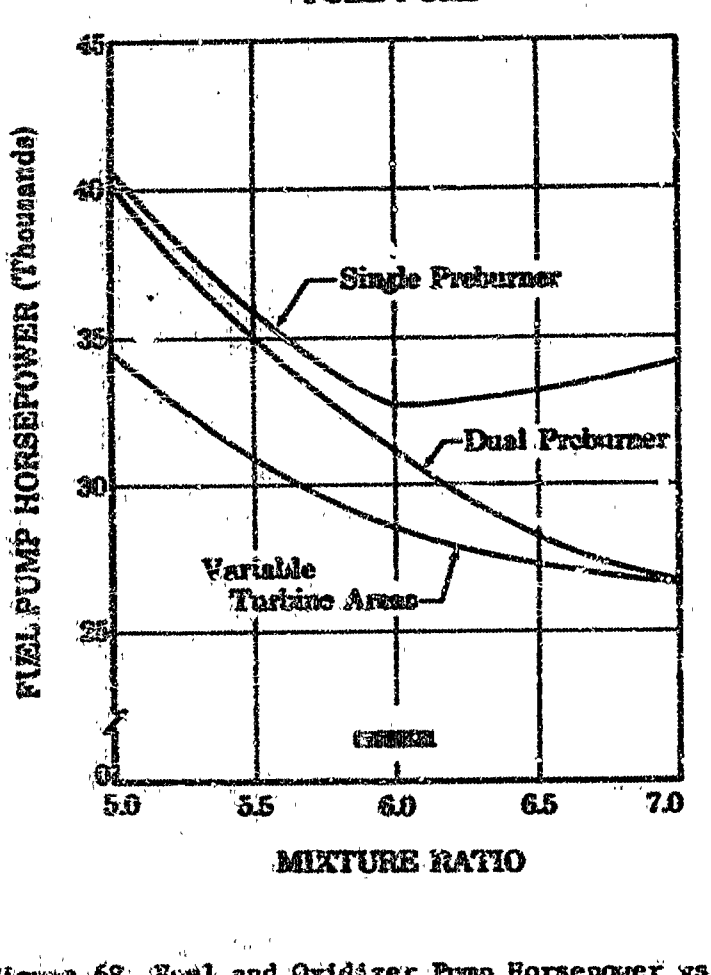


Figure 67. Total Turbine Flow Available vs Mixture Ratio FD 16009A



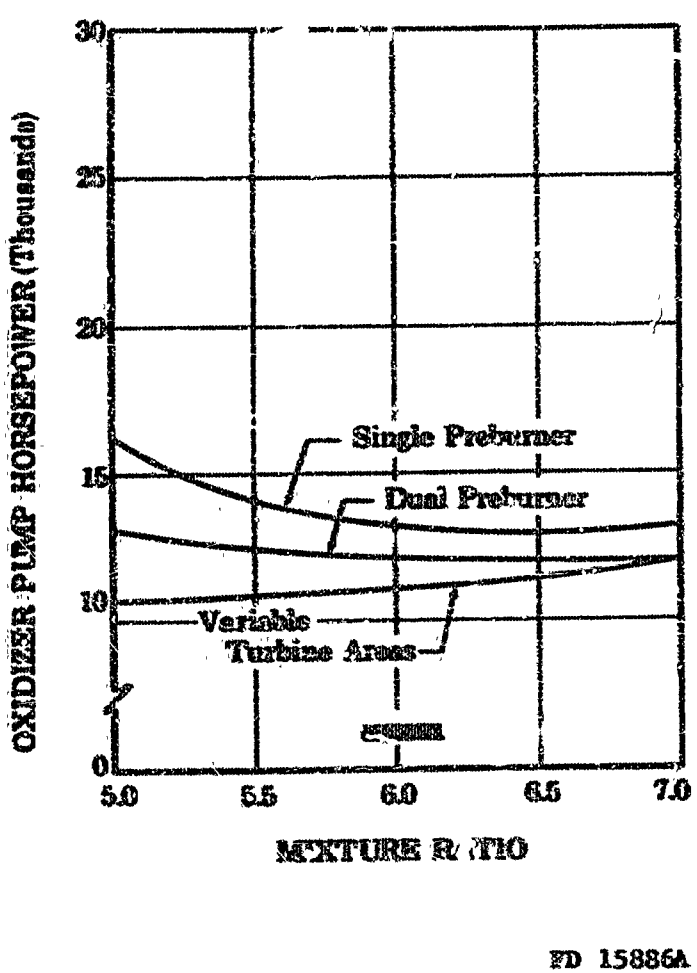


Figure 68. Fuel and Oxidizer Pump Horsepower vs Mixture Ratio

FD 15886A

(U) The limiting balance point of pump horsepower and turbine flow occurs at highest mixture ratio. Therefore, this operating condition must control the setting of the turbine areas. The selection of the turbine area is such that the required mixture ratio excursion may be met without exceeding limits of pump speeds, turbine inlet temperature, etc.

(U) For the single preburner engine, the turbine areas are established to balance the pump requirements with the pump capability over the mixture ratio range. In the dual-preburner configuration the turbine areas are set at the highest mixture ratio because each preburner mixture ratio can be scheduled with engine mixture ratio. The resulting turbine areas are shown in figure 69 along with the desired schedule for variable turbine areas.

(U) Figure 66 and equation (2) show that the turbine inlet pressure has a flow-area restriction to satisfy in addition to the horsepower requirements. Further, the available turbine flow cannot have the desired split according to the horsepower ratio between the two pumps. This effect is shown in figure 70.

(U) This in turn imposes an additional turbine inlet pressure requirement such that at low mixture ratio the pressure ratio must increase. (See figure 71.)

(U) For fixed geometries, the available turbine energy split is constant although the power requirements are not constant with mixture ratio. For a single preburner, the required scheduling of the total turbine energy provided and the constant turbine power split will result in one turbopump to be power balanced and the other to have excess available power. This effect yields the pump characteristics shown in figures 63 to 65. The use of variable area allows the turbine inlet pressure to be set on the basis of power requirements only. It is possible to schedule the maximum available turbine flow at maximum temperature. Therefore, the flow split (figure 70) between the turbines can be varied according to individual pump power requirements. This results in considerably reduced turbine inlet pressure requirements and, thus, reduced pump requirements.

(U) The use of a dual-preburner system provides mixture ratio schedules of each preburner and allows a constant turbine inlet temperature if desired. For the fuel turbine, the maximum available energy is required and therefore the maximum allowable temperature is held as shown in figure 71. Because the dual-preburner allows different turbine inlet temperatures, the oxidizer preburner mixture ratio is reduced with decreasing mixture ratio as shown in figure 72. This reduces the oxidizer pump discharge pressure at low mixture ratio as shown in figure 63. It should be noted, however, that the oxidizer system could be reduced further except that it must provide pressure to the fuel preburner. This is illustrated in the horsepower curves in figure 68. The extreme reduction in oxidizer turbine temperature coupled with the fixed turbine areas, causes a slight reduction in fuel turbine flow (as a percentage of total flow), which is shown in figure 70.

(This page is Unclassified)

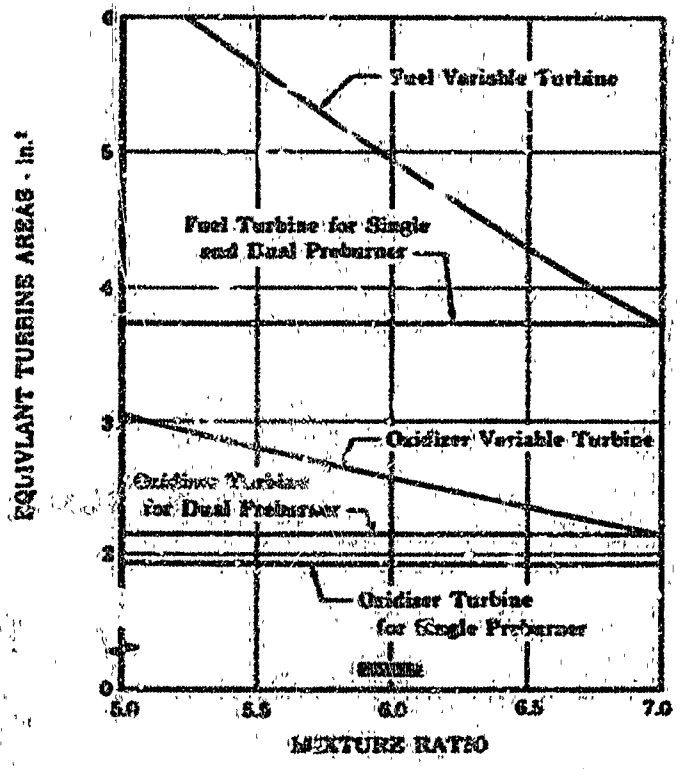


Figure 69. Turbine Areas vs Mixture Ratio FD 16007A

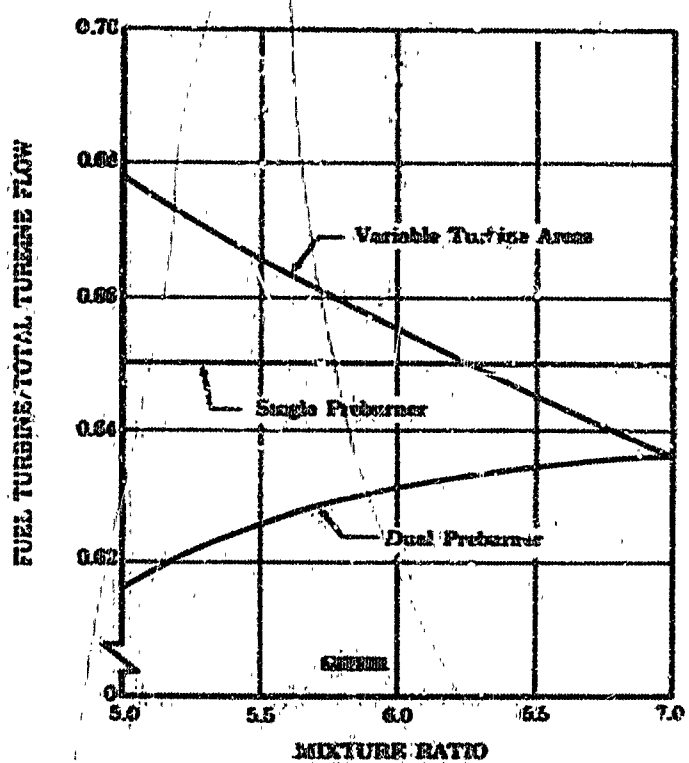


Figure 70. Fuel Turbine Flow Ratio vs Mixture Ratio FD 16008A

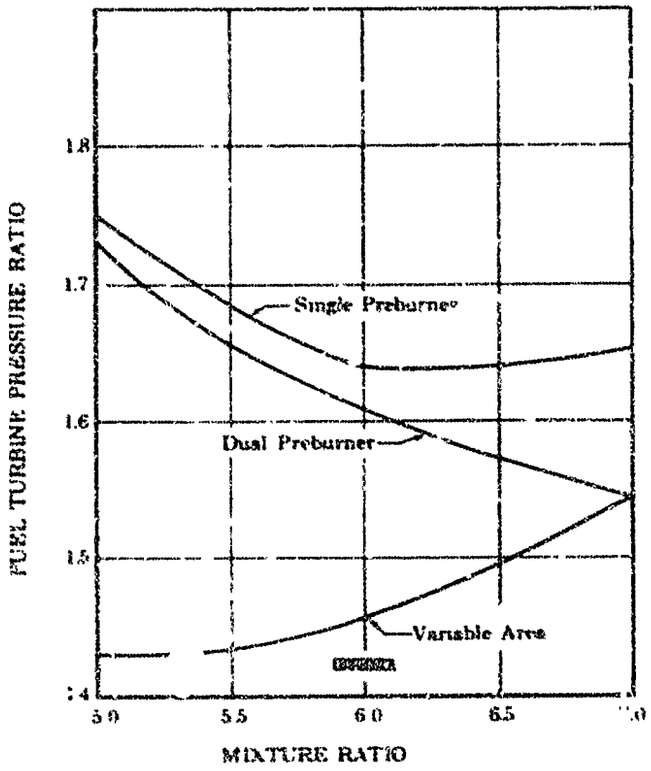


Figure 71. Fuel Turbine Pressure Ratio vs Mixture Ratio FD 16006A

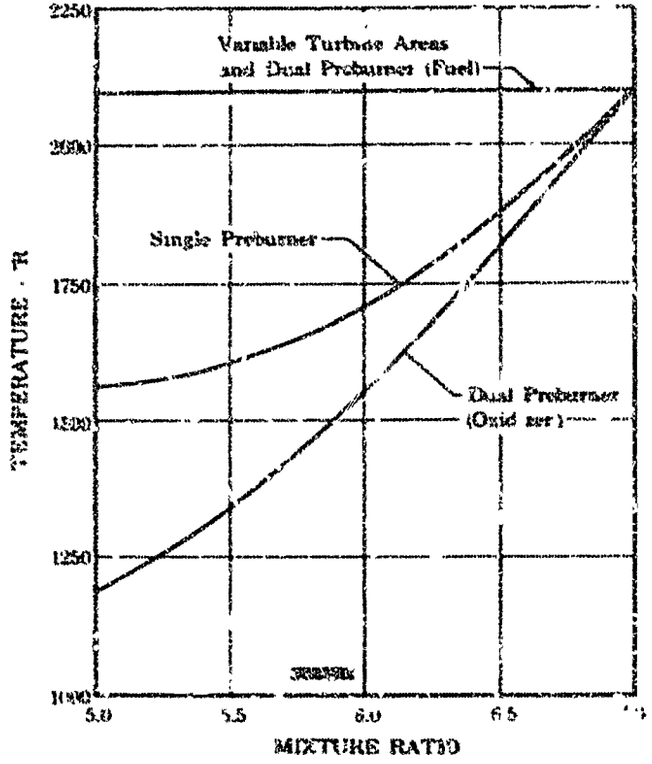


Figure 72. Preburner Temperature vs Mixture Ratio FD 15976

, The small reduction in fuel pump pressure requirements at the low ...ture ratio for the dual-preburner cycle is caused mainly by the ...reased fuel turbine inlet temperature. The ability to individually ...trol the turbine inlet temperatures results in the large reduction in ... oxidizer pressure requirements.

(U) The component arrangement for the dual-preburner configuration is shown in figure 73. An alternative radial arrangement is shown in figure 74. These studies indicated that the overall engine envelope requirements of diameter and length could be retained with the dual-preburner component arrangements. A weight increase over the single preburner system of approximately 50 pounds was estimated.

(U) The additional combustion system and additional control complexity for the dual-preburner cycle would result in a less reliable system. Further additional controls may be required to ensure balanced acceleration and deceleration of the turbopumps.

(U) Pump discharge pressure reductions of 150 psi and 550 psi, at the maximum flow conditions, for the fuel and oxidizer pumps, respectively, are possible with the dual-preburner cycle. Fuel pump requirements are of more interest, however, than oxidizer pump requirements because the fuel pump is generally designed to operate at the technology limit. It was concluded that the dual-preburner cycle did not warrant further consideration because it is considerably more complex than a single-preburner engine, and because it offers no significant performance or weight advantages over the single-preburner cycle.

(This page is Unclassified)

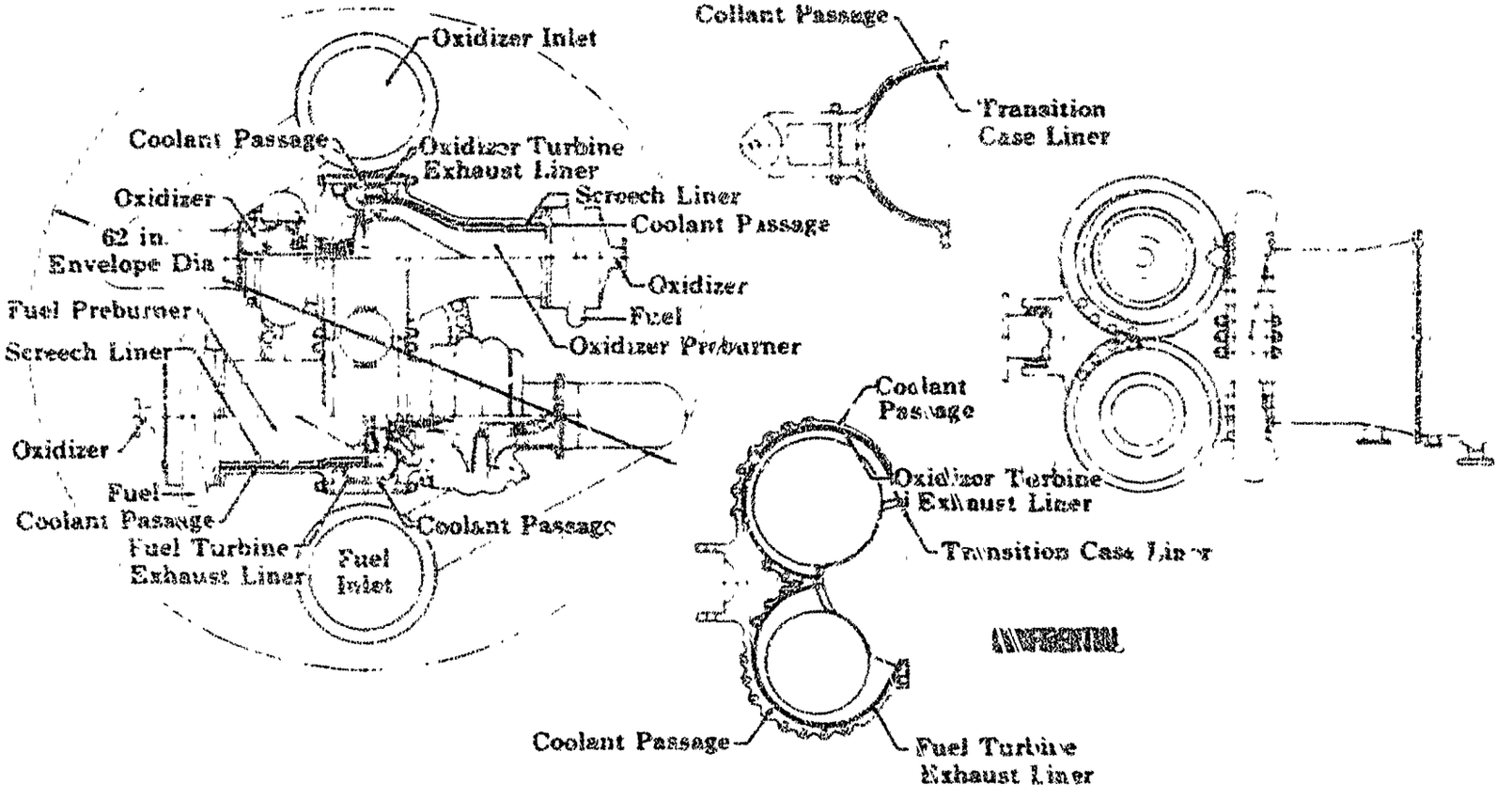


Figure 73. Dual-Preburner Engine Component Arrangement

FD 15834

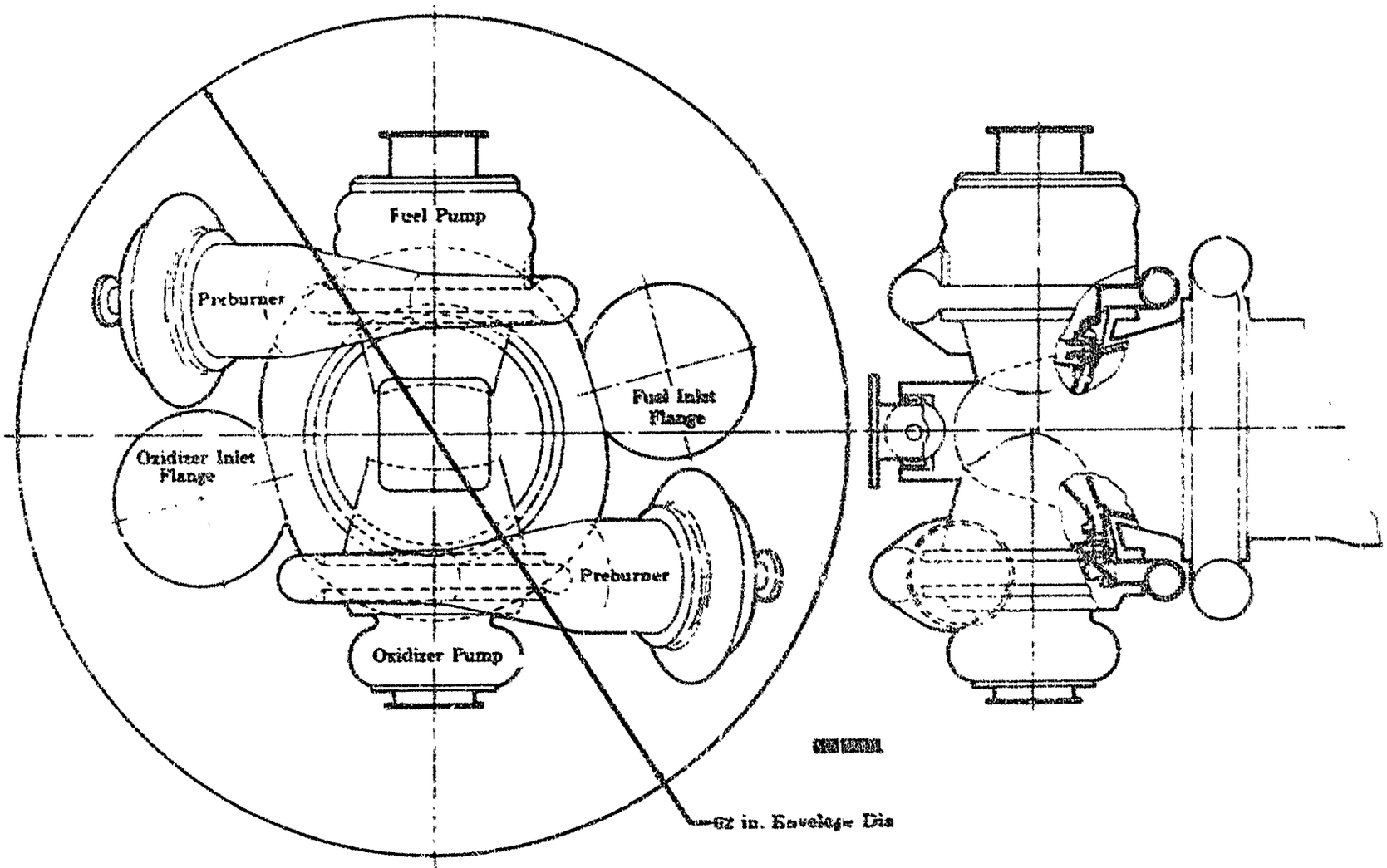


Figure 74. Dual-Preburner Engine Radial Arrangement

FD 15887A

SECTION V
APPLICATIONS STUDY

(U) The overall objective of the Applications Study was to investigate the application of the high performance staged-combustion engine in six representative advanced rocket stages and to determine the resulting performance. A secondary objective was to assess changes in vehicle performance which could result from various engine options or advanced features. A stage figure of merit (referred to as the Performance Index, W_x) was specified and used for performance evaluation. Performance Index included considerations of engine specific impulse, weight, size, and installation features as these parameters affect vehicle performance. Engine associated weight includes items such as thrust structure, feed lines, thrust vector control, failure detection equipment, and propellant tank pressurization.

(C) Six vehicle cases were studied for 250K and 350K vacuum thrust engine sizes. The six cases specified for this study were:

Case 1 - expendable lower stage
Case 2 - expendable upper stage
Case 3 - expendable single-stage to orbit
Case 4 - recoverable lower stage
Case 5 - recoverable upper stage, pick-a-back
Case 6 - recoverable upper stage, tandem.

These application cases are shown schematically for both engine sizes in figures 75 and 76.

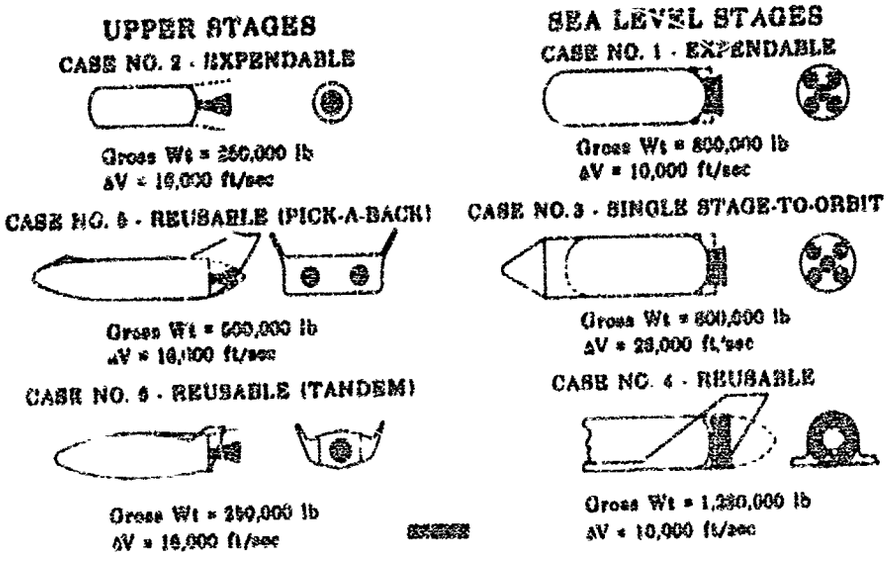


Figure 75. Application Study Vehicles, 250K Engines

FD 21995

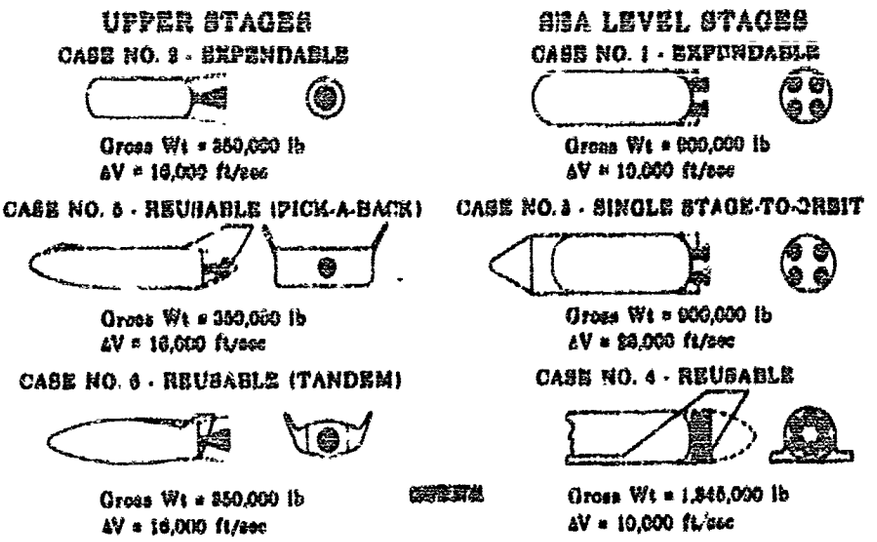


Figure 76. Application Study Vehicles, 350K Engines FD 21996

(U) A single common module was defined by detailed optimization procedures for all of the application cases. A common module was defined as a basic engine power package in which the flow rate and chamber pressure remained constant for all six vehicle applications. The high pressure engine concept permits the same engine power package to be used with nozzle skirts of different area ratio; each skirt is therefore tailored to provide optimum performance for a specific application case. The optimum nozzle expansion ratio varied considerably for each of the six vehicle cases.

(U) The applications study was conducted as a continuing effort throughout the Program. Performance Index (W_x) values have been updated as new or improved engine and engine-vehicle interface data became available. Initial work was done with high pressure engines having fixed regeneratively cooled exhaust nozzles, however, the final W_x values (with the exception of Case 4) are for engines using lightweight two-position nozzles. The nozzle skirt is retracted to reduce engine length and increase sea level thrust and specific impulse with the two-position nozzle concept. Case 4, because of severe diameter constraints and resulting low area ratio requirements, shows slightly better performance with a fixed nozzle. All other cases show a W_x improvement for the lightweight two-position nozzle concept.

(C) Tables XVIII and XIX provide the final W_x values obtained by using the common module. These performance data are based on lightweight two-position nozzle engines, except for Case 4, which used a fixed nozzle. The data for the 250K application cases are summarized in table XVIII and table XIX is the summary for the 350K cases. An expansion ratio of 250 was selected for the basic 250K module and an expansion ratio of 300 was selected for the 350K module. Other pertinent engine and

engine-vehicle interface data are also shown. The application cases require a wide range of engine mixture ratio as shown by the optimum values for each case in tables XVIII and XIX.

(U) Further details on this Application Study can be found in the separate final report, AFRPL-TR-67-270, "Applications Study for a High Performance Cryogenic Staged-Combustion Rocket Engine," November, 1967.

(C) Table XVIII. Performance Index Summary (250K Study)

	Case 1	Case 2	Case 3	Case 4	Case 5	Case 6
Performance Index, W_x (lb)	235,600	66,350	45,180	306,100	80,850	39,350
Engine Description						
Vacuum Thrust, F_v , (lb/engine)	243,400	250,000	245,700	237,000	248,500	250,000
Number of Engines	5	1	5	8	2	1
Chamber Pressure P_c (psi)	3,000	3,000	3,000	3,000	3,000	3,000
Engine Module Size, ϵ_M*	250	250	250	250	250	250
Nozzle Contour	MC_s	MSA	MC_s	MC_s	MSA	MSA
Expansion Ratio, ϵ (Retracted)	35	111	35		89	111
(Translated)	75	250	110	35	200	250
Mixture Ratio, r	5.15	5.9	5.76	5.52	6.4	6.7
Vacuum Specific Impulse, I_{vac} (sec)	455.2	466.3	458.7	443.0	461.3	462.0
Sea Level Specific Impulse, I_{sl} (sec)	396.8	—	389.0	403.2	—	—
Exit Diameter, OD (in.)	64.5	116.7	78.0	44.3	104.5	116.7
Engine Length (in.) (Retracted)	91.3	104.0	122.5		86.5	104.0
(Extended)	143.2	194.0	170.0	104.0	173.0	194.0
Engine Mount Height, MH (in.)	88	73	80	47	52	45
Engine Mount Ring Radius, MR (in.)	101	—	118	98	—	—
Installation Weight, W_e (lb)	18,361	4474	19,258	26,141	8857	4189
Oxidizer Feed Lines (lb)	383	55	385	417	143	55
Fuel Feed Lines (lb)	299	55	300	551	136	55
Thrust Structure (lb)	2190	1285	2610	2335	2500	1000
Heat Shield (lb)	762	—	993	725	—	—
TVC System (lb)	1450	290	1450	2320	580	290
Pressurization System (lb)	152	24	145	233	48	24
Failure Detection System (lb)	275	55	275	440	110	55
Engine(s) (lb)	12,850	2710	13,100	19,120	5340	2710
Fairing Area, AF (ft^2)	711	—	776	1437	2160	412
Interstage Area, A_i (ft^2)	—	977	—	—	—	356

*The area ratio required for 250K vacuum thrust using one common set of preburner, turbopumps, and main chamber hardware.

(C) Table XIX. Performance Index Summary (350K Study)

	Case 1	Case 2	Case 3	Case 4	Case 5	Case 6
Performance Index, W_x (lb)	265,900	95,230	53,960	325,000	51,040	60,800
Engine Description						
Vacuum Thrust, F_{vac} (lb/engine)	340,700	350,000	344,400	330,500	343,800	350,000
Number of Engines	4	1	4	6	1	1
Chamber Pressure, P_c (psi)	3,000	3,000	3,000	3,000	3,000	3,000
Engine Nodule Size, ϵ_M*	300	300	300	300	300	300
Nozzle Contour	MC_s	MSA	MC_s	MC_s	MSA	MSA
Expansion Ratio, (Retracted)	35	140	35		70	140
(Translated)	80	300	135	35	150	300
Mixture Ratio, r	5.00	5.85	5.82	5.48	6.5	6.8
Vacuum Specific Impulse, I_{vac} (sec)	456.4	468.5	461.0	443.5	457.5	463.8
Sea Level Specific Impulse, I_{sl} (sec)	395.2	—	387.5	403	—	—
Exit Diameter (in.)	79.2	151.0	101.5	52.1	107	151.0
Engine Length (in.) (Retracted)	114.1	133.5	169.5		98.6	133.5
(Translated)	170.0	250.0	219.0	116.5	173.5	250
Engine Mount Height, MH (in.)	78	78	60	60	102.5	60
Engine Mount Ring Radius, MR (in.)	100	—	120	88	—	—
Installation Weight, W_e (lb)	18,767	5903	19,684	26,231	4998	5515
Oxidizer Feed Lines (lb)	345	66	336	550	61	71
Fuel Feed Lines (lb)	360	64	398	530	194	71
Thrust Structure (lb)	1930	1730	2210	2720	860	1330
Heat Shield (lb)	780	—	1070	655	—	—
TVC System (lb)	1360	340	1360	2040	340	340
Pressurization System (lb)	152	28	150	236	28	28
Failure Detection System (lb)	220	55	220	330	55	55
Engine(s) (lb)	13,620	3620	13,940	19,170	3460	3620
Fairing Area, AF (ft^2)	696	—	698	1515	250	529
Interstage Area, A_i (ft^2)	—	1219	—	—	—	536

*The area ratio required for 350K vacuum thrust using one common set of preburner, turbopumps, and main chamber hardware.

SECTION VI
COOLING INVESTIGATION

A.	INTRODUCTION	123
B.	SUMMARY AND CONCLUSIONS	123
	1. Summary	123
	2. Conclusions	124
C.	Hardware Description	125
D.	Test Program and Test Results	149
	1. Introduction	149
	2. Combustion Performance	152
	3. Uncooled Testing	156
	4. Cooled Testing	161
	5. Two-Position Nozzle Testing	168
E.	HEAT TRANSFER STUDIES AND MATERIALS EVALUATION	172
	1. Introduction	172
	2. Grooved Wafer Analytical Heat Transfer Model	175
	3. Rigimesh Analytical Heat Transfer Model	185
	4. Material Evaluation	185
	5. Cooled Convergent Tests Sections	190
F.	TEST FACILITIES AND PROCEDURES	192
	1. X-28 Test Facility	192
	2. 50K Test Procedures	193

SECTION VI
COOLING INVESTIGATION

A. INTRODUCTION

(C) The objectives of the cooling investigation were to:

1. Determine the effects of main chamber geometry on performance
2. Investigate various cooling configurations and materials
3. Optimize the main chamber cooling
4. Determine the effect of cooling on performance
5. Demonstrate the feasibility of the two-position translating nozzle concept at the 20 and 100% thrust levels and obtain data that could be used in designing the nozzle for the full-scale hardware demonstration.

B. SUMMARY AND CONCLUSIONS

1. Summary

(C) Staged-combustion 50,000-lb thrust level hardware was designed incorporating the current technology and with features that allowed changing the chamber dimensions to accomplish the program objectives. Hardware fabricated included one cooled chamber, nine uncooled chamber graphite sets, one film-cooled copper chamber liner, one contraction ratio of three main injectors, and one two-position sheet metal nozzle skirt. The 50K preburner hardware and one main injector and chamber available from Contract AF 04(611)-10372 were also used.

(U) A total of 14 successful staged-combustion tests was conducted. Five of the tests were made with the uncooled chambers to evaluate the effects of chamber geometry on performance. Nine of the tests were made with a cooled copper wafer liner to optimize the main cooling flow at full chamber pressure and determine the effect of cooling on performance. The last three cooled tests were conducted to evaluate the two-position nozzle concept.

(C) The 50K two-position nozzle tests demonstrated that the concept can provide the desired flow stabilization over the 5:1 throttling range. These tests also provided design data on the nozzle loads that indicated the translating system could be a lightweight structure. The nozzle was satisfactorily extended and retracted during rig operation. Results indicated that the nozzle could be operated efficiently in the retracted position until the engine had achieved the 100% thrust condition, and then the secondary nozzle extended. The data also indicated this nozzle configuration is more efficient than a conventional bell nozzle at these lower operating pressures.

(C) Studies were conducted to evaluate various materials and configurations for possible use in an advanced cooled chamber. Hardware fabrication was started on one material variation of the present grooved wafer cooling concept and two material variations of a Rigimesh wafer cool configuration.

2. Conclusions

(C) The following conclusions resulted from the 50K cooling investigation:

1. High combustion performance (η_c^* = 98.7% at r = 5.8) was obtained with the 24-spraybar injector with a 13-inch, contraction ratio of 3, chamber. Use of this chamber geometry for the 250K hardware performance demonstration tests was substantiated.

2. Performance trends from the main chamber length tests indicate that the length may be reduced to 11 inches with a contraction ratio of 3 and the 24-spraybar injector without any measurable combustion performance penalties.

3. High efficiency was demonstrated with the optimized cooled main thrust chamber. Vacuum impulse efficiency (η_{Ivac}) was equal to 96.1% at an injector mixture ratio of 6.0 and 1.97% coolant flow.

4. Analysis indicated Rigimesh wafer cooling may provide cooling reductions up to 45% compared with the grooved copper wafers.

5. Analysis indicates grooved nickel wafers significantly reduced cooling requirements in the combustion chamber and divergent nozzle sections relative to copper. The higher strength and greater ductility of nickel promise weight reductions and longer cyclic life.

6. The cooling requirements may be reduced up to 85% compared with the grooved copper wafers by using refractory metals. Molybdenum or tungsten alloyed with rhenium appear to be feasible.

7. The copper wafer cooling flow requirements can be decreased up to 24% by plating with a nickel or a nickel base cermet thermal barrier. The thermal barrier evaluation test (50SC5), using a film-cooled copper liner, demonstrated excellent thermal shock characteristics and thermal barrier effectiveness. Additional effort is required to demonstrate that the platings are consistent with the cyclic life requirements.

THIS PAGE CONTAINS SUBJECT MATTER COVERED BY A SECRECY ORDER WITH A MODIFYING "SECURITY REQUIREMENTS PERMIT" ISSUED BY U S COMMISSIONER OF PATENTS.

C. HARDWARE DESCRIPTION

(C) The high chamber pressure 50K ground test staged-combustion thrust chamber configuration is shown in figure 77. The preburner, which is mounted upstream of the main injector, is run at a nominal mixture ratio of 1.2. The preburner combustion products (nominally 1800°R) are exhausted across the main injector where additional liquid oxygen is injected to increase the overall mixture ratio to a nominal 6.5. The additional oxygen reacts in the main chamber before the gases reach the nozzle throat. The main chamber hardware was designed for both cooled and uncooled tests. The cooled main chamber uses the copper wafer configuration extending from the injector through the throat to an exit area ratio of 4.0. For the uncooled thrust chamber tests, replaceable graphite parts are substituted for the cooled chamber copper wafers. An uncooled nozzle skirt extends from an area ratio of 4.0 to 90. The nozzle skirt is contoured for uniform parallel exit flow at an area ratio of 118 and is truncated to 90:1. The sheet metal nozzle skirt is film cooled by water during transients to and from test conditions.

(C) Two 50K preburner injectors existed from the previous High Chamber Pressure Staged-Combustion Research Program. One was a 320-concentric-element injector that was in good testable condition; the other was a 54-concentric-element injector with ribbon swirlers that required repair.

(C) The 320-concentric-element injector, which is shown in figure 78, has liquid oxygen injector elements with an inside diameter of 0.033 inch and an L/D ratio of 79. The liquid oxygen leaves the elements as small diameter solid streams. The fuel is injected through concentric annuli around each of the liquid oxygen injection elements. The injector faceplate is constructed of Rigimesh that permits passage of about 5% of total fuel flow for injector face cooling.

(C) The 54-element preburner injector, which is shown in figure 79, was repaired by fabricating a new center liquid oxygen injection element block with tangential slot swirler elements. A cross section of the injector is shown in figure 80. The injection element pattern is hexagonal with 54 concentric injection elements. The outermost elements on the hexagonal pattern are tapered on a 30-degree angle to avoid liquid oxygen impingement on the preburner chamber walls. The change from a ribbon swirler to a tangential entry liquid oxygen element was made to provide a better preburner temperature profile because of better mixing associated with the hollow liquid oxygen spray cone. The swirler element has a length-to-diameter ratio (L/D) of 19.8 and a slot width-to-orifice diameter (W/D) of 0.145, which gives an included spray cone angle of approximately 70 degrees.

CONFIDENTIAL

(This page is Unclassified)

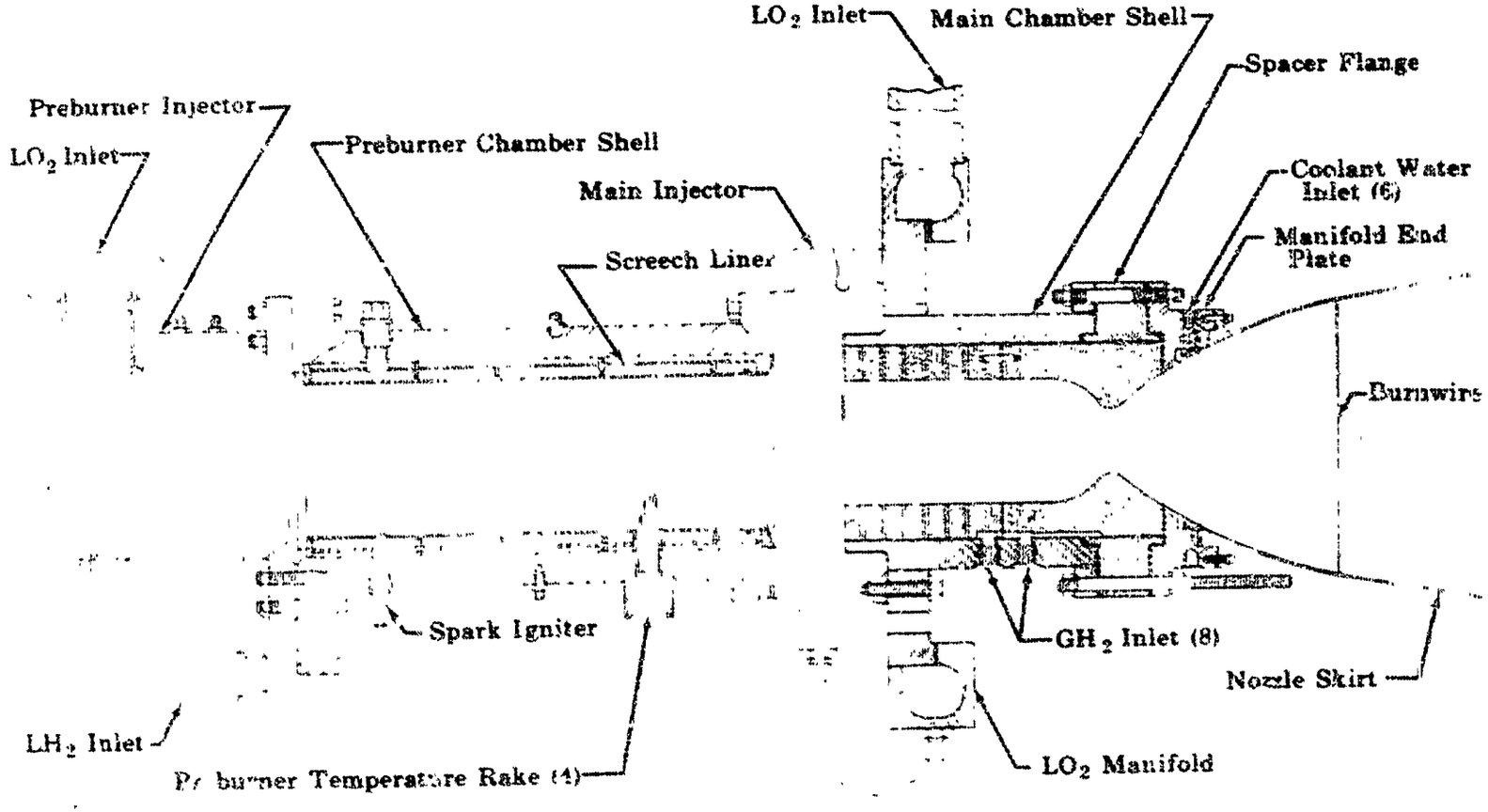


Figure 77. Ground Test Staged-Combustion Configuration

FD 19176

CONFIDENTIAL



CONFIDENTIAL

Figure 78. 320-Element Preburner Injector PE 49954

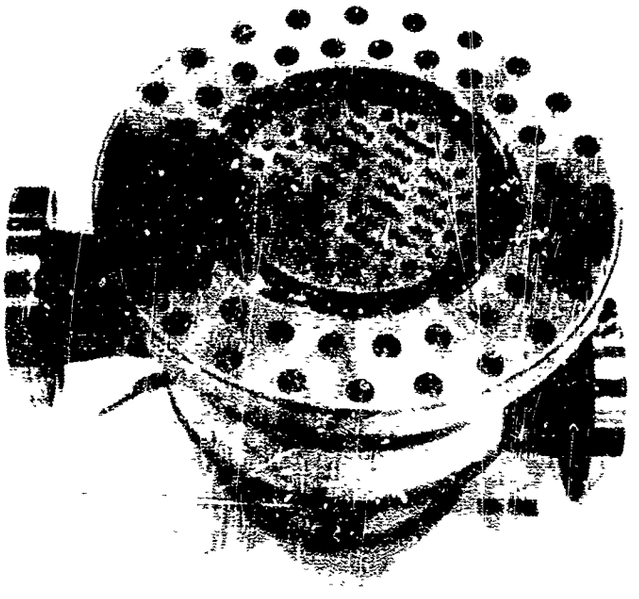


Figure 79. 54-Concentric-Element Preburner Injector Assembly PE 65468

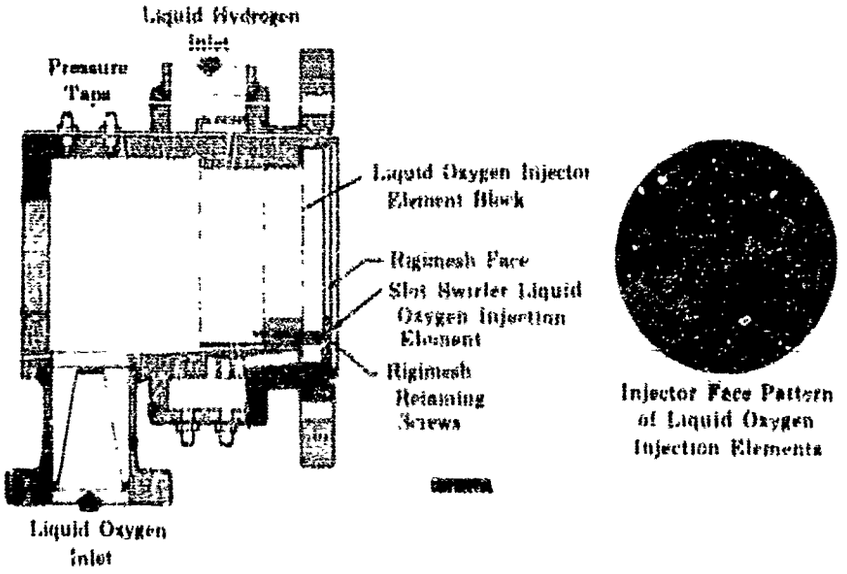


Figure 80. 50K Multiple Concentric Element Preburner Injector PD 16039

(U) Table XX presents a comparison of the principal injector characteristics for the two 50K preburner injectors tested during the High Chamber Pressure Staged-Combustion Research Program (AF 04(611)-10372), and the new 54-element tangential slot preburner injector.

(U) The preburner chamber shell and acoustic liner, shown in figure 81, which was used during the previous High Chamber Pressure Staged-Combustion Research Program (Contract AF 04(611)-10372), was used for all the 50K tests. Four preburner chamber thermocouple rakes were located 17 inches from the preburner injector face to determine the temperature profile. One temperature rake is shown in figure 82.

(C) The 20-spraybar main injector assembly that was tested during the previous High Chamber Pressure Staged-Combustion Research Program (Contract AF 04(611)-10372) was used for the initial 50K chamber test. This injector, which is shown in figure 83, has 20 separate internal liquid oxygen supply manifolds (spraybars) with the injector elements brazed into the spraybar bodies. Each of the 260 liquid oxygen injection elements has a twisted ribbon swirler that causes the liquid oxygen to be injected as full spray cones. A cross section of a spraybar is shown in figure 84. The fuel-rich preburner combustion gas is distributed around the liquid oxygen elements by a slot cut in the Rigimesh faceplate that mounts in front of the spraybar assembly. The Rigimesh faceplate is attached by screws that extend through to an injector support backplate. This injector was designed for use with a thrust chamber with a contraction ratio of 5. A cross section of the injector is shown in figure 85.

(C) Table XX. Preburner Injector Characteristics

Feature	54-Element Injector	New 54-Element Injector	320-Element Injector
Liquid Oxygen Elements	Twisted Ribbon Swirlers. Full Spray Cone	Tangential Slot Swirlers. Hollow Spray Cone	Nonswirl Solid Stream
Spray Cone Angle (Included)	60 degrees	70 degrees	None
Calculated Drop Size	225μ	175μ	900μ
Nominal Spacing Between Elements	0.750 in.	0.700 in.	0.300 in.
Bipropellant Flow	6.1%	6.5%	5.8%
Velocity Ratio	3.99	4.01	2.88
Momentum Ratio	3.75	3.75	2.72
Combustion Chamber Mixture Ratio Profile	0.90-1.10	0.90-1.08	0.88-1.08
Average Chamber Combustion Gas Velocity	141 ft/sec	141 ft/sec	141 ft/sec
Chamber Length	24.675 in.	24.675 in.	24.675 in.
Combustion Gas Stay Time	14.6 ms	14.6 ms	14.6 ms

CONFIDENTIAL

CONFIDENTIAL

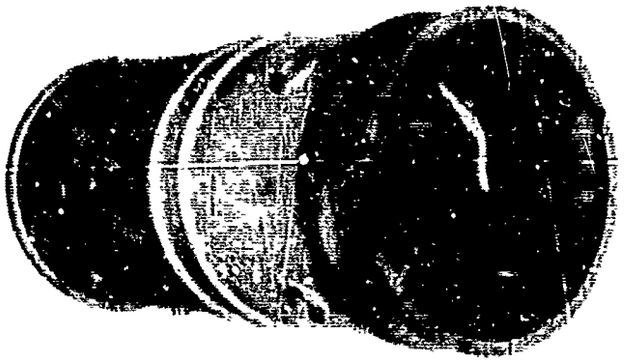


Figure 81. Preburner Chamber Acoustic Liner — FE 54245

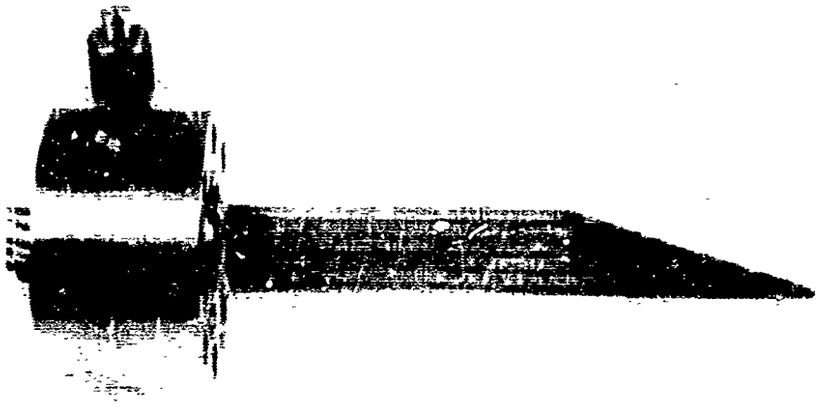


Figure 82. Preburner Chamber Thermocouple Rake — FE 43913

(This page is Unclassified)

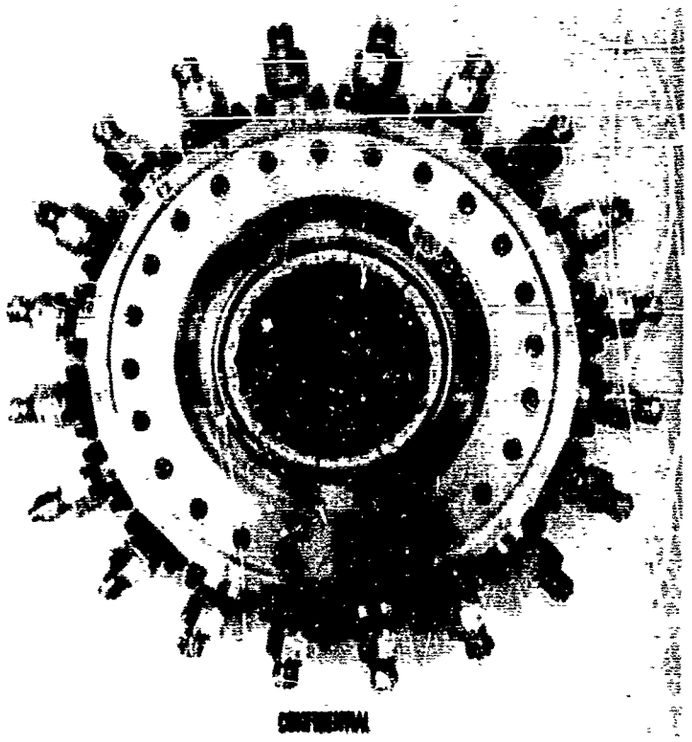


Figure 83. 50K, 20-Spraybar Main Injector FE 62235

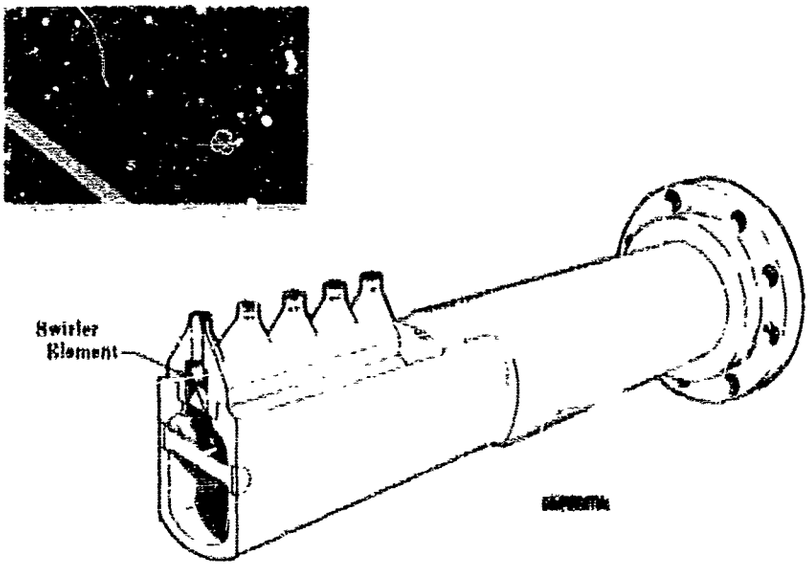


Figure 84. Swirler Spraybar and Rigimesh Faceplece FD 12147A

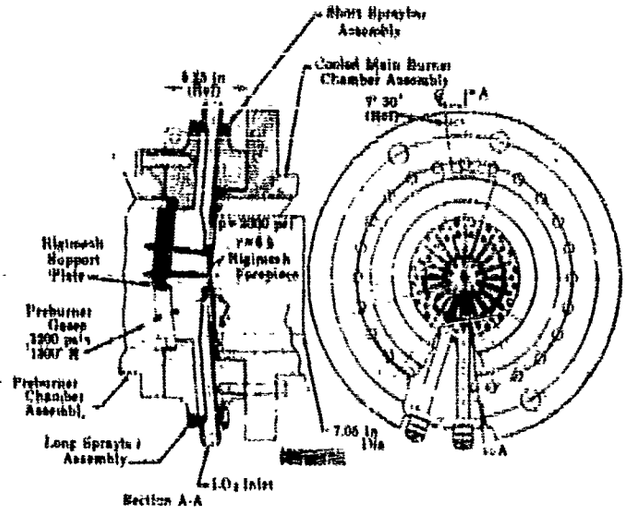


Figure 85. 50K Thrust Level 20-Spraybar Main Burner Injector Assembly FD 12125A

(C) A new 50K main spraybar injector, a cross section of which is shown in figure 86, was designed, fabricated, and tested. The spraybar injector configuration was chosen because the liquid oxygen carrying parts (spraybars) of the injector can be separated from each other, and from the Rigimesh faceplate, which operates in the environment of the hot preburner gases. This allows free different thermal expansion for long thermal cyclic life. Differential expansion has a minimum effect on propellant injection areas because the oxygen injection elements fit into radial slots on the Rigimesh faceplate, thus radial growth has a minimum effect on the position relationship of the elements to the Rigimesh slot. A maximum of 24 spraybars, which are machined as an integral part of the injector body, was dictated by mechanical and hot gas flow area considerations. This injector was designed to allow testing of thrust chambers with a contraction ratio of 3.

(C) The liquid oxygen injection elements are uniformly distributed along the spraybar. Spacing between elements was selected to provide hot gas injection completely surrounding each element and to create a uniform mixture ratio profile along the spraybar.

(C) Dual tangential slot swirler liquid oxygen injection elements, shown in figure 87, were used in the design. The tangential slot swirler element is a simple, one-piece mechanical arrangement that promises high reliability by eliminating the ribbon swirler and provides a hollow spray cone rather than a full cone. A hollow spray cone provides more reaction surface area. Each element has two sets of tangential slots that are independently supplied. The tangential entry forces the liquid oxygen to swirl inside the cylindrical element and provide a self-atomized, hollow spray cone.

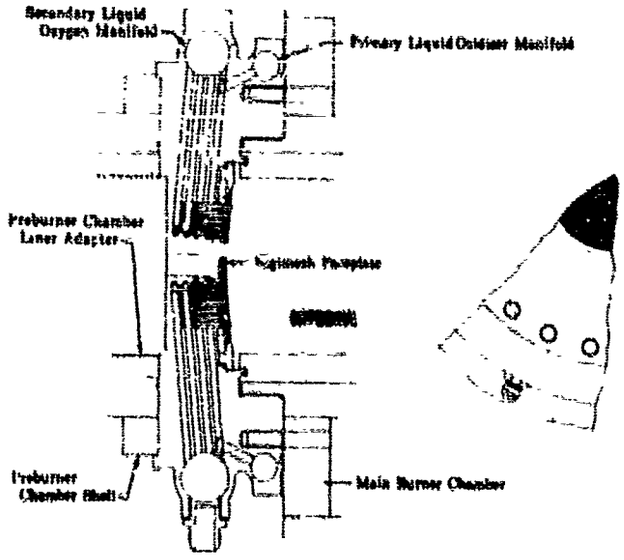


Figure 85. 24-Spraybar 50K Injector Schematic FD 15961

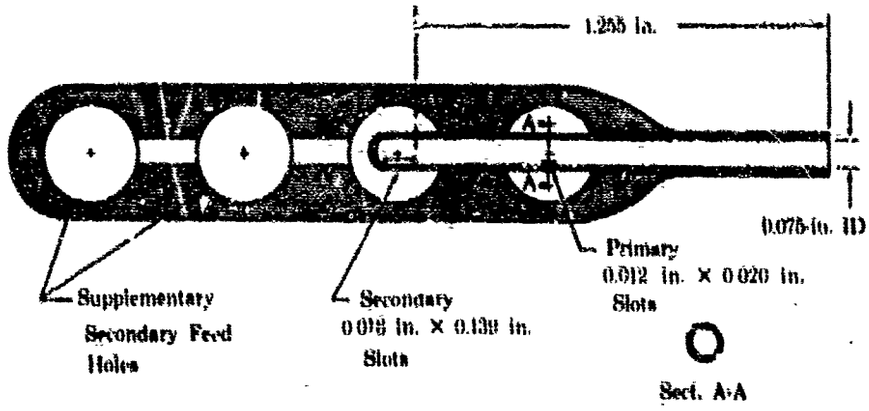


Figure 87. Dual Tangential Slot Swirler Element Configuration FD 16041

(C) The dual slot feature of the element allows large liquid oxygen flow excursions without the large differential pressures required for the same flow excursions with a single fixed area element. For example, a 100 to 1 pressure change is required for a 10 to 1 flow variation with a single orifice element. The primary slots are designed for a high pressure drop at low flows and thus, flow rate becomes insensitive to chamber pressure oscillations caused by normal combustion noise. As the secondary flow passes the primary slots, which operate at a higher pressure drop, there is a momentum interchange to provide good swirl atomization. A total of four liquid oxygen supply manifold holes are provided in each spraybar, one primary and three secondary.

(C) The fuel-rich preburner hot gas is distributed in the main injector around the rows of liquid oxygen injection elements (spraybars) by slots in the Rigimesh injector faceplate. (See figure 88.) Rigimesh was selected as the injector faceplate material because of its good strength and relatively uniform porosity, which provides a purge of fuel-rich preburner combustion products across the injector face. This flow prevents unburned oxygen in the recirculated main chamber combustion products from touching the injector face. The Rigimesh faceplate is welded to a support structure made of the same material. The Rigimesh support structure is designed to allow free radial expansion.

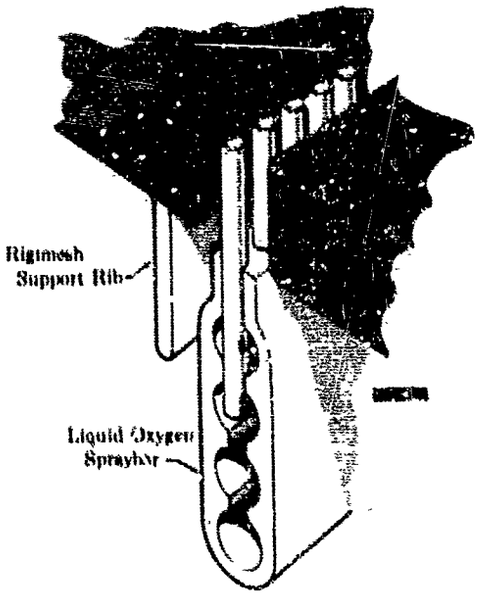


Figure 88. Tangential Entry Liquid Oxygen Injector Elements Shown in Rigimesh Injector Face Slot FD 15994

(C) The Rigimesh face fuel slots were tailored to give an improved mixture ratio profile. The purge flow through the Rigimesh was accounted for in the injector face mixture ratio. Concentric bands were drawn across the injector face (figure 89), and the average mixture ratio for each concentric band was calculated. The source of fuel flow for each band consisted of the purge flow through the Rigimesh plus the fuel flow through the fuel slot in the face. The oxygen flow consisted of the flow through the oxygen elements included in the width of the concentric ring. Because of the low fuel flow rate through the Rigimesh, the calculated mixture ratio variation from band to band was small, except at a diameter outside of the outermost oxygen element. The concentric band outside of the outermost element, being at a large radius, contained a large area and therefore a larger amount of Rigimesh fuel purge flow. To maintain a more uniform mixture ratio profile toward the outer diameter the fuel flow through the outer concentric band was assigned to the two outer oxygen elements in each spraybar. The fuel slot width at these two elements was made narrow

to balance the mixture ratio from the inside of the two outboard oxygen elements to the outside diameter of the Rigimesh. The fuel slot width calculated by this method was narrow at the outer two oxygen elements tapering to a uniform width as the slot approached the center of the faceplate.

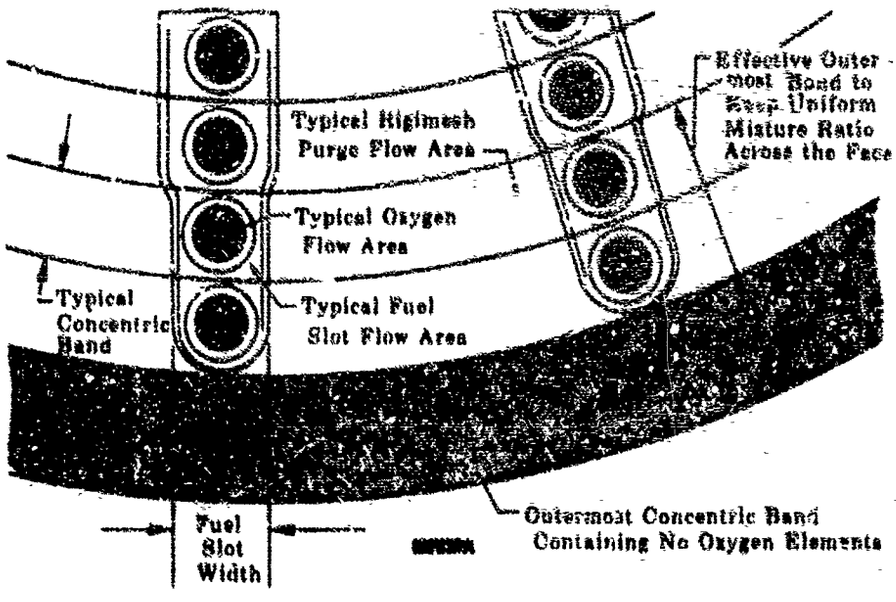


Figure 89. Tailored Fuel Slot FD 23364

(C) Table XXI presents a comparison of the principal injector characteristics for the two 50K main injectors tested previously during the High Chamber Pressure Staged-Combustion Research Program (AF 04(611)-10372), and the new 24-spraybar main injector. The injector faces of the two previously tested main injectors and the new injector face are shown in figure 90.

(C) The procedure used to braze the swirler elements into the main injector housing was developed by fabricating typical sections of a spraybar assembly. Successful braze joints were obtained with gold-nickel braze material in the form of sheet stock drilled to fit around the swirler elements. The use of drilled sheet stock allows accurate control of braze volume and good braze material distribution. The surface of the injector housing in the area near the swirler elements was flashed with nickel plating to assist braze flow toward the element.

(C) Table XXI. Injector Characteristics

Feature	20-Spraybar Injector	Multiconcentric Element Injector	New 24-Spraybar Injector
Liquid Oxygen Elements	250 elements Twisted Ribbon Swirlers Full Spray Cone	192 elements Twisted Ribbon Swirlers Full Spray Cone	272 elements Tangential Slot Swirlers Hollow Spray Cone
Spray Cone Angle (Included)	50 deg	45 deg	55 deg
Calculated Drop Size	180μ	300μ	130μ
Circumferential Spacing of Rows of Elements	0.9[illegible] in. max	0.78 in. max	0.60 in. max
Rigimesh Flow	20%	20%	10.4%
Velocity Ratio	4.65	4.25	5.54
Momentum Ratio	1.35	1.24	1.82
Injector Face Mixture Ratio Profile	3.5 to 8.2	5.4 to 7.1	5.4 to 6.9
Chamber Contraction Ratio	5	5	3
Average Chamber Combustion Gas Velocity	620 ft/sec	620 ft/sec	1030 ft/sec
Chamber Length	19.4 in.	19.4 in.	13.0 in.
Combustion Gas Stay Time	2.33 ms	2.33 ms	0.037 ms

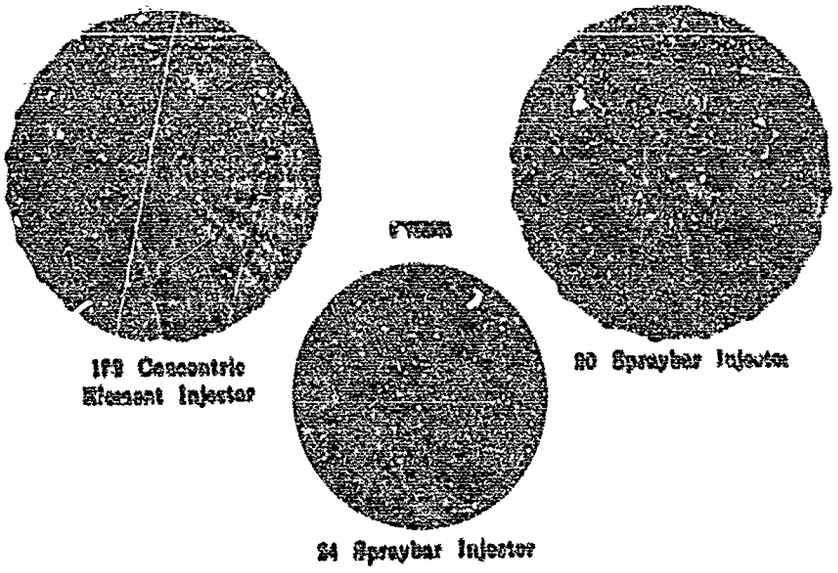


Figure 90. 50K Main Burner Injector Faces FD 16044A

(C) The uncooled main thrust chamber design, which is shown in figure 91, has replaceable graphite nozzle throat and chamber liner sections that permit the chamber length to be varied with a contraction ratio of either 3 or 5. The chamber length can be varied from 8 to 11 inches with one of the steel chamber shells and another shell permits variance from 12 to 14 inches as shown in figure 92. The third chamber is the nominal 18-inch chamber used during Contract AF 04(611)-10372.

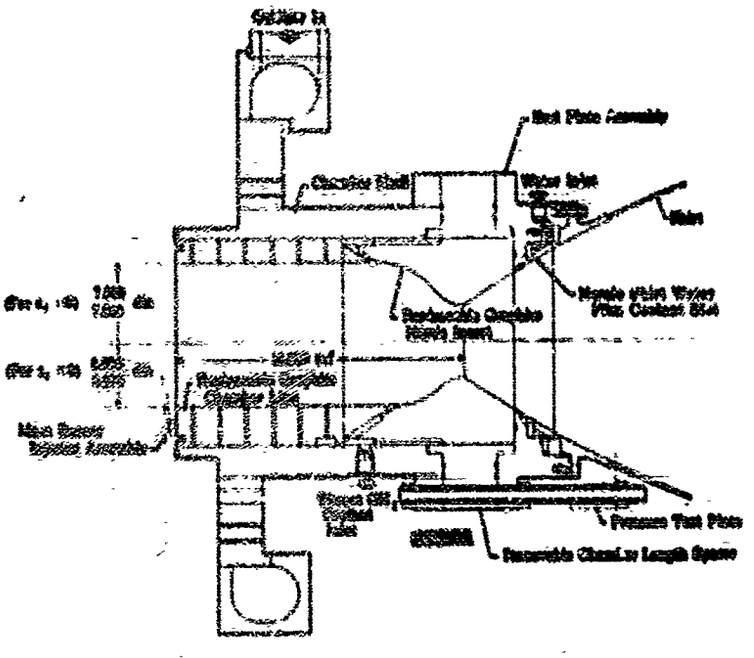


Figure 91. Uncooled Chamber, Variable Geometry Hardware FD 15959A

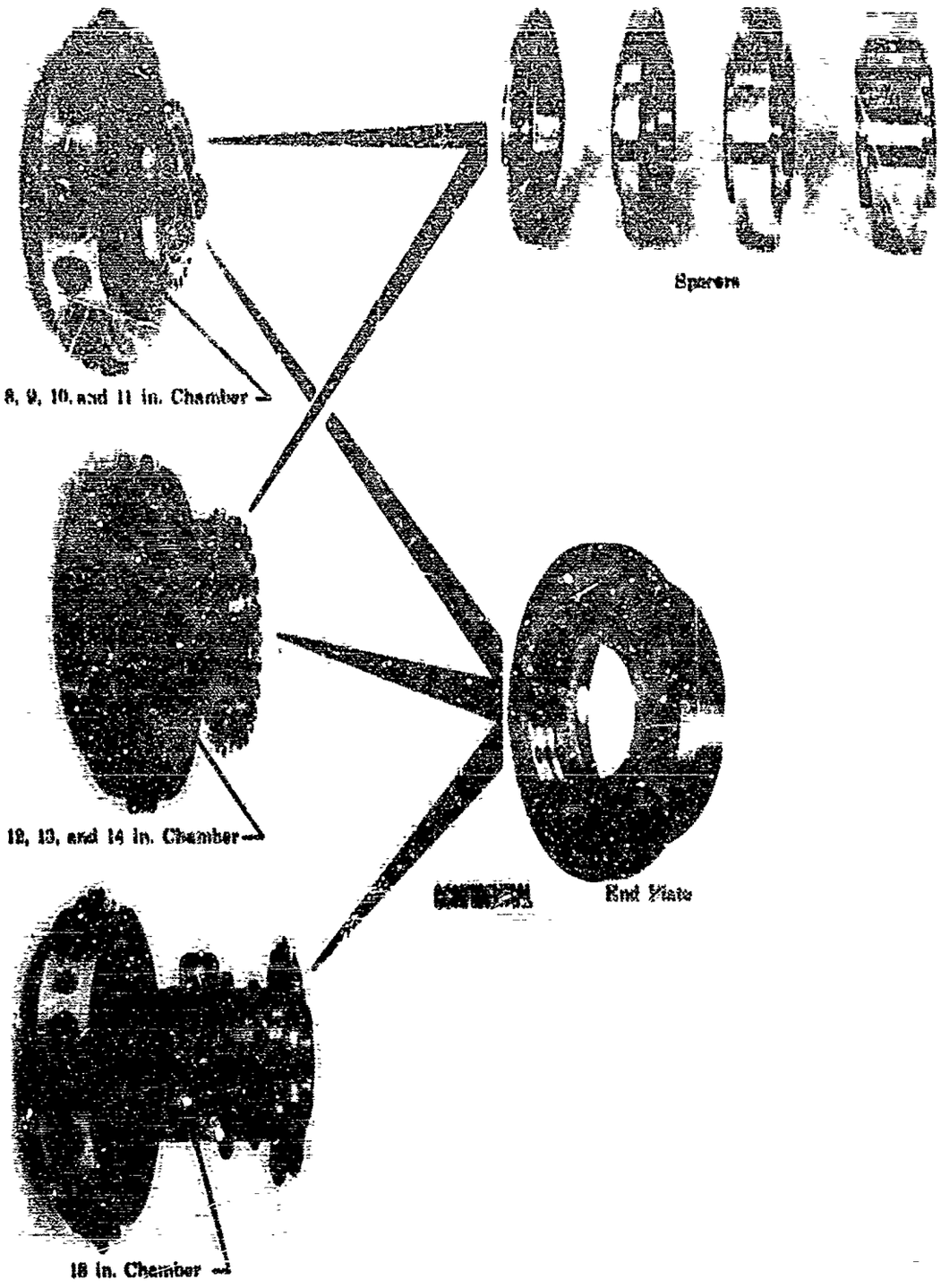


Figure 92. 50K Main Burner Variable Geometry Chambers and Associated Hardware FD 18103

(U) The graphite nozzle throat insert, which is shown in figure 93, had cooling passages that directed coolant (gaseous hydrogen) to the throat region to reduce nozzle erosion during the startup and shutdown periods. When test conditions were reached, the coolant was stopped for data acquisition. The reduction in nozzle throat area erosion allowed a more accurate characteristic velocity (c*) determination.

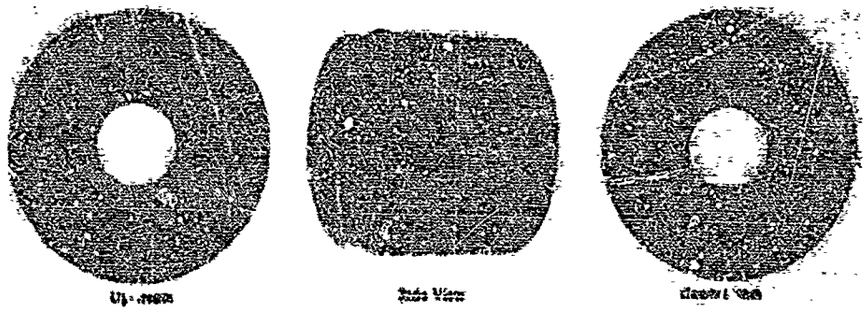


Figure 93. 50K Uncooled Chamber Nozzle Insert FD 18101

(U) The graphite chamber liner, which is shown in figure 94, had radial holes drilled through from the outside diameter to prevent over pressurization of the graphite.

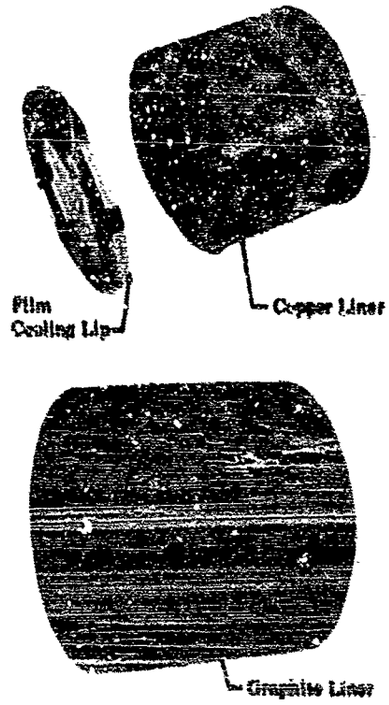


Figure 94. 50K Uncooled Chamber Liners FD 17963

(This page is Unclassified)

(C) A 50K film-cooled copper liner, which is shown in figure 94, was designed to evaluate injector patterns and tested with the new 24-spraybar main injector and 11-inch chamber with a contraction ratio of 3. The liner was electroplated with axial strips of potential thermal barrier and temperature indicating materials, as shown in figure 95. Five thermal barrier materials of 0.010-inch thickness and three very thin (0.0024-inch maximum thickness) surface temperature indicators were evaluated. Silver plate over nickel was selected because silver has a lower melting temperature than copper (2219°R compared to 2440°R). The nickel serves as a diffusion barrier between the silver and copper. Laboratory tests with 0.0002-inch thickness of gold plate on nickel indicated that diffusion of gold into nickel occurs very rapidly above 1950° and 2000°R. Disappearance of the gold would indicate that this temperature range was attained or exceeded during a test. The copper and silver plate over nickel would result in melting at the copper-silver eutectic temperature of 1897°R. Again the nickel is a diffusion barrier. A segment of the liner was not plated so it could be used as a reference.

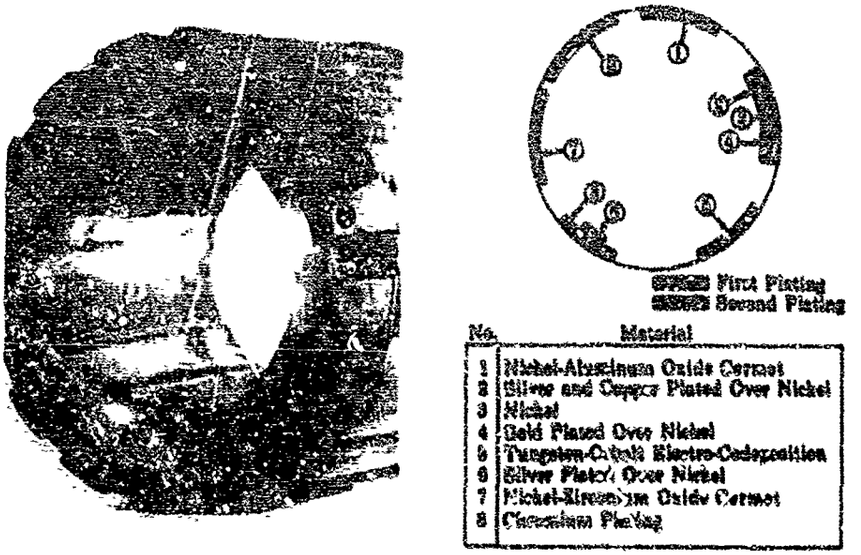


Figure 95. Main Chamber Uncooled Copper Liner FD 19168

(C) The 50K cooled thrust chamber, which is shown in figures 96 and 97, was designed with a contraction ratio of 3 and a 13-inch combustion chamber length; the geometry proposed for the full-scale demonstration chamber. This design was based on the grooved wafer cooling concept. The cooled chamber was divided into 23 coolant zones. Coolant flow from an exterior annular manifold was metered to each zone by four removable metering orifices. This flow enters a zone manifold and is then distributed to individual wafer manifolds passing through the spiral grooves into the combustion chamber.

THIS PAGE CONTAINS SUBJECT MATTER COVERED BY A SECRECY ORDER WITH A MODIFYING "SECRECY REQUIREMENTS PERMIT" ISSUED BY U.S. COMMISSIONER OF PATENTS

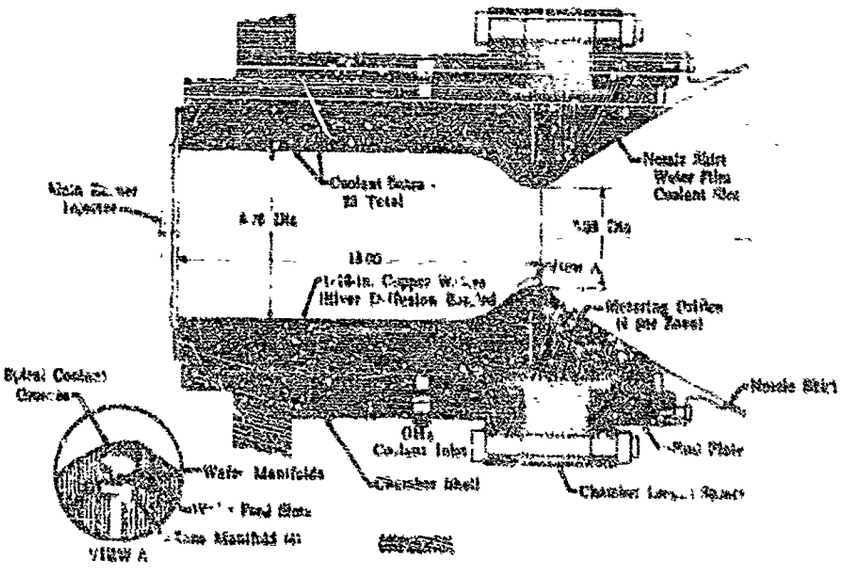


Figure 96. 50K Cooled Main Chamber Configuration FE 54588

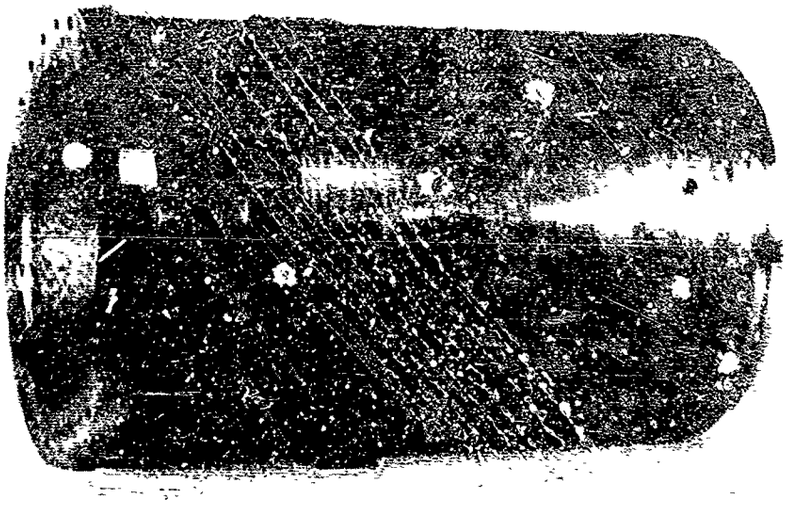


Figure 97. 50% Contraction Ratio of 3, Cooled Chamber FE 54588

(U) The grooved wafer cooling concept is illustrated in figure 98. A mathematical heat transfer model of the wafer cooled thrust chamber was developed to aid in analyzing the relative effects of various wafers and coolant groove geometries as explained in detail later in this section.

CONFIDENTIAL
THIS PAGE CONTAINS SUBJECT MATTER FURNISHED BY A CONTRACTOR UNDER A MODIFYING "SECURITY REQUIREMENTS PERMIT" ISSUED BY U.S. COMMISSIONER OF PATENTS.

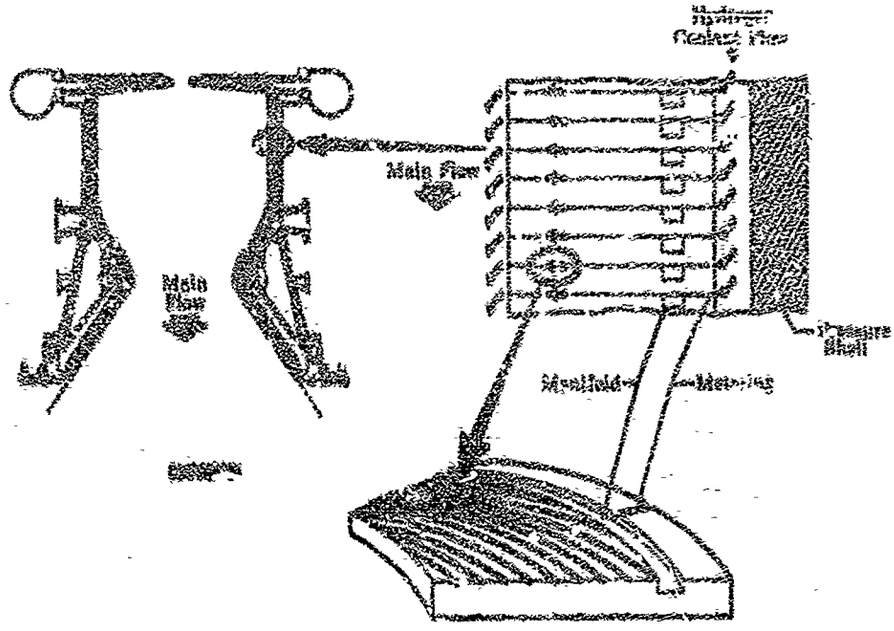


Figure 98. Wafer Cooling Concept F. 15958

(C) A typical wafer plate is shown in Figure 99. Increased coolant efficiency was attained compared to the configuration used for the previous 30K cooled thrust chamber tested under the High Chamber Pressure Staged-Combustion Research Program because of the following design changes:

1. Copper wafers 1/16-inch thick instead of 1/4- and 1/8-inch thicknesses (increased chamber porosity)

2. Change in spiral groove configuration from a 10-degree entrance angle, 0.014 by 0.014-inch groove to a 6-degree 0.010 by 0.010-inch design

3. Chamber geometry change. Less surface area as a result of a decrease in chamber length from 18 inches to 13 inches.

(C) A decrease in contraction ratio from 3.0 to 2.0 causes a slight increase in the theoretically required coolant flow for a given chamber length.

(C) The reduction of wafer thickness to 1/16 inch results in an increased porosity enabling the design to more closely approach pure transpiration cooling. An analysis of the 0.014 by 0.014-inch coolant groove pattern tested previously (AF 04(611)-70375) indicated that the heat transfer coefficient between the coolant and the copper wafer coolant grooves was one of the significant resistances controlling wafer wall heat exchanger efficiency. The copper thermal conductivity was so high that only slight material resistance was present. For the new chamber design, the wafer coolant groove size was reduced to 0.010 by 0.010 inch to increase the heat transfer coefficient between the coolant and the grooves by increasing

THIS PAGE CONTAINS CLASSIFIED MATTER GOVERNED BY A SECRECY ORDER ISSUED BY U.S. COMMISSIONER OF PATENTS.

the Reynolds number. The number of coolant grooves per plate was kept as high as mechanically practical to maximize porosity. Eighty-seven grooves per plate were used in the chamber and fifty per plate in the nozzle section. The lower number in the nozzle is necessary to maintain a minimum land thickness between the grooves on the inside diameter for brazo bonding the plates.

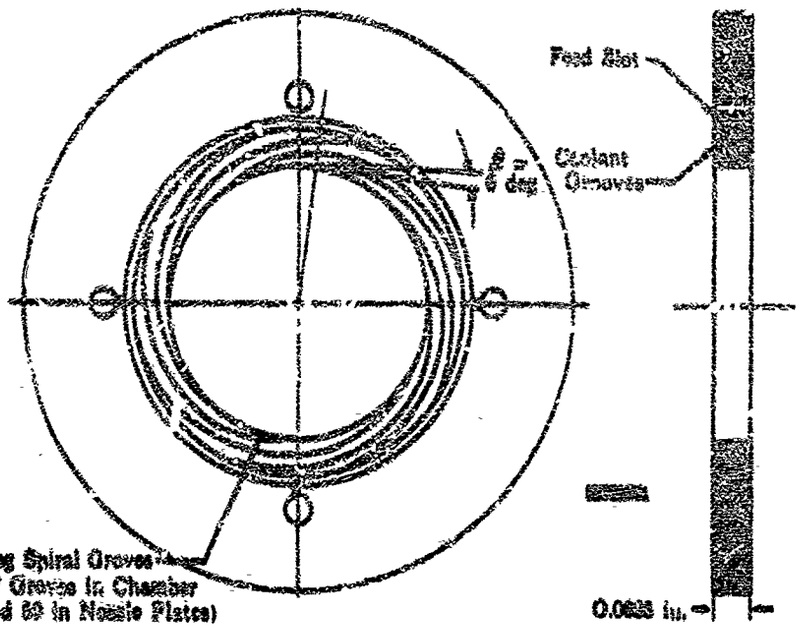


Figure 99. 50K Cooled Wafer Geometry ED 16046

(C) The coolant grooves are etched into both surfaces of each individual wafer plate and form a logarithmic spiral pattern. The grooves form a constant angle with the perpendicular to a radius at any point along the spiral path. An angle of 6 degrees was selected to keep the coolant wall injector angle as shallow as practical, thereby providing a maximum film and a reduced wall heat flux. A shallow coolant groove angle also increases the coolant groove internal surface area in the hottest regions of the wafer. The groove pattern radial width of the wafer was varied to maintain a desired allowable wafer back side wall temperature for the varying heat fluxes throughout the engine.

(C) Copper wafers for the cooled thrust chamber have their groove patterns photoengraved. The process was expedited by photoengraving four plates simultaneously on one sheet of copper. The plates were then finished in detail except for the inside diameter, outside diameter, and coolant metering orifice holes. The bonding surfaces were plated with a 0.0003-inch thickness of silver and the entire assembly joined together by silver-copper eutectic diffusion bonding. A smooth inside contour was obtained by machining the inside diameter in assembly. The outside diameter was machined and the coolant metering orifice locations drilled. After machining, the inside diameter was deburred chemically in a hydrofluoric and nitric acid solution. The assembly was then GOx flowed to verify the absence of flow restrictions and for zone calibration.

THIS PAGE CONTAINS RIGHTS MATERIAL FURNISHED TO A RECIPIENT UNDER A NASA-SPONSORED "GOVERNMENT PURPOSE LICENSE" ISSUED BY U.S. GOVERNMENT PATENTS.

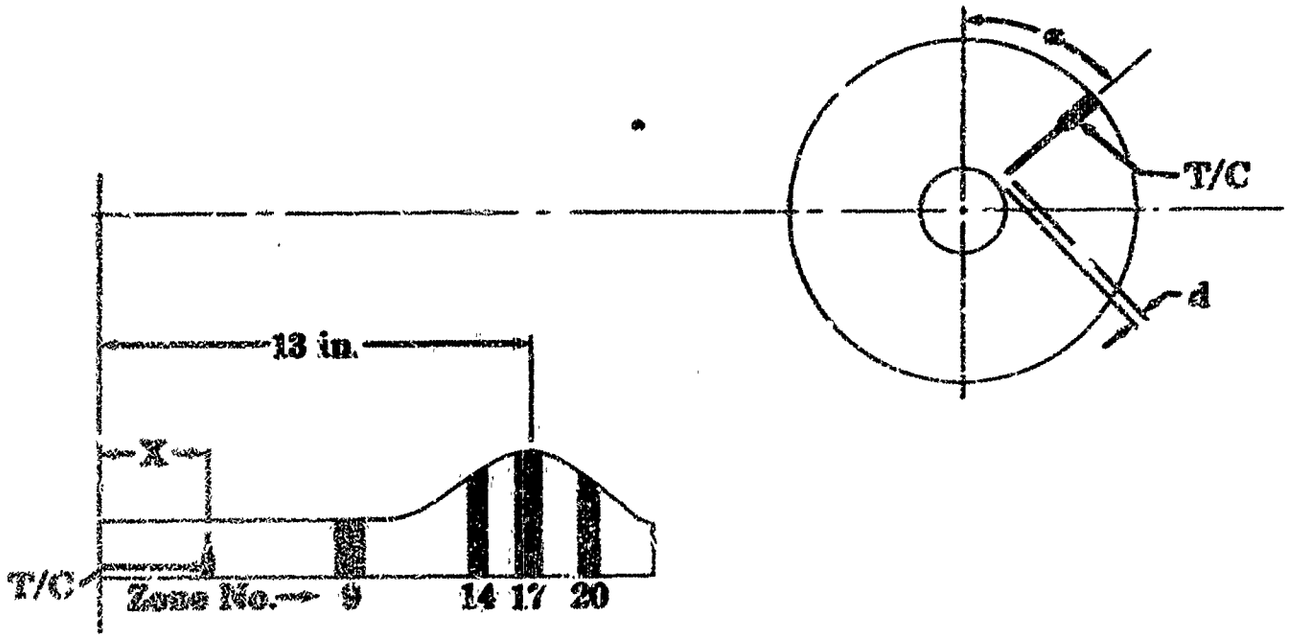
(C) The coolant chamber distribution was controlled by four sharp-edged orifices in each of 23 zones. Sharp-edged orifices were used to precisely meter flow to each zone. The cooled chamber wafer assembly was designed to use the same outer steel chamber walls as for the uncooled tests replacing the graphite parts.

(C) The 50K cooled main chamber was instrumented as shown in figure 100. The thermocouples were radial-entry, 0.010-inch diameter, swaged thermocouple wire in the measurement area spliced to 1/16-inch leadout wires. The small size was desired in the measurement area to minimize the heat flow field disturbance; a larger size is required external to the wafer assembly because of handling and connector considerations. Holes were drilled in the chamber spacer flange and sealed with 1/16-inch swagelocks for the thermocouple wires. The chamber test side wall was electroplated with axial strips of very thin (0.0024-inch total maximum thickness) surface temperature indicators that will melt or change color at known temperatures. Each strip corresponds to a typical sector of the 24-spraybar injector as illustrated in figure 101.

(U) The pressure drop was measured across metering orifices in several of the coolant distribution zones. This allows the exact flow rate to be determined for these zones and verifies the flow rate analysis for all the zones. The downstream orifice pressure was measured by using a hole drilled axially through the assembly from the nozzle side.

(C) The existing nozzle skirts, shown in figure 102, with an area ratio of 118 truncated to 90 were used with the cooled and uncooled chambers. The sheet metal skirts are film cooled by water during accelerations to and from test conditions. The nozzle skirt cooling water is turned off while taking performance data. The nozzle skirts had the inside contour plasma sprayed with refractory material to reduce the skirt temperature and resultant warpage. Each skirt had two rings attached to the outside diameter. These rings prevented the skirt from collapsing during a test and also allowed the skirt to expand freely when hot.

(C) The design of the translating nozzles for the 50K test program was based on the requirement for providing a 250K nozzle configuration that would operate stably over the 5 to 1 throttling range. The conventional bell nozzle design would separate at the off-design operation and cause severe side loading in the nozzle. To eliminate the side loading, stabilization of the primary flow stream over the 5 to 1 throttling range was required. Early tests were conducted on scaled models to establish a configuration that would provide the desired flow stabilization. In a series of cold flows and hot flow tests, it was established that a ventilated nozzle, which introduces secondary airflow at a low area ratio, would allow stable operation over the 5 to 1 throttling range. The secondary airflow was obtained by separating a bell nozzle into a front and rear section and translating the rear section of the nozzle forward (toward the throat) thus creating an opening through which air could pass. The 50K nozzle hardware was designed to further check this nozzle configuration at conditions that closely simulated 250K staged-combustion operation and provide the design data that could be used in the 250K nozzle design.

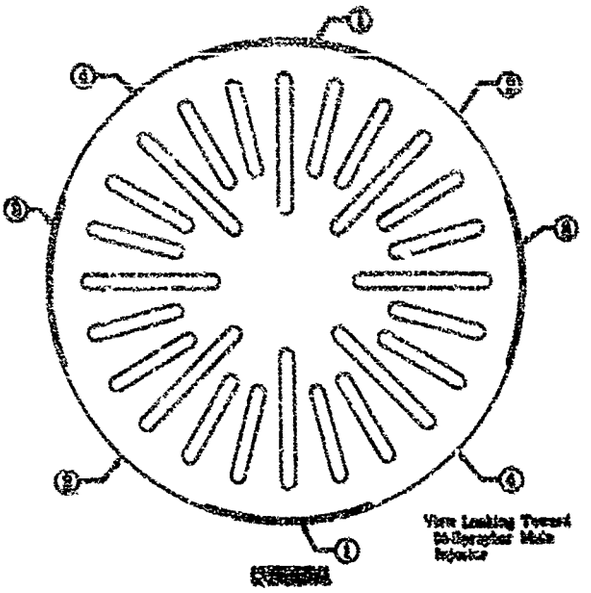


T/C No.	X (inches)	θ (degrees)	Distance From Inj. Face Datum Plane (inches)

P_c No.	Zone	Section	Remarks
1	5	Combustion Chamber	Pressure Measurements Immediately Downstream of Impinging Orifice
2	11	Convergent Nozzle	
3	14	Throat	
4	20	Divergent Nozzle	

Figure 100. 50K Cooled Chamber Temperature and Pressure Locations

ED 19040



	INDICATOR	TEMPERATURE (°R)
①	Copper and Silver on Nickel	1987
③	Gold on Nickel	890 - 950
②	Silver on Nickel	1210
④	Copper (no plating)	1440

Figure 101. Surface Temperature Plating Indications for 50K Cooled Chamber

PD 19061



Figure 102. 50K, Area Ratio 90, Uncooled Nozzle Skirt

PE 5992R

(C) A maximum payload contour 50K nozzle was fabricated, which had a 60:1 area ratio, with a primary nozzle that attached to the transpiration-cooled chamber at an area ratio of 5 and extended to an area ratio of 20. The translating secondary nozzle started at an area ratio of 20 and extended to an area ratio of 60. To expedite the procurement and reduce the cost of the program, these nozzles were fabricated from sheet metal with a zirconium oxide coating. A water manifold at the area ratio of 5 and 20 provided water film cooling during transients to the data point as shown in figures 103 and 104.

(U) A translating system was provided to drive the nozzle open and closed during test operation. The translation was accomplished by driving a ring gear from which four synchronized jackscrews translated the secondary nozzle, as shown in figure 105. The translating system in this configuration was a preliminary design to expedite procurement. In each jackscrew, an instrumented spool was incorporated as shown in figure 106 to permit measuring the loads in the nozzle during all phases of rig operation.

(U) Heat transfer and material studies were conducted to investigate advanced cooling concepts and alternative materials. Promising concepts and materials were selected for testing.

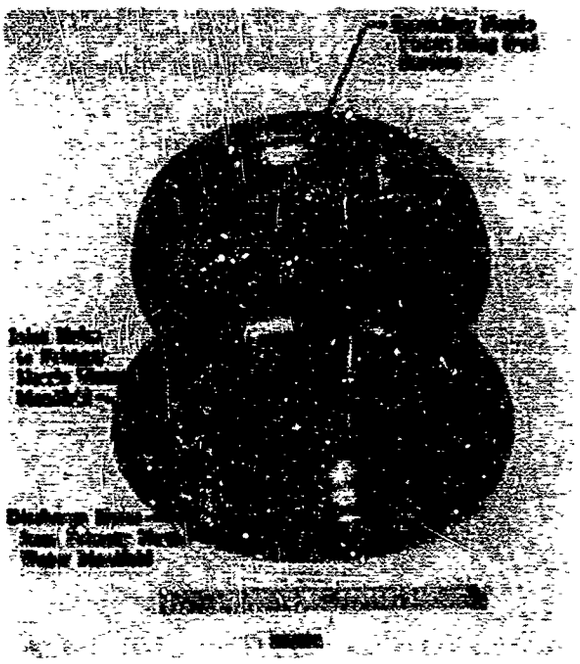


Figure 103. Primary Nozzle With Area Ratio of 4.75 to 20 Showing Cooling Water Holes

FD 19243

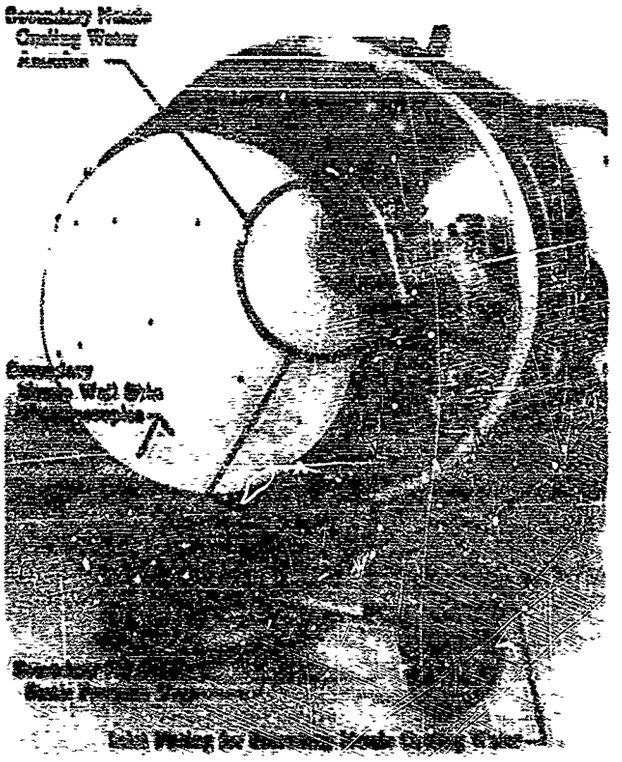


Figure 104. 50K Translatable Nozzle in Closed Position Mounted in Assembly and Transportation Fixture

FD 19244

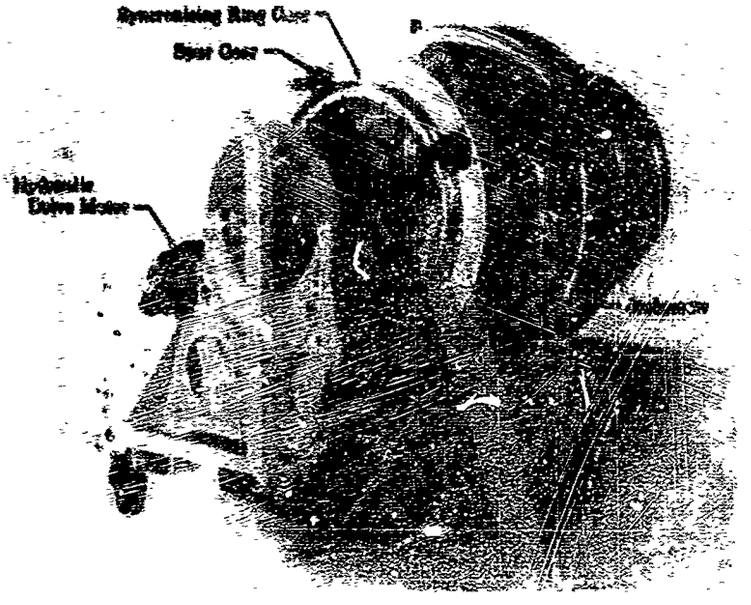


Figure 105. 50K Translatable Nozzle in Open Position Mounted in Assembly and Transportation Fixture

FD 19239

(This page is Unclassified)

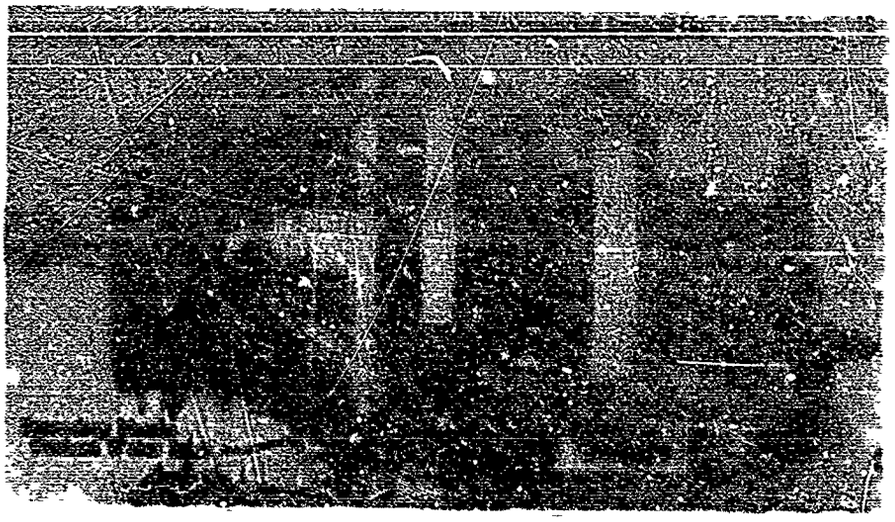


Figure 106. 50K Translatable Nozzle in Open Position Mounted in Assembly and Transportation Fixture — FD 19241

D. TEST PROGRAM AND TEST RESULTS

1. Introduction

(U) Testing of 50,000-lb thrust uncooled and cooled staged-combustion hardware was conducted on the B-2B pressure-fed test facility to determine the following:

1. Influence of chamber dimensions on performance
2. High pressure cooling limits
3. Effects of cooling on performance.

(C) The tests were performed over the injector mixture ratio range from 5.0 to 7.5. The staged-combustion test configuration is shown in figure 77.

(U) Uncooled tests with a graphite liner and nozzle throat section were required to determine chamber geometry effects on performance, because the data would be impaired by the coolant and its associated performance losses.

(C) The existing 20-spraybar main injector and 18-inch combustion chamber hardware with a contraction ratio of 5 was tested initially to re-establish test procedures and provide baseline performance. Tests were then conducted with the new 24-spraybar injector and the new 13-inch combustion chamber with a contraction ratio of 3, which was the chamber geometry proposed for the full-scale main chamber. Additional tests of the new injector and contraction ratio of 3 chamber were conducted at 8- and 11-inch chamber lengths. All tests were performed at a nominal injector mixture ratio of 6.0.

(C) A total of five completely successful uncooled staged-combustion tests was conducted. High performance was obtained with the 24-sprayber injector and a 13-inch chamber with a contraction ratio of 3 and use of this chamber geometry and injection design for the full-scale hardware performance demonstration tests was verified. Characteristic velocity efficiency (η_{c^*}) was 93.7% at an injector mixture ratio of 5.8. Performance trends with chamber length, which are shown in figure 107, indicate that the length may be reduced to 11 inches without any measurable performance penalties.

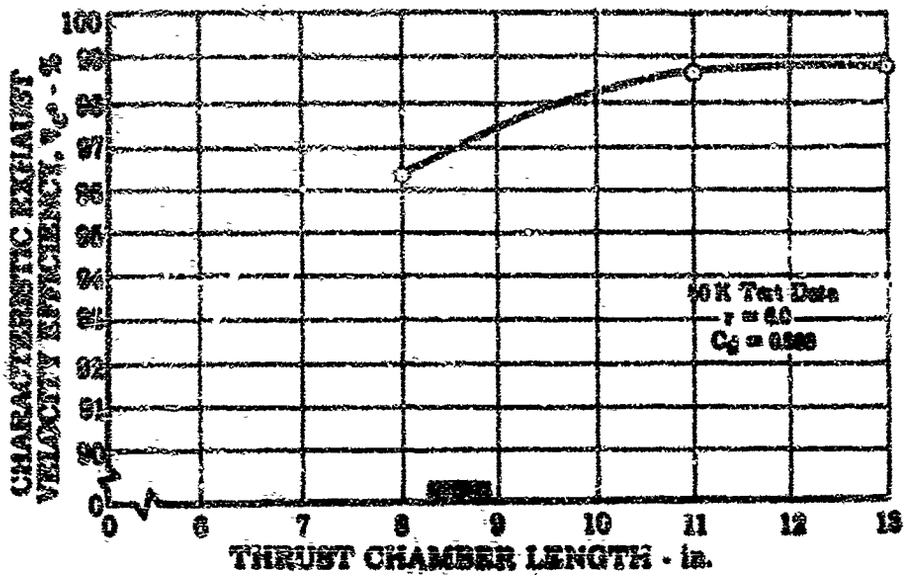
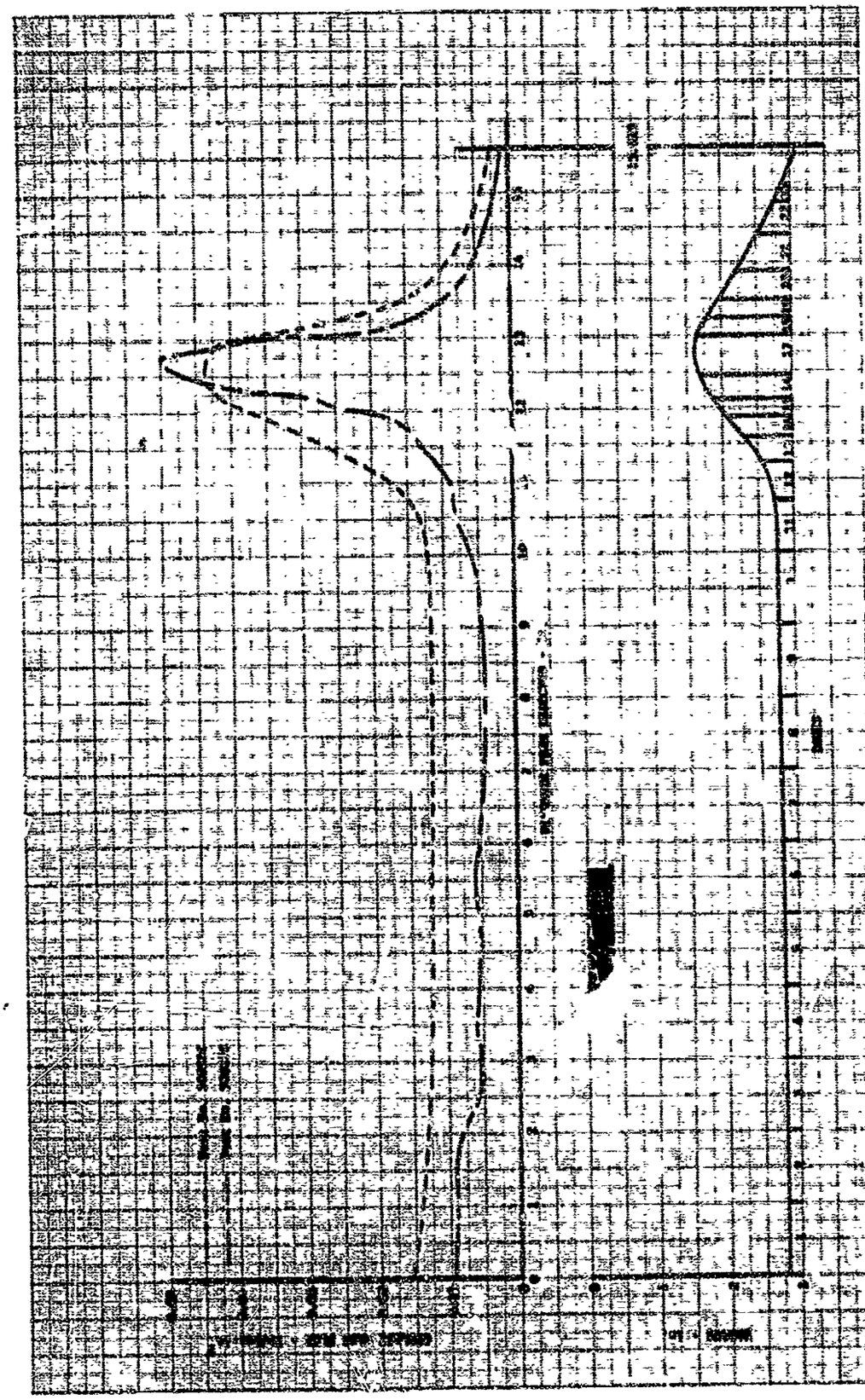


Figure 107. Effect of Chamber Length on Combustion Performance

FD 21114A

(C) The new cooled chamber with the proposed full-scale chamber geometry (13-inch chamber length and contraction ratio of 3) was tested to produce a coolant distribution that provides a uniform surface wall temperature of 1800° to 1900°R throughout the entire chamber and to determine the effects of cooling on performance. Coolant reductions were determined by indications of temperature sensitive plates on the inside diameter surface and surface temperature - coolant flow trends predicted by the analytical heat transfer model. A total of nine completely successful cooled tests was conducted; the last three were conducted to evaluate the two-position nozzle concept. A vacuum impulse efficiency (ηI_{vac}) of 96.1% was demonstrated at an injector mixture ratio of 6.6 with a coolant to total propellant flow rate ($\dot{w}_c/\dot{w}_p$) of 1.97%. Starting and optimized coolant mass flux distributions are shown in figure 108.



DF 59504

Figure 103. Starting and Optimized Coolant Mass Flux

(C) The 50K two-position nozzle tests demonstrated that the concept can provide the desired flow stabilization over the 5:1 throttling range. Test data also showed that nozzle side loads were low (less than 300 lbf), which indicated that the 250K translating mechanism could be designed as a lightweight structure. The nozzle was satisfactorily translated closed and open during rig operation. Results indicated that the nozzle could be operated efficiently in the open position until the engine had achieved the 100% thrust condition, and then the secondary nozzle closed. The data also indicated that at these lower operating pressures, this nozzle configuration is more efficient than a conventional bell nozzle as shown in figure 109.

(C) Vibration levels were low and the condition of all parts remained good.

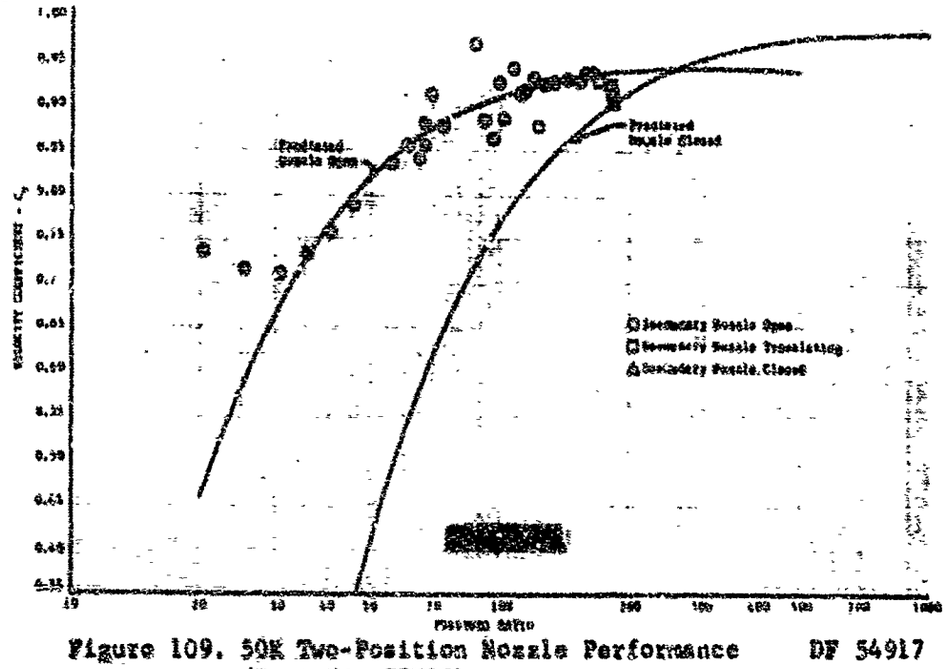


Figure 109. 50K Two-Position Nozzle Performance (Test No. 50M3C) DF 54917

2. Combustion Performance

(U) Summaries of measured and calculated performance test data for the 50K staged-combustion tests are shown in tables XXII and XXIII. Performance is compared to theoretical one-dimensional isentropic equilibrium values as shown in figure 110. The characteristic velocity efficiency values apply to the propellant passing through the chamber throat; however, the vacuum impulse and vacuum thrust coefficient efficiencies are based on all the propellant flow passing through the engine. For uncooled tests, all propellant passes through the chamber throat; and during cooled chamber tests, some of the transpiration coolant is injected downstream of the throat. These data are shown both uncorrected and corrected for nitrogen contamination, aerodynamic throat area, nozzle heat loss, and chamber heat loss of the uncooled chamber tests.

(C) Table XXII. Summary of Measured Data for the 50K Staged-Combustion Test Series

Test Number	Date	Test Duration, sec	Propellant Identification Fuel - Ox. - Solid Ox.	Ambient Pressure, psia	Calculated Thrust, lb_f	Total Oxidizer Flow, pps	Fuel Flow, pps	Coolant Flow, cps	Nitrogen Chamber Purge/Post-Test Purge	Oxidizer Temperature at Flowmeter, °R	Oxidizer Temperature at Preburner Manifold, °R	Oxidizer Temperature at Main Burner Manifold, °R	Fuel Temperature at Flowmeter, °R
Uncooled Tests													
50KU1	12-21-66	0.9	28784-3	14.64	31,913	127.2	1111.1	---	5A[1]/5A	163.7	192	504	54.9
50KU2	12-20-66	1.0	28784-3	14.[illegible]	33,743	571.0	2091.0	---	0A/1.25	168.0	185	164[2]	52.9
50KU3	12-20-66	1.3	28645-1	14.68	37,630	144.8	1258.1	---	2 PS/2.25	165.9	174	182[2]	55.9
50KU4	12-29-66	1.4	28645-1	14.70	38,578	252.6	1282.1	---	0.25/0A	166.6	178	149	53.6
50KU5[3]	1-3-67	1.0	29443-1	14.69	33,585	116.7	1176.7	73.5	1.5A/2.5?	170.3	152	152[2]	54.9
Cooled Tests													
50KC1	1-6-67	2.2	29444-1	14.82	27,845	661.6	1199.1	185.5	1 PS/1.5?	171.2	184	183[2]	61.6
50KC2	1-10-67								Data Not Available				
50KC3	1-10-67	2.0	29441-1	14.78	29,825	338.7	1282.9	154.2	0A/0A	170.3	182	193[2]	59.2
50KC4	1-23-67	2.3	32449-1	14.85	25,715	532.2	1138.9	139.1	0.5A/0A	169.9	184[2]	163[2]	55.4
50KC5	1-13-67	1.9	32449-1	14.79	32,360	565.4	1447.2	148.6	0.5A/0A	168.6	182[2]	183[2]	53.3
50KC6	1-13-67	2.0	32449-1	14.75	35,360	588.9	1651.7	121.5	0.2?A/0A	169.1	181[2]	183[2]	54.7
50KC7	1-13-67	2.0	32449-1	14.74	38,350	588.7	1838.2	94.2	1.4?/2.5?	169.8	180[2]	182[2]	54.2
50KC8[4]	1-20-67	2.2	32449-2	14.85	(5)	634.3	1672.6	130.4	0.3?/1.5?	171.0	193[2]	184[2]	54.4
50KC9[4]	1-21-67	2.0	32449-2	14.76	26,980	660.5	1278.3	143.8	0.5?/1.5?	172.6	182[2]	184[2]	59.3
50KC10[4]	1-21-67	1.9	32449-2	14.84	32,980	638.5	962.2	145.6	0.5?A	171.4	183[2]	184[2]	59.3

Test Number	Fuel Temperature at Preburner Manifold, °R	Coolant Temperature at Flowmeter, °R	Oxidizer Pressure at Flowmeter, psia	Oxidizer Pressure at Preburner Manifold, psia	Oxidizer Pressure at Main Burner Manifold, psia	Fuel Pressure at Flowmeter, psia	Fuel Pressure at Preburner Manifold, psia	Coolant Manifold Pressure, psia	Main Burner Chamber Static Pressure, Injector Fuel, psia	Preburner Injector Oxidizer ΔP, psia	Main Burner Injector Oxidizer ΔP, psia	Preburner Injector Fuel ΔP, psia	Main Burner Injector Fuel Cav ΔP, psia	Coolant Flowrate, lb/in^2	Fuel Flowrate, lb/in^2
Uncooled Tests															
50KU1	72.9	---	4363	3891	3449	4313	3895		----/1725	115	422	119	299	0.126	2.348
50KU2	71.7	---	4619	3839	3755	4355	3969		----/1920	114	535	143	338	0.233	0.126
50KU3	68.8	---	4560	3434	2989	4335	3980		3969/3825	124	572	208	146	0.24	0.160
50KU4	71.2	---	4475	3229	3005	4291	3960		3940/3960	130	504	172	214	0.[illegible]	0.2 [illegible]
50KU5[3]	71.2	537	4343	3263	3179	4440	4389		3969/3969	127	455	135	274	0.[illegible]	0.[illegible]
Cooled Tests															
50KC1	72.9	527	4502	3791	2963	4265	3959	3889	3959/3959	108	379	103	251	0.[illegible]	0.[illegible]
50KC2															
50KC3	72.5	549	4483	3918	2930	4393	3939	4089	3959/3825	117	554	121	243	0.[illegible]	0.[illegible]
50KC4	68.9	529	4469	3791	3063	4325	3969	3969	3939/3969	115	512	191	198	0.[illegible]	0.[illegible]
50KC5	72.9	531	4535	3844	3988	4325	3969	4025	3969/3969	98	1,000	131	300	0.[illegible]	0.[illegible]
50KC6	72.9	534	4595	3825	3925	4389	3985	3969	3959/3959	98	1000	135	185	0.[illegible]	0.[illegible]
50KC7	73.0	537	4577	3969	4063	4389	3969	3969	3825/3825	169	963	194	284	0.[illegible]	0.[illegible]
50KC8[4]	Na	543	4459	3919	3825	4389	3969	3825	----/3969	122	540	160	234	0.[illegible]	0.[illegible]
50KC9[4]	Na	534	4469	3919	3739	4395	3969	NA	----/3969	165	617	148	198	0.[illegible]	0.[illegible]
50KC10[4]	Na	519	4435	3946	3900	4389	3969	NA	----/3969	130	735	158	199	0.[illegible]	0.[illegible]

Notes:

(1) Coolant was completely shut off during this period. Remainder copper blend burned.

(2) Data are available; assumed to be value desired.

(3) Na - Data not available.

(4) Preliminary results given.

(5) Gas valve ran at 0.5% coolant flow to remain.

(c) Table XXIII. Summary of Calculated Performance for the 50K Staged-Combustion Test Series

Test Number	Date	Test Duration, sec	Oxidizer Manifold Pressure, psia	Fuel Temperature, °F	Chamber Pressure, psia	Specific Gravity,	C^*_{act} (1) (ft/sec)	C^*_{ideal} (ft/sec)	I_{sp} (Vacuum), sec	$C_{F_{act}}$ (Vacuum),	$I_{sp_{act}}$ (Sea Level),	η_{C^*} (Efficiency), %	$\eta_{I_{sp}}$ (Efficiency), %	η_{C_F} (Efficiency), %
Uncooled Runs														
Cooled Runs														

Test Number	Total Mfg Flow Rate, lb/sec	Fuel Flow Rate, lb/sec	Oxidizer Flow Rate, lb/sec	Total Propellant Flow Rate, lb/sec	O/F_{act}	O/F_{ideal}	$\Delta O/F$	$\eta_{O/F}$	$I_{sp_{act}}$ (Vacuum), sec	$\eta_{I_{sp}}$ (Vacuum), %	Chamber Length, in.	Chamber Diameter, in.	Expansion Ratio	Nozzle Contour,	Heat Sink Material Properties Ratio	Heat Sink Material Properties Exposure Time, sec	Heat Sink Material Properties Heat Capacity, Btu/lb-°F
Uncooled Runs																	
Cooled Runs																	

Notes:

(1) Uncorrected data - by comparison with chamber contents of throat area and throat temperature measured at data point. (See Appendix B.)

(2) Open's Data Reference for the uncooperative, should not chamber pressures below early test runs, and error data throat analysis. Most propellant flow variation between runs.

(3) Duration was controlled by... and manual test control. Engine vacuum flows varied.

(4) Transducing nozzle cooled.

(5) Run aborted due to fuel pressure drop to nozzle.

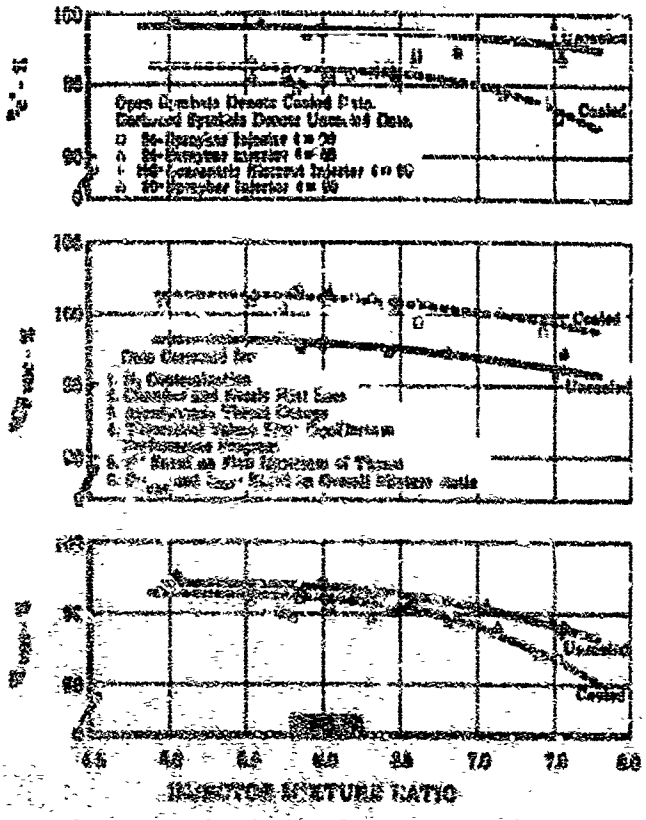


Figure 110. 50K Performance Trends FD 211404

(U) Figure 111 shows the preburner temperature profile as measured by the thermocouple rakes located 17 inches from the injector face.

(U) Vacuum thrust coefficient efficiencies for the cooled chamber tests appear high because of the transpiration coolant injection downstream of the throat and the shift of theoretical, based on the overall propellant mixture ratio. Transpiration coolant shifts the overall mixture ratio down from that at which the combustion core is operating. The theoretical values for characteristic velocity, thrust coefficient, and impulse are all based on the overall propellant mixture ratio. Performance data reduction methods and a data acquisition error analysis are presented in Appendix IV.

(U) The sources of performance losses may be grouped as follows:

1. Combustion and Cooling

   a. Inadequate atomization and incomplete vaporization
   b. Incomplete combustion (total enthalpy release)
   c. Incomplete mixing (mixture ratio profile)

      (1) Injector profile
      (2) Coolant profile

2. Aerodynamic Nozzle Expansion

a. Divergence
b. Skin friction and other boundary layer effects
c. Imperfect contour.

(U) Analytical models have been used to correlate the 50K test data to determine the sources and nature of the performance losses. These are discussed in Appendix IV. The apparent magnitude and sources of the 50K performance losses are shown in figure 112. The present injector configuration provides excellent atomization of the liquid oxygen. Incomplete atomization, vaporization, and total enthalpy release do not appear to be performance limiting factors for chamber lengths of 11 inches or more, as shown in figure 107. The injector mixture ratio profile appears not only to be the major factor in combustion (c*) performance loss but, in addition, contributes to thrust coefficient (C_F) loss.

3. Uncooled Testing

(U) The main chamber used in uncooled testing is shown in figure 91. This chamber can be modified to change chamber length and diameter.

(U) Five uncooled tests were conducted to establish starting and operational sequences, to determine the effect of chamber length, and contraction ratio on performance and to verify predicted performance levels.

(C) Initial run attempts were made with a 54-element, preburner injector. Preburner combustion low-frequency chugging was encountered during start and required replacement of the 54-element preburner injector with the 320-element unit. The chugging problem was attributed to an instability of the tangential slot swirler liquid oxygen injection elements because of an excessively low pressure drop through the element and the resultant high sensitivity of the injection flow to minor fluctuations in the preburner chamber pressure. No further problems were encountered after changing to the 320-element unit shown previously in figure 82. All of the uncooled and cooled tests were conducted with this 320-element preburner injector and the staged-combustion thrust chamber configuration shown previously in figure 77. The first two tests (50SC1 and 50SC2) were conducted with a 20-sprayber main injector, 18-inch chamber length, and a contraction ratio of 5. The subsequent three uncooled tests (50SC3 through 50SC5) were conducted with a 24-sprayber main injector: 13-, 8-, and 11-inch chamber lengths, respectively, and a contraction ratio of 3.

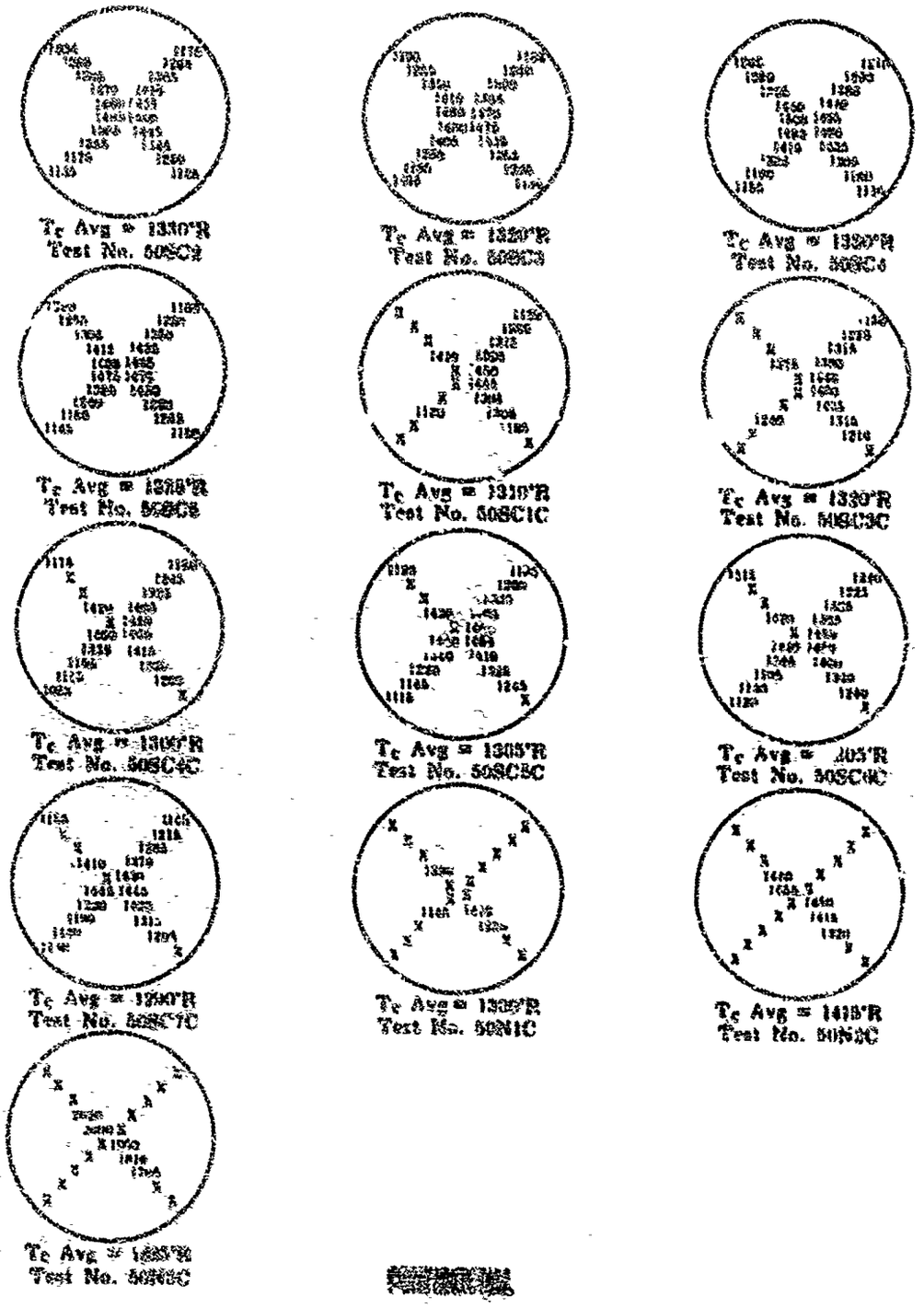


Figure 111. 50K Preburner Combustion Chamber Temperature Profiles

FD 23365

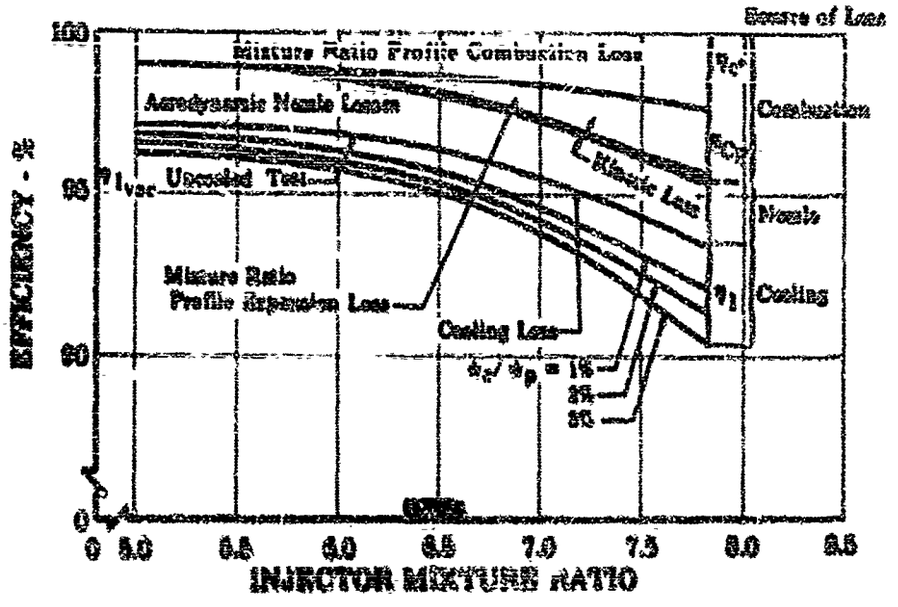
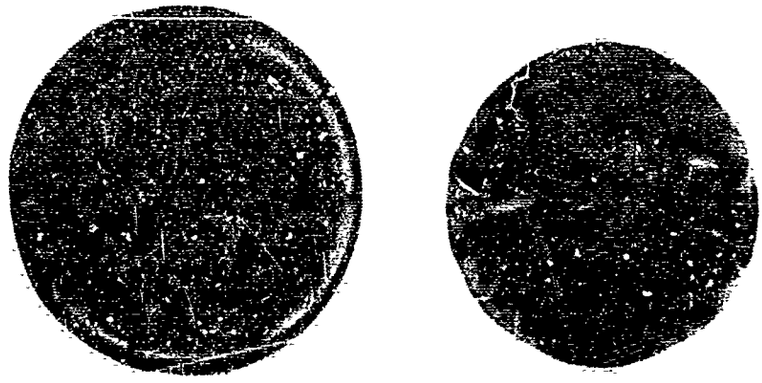


Figure 112. Sources of Performance Losses FD 21113

(C) A comparison of the 20- and 24-spraybar main injector after the uncooled tests is shown in figure 113. The chrome plating on the 24-spraybar injector Nichrome face turned noticeably blue during test 50SC5 when the injector hot gas pressure drop momentarily approached zero during the shutdown transient. The appearance changed only slightly during the subsequent tests. The 24-spraybar injector after the cooled and two-position nozzle test series is shown in figure 114. Uncooled graphite liners were used during tests 50SC1 through 50SC4, the film-cooled copper chamber liner was installed for test 50SC5. The copper liner was used to determine the main injector chamber wall combustion pattern on the copper liner, prior to proceeding with the cooled chamber testing. In addition, potential thermal barrier materials were tested for the [illegible] heat resistivity and relative thermal barrier characteristics. [illegible] temperature indicating materials were also evaluated. The [illegible] patterns are shown in figure 115 and the results are summarized in [illegible]. The pure nickel and cermet platings demonstrated very [illegible] heat shock qualities and the zirconium oxide cermet platings [illegible] superior thermal barrier capability. Further effort into thermal [illegible] appears warranted. However, because the main chamber has [illegible] to its life requirements, the zirconium oxide cermet plating was not [illegible] the MSC of full-scale hardware because its cyclic life could not be verified by laboratory testing.

(C) Throughout the uncooled tests, the preburner mixture ratio was controlled at 0.75 producing a hot gas discharge nominal temperature of 1600°R to the main burner. The graphite and copper nozzle throats were hydrogen-film-cooled during transient conditions but uncooled during the steady-state data acquisition period. The sheet metal nozzle skirt (expansion ratio of 90) was water-film-cooled during transient conditions, but uncooled during the steady-state data acquisition period.



20-Spraybar Injector [redacted] 24-Spraybar Injector

Figure 113. Main Injectors After the Uncooled Test Series FD 20086

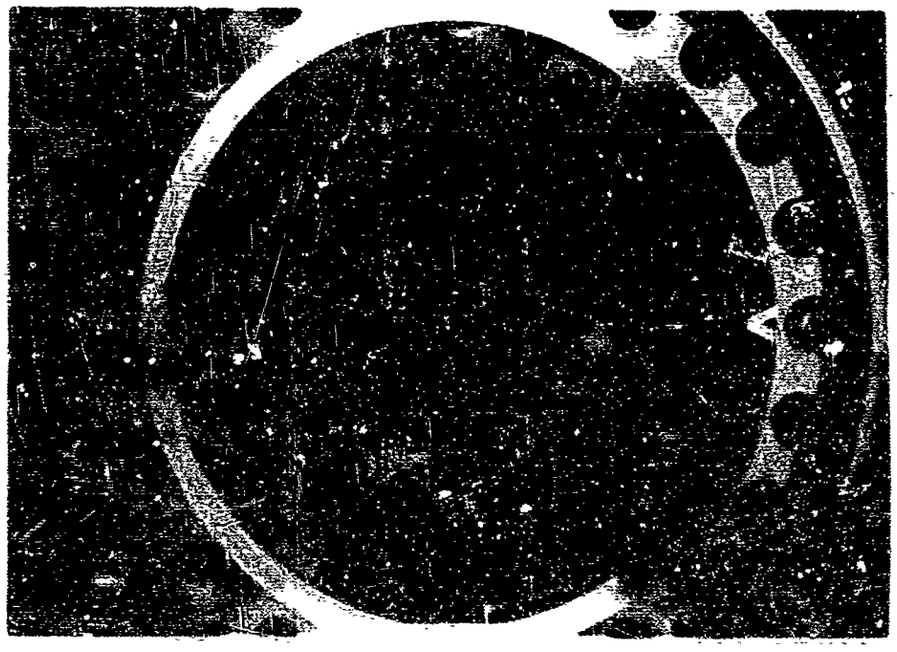
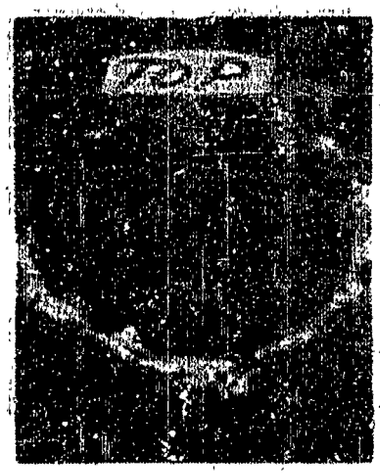
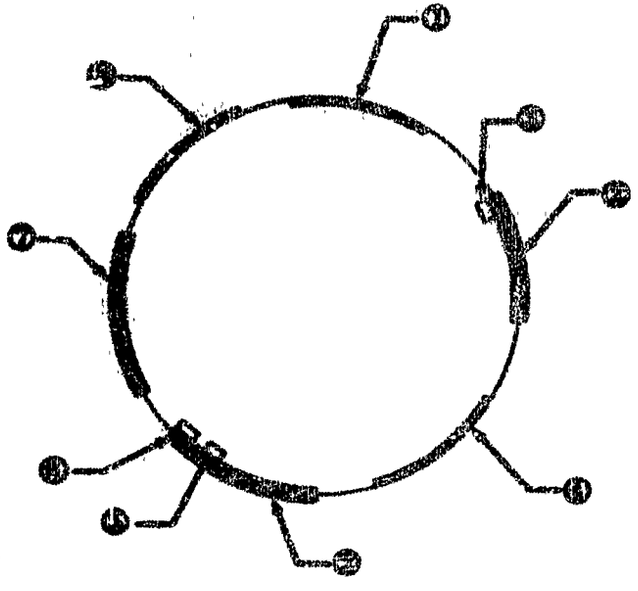


Figure 114. 24-Spraybar Injector, Post-Test No. 50N3C FE 68097

THIS PAGE CONTAINS SUBJECT MATTER COVERED BY A SECRECY ORDER WITH A DESCRIPTION IDENTICAL HEREWITH ISSUED BY U.S. COMMISSIONER OF PATENTS.



(a) 12:00 O'Clock



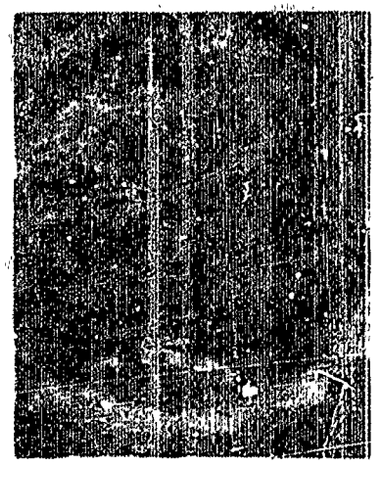
① Nickel - Aluminum Oxide Cermet
② Nickel
③ Silver
④ Tungsten - Cobalt
⑤ Gold
⑥ Copper and Silver
⑦ Nickel - Zirconium Oxide Cermet
⑧ Chromium



(b) 3:00 O'Clock



(c) 6:00 O'Clock



(d) 9:00 O'Clock

Figure 115. Film-Cooled Copper Liner Wall Erosion Patterns (Post-Test 50SC5)

FD 20157

(U) Table XXIV. Potential Thermal Barrier and Temperature Sensitive Materials Test Evaluation (Test No. 50SC5)

Thermal Barriers (0.010-Inch Thickness)

	Thermal Shock Capability	Thermal Barrier Effectiveness	Comments
1. Cermets (nickel base)			
a. Aluminum Oxide	Excellent	Good	—
b. Zirconium Oxide	Excellent	Very good	—
2. Nickel	Excellent	Good	—
3. Tungsten-Cobalt	—	Poor	Incomplete plating achieved
4. Chromium	—	—	Poor plating achieved

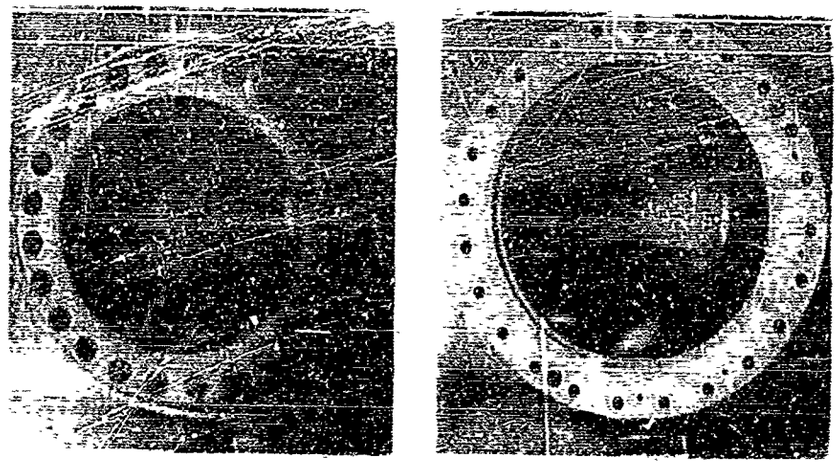
Temperature Sensitive Materials (0.0002- to 0.0010-Inch Thickness) (0.010-Inch Nickel Base)

	Predicted Indicating Temperature, °R	Thermal Shock Capability	Comments
1. Silver	2220	Excellent	Well defined melt
2. Silver-Copper	1897	Good	Some blistering, well defined melt
3. Gold	1950-2000	Excellent	Well defined diffusion line

4. Cooled Testing

(C) A total of nine completely successful cooled chamber tests was conducted. The objective of the first six tests, 50SC1C through 50SC7C, was to optimize the chamber cooling for the selected geometry of 13-inch chamber length and contraction ratio of 3 and determine the effects of cooling on performance. The objective of the final three company-funded cooled tests was to evaluate a two-position nozzle.

(U) The same rig as used for the uncooled tests, shown in figure 77, was used for the cooled tests by replacing the uncooled main chamber graphite liner parts with the transpiration cooled copper wafer liner (figure 116).



Injector End Nozzle End

Figure 116. 50K Cooled Chamber Pretest Condition FD 20088

(U) The cooled chamber liner was GN_2 flow calibrated prior to the testing, and the metering orifices were sized to provide a coolant mass flux distribution close to the predicted requirements. The predicted requirements were based on the results from the analytical heat transfer model and on the results from prior 50K cooled testing, and are shown in figure 117. Each zone was flow checked after the orifices were sized to verify the orifice size and flow calculations.

(C) During this series of cooled tests, no changes were made to the hardware other than orifice size changes required to change the coolant distribution, and the replacement of the 90:1 expansion ratio fixed nozzle with the 60:1 expansion ratio two-position nozzle. The first cooled test was conducted with a main chamber pressure of 2600 psia to ensure that all areas of the transpiration cooled liner inside diameter were adequately cooled. Tests 50SC3C through 50SC7C were conducted at the design chamber pressure of 3000 psia. The coolant distribution was progressively changed and the total coolant flow was reduced.

(U) The progression of these changes is shown in figures 118, 119, and 120.

(C) The condition of all parts was good after testing. The temperature indicating coatings, the locations of which were shown previously in figure 101, indicated the areas of the chamber inner surface that reached temperatures between 1900° and 2440°R during each test.

THIS PAGE CONTAINS SUBJECT MATTER COVERED BY A SECRECY ORDER WITH A MODIFYING "SECURITY REQUIREMENTS PERMIT" ISSUED BY U.S. COMMISSIONER OF PATENTS.

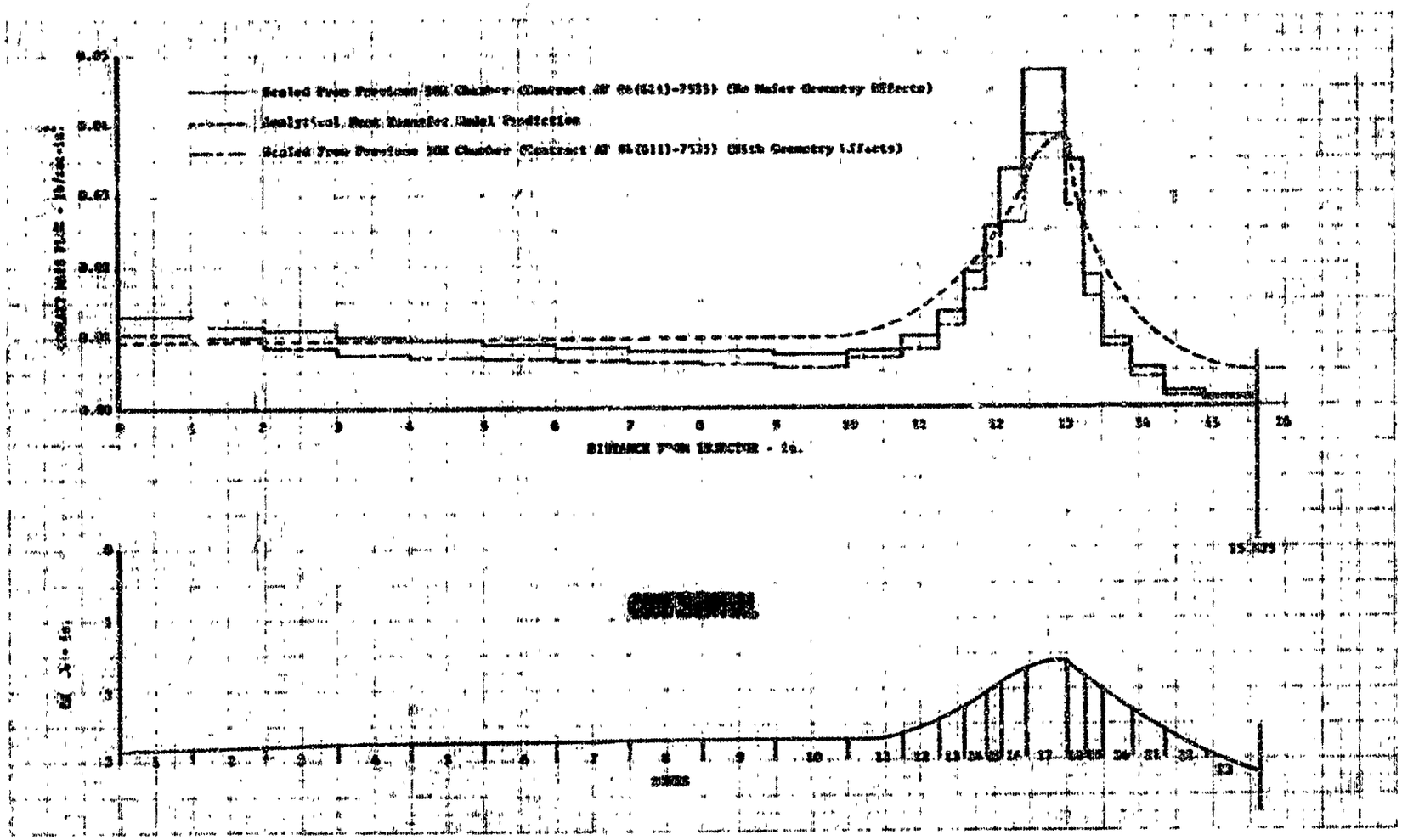


Figure 117. 50K Transpiration Cooling Requirements

DF 59503

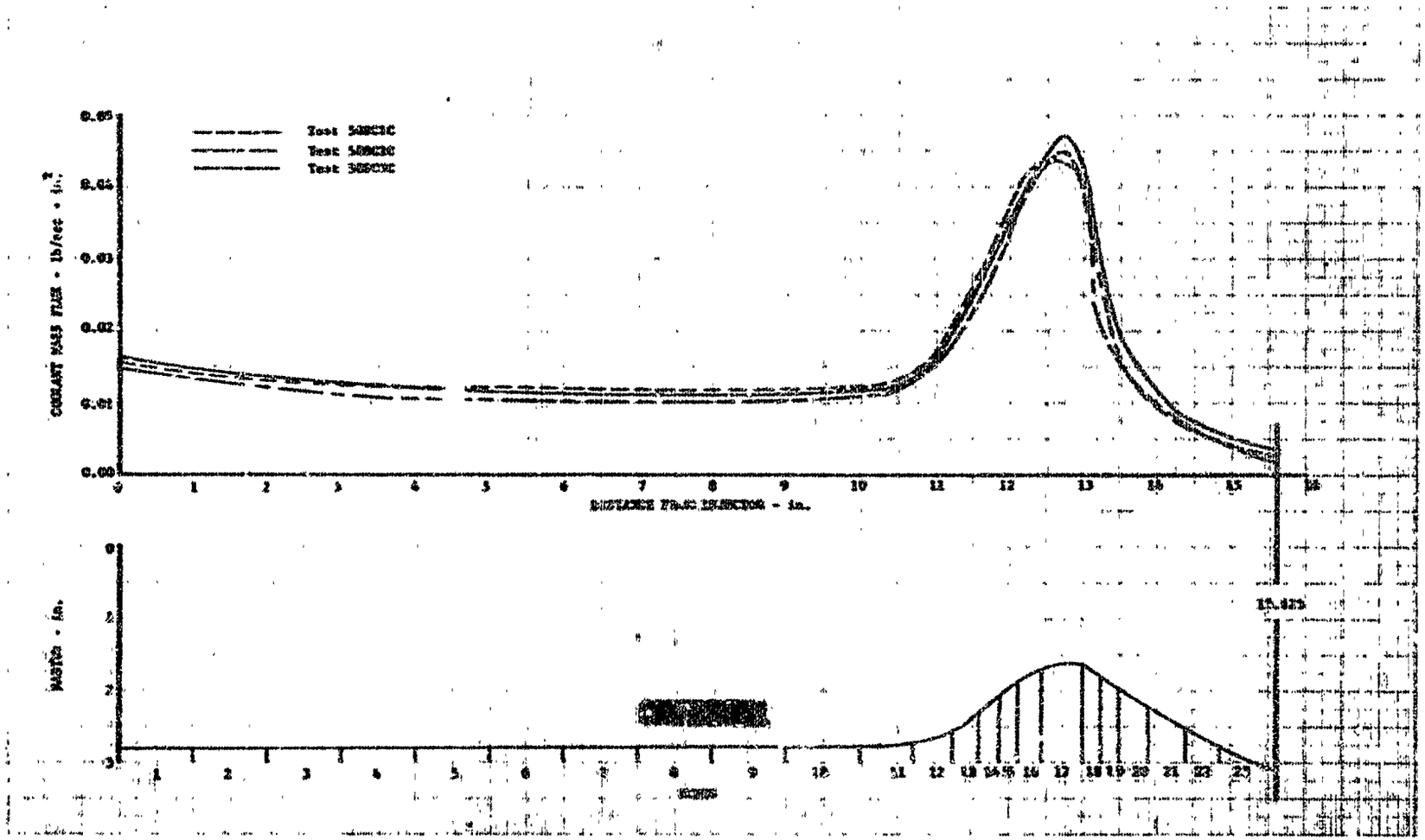


Figure 118. 50K Transpiration Cooling Flux - Distribution 1

DF 54013

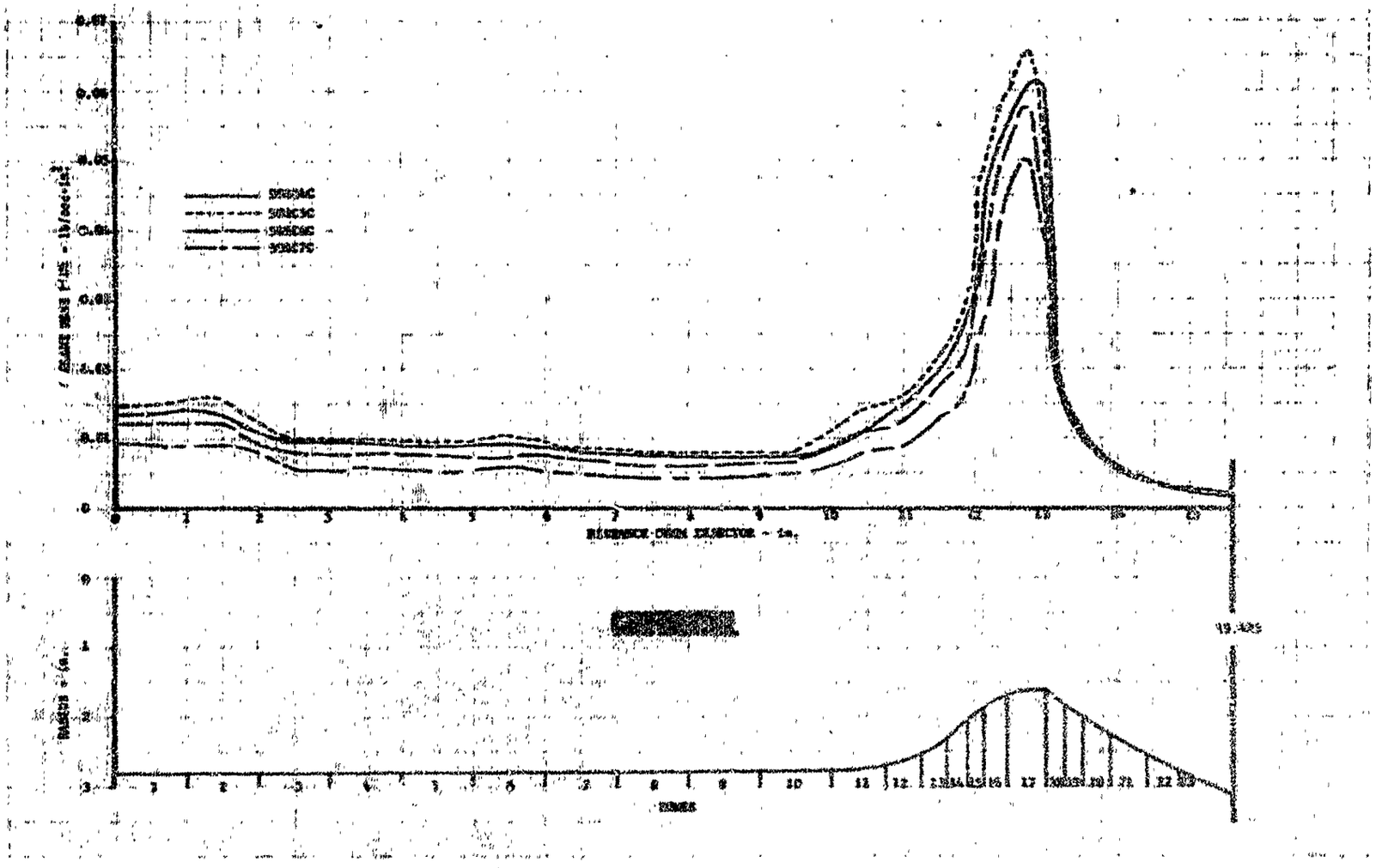


Figure 119. 50K Transpiration Cooling Flux - Distribution 2

DF 54016

CONFIDENTIAL

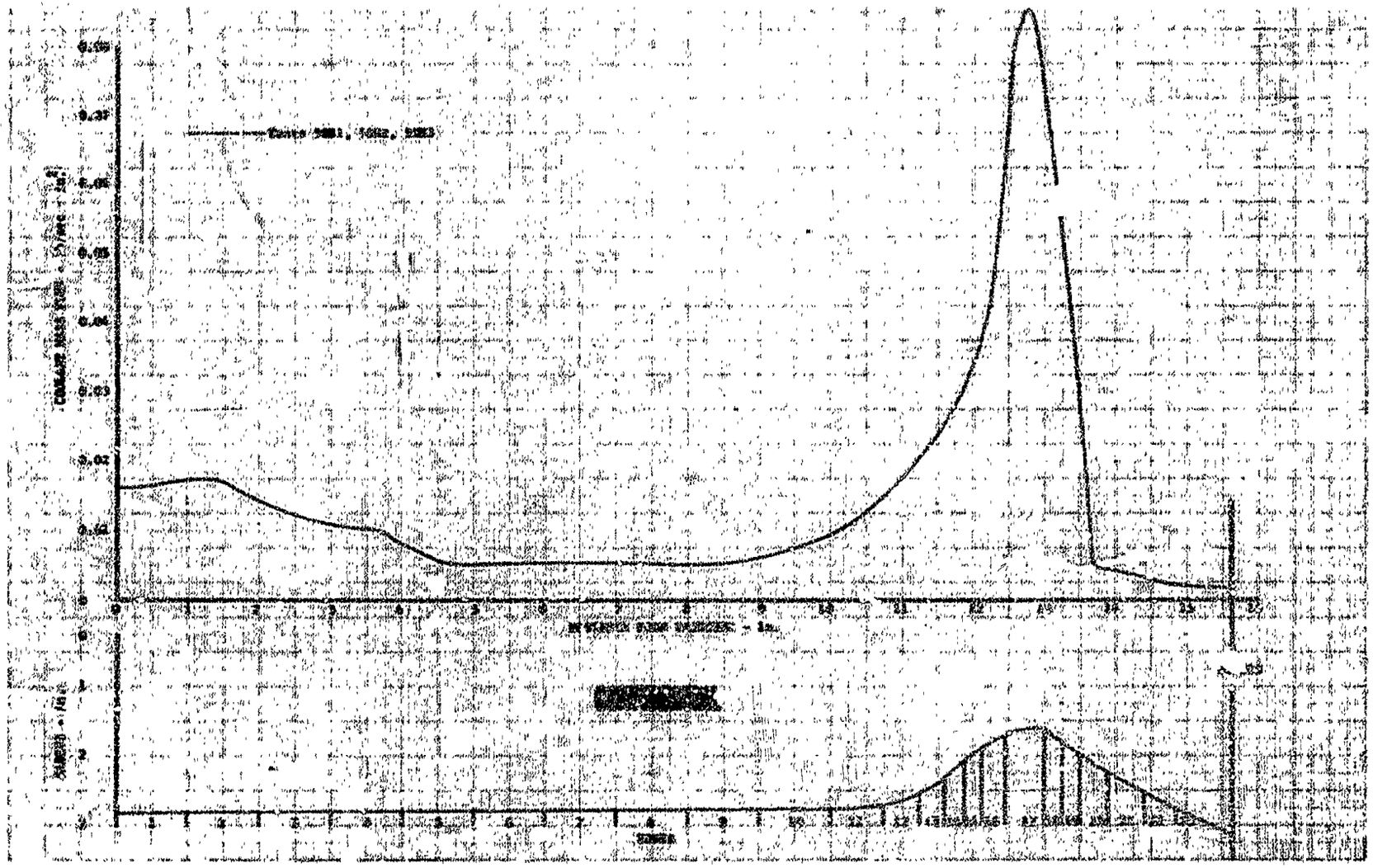


Figure 120. 50% Transpiration Cooling Flux - Distribution 3

DF 54017

CONFIDENTIAL

(C) The chamber inside surface temperatures were plotted on coolant mass flux-surface temperature curves for the particular chamber locations and curves, the slopes of which were predicted by the analytical heat transfer model, were drawn through the points. This enabled a new coolant mass flux to be determined for a desired surface temperature. Minor melting of the silver-copper coating occurred in Zone 2[3] after test 50SC2C. The chamber was re-orificed after test 50SC3C with flow slightly increased in Zones 1 and 2. Some further indication in the silver-copper band occurred in Zones 3 through 10 during test 50SC7C, as shown in figure 121.

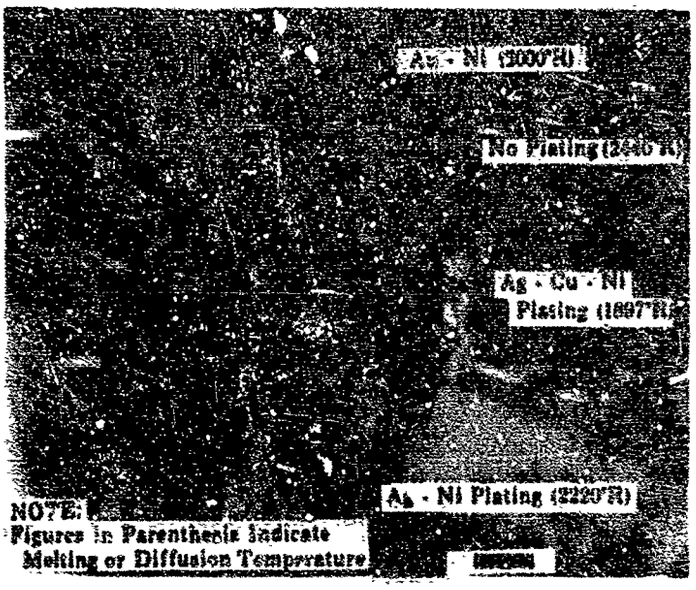


Figure 121. 50K Cooled Chamber, Post-Test 50SC7C, 3 O'clock Position FD 20087A

(C) Figure 122 shows the condition of the throat after test 50SC7C. One small area of the throat was damaged by local melting because of marginal throat cooling flow during the minimum cooling flow test. Some separation between several wafers was evident after test 50SC3C, but no discernible increase in plate separation occurred during subsequent tests. The separations are thought to be closed during testing when surface temperature is high.

(C) The chamber coolant orifices were changed a second time (distribution 3) prior to the two-position nozzle tests. All of the temperature indicating coatings detected higher than desired temperatures in Zones 5 through 10 during test 50N1C. Because the coolant distribution was marginal in adequately cooling these zones, coolant pressure drop could not be reduced after test 50N1C; however, coolant flow reduction would have been possible in the convergent and divergent nozzle. No high temperature indications were visible after tests 50N2C and 50N3C.

[3] Zones 1 through 10 comprise the cylindrical combustion chamber, 11 through 17 the convergent nozzle, and 18 through 23 the divergent nozzle.

CONFIDENTIAL THIS PAGE CONTAINS SUBJECT MATTER COVERED BY A SECRECY ORDER WITH A SECRECY "SECURITY REQUIREMENTS PERMIT" ISSUED BY U.S. COMMISSIONER OF PATENTS.

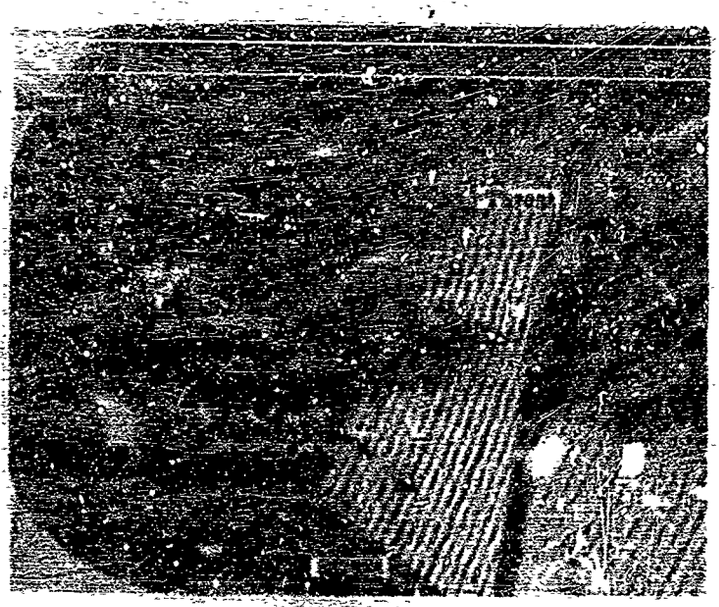


Figure 122. Closeup of Throat, Post-Test 50SC7C FD 20089A

(U) Vibration levels on all tests were low with the only significant level of vibration occurring during the acceleration transients. Figure 123 shows the vibration traces for tests 50SC3C and 50SC7C and the same type of vibration data for a production RL10 engine.

(C) Valid cooled chamber internal wall temperature readings from the 0.010-inch diameter chromel-alumel thermocouples were not obtained because of inability to bottom the thermocouple in the eloxed hole and the fragile nature of the wires that were broken or shorted during installation and testing.

5. Two-Position Nozzle Testing

(C) The two-position nozzle consists of a stationary primary (ϵ_A = 20) and a movable secondary nozzle (ϵ_A = 60). The secondary would be in the retracted (open)[4] position at low altitude and the extended (closed) position at high altitude. For ground testing the nozzle was extended to the high altitude position at full thrust only to minimize side loads and heating that would result from exhaust separation at lower (sea level) pressure ratios.

[4]With reference to permitting airflow into the secondary.

THIS PAGE CONTAINS CURRENCY MATTER COVERED BY A SECRECY ORDER WITH A MODIFYING "SECURITY REQUIREMENTS PERMIT" ISSUED BY U.S. COMMISSIONER OF PATENTS.

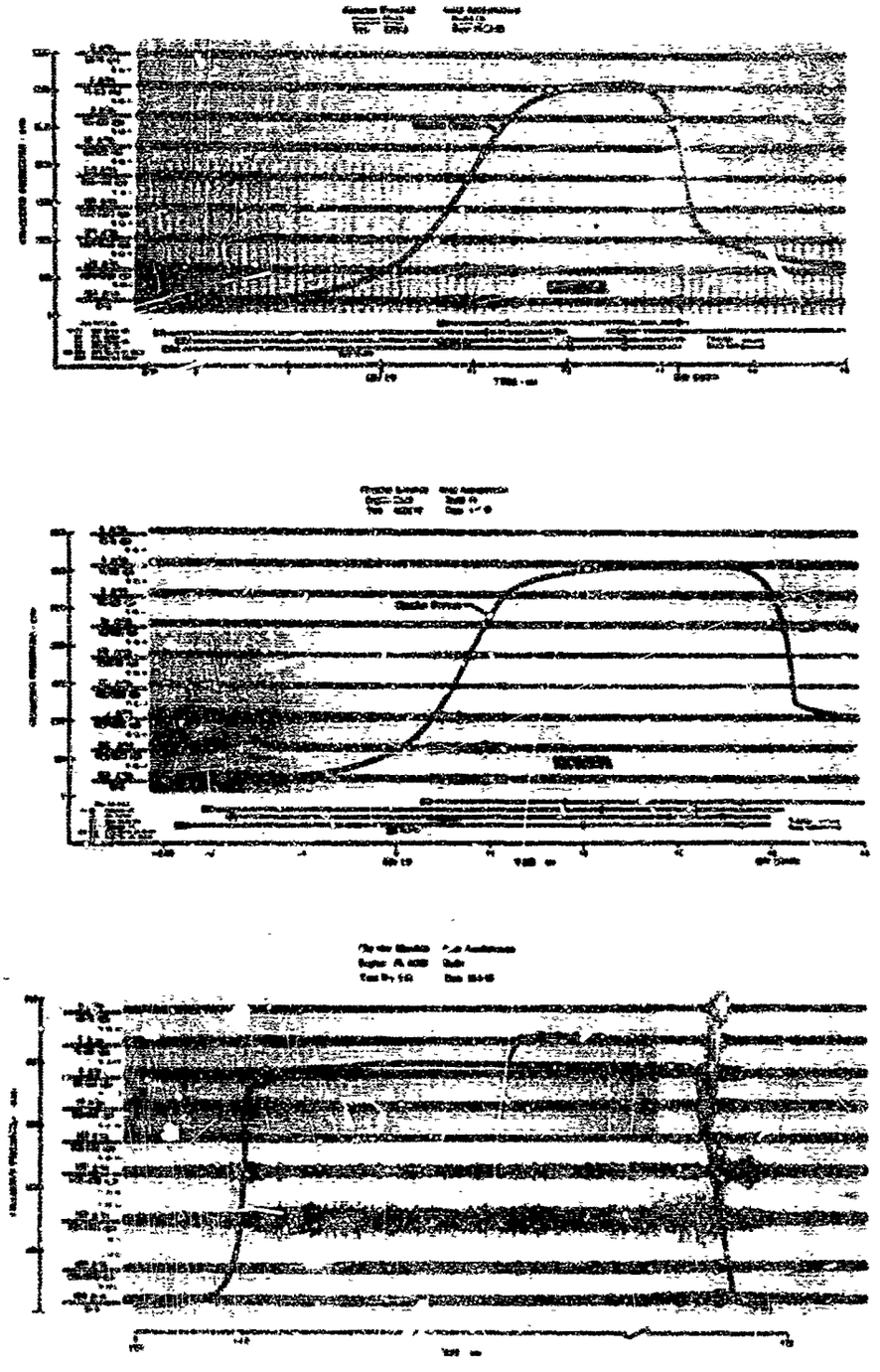


Figure 123. Vibration Traces for Cooled Test, FD 20159
Uncooled Test, and RL10 Production FD 19957
Engine FD 20158

(C) In the first test (50N1C) the cooling water was turned off to take data three times. The rig was started with the water on, and remained on until a pressure ratio of approximately 70 was attained. The water was then shut off for the next part of the acceleration transient and turned on during the final part of the acceleration transient to full thrust. The nozzle was in the full open position for the start sequence of the rig and was translated closed in 0.8 second after the cooling water turned off and the rig operated at 2650 psia chamber pressure. The nozzle remained in the closed position with the cooling water on and then translated to the maximum open position in 0.9 second while the cooling water was off and the rig operated at 2650 psia chamber pressure. After the nozzle was full open, the water was turned on and the rig was shut down. In this test, reattachment of the primary stream to the secondary nozzle wall was not noted until the nozzle started to translate closed, at which time the rig was operating at a pressure ratio of 178. The calibrated load cells indicated that the maximum side load was only 270 lb. Nozzle wall temperatures were considerably lower than had been predicted. A post-test review of the data indicated that the cooling water had failed to cut off completely because of an improper plumbing hook-up. This was corrected to prevent recurrence during the remaining tests.

(C) In test 50N2C, the cooling water was turned on for a total of 1.5 seconds. The rig was started with the two-position nozzle in the open position and translated closed in 0.8 second when the rig reached 2650 psia chamber pressure. The cooling water was turned on and the nozzle returned to the open position in 0.9 second, then the cooling water was turned off and the rig shut down. Reattachment pressure ratio data, wall temperature, and side load data, all indicated agreement with the data from the first test.

(C) Test 50N3C was run entirely with the cooling water off to both the primary and secondary nozzle. The rig was started with the two-position nozzle in the full open position. After the acceleration transient was completed, the nozzle was translated to the full closed position in 0.65 second while the rig operated at approximately 2500 psia chamber pressure. After operating at steady-state for approximately 0.5 second, the nozzle was translated to the full open position in 0.75 second and then the rig was shut down. Data obtained during this test were in good agreement with the data from the two previous successful tests. The maximum side load measured with the calibrated load cells was 275 lb as shown in Figure 124. The maximum axial load transmitted through the nozzle was 1640 lb as shown in figure 125. The nozzle wall outer skin thermocouples indicated temperatures of approximately 1160°R even though there was no water on for film cooling. Reattachment of the primary exhaust gases on the secondary nozzle wall did not occur with the nozzle in the full open position. Secondary nozzle airflow decreased to zero flow rate only after the nozzle had started to close.

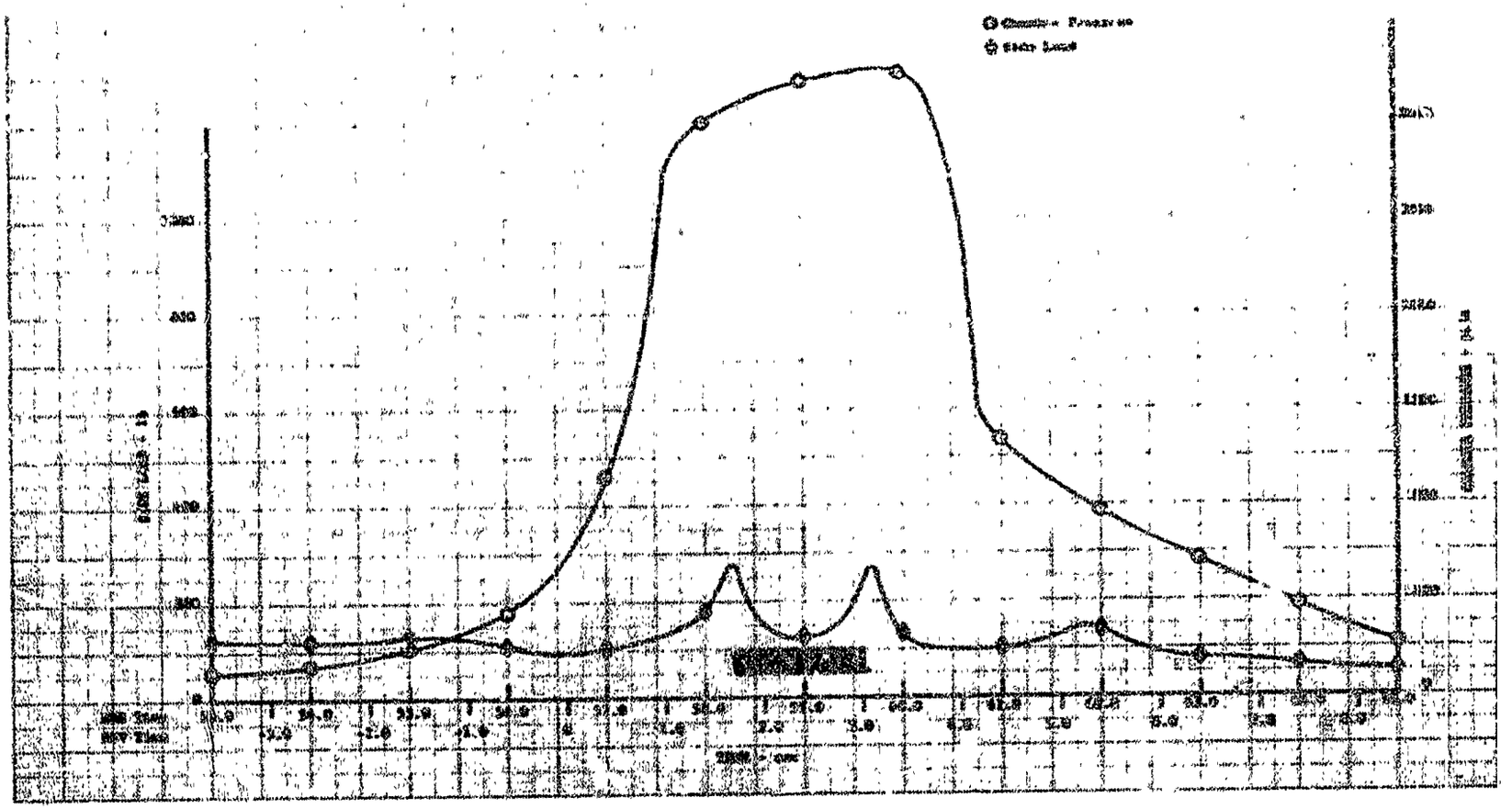


Figure 124. 50K Translating Nozzle, Chamber Pressure Ratio and Side Load

BF 50599

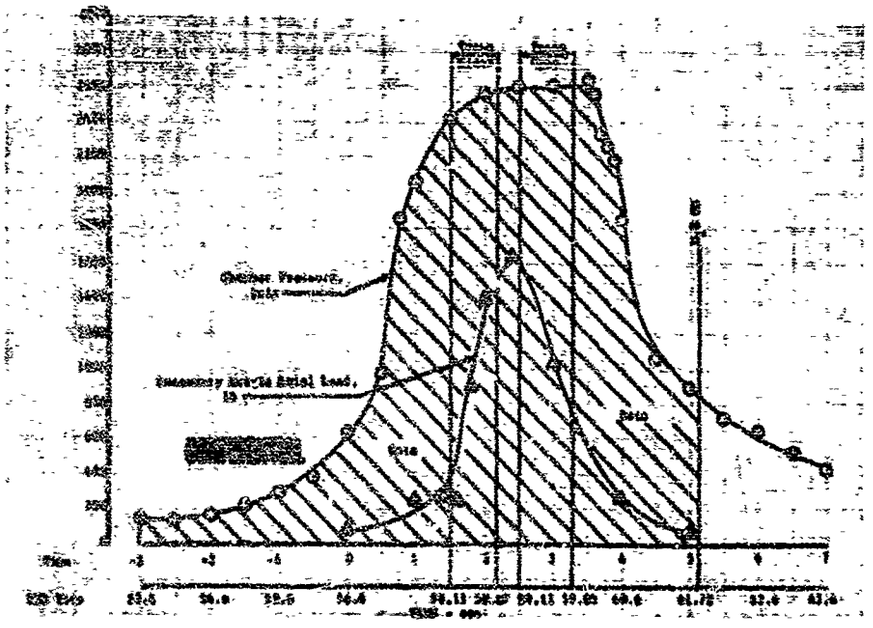


Figure 125. Load Cell Data for Secondary Nozzle DF 54398

(C) The decrease in secondary airflow was measured in these tests as shown in figure 126. The operation of this nozzle in the open and closed position was further verified by the nozzle wall static pressure data as shown in figure 127. The static pressure in the nozzle was essentially ambient when the nozzle was open and readjusted to the ideal wall pressure level when the nozzle was closed. An analysis of the performance was similar to a 20:1 area ratio nozzle until the secondary nozzle closed and then the nozzle performance duplicated the 60:1 area ratio nozzle as shown previously in figure 109. During all the tests, the nozzle did not experience any high temperatures when operating uncooled. The outer skin temperature reached a maximum level of 1160°R when the nozzle was closed as shown in figure 127.

(U) These tests provided data that were required to design a lightweight nozzle and translating system for the 250K two-position nozzle.

E. HEAT TRANSFER STUDIES AND MATERIALS EVALUATION

1. Introduction

(C) Studies were conducted to develop a mathematical heat transfer model to aid in analyzing the relative effects on cooling requirements of various wafer materials and geometries for the grooved wafer and porous media (Rigimesh) transpiration cooling concepts shown in figure 128. In addition, a material survey was conducted for application in either or both concepts. Fabrication of test samples was partially completed prior to discontinuation resulting from program redirection.

THIS PAGE CONTAINS SUBJECT MATTER CONCEIVED BY A MEMBER UNDER WITH A REGISTERED "SECURITY AGREEMENT PERMIT" ISSUED BY U.S. COMMISSIONER OF PATENTS.

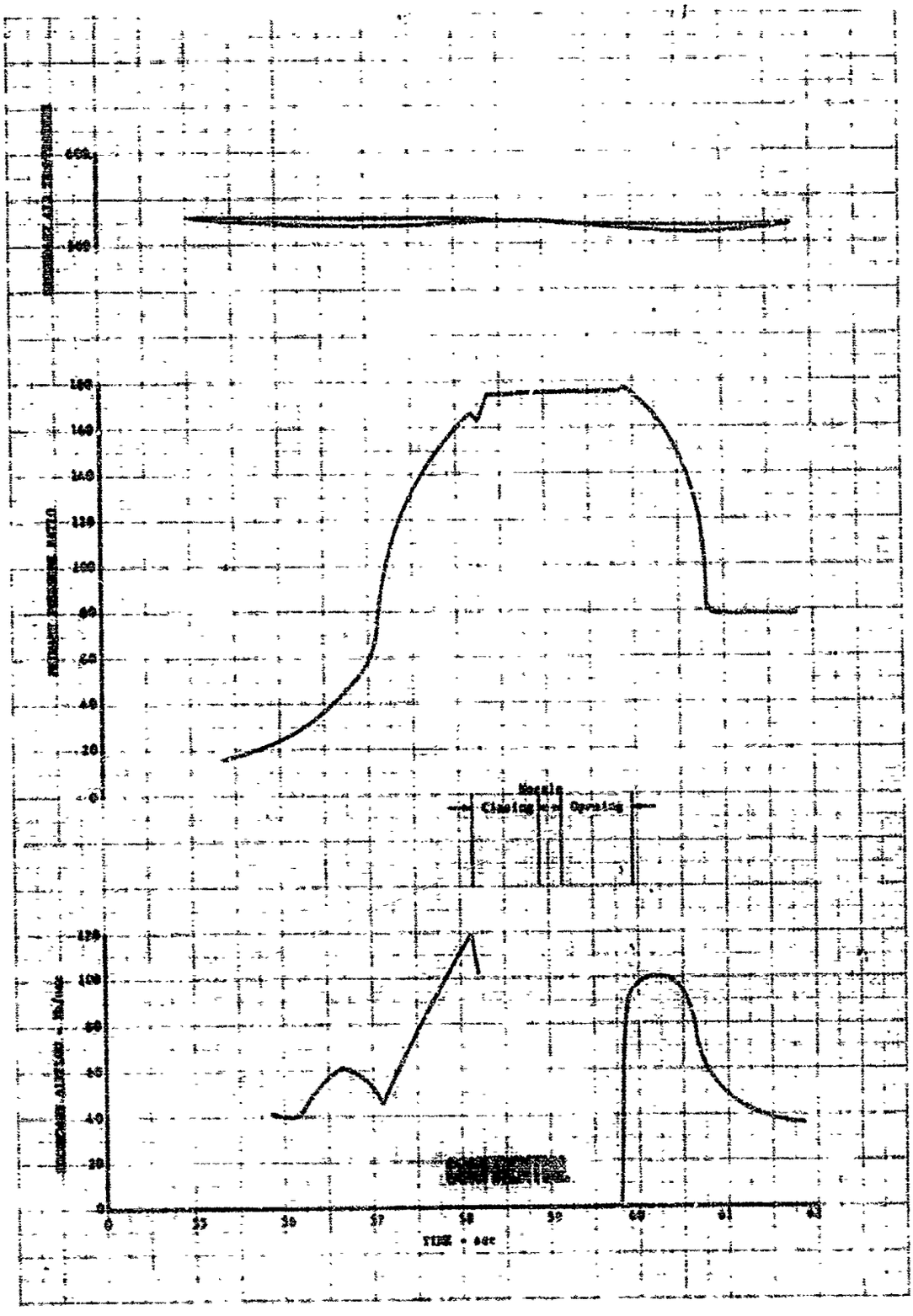


Figure 126. 50K Translating Nozzle Tests

DF 54597

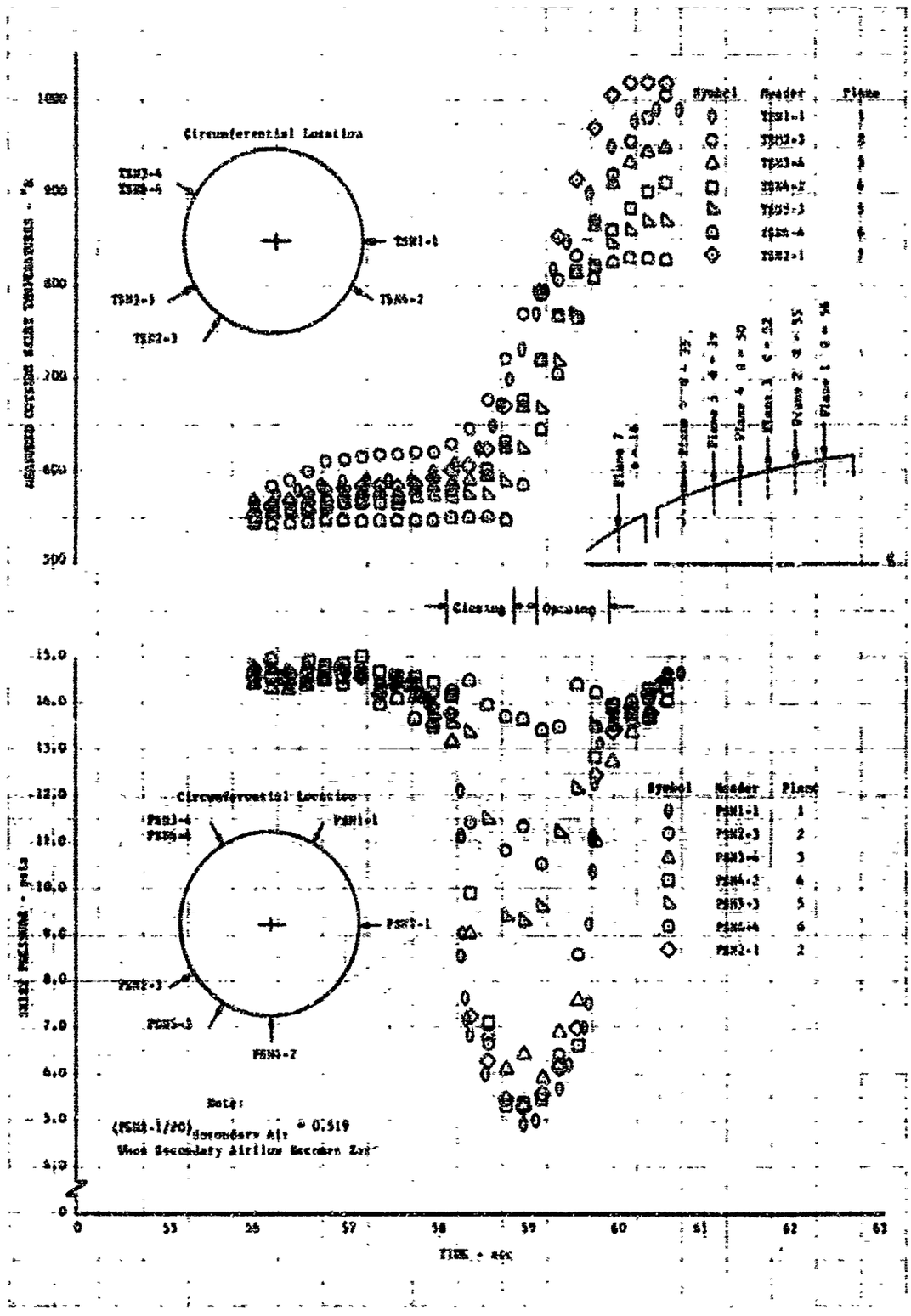


Figure 127. Translating Skirt Wall Pressure and Temperature DF 54600

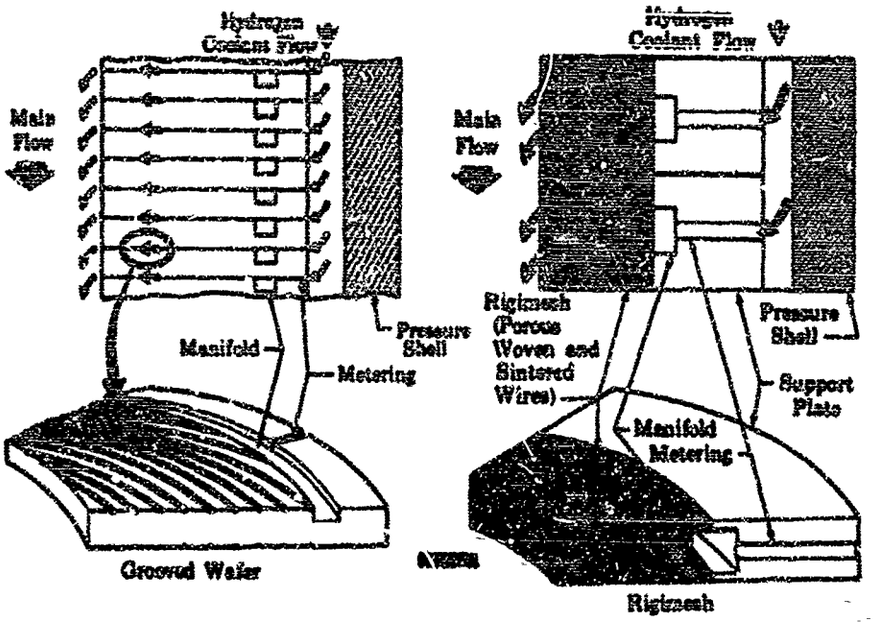


Figure 128. Grooved Wafer and Rigimesh Cooling Concepts FD 21445

(C) Results of the studies indicate the following:

1. The Rigimesh cooling concept promises coolant reductions up to 45% compared with grooved copper wafers (current design).

2. Nickel offers significant reduced cooling requirements relative to copper in both the grooved wafer and Rigimesh concepts. The material can be fabricated as a grooved wafer or Rigimesh.

3. The cooling requirements can be reduced to 85% of grooved copper wafers by using refractory materials. Molybdenum or Tungsten alloyed with Rhenium appears attractive. The feasibility of fabrication into grooved wafers or Rigimesh needs to be demonstrated.

2. Grooved Wafer Analytical Heat Transfer Model

(C) The 50K cooled thrust chamber design was based on the grooved wafer-cooled chamber concept as illustrated in figure 128. A mathematical heat transfer model of the wafer cooled thrust chamber was developed to aid in analyzing the relative effects of various wafer materials and coolant groove geometries. The analytical model is a modified version of the basic porous wall model proposed by R. P. Berniker of MIT under Contract AF 49(638)-245. Berniker's model consisted of a system of equally spaced cylindrical channels. A series of differential equations was developed by equating the heat transferred to the coolant

CONFIDENTIAL THIS PAGE CONTAINS SUBJECT MATTER COVERED BY A SECRECY ORDER WITH A MODIFYING "SECURITY REQUIREMENTS NOTICE" ISSUED BY U.S. COMMISSIONER OF PATENTS.

in the spiral grooves to the heat removed from the solid portion of the wall. The basic physical model was modified to account for the particular coolant flow path associated with the wafer-type heat exchanger system, the noncylindrical cross-sectional coolant groove geometry, and the non-homogeneous coolant groove spacing.

(U) The solution of the heat transfer equations for any given set of wall and coolant parameters results in a heat exchanger efficiency for the porous wall heat transfer process. The efficiency of the wall, θ_w is defined as:

$$\theta_w = \frac{T_c - T_o}{T_w - T_o} \tag{3}$$

where:

T_c = Coolant temperature at exit into chamber

T_w = Wall hot side temperature

T_o = Coolant ambient (reservoir) temperature.

(U) The heat picked up by the coolant represents the heat flow out of the wafer (Q_{out}):

$$Q_{out} = \dot{w}C_p(T_c - T_o) = \dot{w}C_p(T_w - T_o)\theta_w \tag{4}$$

where:

$\dot{w}$ = Coolant mass flow rate

C_p = Coolant specific heat.

(U) If transpiration cooling was not present, the heat flow into the wall (Q_{in}) would be:

$$Q_{in} = h_o A_s (T_{adw} - T_w) \tag{5}$$

where:

h_o = Undreduced (uncooled) heat transfer coefficient

T_{adw} = Adiabatic wall temperature

A_s = Surface area.

(U) The unreduced heat transfer coefficient, h_o, must be modified by a "film factor," $(1/\eta_f)$, to account for the reduction in heat transfer because of mass addition to the boundary layer.

$$\frac{1}{\eta_f} = \frac{h}{h_o} \tag{6}$$

THIS PAGE CONTAINS SUBJECT MATTER COVERED BY A SECRECY ORDER WITH A SCRIPTING "SECURITY REQUIREMENTS PERMIT" ISSUED BY U S COMMISSIONER OF PATENTS.

where:

h = Actual (cooled) heat transfer coefficient.

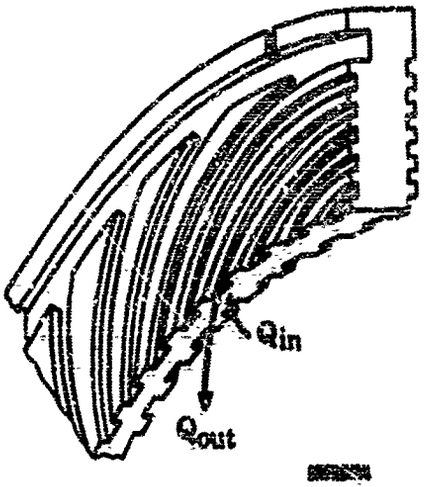
Therefore,

$$Q_{in} = h_o A_s (T_{adw} - T_w) \frac{1}{\eta_f} \tag{7}$$

(U) When steady-state conditions are present $Q_{in} = Q_{out}$. Thus, to determine the required transpiration mass flux ($\dot{w}/A_s$) for any particular set of heat transfer parameters, equations (4) and (7) can be combined.

$$\frac{\dot{w}}{A_s} = \frac{h_o (T_{adw} - T_w)(1/\eta_f)}{C_p (T_w - T_o)\theta_w} \tag{8}$$

(U) Figure 129 illustrates the wafer configuration and lists the heat balance equations.



$$Q_{in} = h_o A_s (T_{adw} - T_w)\left(\frac{1}{\eta_f}\right)$$

$$Q_{out} = \dot{w} C_p (T_w - T_o)\,\theta_w$$

$$Q_{in} = Q_{out} \text{ (Steady State)}$$

$$\frac{\dot{w}}{A_s} = \frac{h_o (T_{adw} - T_w)}{C_p (T_w - T_o)} \left(\frac{1}{\eta_f}\right) \frac{1}{\theta_w}$$

Figure 129. Transpiration Heat Transfer Analysis FD 16040

(U) Factors such as h_o, C_p, and T_{adw} are determined when the chamber pressure, mixture ratio, and chamber contour are fixed. Therefore, coolant flux ($\dot{w}/A_s$) is reduced by maximizing both the wall temperature (T_w) and the wall efficiency (θ_w) and minimizing the film factor ($1/\eta_f$) with proper design.

CONFIDENTIAL THIS PAGE CONTAINS SUBJECT MATTER COVERED BY A SECRECY ORDER WITH A NODIFYING "SECURITY REQUIREMENTS PERMIT" ISSUED BY U.S. COMMISSIONER OF PATENTS.

(C) The film effect resulting from mass addition has been investigated by Eckert, Rubesin, and others (References 1, 2, and 3). Their results are compared with data from previous water cooled chamber testing in figure 130. The film factor is a function of the following:

1. Main gas stream parameters
   a. Reynolds No. (Re)
   b. Nusselt No. (Nu)
2. Coolant mass flux ($\dot{w}/A_g$)
3. Coolant entrance angle (β)
4. Number of grooves per plate (S).

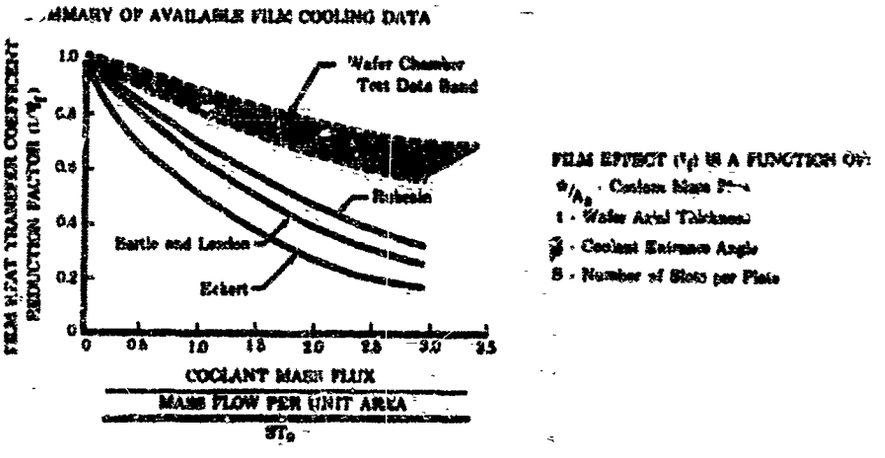


Figure 130. Mass Addition Film Effect (η_f) FD 16045

(U) Figure 131 illustrates the wafer geometry and compares the wall efficiency of the previous cooled main chamber to the new design.

(C) The analytical cooled wafer chamber model defines the significant design variables that affect the coolant mass flux. Although existing experimental data are not adequate to determine the exact influence of each variable, the model is very useful in predicting the trend caused by a particular variable change. Thus, in the design of the new 50K cooled chamber, each design variable was allowed to change and its relative effect on the dependent variable, the coolant mass flux, was determined. The design variables are:

1. Wall material
2. Wafer axial and radial thickness
3. Coolant groove pattern
   a. Groove cross section at area, Ag
   b. Entrance angle, β
   c. Length, L
   d. Number of grooves per plate, S

(U) Figure 132 shows the influence of groove geometry on coolant flow.

THIS PAGE CONTAINS SUBJECT MATTER COVERED BY A SECRECY ORDER WITH A MODIFYING "SECURITY REQUIREMENTS PERMIT" ISSUED BY U.S. COMMISSIONER OF PATENTS.

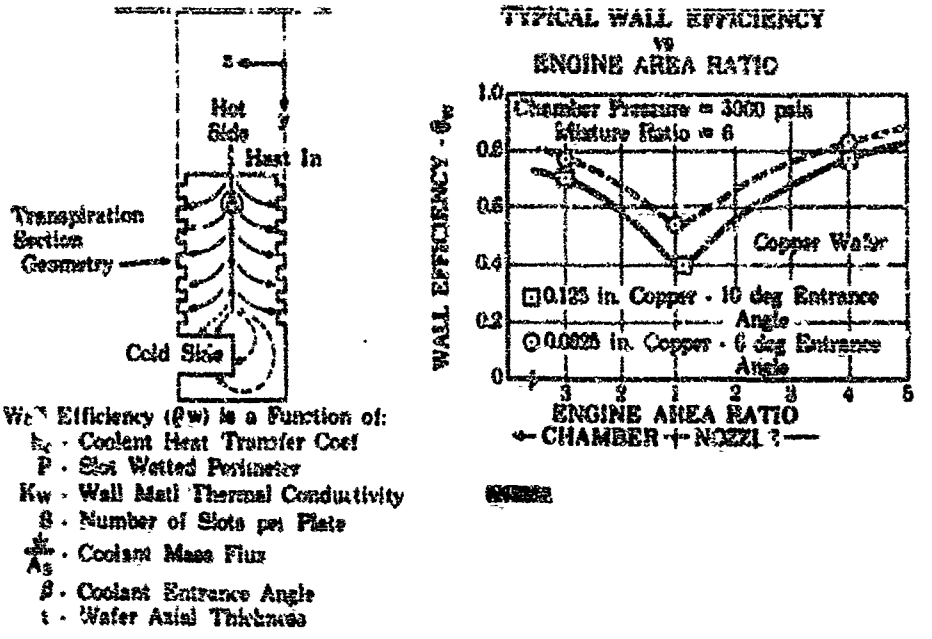


Figure 131. Transpiration Section Wall Efficiency (θ_w) FD 16050

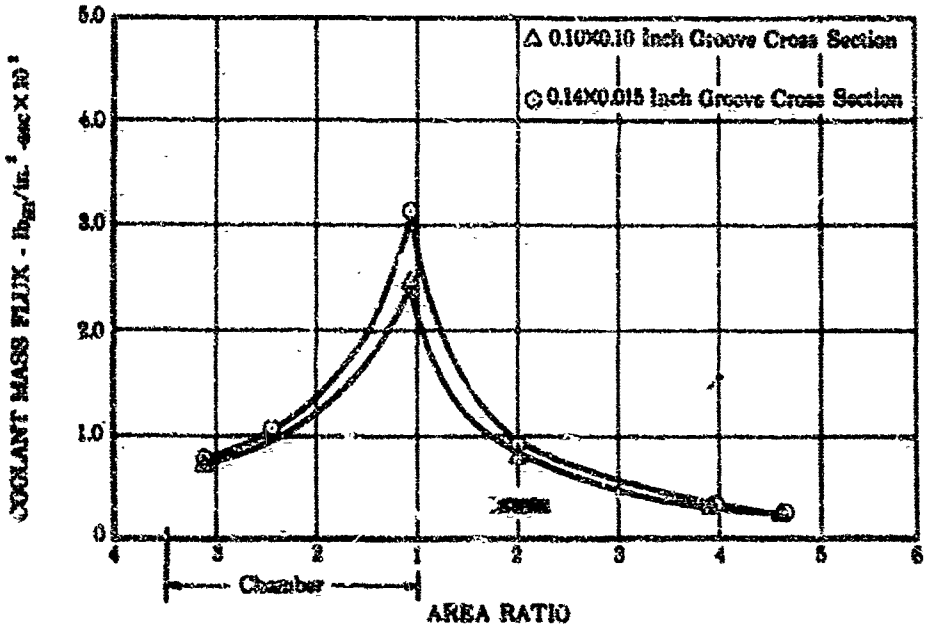


Figure 132. Influence of Wafer Groove Geometry on Required Coolant Mass Flux FD 16049

CONFIDENTIAL
THIS PAGE CONTAINS SUBJECT MATTER COVERED BY A SECRECY ORDER WITH A DISSEMINATION "SECURITY REQUIREMENTS PERMIT" ISSUED BY U.S. COMMISSIONER OF PATENTS.

(C) The 6-degree entrance angle 0.010 by 0.010-inch spiral groove dimensions were selected to minimize the required coolant while maintaining adequate surface bonding area and wafer structural strength.

(U) The effects of wafer axial thickness on coolant mass flux requirements were investigated at three locations (chamber, throat, and nozzle exit) and are shown in figure 133. The coolant requirements decrease with thickness; the effect being most pronounced in the throat. Wafers 1/16-inch thick were selected and while they are desirable for the coolant requirements, they incur penalties in increased cost and complexity, and require very careful handling during detail fabrication operations.

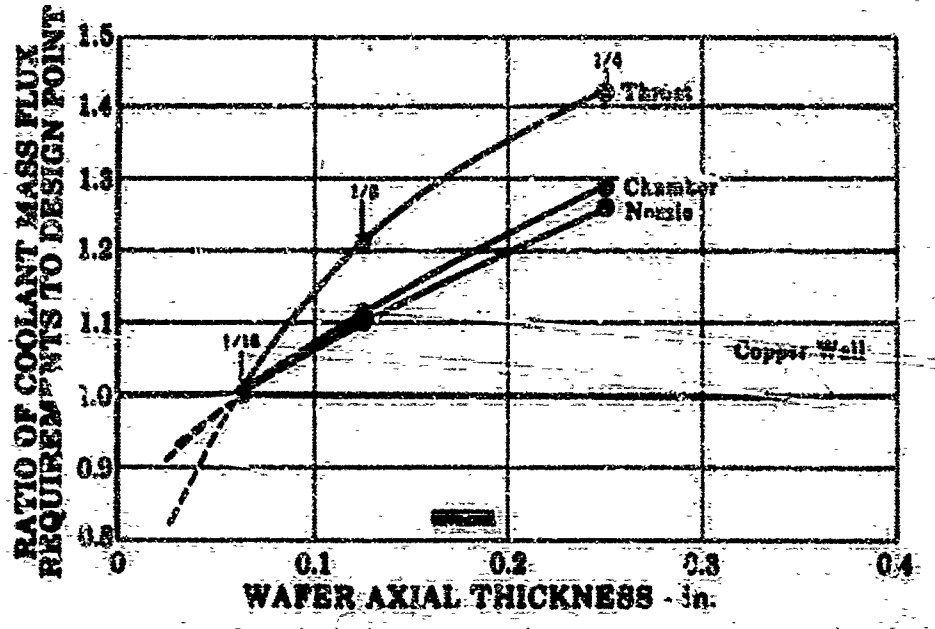


Figure 133. Effect of Wafer Axial Thickness on Coolant Mass Flux Requirements FD 21043

(U) The requirement for a high thermal conductivity metal to transfer the heat to the coolant and ease of photoengraving resulted in the selection of commercially pure copper as a wafer material. The thermal conductivity variation with temperature for several metals is shown in figure 134.

(U) The hot side wall of the copper wafer chamber can be plated with a thin layer of metal to increase the allowable surface wall temperature. Ductile materials such as stainless steel with low thermal conductivity and thermal expansion coefficients similar to copper are particularly desirable because ideal thickness requirements are low.

(C) Figure 135 shows the desired plating thickness of nickel and stainless steel to obtain a surface temperature of 2500°R and copper interface temperature of 1700°R. Plated specimen tests have indicated that 0.010 inch of nickel can be electrochemically plated without excessive restriction of the coolant grooves caused by side plating. Use of platings such as nickel in chambers with high cyclic life requirements is questionable because the very high temperature gradients produce high thermal strains that minimize cyclic life. Because of the inability to validly test the cyclic life of nickel plated over copper in a laboratory test no thermal barriers were used for the 50K or full-scale hardware.

THIS PAGE CONTAINS SUBJECT MATTER COVERED BY A SECRECY ORDER WITH A PROHIBITING "SECURITY REQUIREMENTS PERMIT" ISSUED BY U S COMMISSIONER OF PATENTS.

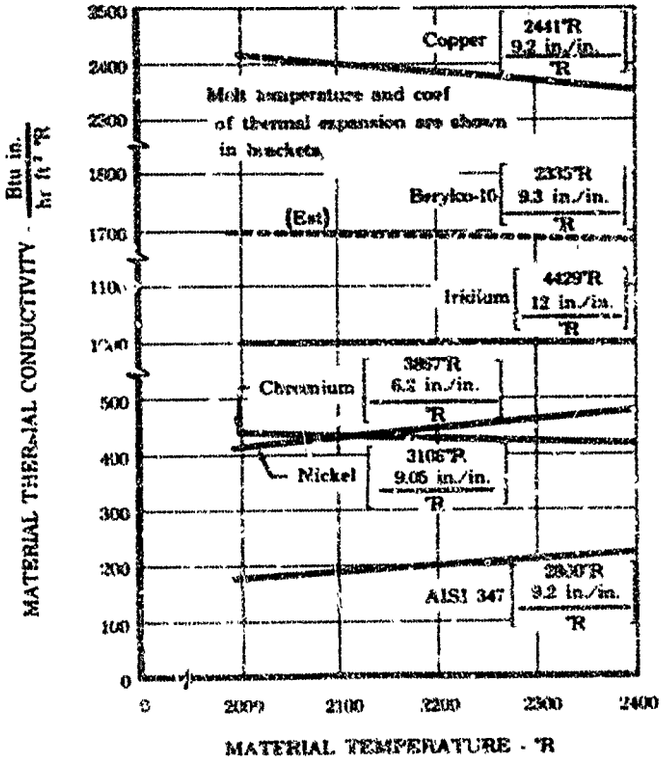


Figure 134. Material Thermal Conductivity vs Temperature FD 16043

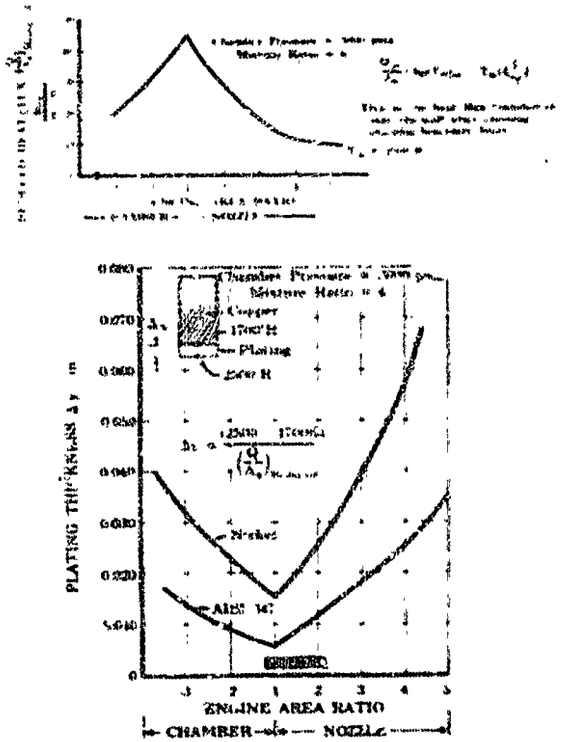


Figure 135. Typical Plating Thickness Requirements for 2500°R Wall Temperature FD 15960

(C) The analytical heat transfer model was utilized to permit a parametric study of coolant mass flux as a function of thermal conductivity and wall temperature at different chamber locations for the new 50K cooled chamber spiral grooved wafer geometry. The study was extended to a composite plate with copper as the basic wafer material, which has an allowable interface temperature of 1700°R. The analysis was useful to compare materials in general transpiration cooling concepts where heat transfer in the cooling material and film effects of mass addition in the boundary layer are both significant. Figures 136, 137, and 138 and table XXV show cooling requirements for selected materials in the combustion chamber (ϵ_c = 3), nozzle throat (ϵ = 1), and the end of the transpiration cooling (ϵ_x = 4). Included is the composite wafer of copper with an optimum nickel thickness to produce an allowable 2500°R hot gas side wall temperature. In areas of high heat flux, such as the throat, heat transfer in the wafer itself becomes very important and the material thermal conductivity becomes more important, relative to allowable surface melting temperature, in determining required coolant flow. In areas of lesser heat flux, such as the combustion chamber and high expansion ratios, higher allowable surface temperatures become more important.

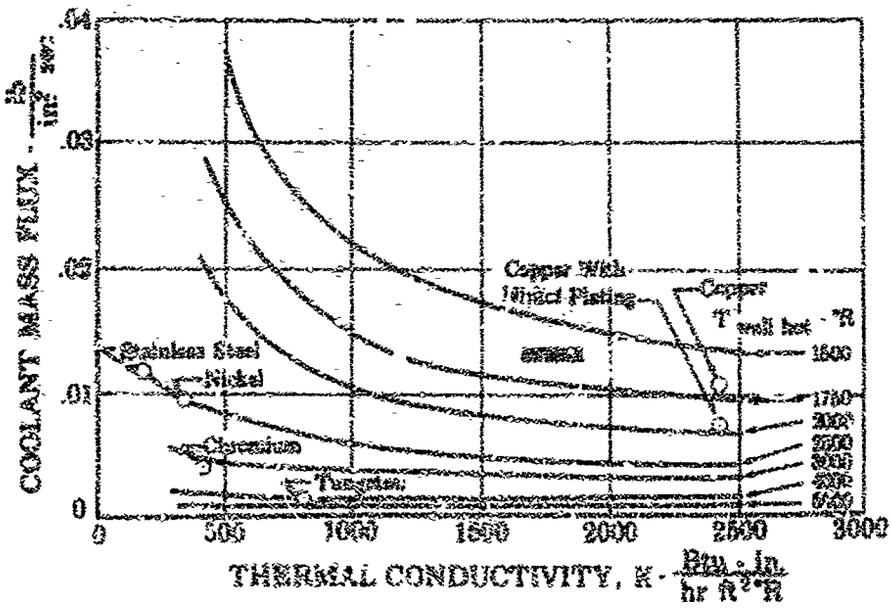


Figure 136. Grooved Wafer Cooling Requirements as Thermal Conductivity (Contraction Area Ratio Equal to 3.0) FD 18229

THIS PAGE CONTAINS SUBJECT MATTER COVERED BY A SECRECY ORDER WITH A MODIFYING "SECURITY REQUIREMENTS PERMIT" ISSUED BY U.S. COMMISSIONER OF PATENTS

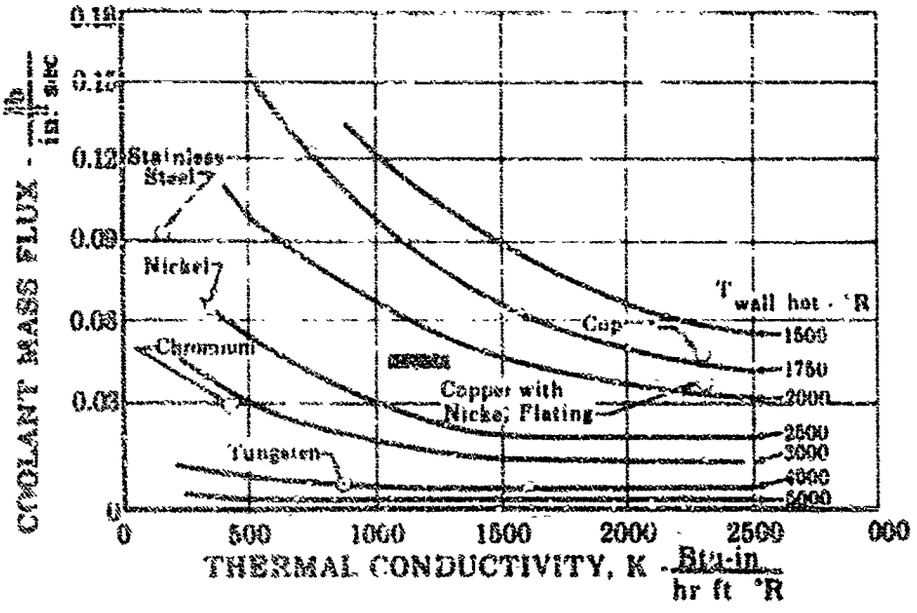


Figure 137. Grooved Wafer Cooling Requirements vs Thermal Conductivity (Expansion Area Ratio Equal to 1.0) FD 18236

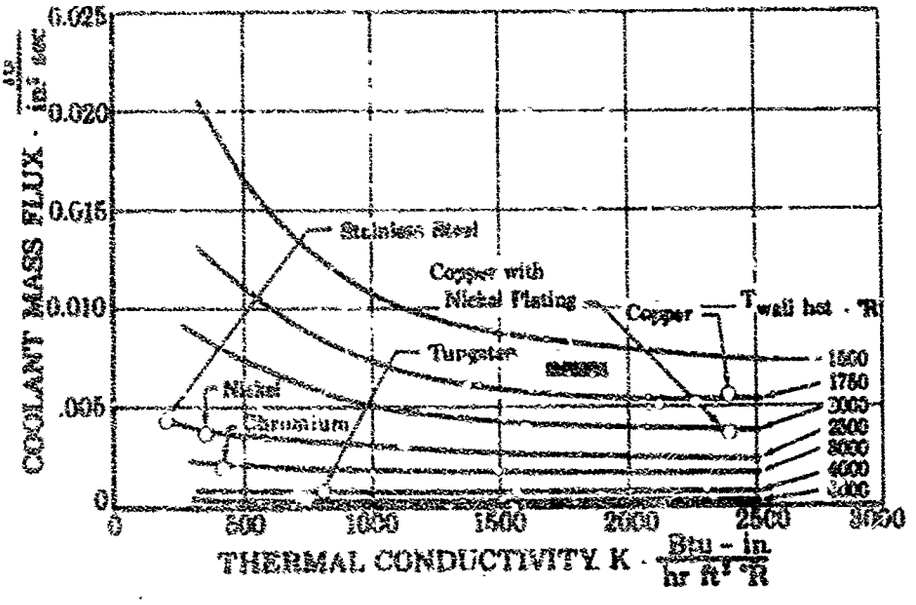


Figure 138. Grooved Wafer Cooling Requirements vs Thermal Conductivity (Expansion Area Ratio Equal to 4.0) FD 18235

(C) Table XXV. Grooved Wafer Relative Cooling Requirements for Selected Materials

Material	Maximum Allowable Temperature, °R	Thermal Conductivit,, $\frac{\text{Btu-in.}}{\text{ft}^2\text{-sec-}^\circ\text{R}}$	Relative Coolant Flow Rate			
			Combustion Chamber, ($\epsilon_c = 3$)	Throat ($\epsilon_x = 1$)	$\epsilon_x = 4$	Relative Total
Copper	1700	2400	1.00	1.00	1.00	1.00
Copper with Optimum Nickel Coating	1700-Copper 2500-Nickel	2400	0.78	0.74	0.715	0.76
Nickel	2500	400	0.96	1.58	0.715	1.02
AISI 347	2500	200	1.20	2.23	0.79	1.38
Chromium	3100	420	0.45	0.65	0.39	0.49
Tungsten	4000	800	0.15	0.14	0.14	0.15

Note: The cooling flow rate requirements are relative to a copper chamber. All plates are assumed to have a 6-degree, 0.010- by 0.010-inch groove pattern.

3. Rigimesh Analytical Heat Transfer Model

(C) An analytical heat transfer program for Rigimesh was completed and a parametric study was conducted. The program model was derived from the work done by R. P. Berniker under USAF Contract AF 49(638)-245. Berniker's technique predicts internal heat exchanger efficiency and temperature gradients in a porous media such as Rigimesh, taking into account the thermal conductivity, internal geometry, and coolant properties. Certain refinements had to be made to the model to produce the analysis of a wafer type heat exchanger. To use the same model in applying the Berniker technique to Rigimesh, the effective flow path length and diameter had to be determined. It was necessary to first determine the flow/pressure-drop relationship and porosity of the Rigimesh, which was available for use with the cooled convergent nozzle test sections. The results of this study are shown in figure 139, which also shows the corresponding mass flux required for the new 50K chamber wafer liner. The indicating reduction in the coolant required for Rigimesh as compared to wafers is attributed to the increased internal heat transfer efficiency achieved with the more favorable heat transfer surface area to volume relationship of Rigimesh. The coolant, by being injected into the boundary layer more uniformly and with less turbulence by the Rigimesh than by the wafers, should decrease the hot side wall heat transfer coefficient and permit a further reduction in coolant.

4. Material Evaluation

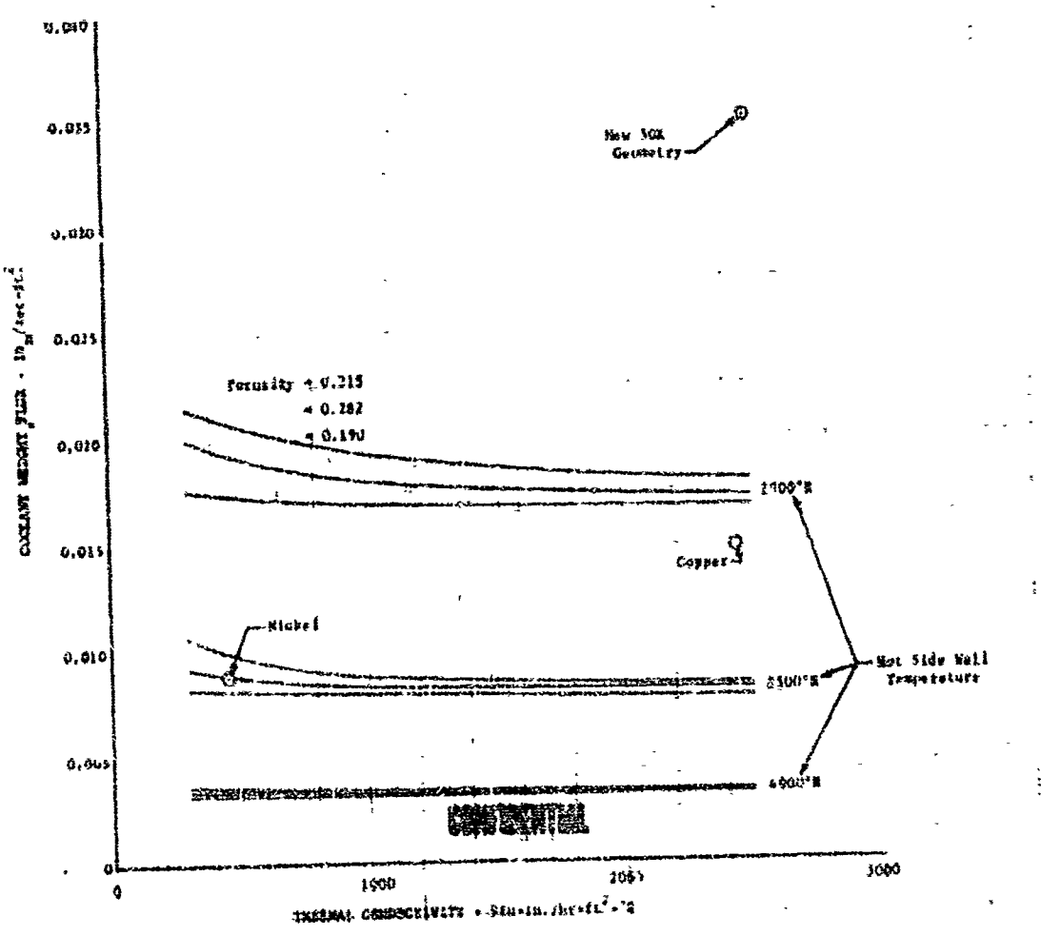
(C) Materials were evaluated as candidates for the spiral grooved wafer and Rigimesh wafer cooling concepts. In addition, thermal barriers plated on the inside diameter surfaces of the grooved wafers were investigated and attractive candidates were tested in the film-cooled copper liner (test No. 50SC5). Further study into thermal barriers was discontinued because of the question of barrier cyclic life in application to high cyclic life chambers. Table XXVI outlines rating considerations and evaluation results are included in table XXVII.

(U) Nickel offers reduced cooling requirements in both the grooved wafer and Rigimesh chambers, except in the grooved wafer throat region compared to copper because of the higher allowable wall temperature, as shown in figure 140. In addition, the superior ductility of nickel (205% elongation at 2500°R) is desirable for long cyclic life. The material can be fabricated as a wafer or Rigimesh.

(C) Grooved wafer and Rigimesh wafer cooling requirements can be significantly reduced by using refractory materials that increase the allowable surface temperatures above 3000°R, as shown in figure 141. Molybdenum and tungsten alloyed with rhenium appear to be the most attractive of the high temperature refractory materials. Addition of rhenium to both tungsten and molybdenum prevents the ductile-to-brittle transition of the recrystallized pure material. Both alloys can be produced as sheet or wire and production is becoming commercially feasible. The feasibility of fabrication into wafers or Rigimesh needs to be demonstrated.

CONFIDENTIAL

THIS PAGE CONTAINS SUBJECT MATTER COVERED BY A SECRECY ORDER WITH A MODIFYING "SECURITY REQUIREMENTS PERMIT" ISSUED BY U.S. COMMISSIONER OF PATENTS



DF 54498

Figure 159. Rig/nesh Coolant Mass Flux vs Thermal Conductivity (Nozzle Throat)

(U) Table XXVI. Wafer and Rigimesh Properties

Property	Requirement
Thermal Conductivity and Melting Tempera ure	Properties combination that allows cooling mass fluxes equal to or less than those possible with copper wafers, as predicted by an analytical heat transfer model. (See figure 141.)
Density	Greater than copper only if cooling mass flux can be significantly reduced or higher strength permits same overall weight by reducing thickness.
Hydrogen Corrosion Resistance	Must be excellent.
Oxygen Corrosion Resistance	Not required because walls are transpiration cooled with H_2. Resistance is desirable.
Ductility	Sufficient to ensure that low cycle fatigue life requirements can be met.*
Strength	Desirable to minimize weight but high strength not essential.
Fabrication:	
Machineability	Capable of being machined
Bonding	Practical
Photoengraving (wafer application)	Capable of being photoengraved
Rigimesh Requirements	Possesses sufficient elongation (>10%) to allow drawing and weaving. Capable of being sintered.
Material Cost	Not prohibitive

*Axial and circumferential thermal reliefs may be feasible to decrease ductility requirements.

(U) Table XXVII. Wafer Rigimesh Material Evaluation

Material	Thermal Conductivity, $\frac{Btu\text{-}in.}{hr\text{-}ft^2\text{-}°R}$	Melting Temperature, °R	Density, lb/ft^3	Corrosion Resistance in Hydrogen	Percent Elongation	Potential Wafer or Rigimesh Material	
						Yes	No
Beryllium	624 (1500°R)	2805	110	Good	7 (1935°R)		4,5
Beryllium-Cu	1260 (528°R)	2100	513	Good	10 (1160°R)		1,7 (Copper)
Chromium-Cu	900 (528°R)	2605	555	Good	35 (1935°R)		1
Chromium	420 (2000°R)	3865	448	Good	< 3 (540°R)		4,5
Cobalt	480 (528°R)	3180	555	Good	20 (2160°R)		1,5
Columbium	450 (3000°R)	4935	536	Unsatisfactory	42 (2360°R)		3
Copper	2435 (1500°R)	2440	557	Good	25 (1250°R)	X	
Iridium	1008 (600°R)	4910	1400	Good	80 (2290°R)		3
Iron	276 (1500°R)	3255	490	Good	>50 (1860°R)		1
Molybdenum	617 (3000°R)	5190	636	Good	< 1 (540°R)		4
Molybdenum-30% Rhenium	600 (3000°R)	6400	1042	Good	9 (3500°R) 4 (540°R)	X	
Nickel	354 (1500°R)	3105	555	Good	205 (2460°R)	X	
Platinum	468 (2000°R)	3675	1335	Unsatisfactory	---		2,3,6
Rhodium	1056 (550°R)	4020	780	Good	---		2,6
Stainless Steel (AISI 347)	154 (1500°R)	3000	500	Good	80 (2260°R)		1
Tantalum	540 (3000°R)	5885	1040	Unsatisfactory	>20 (3960°R)		2,3
Tungsten	744 (3000°R)	6630	1205	Good	< 1 (540°R)		4
Tungsten - 25% Rhenium	700 (3000°R)	6070	1227	Good	10 (3370°R) > 6 (540°R)	X	
TD Nickel	400 (2600°R)	3110	576	Good	5 (2460°R)		4,7 (Nickel)

Notes: (1) Predicted cooling mass flux requirements too high
(2) Predicted chamber weight excessive
(3) Hydrogen corrosion or embrittlement resistance insufficient
(4) Ductility insufficient to achieve cyclic life requirements
(5) Fabrication impossible or possible only with excessive difficulty
(6) High material cost
(7) Similar material with superior rating.

UNCLASSIFIED

UNCLASSIFIED

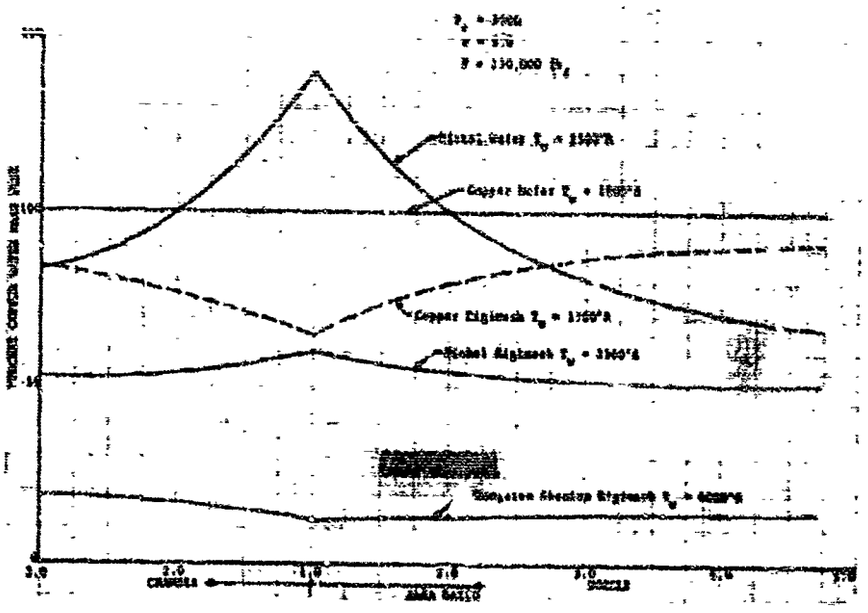


Figure 140. Wafer and Rigimesh Coolant Mass Flux Requirements

DF 57175

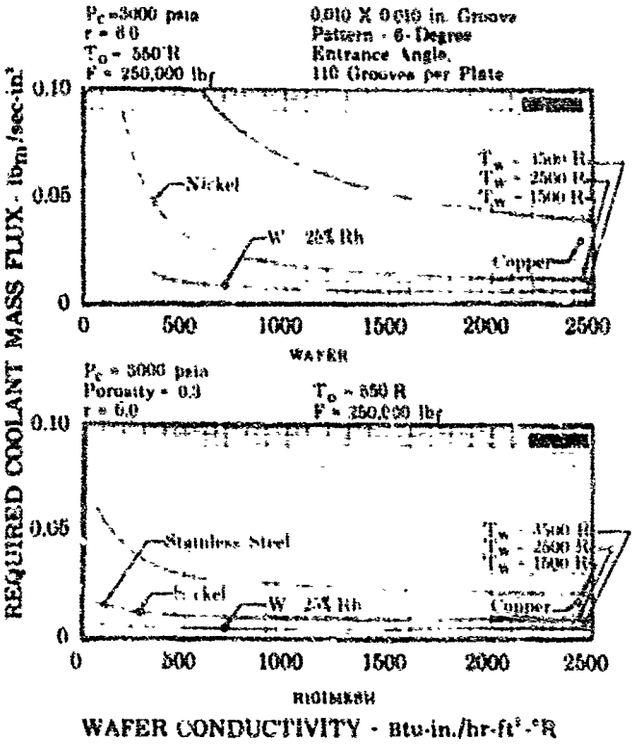


Figure 141. Effect of Thermal Conductivity and Surface Wall Temperature on Wafer and Rigimesh Thrust Cooling Requirements

FD 21444

5. Cooled Convergent Tests Sections

(U) Attractive cooling configurations that analytically promised advantages over the copper grooved wafer concept were designed and partly fabricated. The test sections comprise a 1-3/4-inch axial length convergent nozzle section extending 1 1/4 inch downstream of the throat and were scheduled for tested in the 50K uncooled chamber as shown in figure 142. A copper combustion chamber liner with a coolant film slot establishes a coolant boundary layer upstream of the test section.

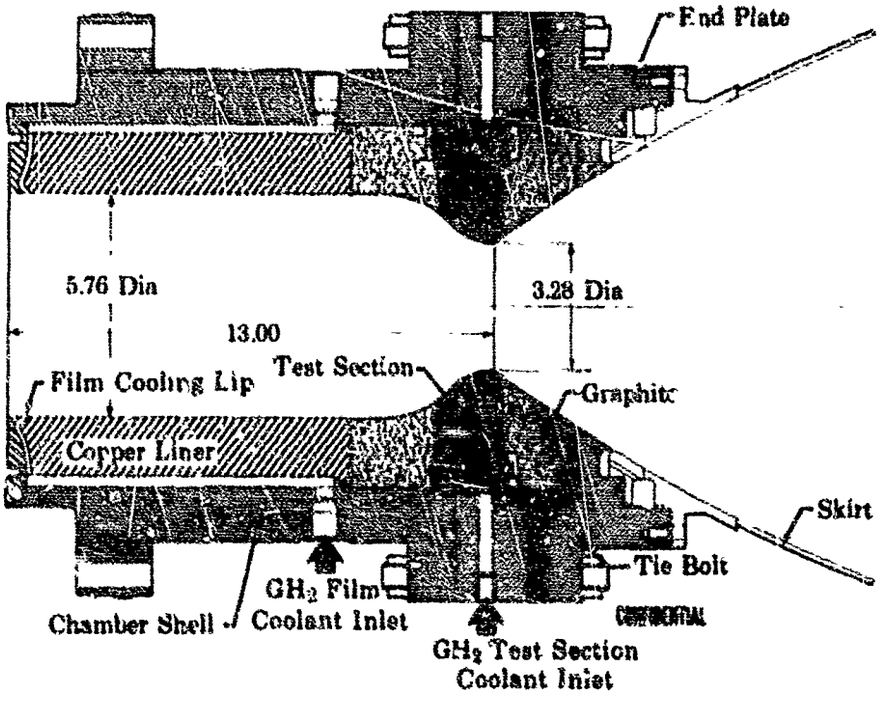


Figure 142. Cooled Convergent Nozzle Test Rig FD 15964

(U) The following four test sections were in the process of fabrication:

1. Copper wafers
2. Nickel wafers
3. Copper Rigimesh
4. Nickel Rigimesh.

(C) The copper and nickel wafer test sections are shown in figure 143. The copper test section serves as a comparison standard. The nickel would evaluate the cooling requirements of a higher melting temperature, but lower conductivity material, and provide data for the verification of the analytical heat transfer model. The test sections are divided into seven zones, consisting of four plates each. Coolant flow is metered to each zone by four removable metering orifices. The spiral-groove passages will be 6-degree, 0.010- by 0.010-inch with 50 slots per plate identical to the current cooled chamber design.

THIS PAGE CONTAINS SUBJECT MATTER COVERED BY A SECRECY ORDER WITH A MODIFY NO. SECURITY REQUIREMENTS PERMIT ISSUED BY U.S. COMMISSIONER OF PATENTS

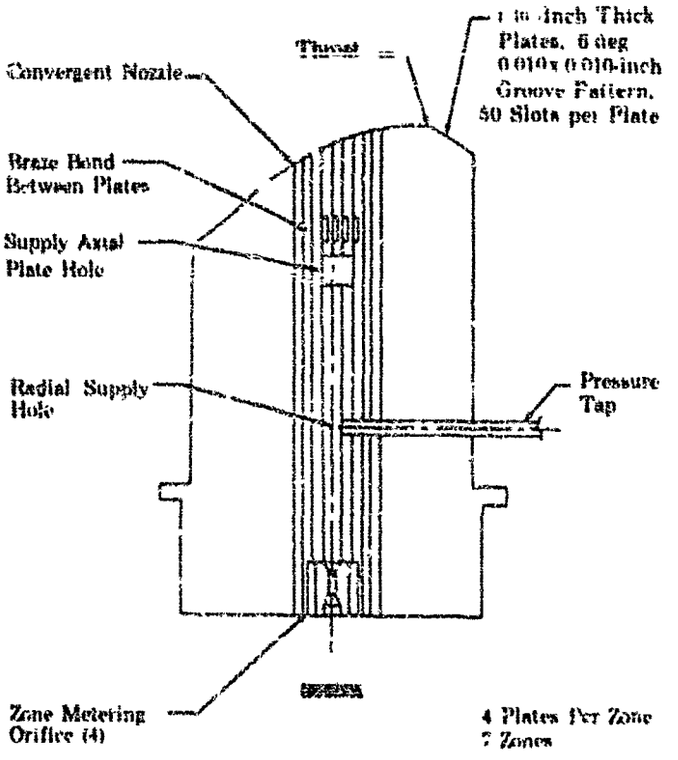


Figure 143. Transpiration Cooled Convergent Test Section FD 18271

(C) The copper and nickel Rigimesh test sections, shown in figure 144, were selected to demonstrate the Rigimesh cooling concept and evaluate cooling requirements of a higher melting temperature but lower thermal conductivity material relative to copper. The Rigimesh consists of seven 1/4-inch thick plates, 1/2-inch in radial thickness, and electron beam welded to a support plate. Coolant flow is metered to each plate by four removable metering orifices. The Rigimesh was fabricated with each ply rotated at a 45-degree angle relative to the adjacent ply to provide a more uniform radial flow. Three different porosities were ordered: (1) 1000 scfm air at 35 psia to atmosphere; (2) 3000 scfm air at 40 psia to atmosphere; and (3) 6000 scfm air at 45 psia to atmosphere. The porosities were established to simulate the Reynolds number of the starting flow of the cooled chamber.

(C) Fabrication of cooled convergent nozzle test sections was discontinued as a result of contract redirection of effort. The copper wafer detail operations were 90% complete. Photoengraving of the nickel wafer material was 20% completed. All the copper and nickel Rigimesh material was received and fabrication was initiated in the PWA experimental shop. Samples were flow calibrated and were determined to be consistent with the vendor's calibration.

CONFIDENTIAL
THIS PAGE CONTAINS SUBJECT MATTER COVERED BY A SECRECY ORDER WITH A MODIFIED SECURITY REQUIREMENTS PERMIT ISSUED BY U.S. COMMISSIONER OF PATENTS

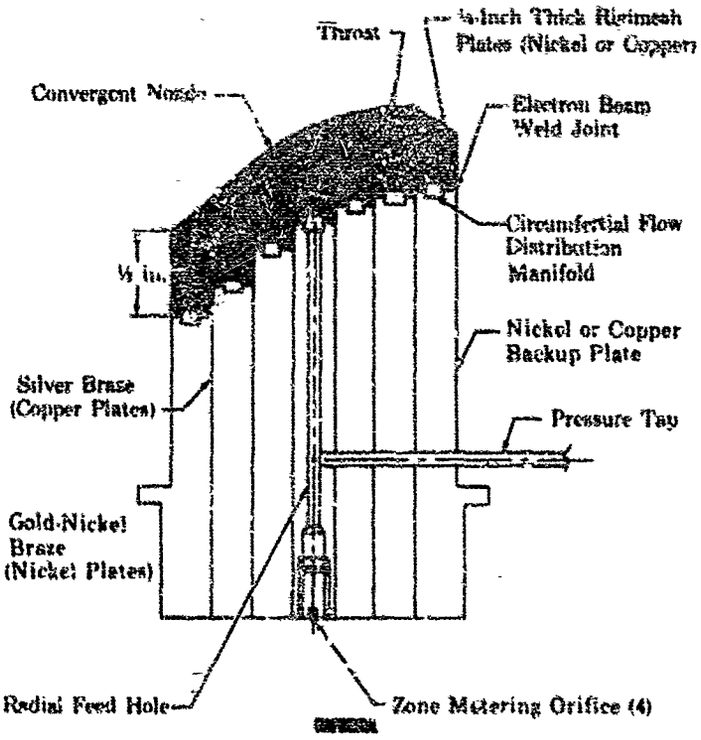


Figure 144. Rigimesh Cooled Convergent Test Section FD 18273

F. TEST FACILITIES AND PROCEDURES

1. B-28 Test Facility

(U) This test stand is a part of the Liquid Propellant Research Facility (LPRF) at FRDC. The stand consists of three horizontal test bays rated for 1000, 10,000, and 50,000 pounds of thrust. Propellant supply pressure capabilities extend beyond 5000 psi. The Liquid Propellant Research Facility is shown in figure 145.

(U) The B-28 test stand, which is the 50,000-pound thrust bay in the center of the LPRF, was the stand used for the cooling investigation and two-position nozzle tests.

(U) A basic schematic of the B-28 test stand is shown in figure 146. Servohydraulic-actuated propellant run valves are located on the thrust mount for close-coupling to the preburner and main chamber.

(U) A 50-channel digital sequencer is used for test sequencing and a 64-amplifier analog computer is programmed to provide propellant servohydraulic-actuated run valve ramping and pressure control. Over 100 measurement channels are available in the facility. Data measurements include pressure, temperature, thrust, and flow rate. Excellent measurement precision and response are available through a 96-channel, low-level input, analog-to-digital converter that records on magnetic tape.

Thirty-six oscillograph channels and 10 channels of direct-inking strip charts are also available. Isolation amplifiers are provided to permit redundant analog recording of 10 channels of digital data. A separate system - including an Ampex FR-100 high speed 14-track tape recorder, amplifiers, and transducers provides high-frequency data capability of 20,000 cycles per second. The data acquisition system is shown schematically in figure 147. A 6-channel closed circuit TV system is available for test stand observation. A telescope can also be used for direct view of the exhaust flame.

(U) An important feature of the data system is the ease of changeover from one test facility to another. Channel selection and electrical calibration are accomplished by remote switching. Signal conditioning equipment, transmission cable, and recorder are selected through quickchange patch panels.

2. 50K Test Procedures

(U) The test sequence control schematic is shown in figure 148. A 50-channel digital sequencer was used for test sequencing, and a 40-amplifier analog computer was used to provide propellant run valve ramping and pressure control. The main propellant run valves were servohydraulic actuated and are close-coupled to the thrust chamber.

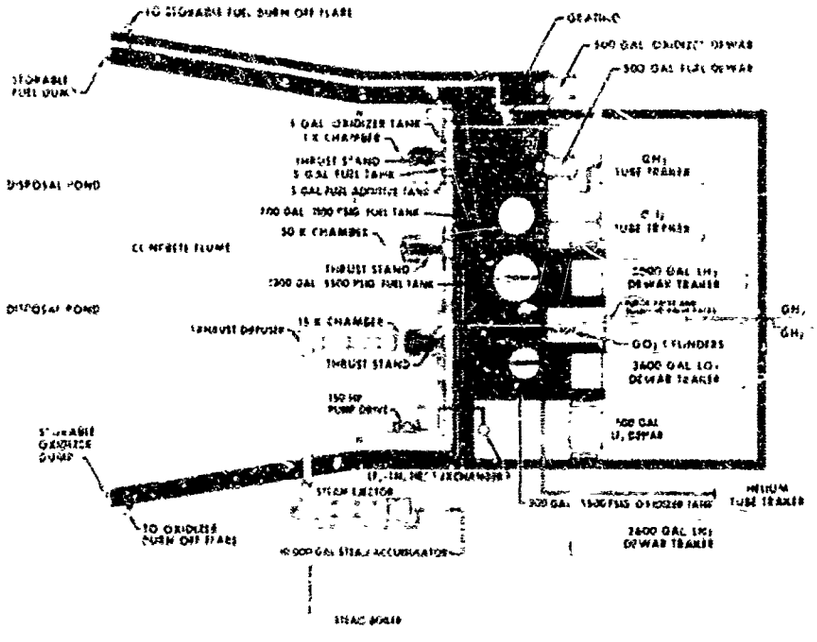


Figure 145. Liquid Propellant Research Facility Test Stand Layout

ID 5455B

UNCLASSIFIED

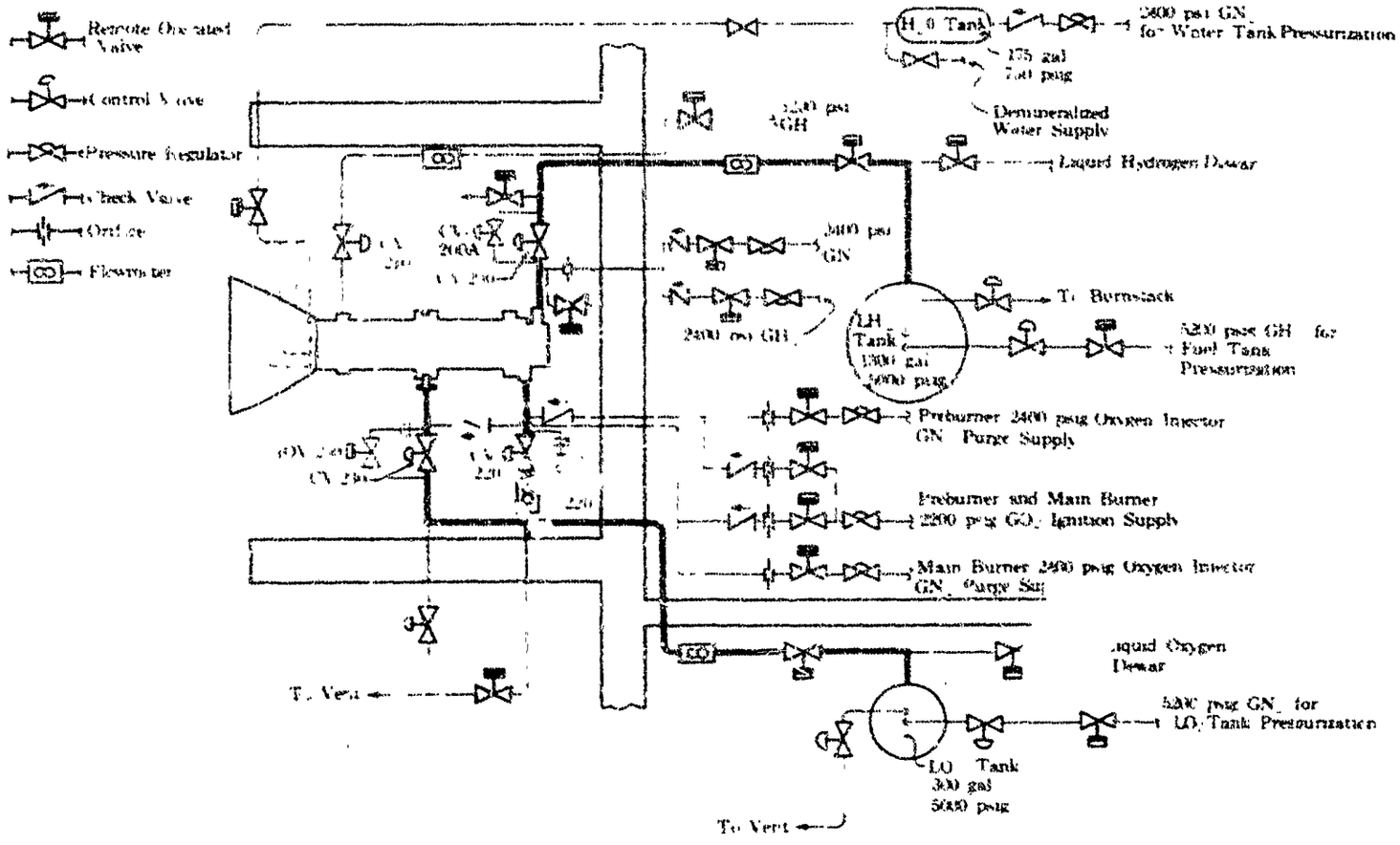


Figure 1.6. B 28 Test Stand Schematic

FD 10805A

UNCLASSIFIED

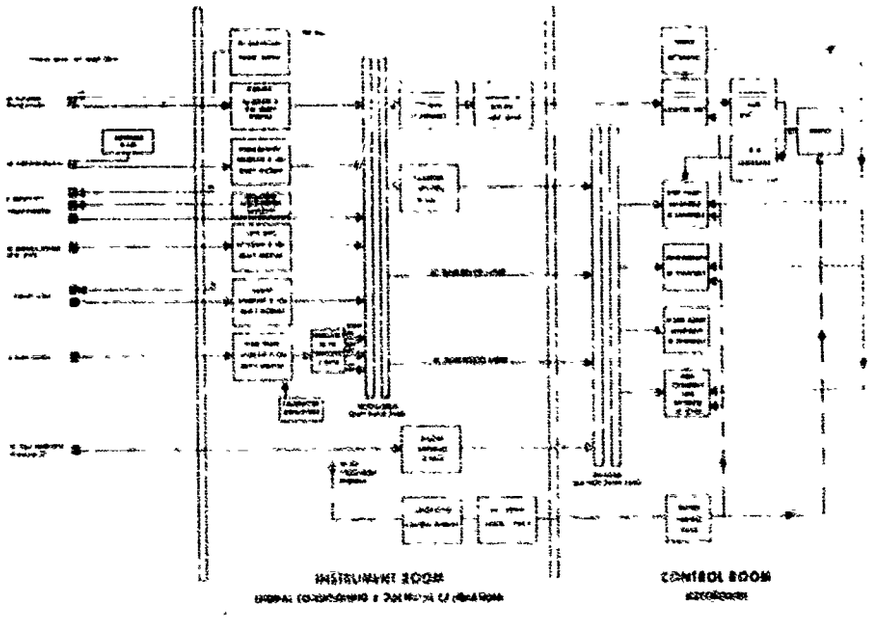


Figure 147. B-28 Data Acquisition System Schematic FD 5456

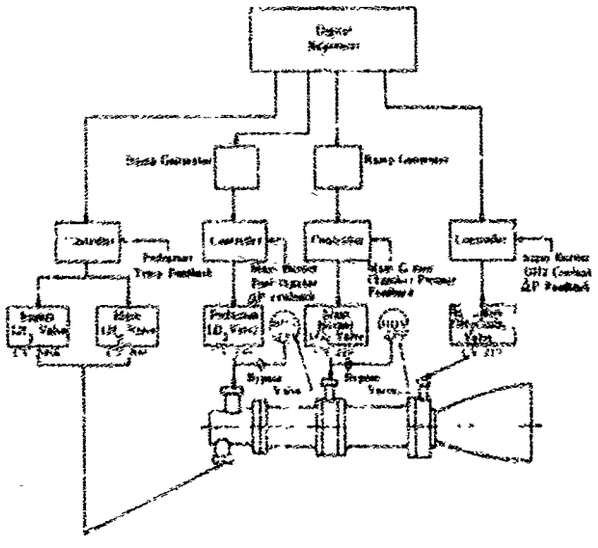


Figure 148. 50K Thrust Level Staged-Combustion Test Rig Control System FD 12784B

(U) The staged-combustion test sequence is shown in figure 149. Smooth and reliable ignition and acceleration to full chamber pressure were achieved by a stepped-type starting procedure. Pilot ignition gaseous oxygen was provided to the preburner and main burner injectors and gaseous hydrogen to the preburner injector from sources at approximately 1000 psig. Flows to the injectors were controlled by small choked orifices in each of the supply lines. The orifices were sized to provide flows producing approximately 100 psia main chamber pressure when ignited at a mixture ratio of approximately 0.5 in the preburner and 4.0 in the main chamber. Injector nitrogen purges were sequenced off when the pilot ignition flows were sequenced on. Ignition in the preburner was initiated by a spark plug mounted in the chamber wall, and in the main chamber by autoignition between the main burner injected gaseous oxygen and the hot preburner gases. Satisfactory ignition of the pilot ignition flows were sensed in the preburner by thermocouple probes and in the main chamber by a throat-inserted burnwire. If satisfactory ignition was not sensed during a prescribed time interval of the test sequence, the test was automatically aborted before main propellant flows were started. After satisfactory ignition was verified, orificed bypass lines around the main liquid oxygen run valves were sequenced open to provide repeatable liquid oxygen injector fill transients. A small liquid hydrogen control valve was used to control the liquid hydrogen flow to the preburner injector during the liquid oxygen injector fill portion of the acceleration transient to maintain the desired preburner combustion gas temperature. The pilot gaseous ignition flows were cut off by check valves as the injector pressures increase above supply pressures.

(U) A ramped main chamber pressure control signal (to full chamber pressure) was applied after the inlet lines and the injector were full of liquid propellants. The main chamber liquid oxygen run valve was opened to provide the desired main chamber pressure, controlled by a feedback error signal (produced by comparing the measured main chamber pressure to the desired chamber pressure ramp control signal). The preburner liquid oxygen run valve was programmed to maintain a predetermined hot gas pressure drop across the main injector. The preburner liquid hydrogen run valve was controlled to provide the desired preburner combustion gas temperature.

(U) Shutdown from full chamber pressure was controlled in the same manner as the acceleration transient, except that the fuel run valve was lagged to assure a fuel-rich shutdown. The liquid oxygen run valves were stepped closed from the near-closed position to ensure a clean shutoff of the liquid oxygen.

(U) The gaseous hydrogen transpiration coolant for the main burner combustion chamber was supplied directly to the [illegible] flow was controlled by a servohydraulic valve in the coolant supply line, controlling to a scheduled differential pressure between chamber pressure and coolant inlet pressure. Controlling the coolant inlet pressure as a function of chamber pressure assure the desired coolant flow throughout the test sequence without the uncertainty of attempting to match pressure ramps.

(U) The large area ratio nozzle skirt was formed of sheet metal and was film-cooled with water during the acceleration to the desired test conditions. The water was shut off during the data period of the test.

UNCLASSIFIED

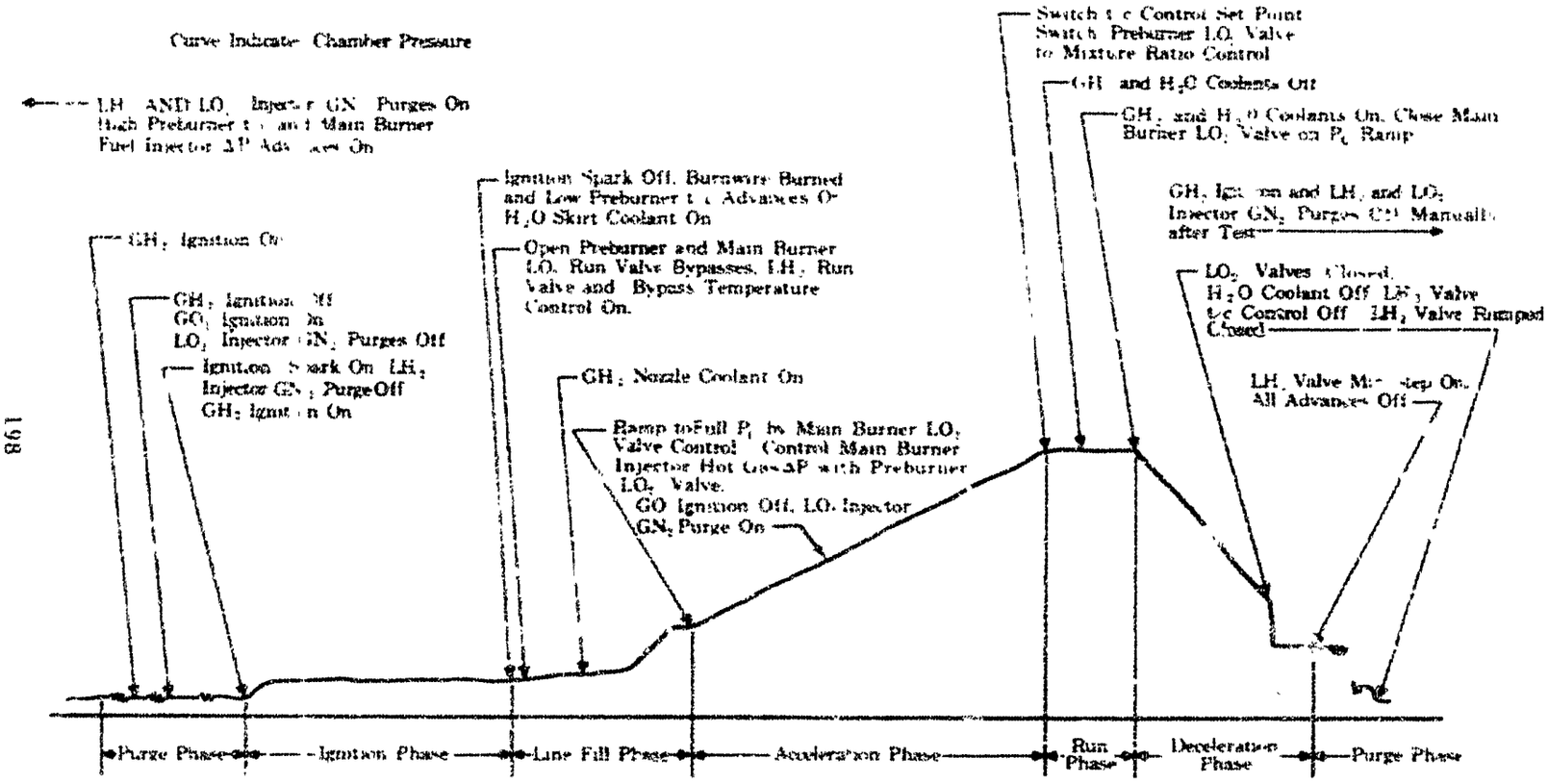


Figure 1-6. 50K Thrust Uncooled Staged-Combustion Test Sequence

TD 12741A

UNCLASSIFIED

SECTION VII
TURBOPUMP COMPONENTS

A.	INTRODUCTION	199
B.	SUMMARY AND CONCLUSIONS	199
C.	HARDWARE DESCRIPTION	200
	1. Bearing Test Rig	200
	2. Bearing Configuration Selection	201
D.	TEST PROGRAM AND TEST RESULTS	212
	1. Cage Spin Testing	212
	2. Cage and Bearing Geometry Screening	217
	3. Endurance Tests	236
E.	TEST FACILITY AND PROCEDURES	244
	1. Test Facility	244
	2. Test Procedures	244

SECTION VII
TURBOPUMP COMPONENTS

A. INTRODUCTION

(C) The objective of the turbopump components program was to demonstrate a 10-hour bearing life at the design speed and the maximum radial load on the bearing configuration established for the preliminary 250K fuel turbopump design. The fuel turbopump bearing configuration and requirements as established for the preliminary 250K turbopump design are (1) 55mm inside diameter roller bearing, (2) design speed of 48,000 rpm, and (3) maximum radial load of 1700 lb.

B. SUMMARY AND CONCLUSIONS

(C) The turbopump bearing test program was composed of three phases; (1) spin tests to provide a relative ranking of mechanical integrity of candidate cages, (2) cage and bearing geometry screening tests, and (3) endurance testing of the selected bearing configuration with AISI 440C (AMS 5630) bearings to demonstrate a 10-hour life capability.

(U) Eight spin tests were conducted to provide a relative ranking of mechanical integrity of candidate cages. Armalon and Polyimide SP-1 were the only materials tested that exceeded the cage design speed (approximately 25,000 rpm) without external armor and these materials were selected for evaluation in the bearing rig tests. Nylon-M with armor was also evaluated because of good experience with this material in other programs and its characteristic for transferring lubricant to other elements of a bearing.

(U) Eleven tests were conducted for cage and bearing geometry screening tests. As a result of these tests, a bearing configuration was selected for endurance testing that consisted of AISI 440C material rollers and races, and an outer-race-piloted Armalon Cage with 0.040-inch total roller end to inner race flange clearance. Negative internal radial clearance was used to provide roller preload.

(C) A total of 12 hours and 35 minutes of endurance testing was accumulated on the second roller bearing test in the reaction position (85% load). This bearing remained in excellent condition with roller end wear less than 0.001 inch. The first roller bearing failed because of roller skewing at 1 hour and 32 minutes. Three bearings were tested in the load ring position and these failed because of roller skewing at 7 hours and 26 minutes, 1 hour and 19 minutes, and 3 hours and 50 minutes, respectively, during their endurance testing.

(C) This program was limited both in number of tests and number of bearing configuration variables tested but the following conclusions and recommendations are made:

1. A life of 10 hours for a 55mm roller bearing with a DN of 2.64×10^6mm rpm and 1700 lb radial load appears feasible based on the 12 hours and 35 minutes duration achieved

with one reaction bearing, however, further development is necessary to solve the problem of roller skewing.

2. Roller end wear can be minimized or effectively eliminated by techniques similar to those employed during these tests.

3. The failure of two slave ball bearings on the drive turbine and three roller bearings in the load ring location of the test rig, indicate that additional testing and modifications to the test rig are required.

4. Additional testing is required to demonstrate high reliability and durability of the test bearings in both locations of the test rig.

C. HARDWARE DESCRIPTION

1. Bearing Test Rig

(U) A cross section of the bearing test rig for this program is shown in Figure 150. Figure 151 is a photograph of the test rig showing the gaseous nitrogen drive turbine and the pneumatic actuator for applying the radial load to the test bearings. This rig is capable of testing two roller bearings at the same time to speeds in excess of 50,000 rpm with a radial load of 2500 lb.

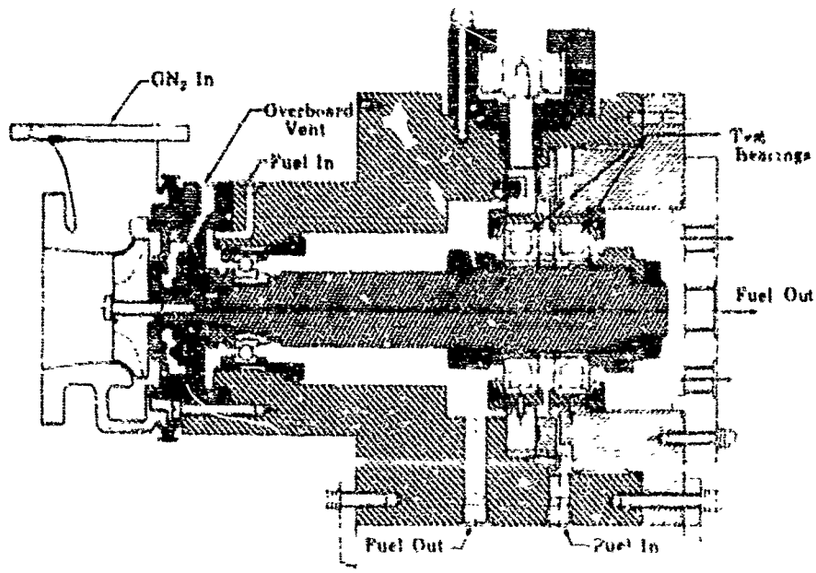


Figure 150. Roller Bearing Test Rig Cross Section FD 19278C

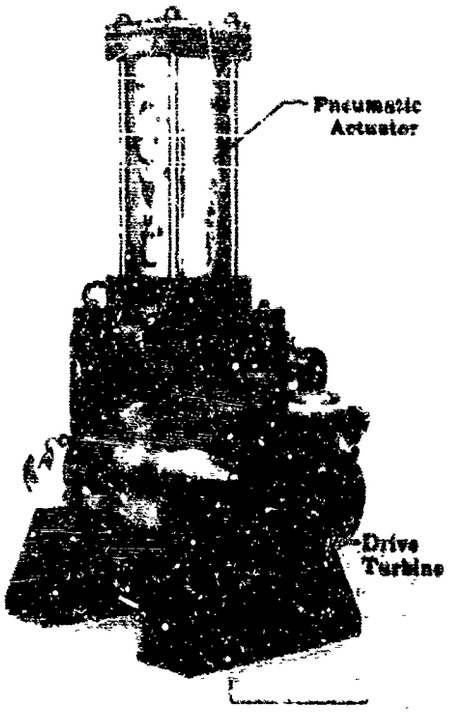


Figure 151. Roller Bearing Test Rig FD 70647

(U) The roller bearing nearest the turbine is the load bearing and is mounted in a load ring that moves radially under the applied radial load. The squareness of this load ring is maintained by a wave washer that holds the load ring against the mating face of the housing. The other roller bearing is the reaction bearing and absorbs 85% of the radial load applied to the load bearing. The remaining 15% of the radial load is applied to the slave ball bearing on the turbine drive end of the test rig. This ball bearing also absorbs the axial load of the rotor assembly.

2. Bearing Configuration Selection

(U) Based on experience in the fuel pump technology program under Contract NAS8-11714, a roller bearing was incorporated in the preliminary design of the 250K turbopump to provide increased radial stiffness to minimize any instabilities associated with the rotor bouncing or rocking modes.

(U) Spring rate and capacity characteristics of various ball, roller, and duplex bearing configurations were evaluated and compared to the requirements for the fuel turbopump. On the basis of this study, a 55mm x 100mm roller bearing configuration was selected for test evaluation.

(C) A turbopump design speed of 43,000 rpm and a shaft diameter of 55mm has been established in the module design, resulting in a DN requirement of 2.64 x 10⁶mm-rpm.

(U) The characteristics of ball bearings of the required size are presented in figures 152 through 160. Figure 152 shows the relationship of radial spring rate vs speed for various applied axial loads with zero radial load. The radial spring rate shows a significant decrease with increasing speed. This effect is caused by a change in ball contact angle because of centrifugal loading of the ball. Higher inner race contact angles result in a lower spring rate. Additional thrust load stiffens the bearing by reducing the effect of centrifugal loading on contact angle. The relationship of radial spring rate to radial load with 500 lb and with 1000 lb applied thrust loads is illustrated in figures 153 and 154. As radial load is increased, the contact angle of the bearing is reduced until a point is reached where the ball is riding near the bottom of the race groove. At this point, any effect of speed (centrifugal load) is essentially eliminated. Further increases in radial load increase stiffness because of increased ball to race contact area. Figure 155 shows the relationship of radial spring rate vs radial load for various classes of bearings. Significant differences in spring rate occur only for high radial loads (above 1500 pounds) where the bearing life would be compromised. Figure 156 shows the 10-hour load capacity curves for various classes of 55mm bearings. The largest bearing (55mm x 100mm) has the greatest capacity, and could be designed to operate at a maximum load of approximately 1300 pounds with 1000 pounds axial load. Figure 157 shows the relationship of radial spring rate vs radial load for various inside diameter sizes of the same class and figure 158 shows the corresponding 10-hour load capacity curves for these bearings. For these bearings, also, the spring rate is nearly the same, except at high radial loads that are in excess of the allowable load for the desired design life. The load capacity of this largest bearing is reduced below that attainable with the largest bearing with a 55mm bore diameter because the DN value is higher and the ball diameter is less. Figure 159 shows the relationship of radial spring rate vs radial load for various ball contact angles and figure 160 shows the corresponding 10-hour load capacity curves. While the smaller contact angle produces the stiffest bearing in the low radial load range because the centrifugal loading effects are minimized, radial load capacity is sacrificed for a given design life.

(U) These load capacity curves neglect the cage and were determined by the standard AFMBA method (Reference 4).

(C) [illegible] approximately 1300 lb as shown in figure 156, and the maximum radial spring rate is approximately 1.[illegible] x 10⁶ lb/in. as shown in figures 154, 155, 157, and 159 for a design life of 10 hours.

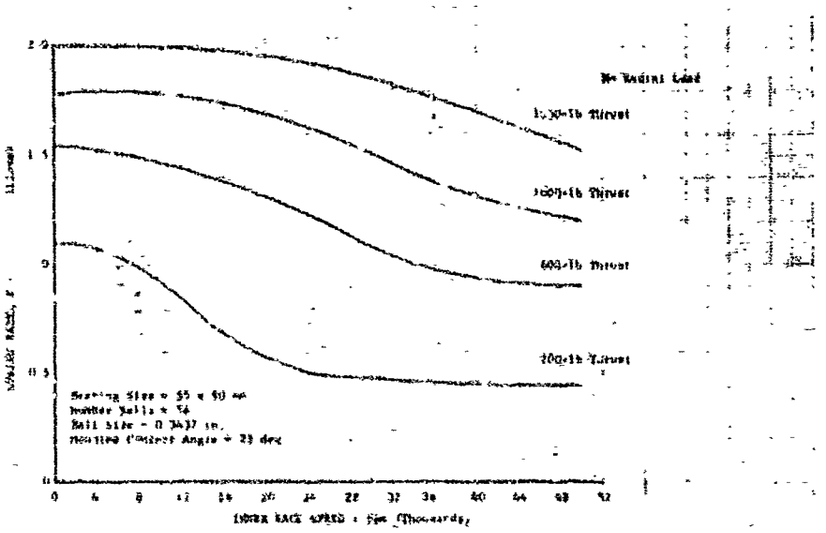


Figure 152. Radial Spring Rate vs Inner Race Speed (Single Ball Bearing) DF 52746

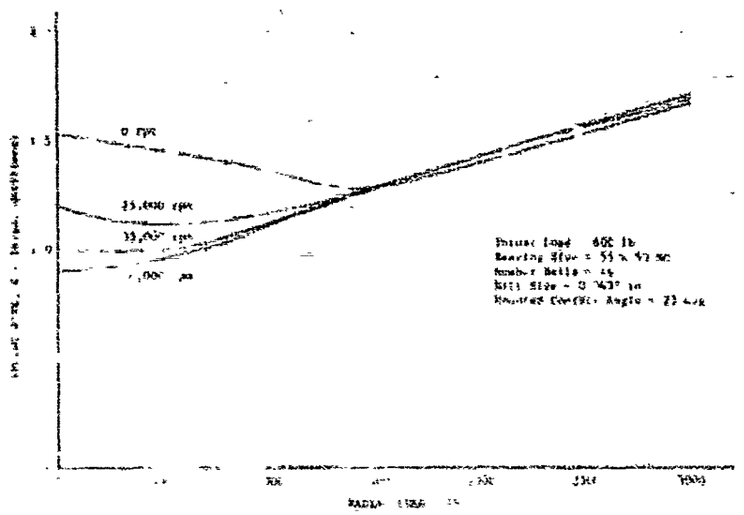


Figure 153. Radial Spring Rate vs Radial Load (Single Ball Bearing, 600 lb Thrust Load) DF 52747

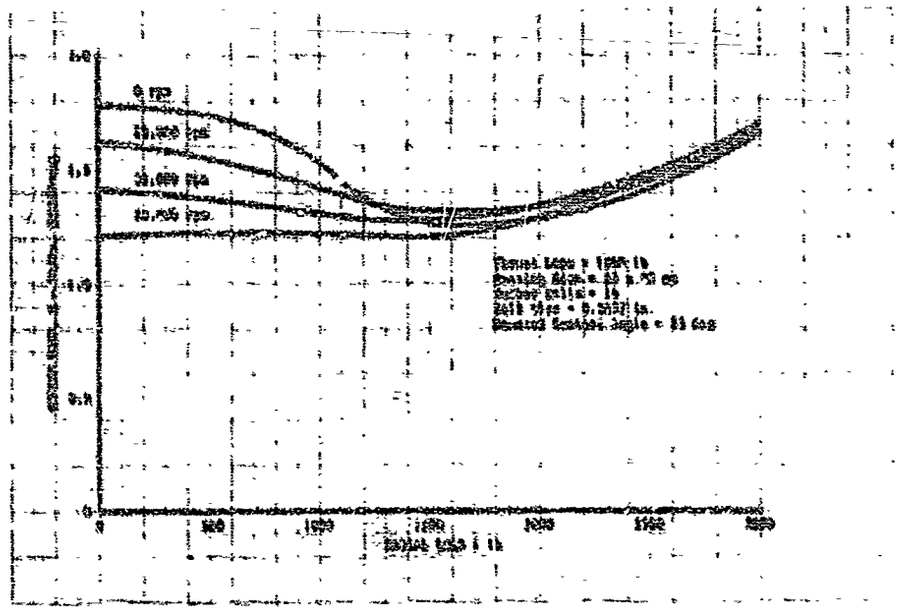


Figure 154. Radial Spring Rate vs Radial Load (Single Ball Bearing, 1000-lb Thrust Load) DF 52743

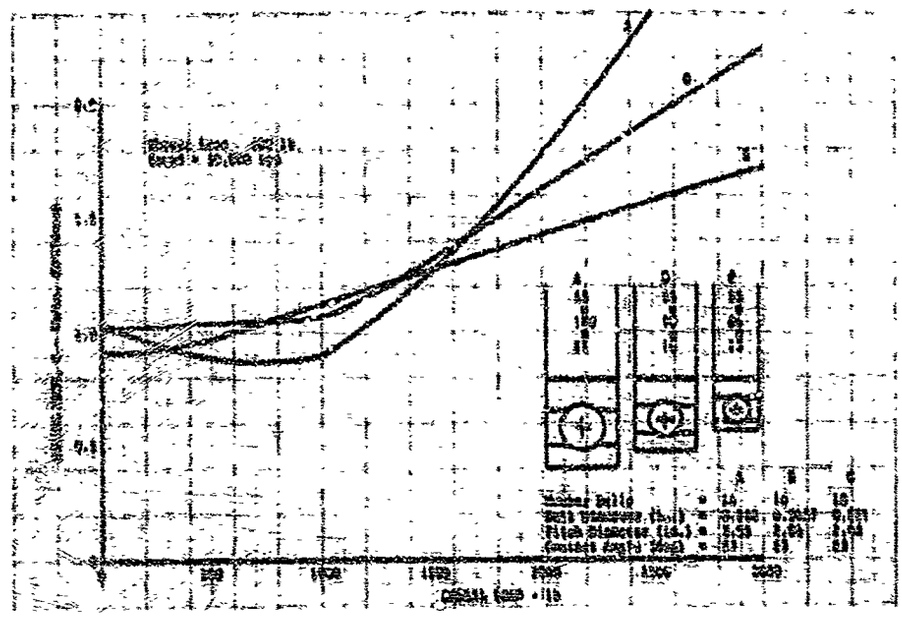


Figure 155. Radial Spring Rate vs Radial Load (Single Ball Bearing) DF 52708

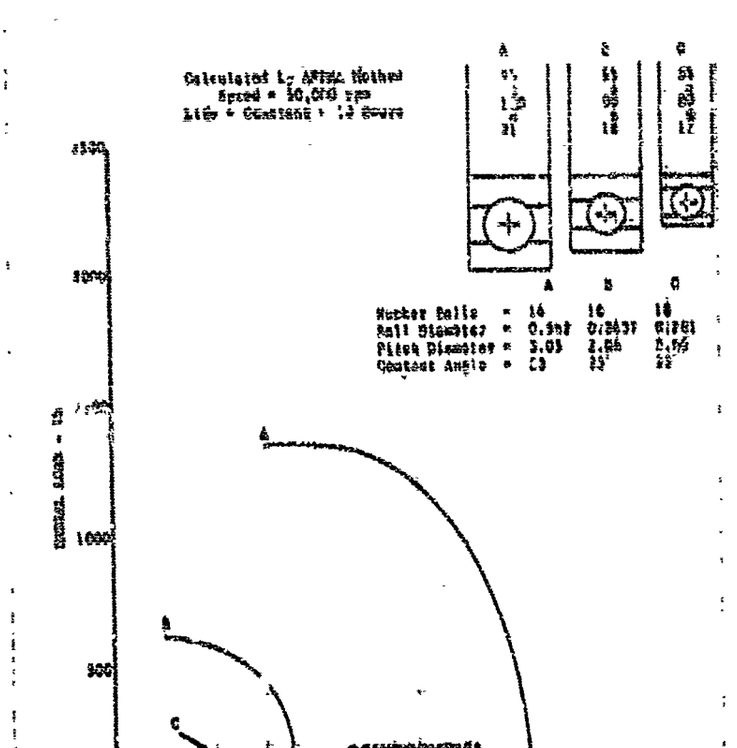


Figure 156. Ball Bearing Load Capacity DF 52745

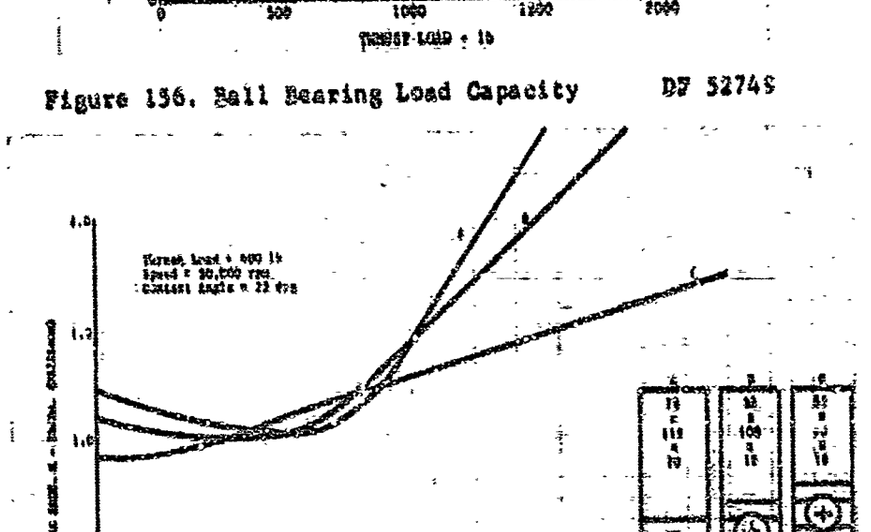


Figure 157. Radial Spring Rate vs Radial Load (Single Ball Bearing) DF 52746

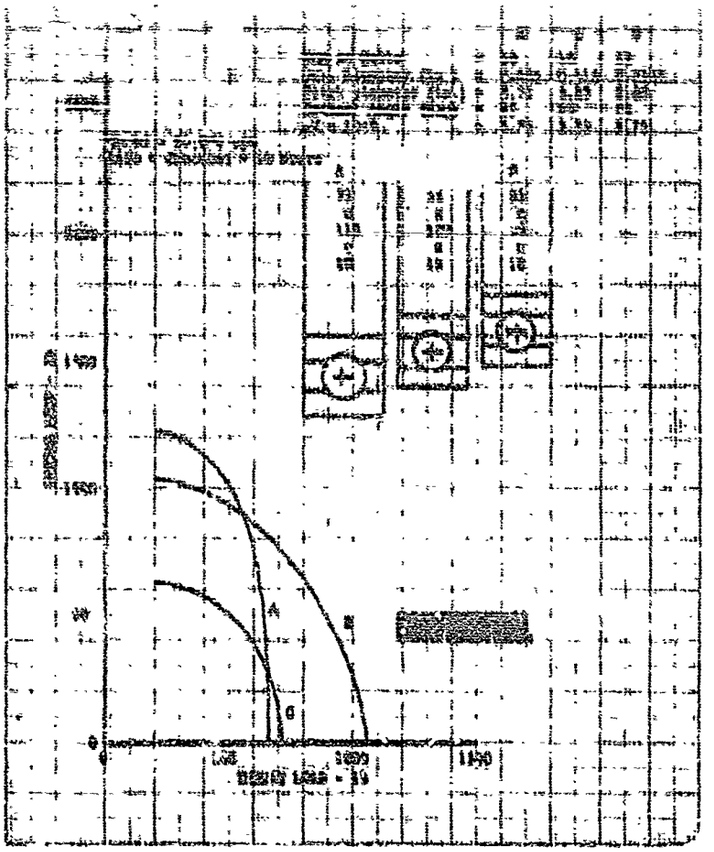


Figure 158. Ball Bearing Load Capacity DF 52791

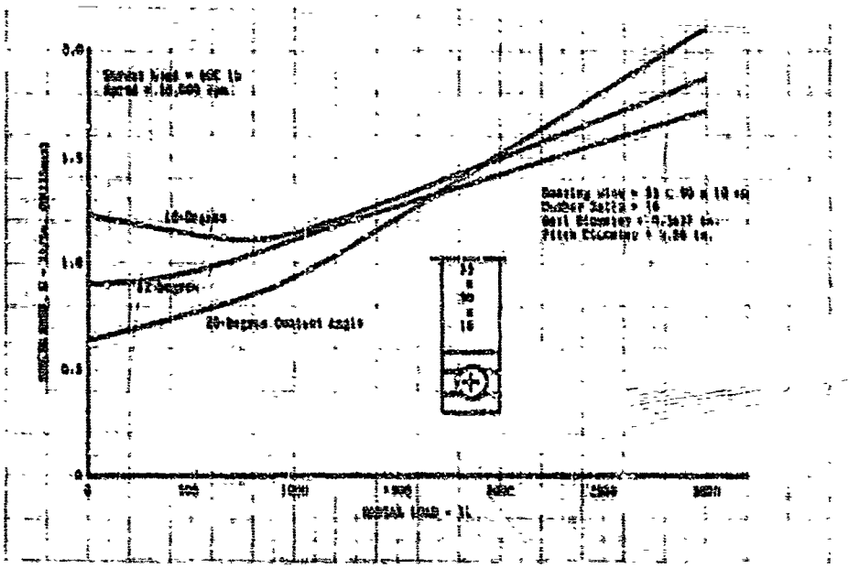


Figure 159. Radial Spring Rate vs Radial Load (Single Ball Bearing) DF 52790

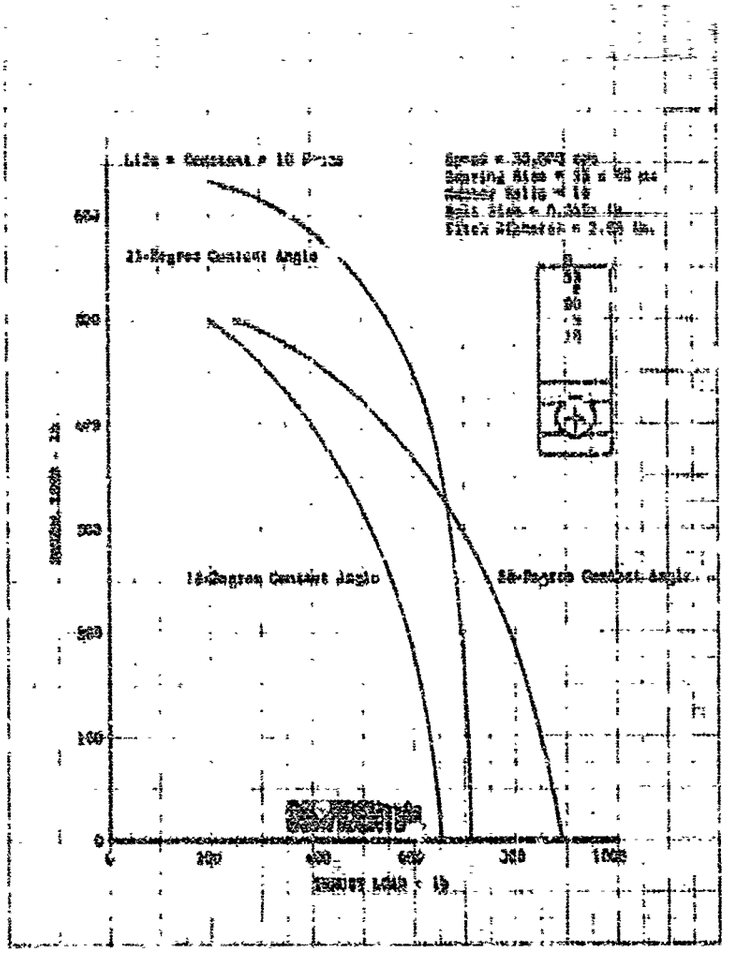


Figure 160. Ball Bearing Load Capacity DF 52783

(U) The characteristics of roller bearings of the required size are presented in figures 161 through 165. Figure 161 shows the relationship of radial spring rate vs radial load for various speeds. The radial spring rate of roller bearings is nonlinear with load but speed has very little effect. This nonlinearity is caused primarily by a varying number of loaded rollers as load is increased. At very low loads, if the bearing has internal clearance, only one roller is in contact. As the radial load is increased, additional rollers come in contact, approaching one half of the total. Figure 162 shows the relationship of radial spring rate vs radial load for various classes of bearings. The larger bearings exhibit no significant increase in spring rate. Figure 163 shows the load capacity curves for various classes of 35mm bearings. The largest bearing has the greatest load capacity for a given life because more roller area is in contact with the race (longer rollers). Figure 164 shows the relationship of radial spring rate vs radial load for various inside diameter sizes of the same class and figure 165 shows the corresponding load capacity curves. Here again, the larger bearing shows no major gain in spring rate. However, the radial capacity for a given life is less in the low to intermediate

CONFIDENTIAL

load range since the EF is higher. Figure 160 shows the relationship of radial spring rate vs radial load for various internal clearances. At low radial loads a slightly negative internal clearance can increase spring rate significantly by assuring contact of many rollers. As radial load is increased, this effect diminishes because some marginally loaded rollers will lose load as the heavily loaded rollers deflect.

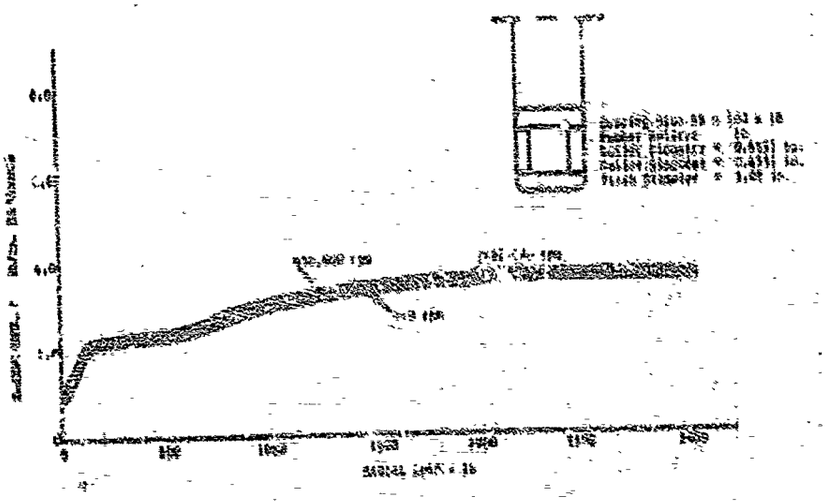


Figure 161. Radial Spring Rate vs Radial Load (Roller Bearings) DF 52792

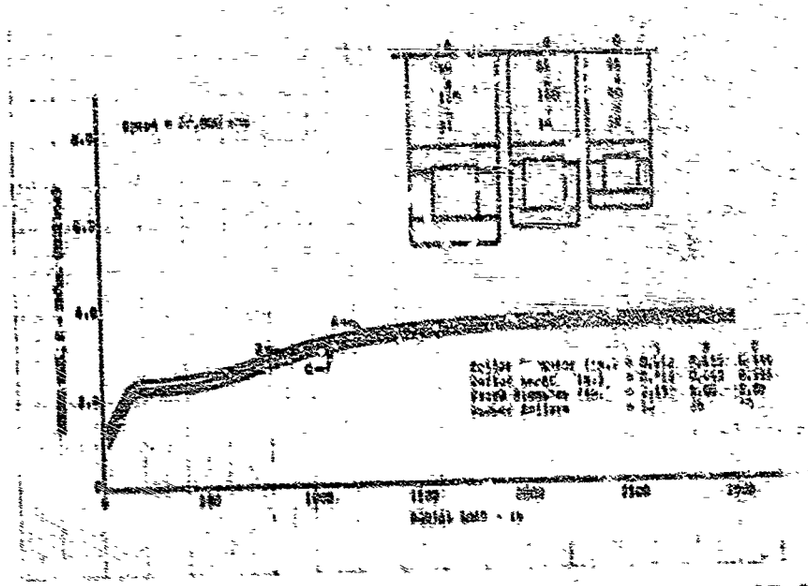


Figure 162. Radial Spring Rate vs Radial Load (Roller Bearings) DF 5[illegible]

CONFIDENTIAL
(This page is Unclassified)

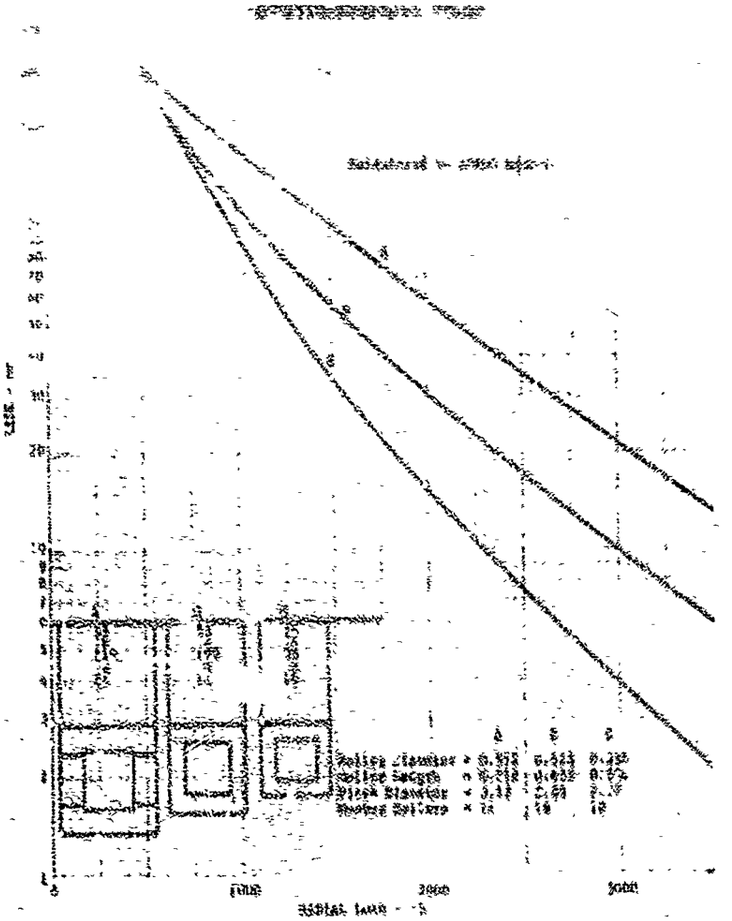


Figure 163. Roller Bearing Fatigue Life vs Radial Load (30,000 rpm) DF 52736

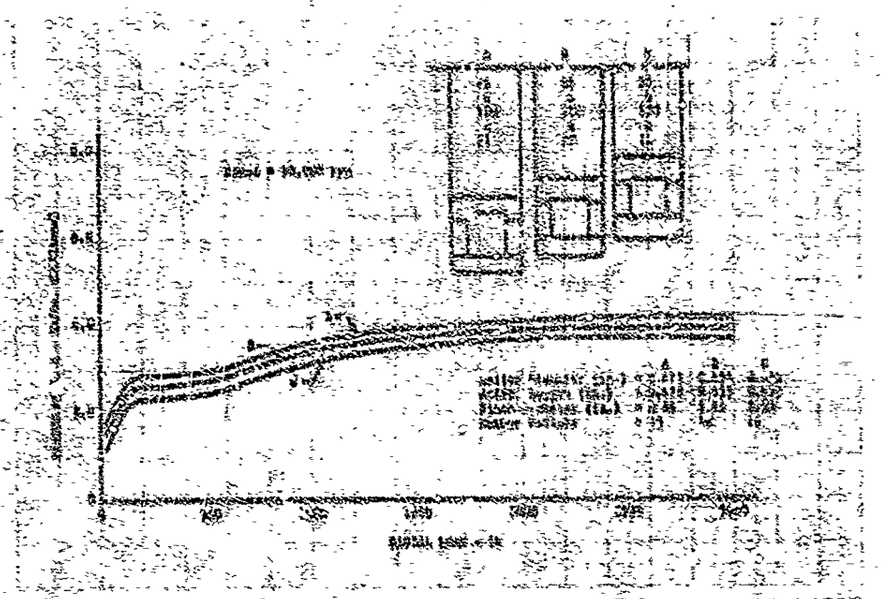


Figure 164. Radial Spring Rate vs Radial Load (Roller Bearings) DF 52737

UNCLASSIFIED

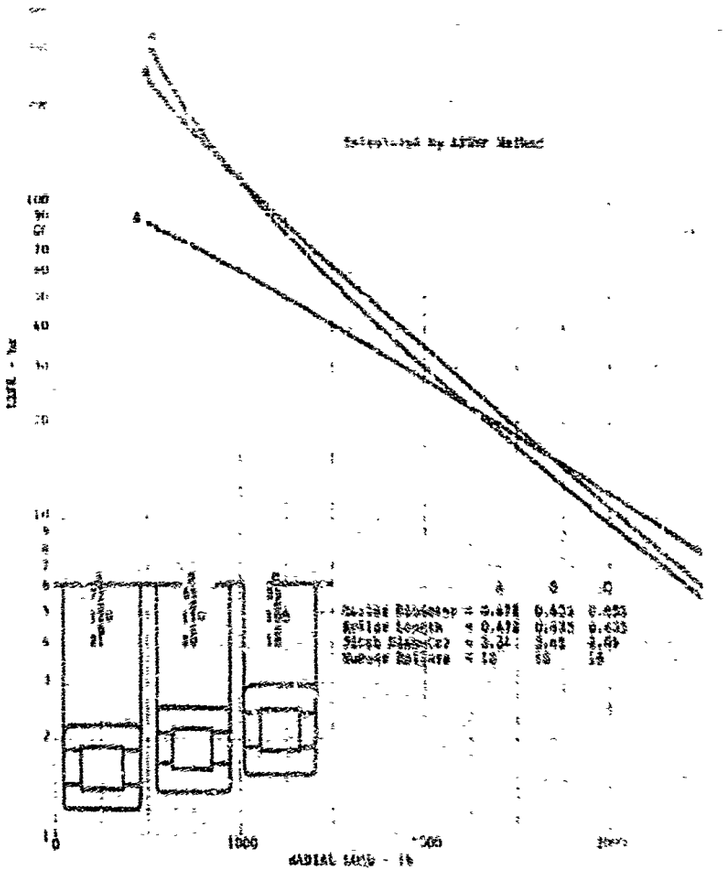


Figure 165. Roller Bearing Fatigue Life vs Radial Load (30,000 rpm) DF 52745

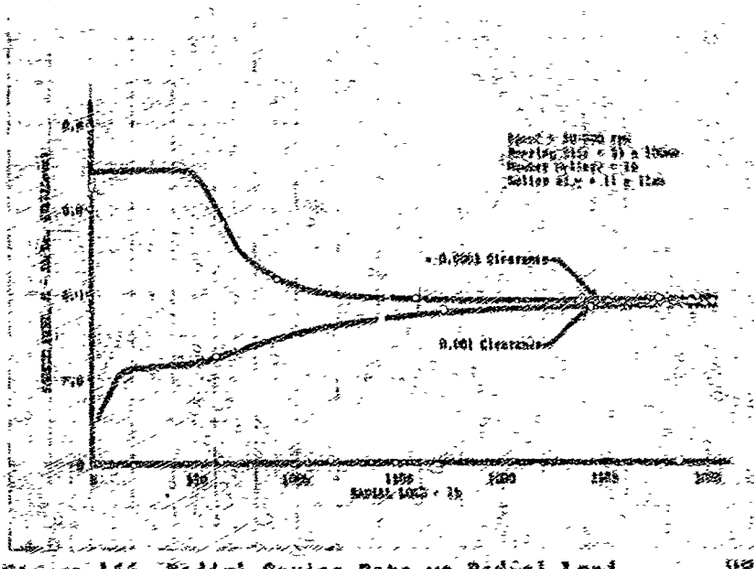


Figure 166. Radial Spring Rate vs Radial Load (Roller Bearings) DF 52744

UNCLASSIFIED

(C) In summary, the thrust capacity of a three row radial contact ball bearing is as shown in figure 166, and the radial spring rate is in excess of 3 x 10^6 lb/in. as shown in figure 167.

(D) Doubling of ball bearings theoretically will increase the radial spring rate and load capacity. In practice, however, it is difficult to assure that both are carrying load. The requirement for outside diameter sliding clearances plus misalignment on the shaft and manufacturing tolerances could cause one bearing to accept greater load, thereby causing spring rate and life characteristics to approach those of a single ball bearing.

(U) The fuel turbopump requirements are presented in the following paragraphs.

(U) Figure 167 shows the relationship of the bounce-mode and rocking-mode critical speeds vs total overall rotor support spring rate (housing and bearing - both ends) for the fuel turbopump preliminary design. Lines of typical overall spring rate for ball bearings and roller bearings are indicated. Experience has shown that most experimentally observed instances of whirling motion asychronous with speed have their onset at a speed approximately twice the frequency of the induced whirling motion. The whirling motion generally occurs at a natural frequency of the rotor and support system. To prevent onset of this type of instability, it is therefore desirable to keep all rotor and support system critical speeds above 50% of design speed. It is shown in figure 167 that the ball bearing system will not satisfy this requirement.

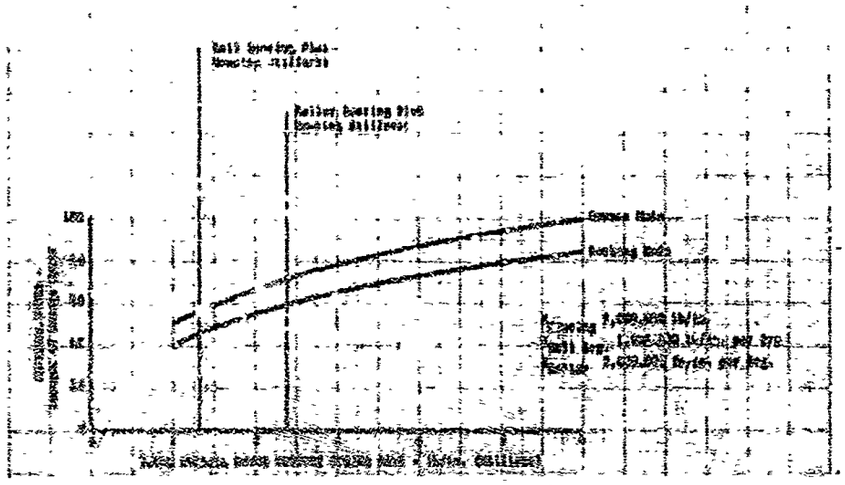


Figure 167. Predicted 250K Fuel Turbopump Critical Speeds DF 92809

CONFIDENTIAL

(C) Figures 168 and 169 show the calculated radial loads for the front and rear bearings for the fuel turbopump preliminary design as a function of speed. Estimated hydraulic loading caused by circumferential pressure variations, vehicle loading caused by vehicle maneuvers, maneuver and gyro loading caused by engine gimbal motion, and loadings caused by dynamic unbalance are included. The magnification of the unbalanced loads at critical speeds are indicated. A larger value of residual unbalance has been assumed for a turbopump rotor using roller bearings based on early experience with the 350K liquid hydrogen pump on Contract NAS8-11714. These loads were taken in planes perpendicular and parallel to the vehicle axis. The vehicle loading, maneuver loading, and gyro loading were then summed vectorially. The hydraulic loading and dynamic unbalance loading were then added to this vector to provide the maximum radial loading of the bearing as shown in figure 170. The maximum loading occurs on the front bearing and is approximately 1390 lb for a ball bearing and 1800 lb for a roller bearing. Figures 156 and 163 indicate that 55mm x 100mm ball or roller bearings have approximately the required 10-hour capacity with these loads. The ball bearing is marginal and cannot accept greater load without reducing life. The roller bearing indicates a 62-hour fatigue life at this condition or the capacity to accept loads up to 3000 pounds at 10-hour life.

(C) Because of the marginal life and inadequate spring rate of ball bearings, a 55mm x 100mm roller bearing configuration was selected for test evaluation.

(C) A 1700-lb radial load was selected for the bearing tests because this was the maximum loading in an arbitrary plane perpendicular to the vehicle axis. Since a large value of residual unbalance (0.10 in.-oz) was assumed for a turbopump rotor with roller bearings during the analysis, it was anticipated that a lower value of residual unbalance could be achieved as the balance techniques were improved. Later experience on Contract NAS8-11714 demonstrated that a residual unbalance approximately equal to that with a ball bearing could be achieved on a pump with roller bearings. Therefore, the 1700-lb radial load used during these tests was conservative by approximately 310 lb.

E. TEST PROGRAM AND TEST RESULTS

(C) The turbopump bearing test program was composed of three phases, (1) spin tests to provide a relative ranking of mechanical integrity of candidate cages, (2) cage and bearing geometry screening tests, and (3) endurance testing of the selected bearing and cage configuration with AISI 440C (AMS 5630) bearings to demonstrate a 10-hour life capability. These tests are discussed in detail below.

1. Cage Spin Testing

(U) The spin testing of candidate cage materials was completed and the results are shown in table XXVIII. Growth measurements, where available at 100% and 115% of bearing design conditions, are indicated in this table. These spin tests provided a relative rating of the mechanical integrity of candidate cage materials for selection of materials for

evaluation in the bearing rose rig. The unarmored Salox-M of test No. 3 failed at less than 10% of the calculated burst speed. A failure analysis indicated that the failure originated at the roller pocket corners, which was typical of the other failures during these spin tests. No irregularities were observed in the material. A repeat spin test was conducted with a second sample of Salox-M. The second cage failed at 12,200 rpm, which is 86% of predicted burst speed.

(C) As seen from table XXVIII, Armalon and Polyimide SF-1 are the only materials that exceeded the cage design speed (approximately 25,000 rpm) without external armor, and these materials were selected for evaluation in the bearing rig screening tests. Salox-M with armor was also selected because of good experience with this material in other programs and its characteristic for transferring lubricant to other elements of a bearing.

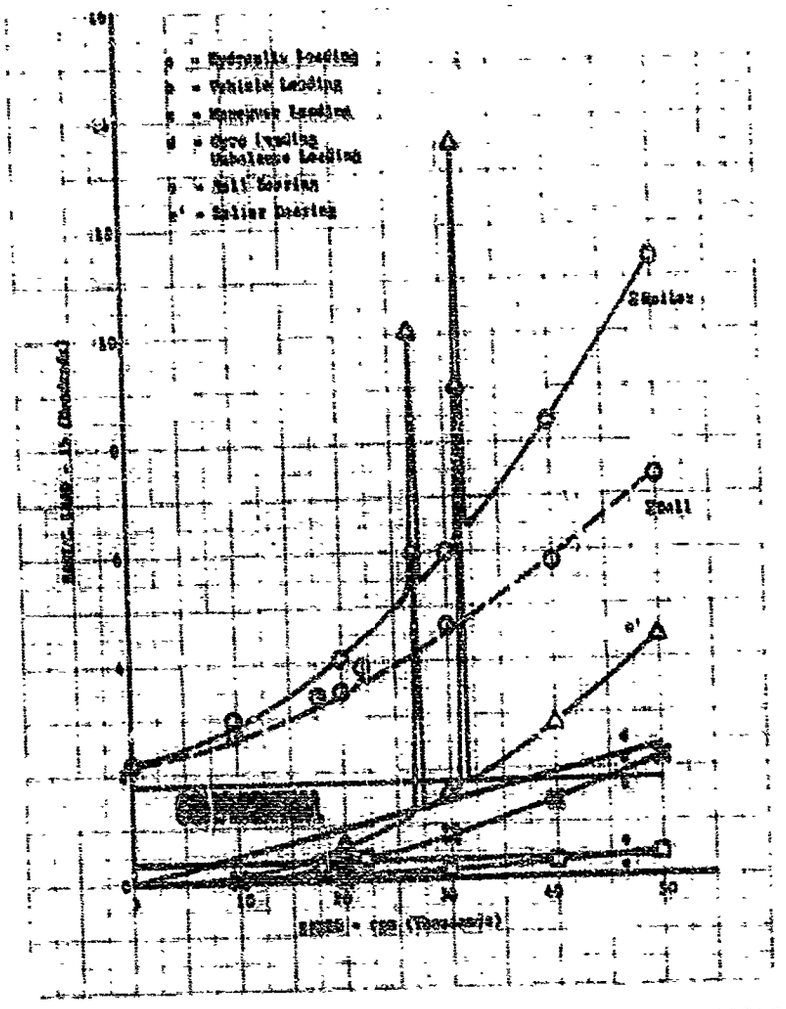


Figure 168. 230K Fuel Pump Maximum Radial Loading of Rear Bearing (Loaded 51.4 Degrees from Vehicle Axis) DF 60312

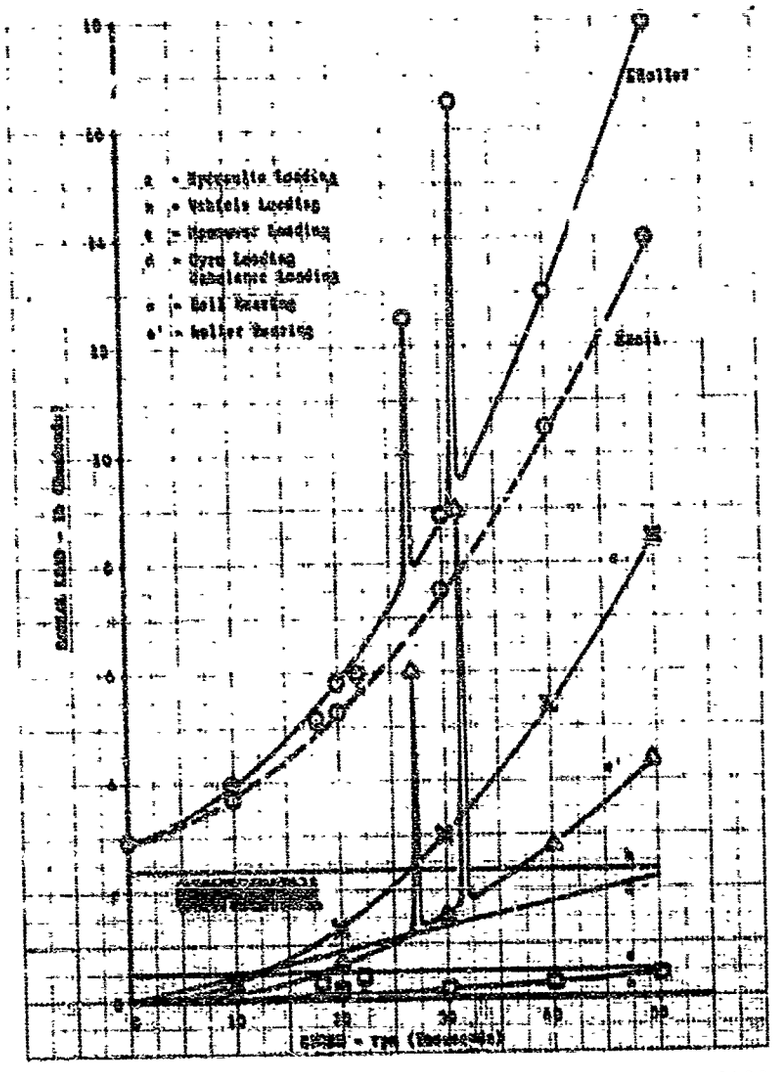


Figure 169. 250K Fuel Pump Maximum Radial Loading of Front Bearing (Loaded 47.4 Degrees from Vehicle Axis)

DF 60311

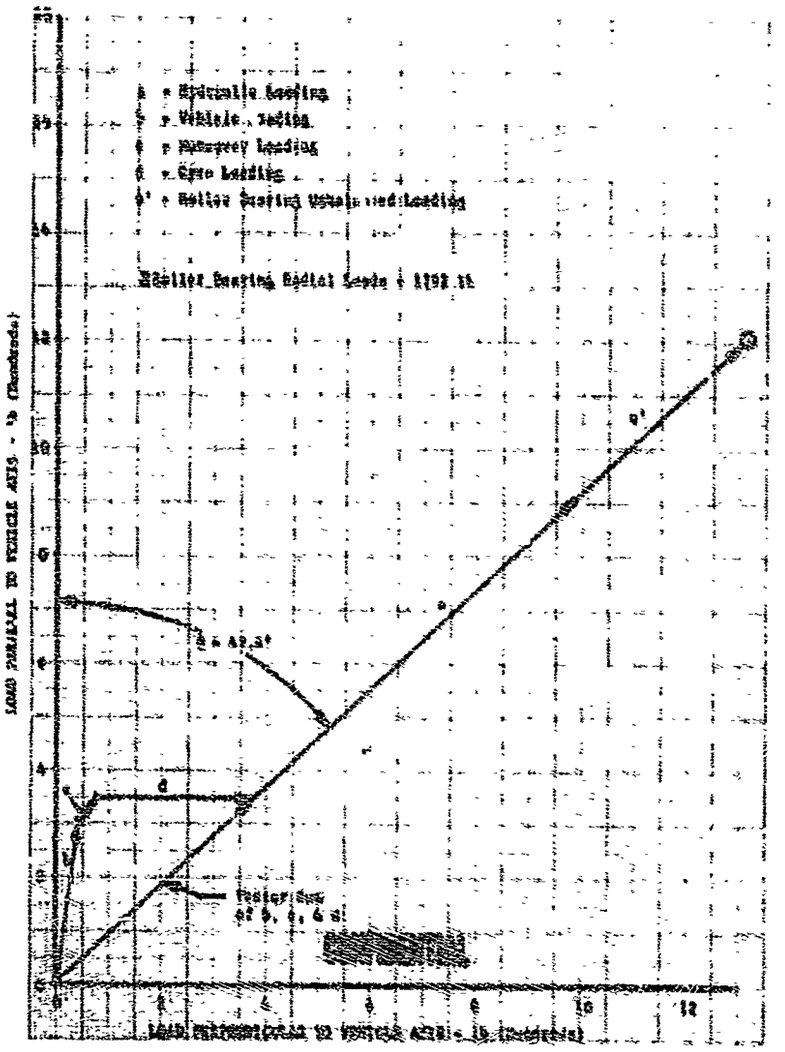


Figure 170. 250K Fuel Pump Maximum Radial Loading of Front Bearing Vector Load Diagram

DF 60313

(U) Table XXVIII. Cage Material Spin Test Summary

Test No.	Yield Strength	Calculated Burst Speed, rpm	Date	Cage Material	Cage Test Speed, rpm	Remarks
1	20,000	60,000	12/2/66	Armalon	75,400	Cage successfully tested to 75,400 rpm. A maximum growth of 2.25% occurred between the roller pockets.
2			12/8/66	Armored Salox-M	36,270	Failure originated at the armor rivet location between the roller pocket.
3	1,935	14,000	1/12/67	Unarmored Salox-M	1,390	Failure originated at pocket corners. Speed at failure was 8.8% of calculated speed.
4	1,400	15,800	1/17/67	Rulon A	13,630	Failure originated at pocket corners.
5	13,000	58,000	1/23/67	Polyimide SP-1	44,860	Cage was inspected at 24,000 and 32,000 rpm with no evidence of distortion or dimensional changes. Failure originated at pocket corners.
6	2,950	13,800	1/26/67	Lubraflon	13,600	Failure originated at pocket corners.
7	9,000	32,600	1/27/67	Polyimide SP-4	12,500	Failure originated at pocket corners.
8	1,935	14,000	2/7/67	Unarmored Salox-M	12,300	Repeat of test No. 3. Failure originated at pocket corners.

Notes: 1. Armalon is a glass fabric reinforced Teflon
2. Salox-M is a bronze-filled Teflon
3. Rulon A is a silicon-filled Teflon
4. Polyimide S. 1 is a thermoplastic Polyimide
5. Lubraflon is a lubricant matrix-filled Teflon
6. Polyimide SP-4 is a bronze-filled thermoplastic Polyimide.

2. Cage and Bearing Geometry Screening

(C) The cage and bearing geometry screening tests and the endurance tests are summarized in table XXIX. Eleven tests were conducted for cage and bearing geometry screening tests. As a result of these tests a bearing configuration was selected for endurance testing consisting of AISI 440C material rollers and races, an outer race piloted Armalon cage with 0.040-inch total roller end to inner race flange clearance. Negative internal radial clearance was used to provide roller preload. These tests and the bearing design approach are discussed in detail in the following paragraphs.

a. Design Approach

(C) Previous tests were conducted on similar roller bearings for the high pressure liquid hydrogen pump (Contract NAS8-11714) and on the IRAD bearing program. These tests indicated that after selecting a cage with sufficient integrity, roller end wear was most likely to be the main problem in obtaining a 10-hour bearing life.

(U) The approaches for end-wear control in these schemes are: (1) the use of cage materials that transfer coatings to the races, rollers, and rails, and (2) the use of more compatible wear materials for the rollers and rails. The following schemes shown in figure 171 were evaluated in the bearing test rig:

1. Scheme 1 consists of an inner-land-riding, aluminum-shrouded Salox-M cage, which is constructed such that the Salox extends into the flanged inner race, thus, transferring the Salox-M lubricant to the rails of the inner race and the roller ends.

2. Scheme 2 consists of a flanged outer race incorporating Berium 4-10 leaded-bronze inserts as a wear surface for the roller ends. An inner-land-riding Armalon cage is used.

3. Scheme 3 consists of a flanged outer race assembly incorporating Polyimide (SP-4) inserts as wear surfaces for the roller ends. An inner-land-riding armored Salox-M cage is used.

4. Scheme 4 consists of a flanged inner race and inner race side rails incorporating flame-deposited tungsten-carbide-coated inserts as wear surfaces for the roller ends. An outer-land-riding Polyimide SP-1 cage is used.

5. Scheme 5 incorporates a lubricant coating on the roller ends. The coating consists of a mixture of graphite and gold powder with molybdenum disulfide. An outer-land-riding Armalon cage is used.

(C) Table XXIX. LH_2 Roller Bearing Test Summary

Test No. and Phase Reference	Date	Bearing S/N	Cage Material and Configuration	Speed, rpm	Time, min	Cooling Flow, gpm	Roller End Wear	Load on Each Bearing, lb	Cage Condition	Remarks
1 Scheme 5 Screw - Standard Rollers - End Crowned	3-28-67	R1-RRF-IRF R2-RRF-IRF	Armalon - OLR Armalon - OLR	48,000 48,000	15 15	20 20	0.0032 0.0116	1445 1700	R1 - No Damage Light OD Rub R2 - No Damage Light OD Rub	Baseline Test for Cage Screening
2 Scheme 4 Tungsten Carbide Side Rails Rollers - Standard	4-11-67	C1-RRF-IRF C2-RRF-IRF	Polyimide (SP-1) - OLR Polyimide (SP-1) - OLR	Less Than 1000	N/A	22 22	None None	N/A 1700	C1 - No Damage C2 - No Damage	C1 - No Damage C2 - Inner Side Rails Worn
3 No. 1 Bearing From Test No. 2 Scheme 4 No. 2 Bearing - Standard OMF	4-18-67	C1-IRF-IRF C2A-IRF-ORF	Polyimide (SP-1) - OLR Armalon - OLR	48,000	7 7	23 23	0.0005 0.0003 Groove	1445 1700	C1 - Light OD Rub C2A - 0.030 Groove Pulled 4 Pockets Axial Dimensional Wear on OD to Contact With Side Rails	Test Terminated Due to Excessive Temperature of C2A Outer Race
4 No. 1 Bearing* - Standard OMF No. 2 Bearing* - SP-4 Outer Race Side Rails Scheme 3	5-9-67	F1A-IRF-ORF F2A-IRF-ORF	Shrouded Saleu-M - ILR Shrouded Saleu-M - ILR	48,000 48,000	1.0 1.0	23 23	None None	1445 1700	F1A - Cage Failed at Front Location F2A - Multiple Axial Cracks at Front Location	SP-4 Side Rail Inserts in Good Condition
5** No. 1 AISI 440C Material No. 2 AISI 440C Material	5-24-67	R1-ORF-IRF R2-ORF-IRF	Polyimide (SP-1) - OLR Polyimide (SP-1) - OLR	20,000 20,000	N/A N/A	32 32	None None	1445 1700	R2 - Cage Shows No Signs of Distress R2 - Cage Failed During Acceleration at 20,000 rpm.	
6** No. 1 AISI 52100 Material No. 2 AISI 440C Material	6-13-67	J1-IRF-IRF J2-IRF-IRF	Armalon - OLR Armalon - OLR	48,000 48,000	15 15	32 32	0.0003 None	1445 1700	J1 - No Damage J2 - No Damage	
7 Scheme 3 No. 1 AISI 52100 No. 2 AISI 52100	6-22-67	R1-IRF-ORF R2-IRF-ORF	Shrouded Saleu-M - ILR Shrouded Saleu-M - ILR	N/A N/A	N/A N/A	32 32	N/A N/A	850 1200	R1 - Side Pocket Wear R2 - Side Pocket Wear	Failed on Acceleration Following LH_2 Emptying
8 Scheme 4 No. 1 Tungsten Carbide Side Rails No. 2 Tungsten Carbide Side Rails	6-27-67	L1-IRF-IRF L2-IRF-IRF	Armalon - OLR Armalon - OLR	48,000 48,000	15 15	20 20	0.0003 0.0029	1445 1700	L1 - Wear Pad Delamination L2 - No Damage	Roller End Wear on Both Sides
9 Scheme 3 No. 1 Outer Race Side Rail (SP-4) No. 2 Outer Race Side Rail (SP-4)	7-12-67	R1-IRF-ORF R2-IRF-ORF	Shrouded Saleu-M - ILR Shrouded Saleu-M - ILR	30,000 30,000	N/A N/A	N/A N/A	N/A N/A	1445 1700	R1 - Cage Failed at Two Pockets. Aluminum Armor Pulled at Two Locations R2 - Light Rub on Side of Pockets	

*Double Flanged Bearing
**Contractors Independent Prog am Test No. 1
***Contractors Independent Program Test No. 2

No. 1 Bearing - Reaction Bearing
No. 2 Bearing - Load Ring Position
IRF - Inner Race Flanged
ORF - Outer Race Flanged
OLR - Outer Race Piloted
ILR - Inner Race Piloted

(C) Table XXIX. LH_2 Roller Bearing Test Summary (Continued)

Test No. Test Liner Material	Date	Bearing I/D	Cage Material and Configuration	Speed, rpm	Time, min	Cooling Flow, gpm	Roller End Play	Load on Each Bearing, lb	Cage Condition	Remarks
10 Balance: 2 No. 1 Outer Race Loaded Bearing Retainer No. 2 Outer Race Loaded Bearing Retainer	7-20-67	#1-SRF-CRF #2-SRF-CRF	Armalon - 112 Armalon - 114	48,000 48,000	1 1	30 30	0.00895 0.00898	1464 1700	#1 - Heavy SS Rub on Outer Race Side Ratio. Heavy Side Pocket Rub. #2 - Light SS and CS Rub	#1 - Loaded Average 2500 Ball Reverse Contact on One Location. (2.500-Inch Bore.) #2 - Loaded Average 2500 Ball Reverse Contact on One Location. (2.500-Inch Bore.)
11 Balance: 1 No. 1 Inner Race Uncoated No. 2 Inner Race Uncoated	8-7-67	#1-SRF-IRF #2-SRF-IRF	Open End Sales - 112 Uncoated Sales - 114	48,000 48,000	9 9	30 30	0.00812 0.0087	1443 1700	Heavy SS Rub One Location	Execution Bearing Inner Race Cracked.
12 No. 1 AISI 440C Material No. 2 AISI 440C Material	8-15-67	#1-SRC-IRF #2-SRC-IRF	Armalon - 112 Armalon - 112	48,000 48,000	22 22	30 30	0.0[illegible] 0.0086	1443 1700	#1 - One Pocket Worn Light CS Rub #2 - SS Smear Light CS Rub	#1 - Rubber Cage Rather #2 - No Change
13 No. 1 AISI 440C Material No. 2 AISI 440C Material	8-30-67	#1-SRC-IRF #2-SRC-IRF	Armalon - 112 Armalon - 112	48,000 48,000	205 205		0.00823 0.00895	1443 1700		Worn Bearing Ruined After 4 Hours and 19 Minutes. This Bearing Replaced. Tested Again After 15 Additional Minutes at Design Speed.
14 No. 1 AISI 440C Material No. 2 AISI 440C Material	9-13-67	#1-SRC-IRF #2-SRC-IRF	Armalon - 112 Armalon - 112	48,000 48,000	446 441		0.00800 0.00813	1443 1700	#1 - Light Rub on Cage Area #2 - Light Rub on Lower of One Pocket Pocket	Big Spalls Both Inner Race Bearings and One Worn Bearing and Broken Rubber. One Rubber in Load Bearing. Ran 446 After 2 Hours and 42 Minutes.
15 No. 1 AISI 440C Material No. 2 AISI 440C Material	9-22-67	#1-SRC-IRF #2-SRC-IRF	Armalon - 112 Armalon - 112	48,000 48,000	535 79		0.00823 Loss	1443 1700	#1 - Light Rub in One Area #2 - One Damaged Pocket; Light Rub 180 degrees from Damaged Pocket	One Load Bearing and Worn Bearing Inspected. One Rubber in Load Bearing Ruined After 1 Hour and 19 Minutes.
16 No. 1 AISI 440C Material No. 2 AISI 440C Material	9-29-67	#1-SRC-IRF #2-SRC-IRF	Armalon - 112 Armalon - 112	48,000 48,000	735 238		0.00744 Loss	1443 1700	#1 - Light Rub in One Area #2 - Rubber Rub 180 degrees SS	One Load Bearing and Worn Bearing. Locations of Damage and Degradation on Load Bearing Cracked Bearings. Load Bearing Cracked Outer Race, Chipped Inner Ridge, and Two Damaged Pocket Rubber 3 Hours and 59 Minutes.

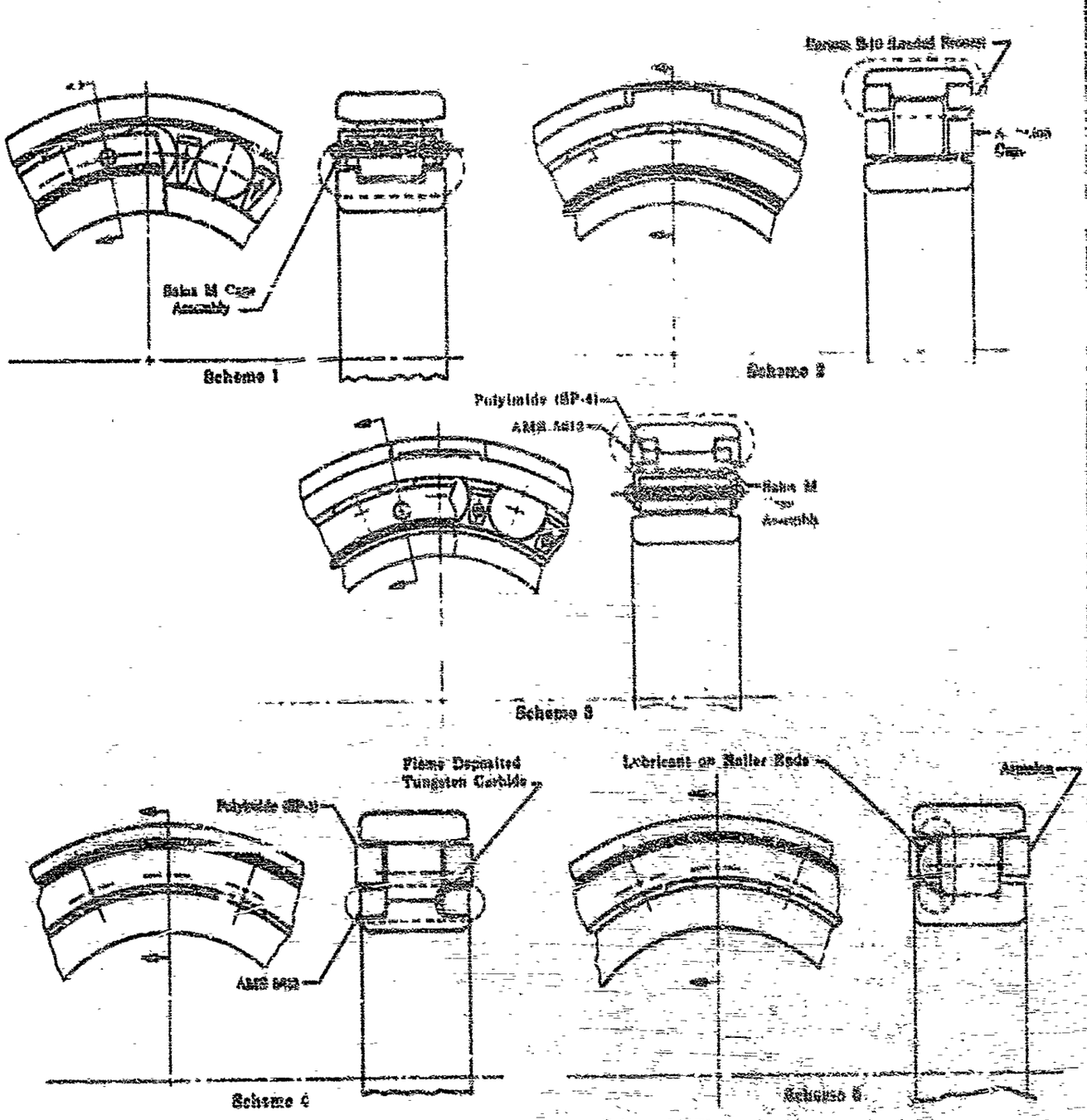


Figure 171. Bearing Configurations

(This page is Unclassified)

b. Tests

(U) The tests conducted to evaluate these roller end wear schemes and to screen the candidate cage and bearing geometries are discussed in detail in the following paragraphs.

(C) Test No. 1 incorporated standard inner race flanged AISI 52100 material bearings with Armalon outer-race-piloted cages (Scheme 5). The roller ends were coated with a lubricant consisting of a mixture of graphite and gold powder with molybdenum disulfide. To establish a baseline for comparative evaluation of designs for minimizing roller end wear, this configuration completed a 15-minute test at 48,000 rpm with a radial load of 1700 lb. A post-test inspection of the bearings indicated high roller end wear, and slight cage delamination had started at two locations on one of the Armalon cages. The test bearing, which is located directly under the applied load, showed roller end wear on both ends of the rollers for a total of 0.0116 inch, while the other bearing had an average of 0.0032-inch roller end wear only on the end away from the loaded bearing. The post-test condition of the cage and rollers is shown in figures 172, 173, and 174.

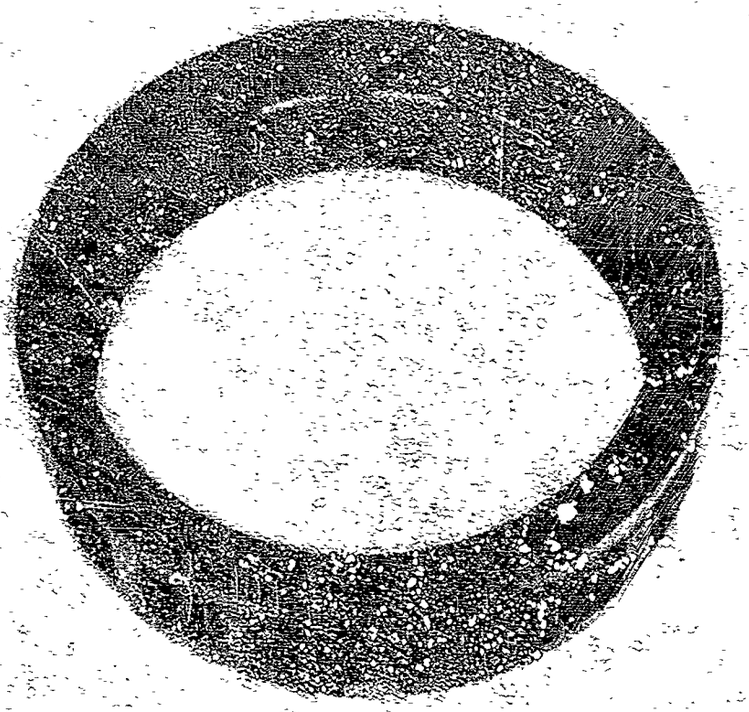


Figure 172. Armalon Cage from Bearing S/N B-1 Showing Delamination After 15 Minutes at 48,000 rpm

72 68185



Figure 173. Rollers from Bearing S/N B-1 After 15 Minutes at 45,000 rpm — FR 68182



Figure 174. Rollers from Bearing S/N B-2 Showing End Wear After 15 Minutes at 48,000 rpm — FR 68183

(U) Test No. 2 incorporated two test bearings that had flanged inner races with side rails incorporating flame-deposited tungsten-carbide as wear surfaces for the roller ends and outer-land-riding Polyimide (SP-1) cages. Test No. 2 was conducted on 11 April 1967. However, the rig failed to accelerate following the LH_2 cooldown. A teardown inspection revealed heavy wear of the side rails of the test bearing located under the load ring. The maximum speed attained during this test was less than 1000 rpm. The post-test condition of the side rails is shown in figure 175. The Polyimide (SP-1) cage showed no signs of distress. The other test bearing showed no evidence of damage and was used in the following build of the test rig.



Figure 175. Inner Race from Bearing S/N C-2 Showing Worn Side Rails After Operation at Speed Less than 1000 rpm PE 68704

(C) In test No. 3, the bearing configuration under the load ring was an off-the-shelf flanged-outer-race bearing with an outer-land-riding Armalon cage. This configuration was tested to establish a baseline for evaluating flanged-outer-race end wear schemes. The other test bearing was the flame-plated tungsten-carbide inner side rail and Polyimide (SP-1) cage configuration used in test No. 3. The test on this configuration was terminated after 7 minutes at 48,000 rpm upon indication of an excessive bearing outer race temperature and high rig power requirements. Inspection after disassembly revealed that the Armalon cage, under the applied radial load, had severely burnished on the outside diameter in contact with the side rails and failed in four of the roller pockets as shown in figure 176. The severe burnishing of the cage in contact with the outer race side rails was caused by a cage diametral growth of 0.030 inch on the outer diameter of the ribs between the roller pockets where some delamination of the ribs had started because the fibers were cut by the side rail edges. The ribs between the roller pockets were unsupported by the outer race. The area in contact with the outer race side rails had a total wear of 0.032 inch on the diameter. The rollers, except the two from the failed roller pockets, had experienced a growth of 0.0002 to 0.0005 inch in

overall length because of material transfer from the outer race side rails. Two rollers in the failed roller pockets had heavy (0.040 inch) end wear. The post-test condition of the rollers from this bearing is shown in figure 177. The side rails on the other bearing were worn heavily, similar to the wear on the bearing of the same configuration that was tested in Build No. 2 as shown in figure 178. The Polyimide (SP-1) cage was in excellent condition with slight wear patterns on the cage outside diameter and roller pockets as shown in figure 179. The rollers had an average total end wear of only approximately 0.0005 inch despite the poor condition of the side rails, which wore heavily during the test. The post-test condition of the rollers is shown in figure 180.

(U) A failure investigation was completed on the flame-placed tungsten-carbide side rails from bearing S/N C-1 used on tests No. 2 and 3 and bearing S/N C-2 used on test No. 2 only. A metallographic analysis showed that the rollers had rubbed against the base metal and not the tungsten-carbide surface as intended. It was determined that during the finishing operation, after plating, the vendor had ground and lapped the unplated side. From visual inspection, the part was installed in a manner that allowed the rollers to rub against the base material. Changes to the side rail design consisting of a chamber on one side only were made to establish a reference surface before the flame plating is applied. Following the flame plating, this same reference was used to grind the plating to the desired thickness. Additional side rails to this new configuration were procured and tested on test No. 8.

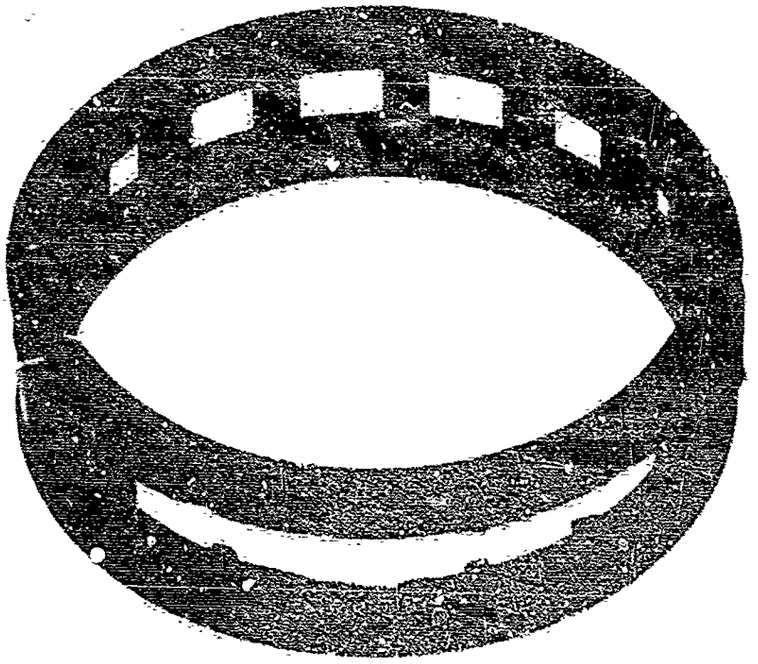


Figure 176. Armalon Cage With Failed Pockets from Bearing S/N C-2A After 7 Minutes at 48,000 rpm FE 68859

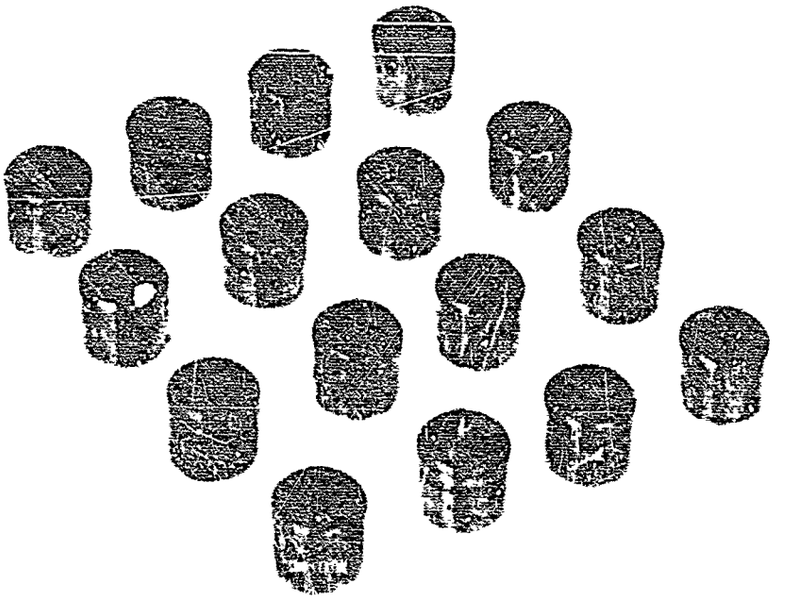


Figure 177. Rollers from Bearing S/N C-2A Showing End Wear After 7 Minutes at 48,000 rpm — FE 68861

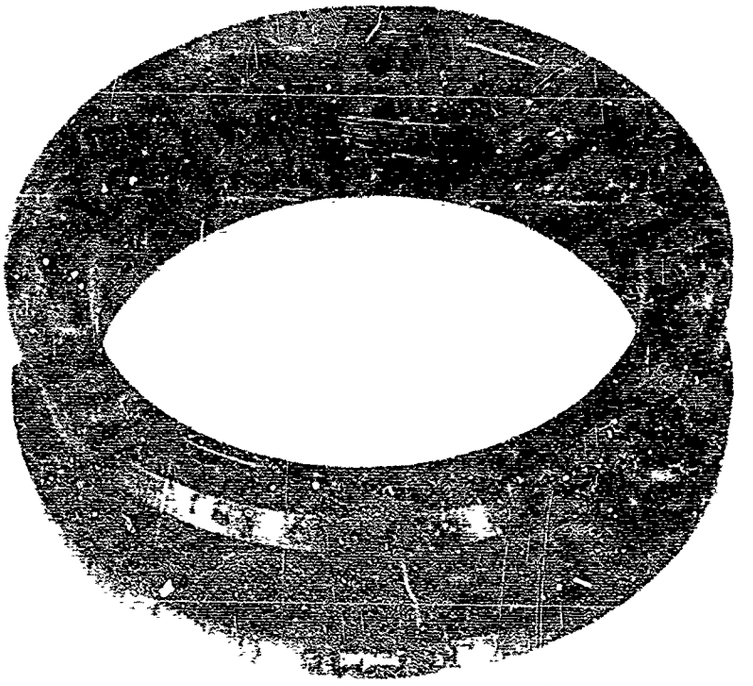


Figure 178. Inner Race from Bearing S/N C-1 Showing Side Rail Wear After 7 Minutes at 48,000 rpm — FE 68863

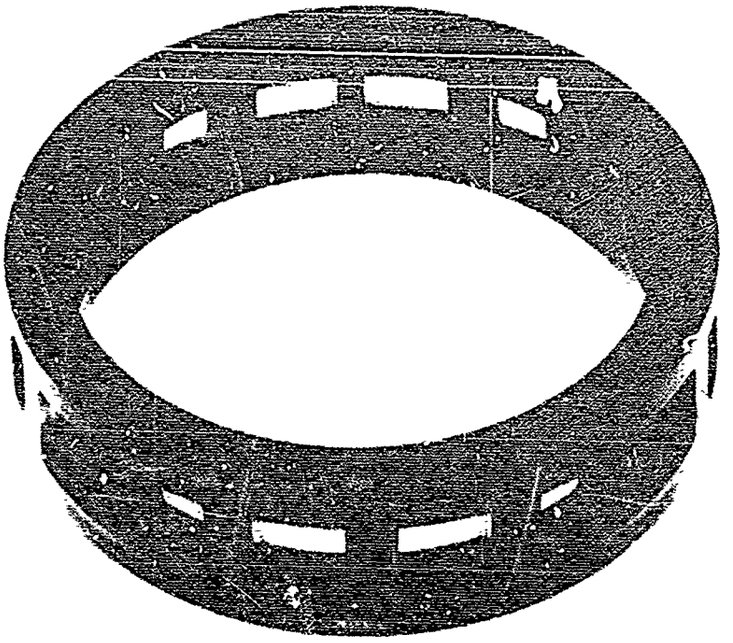


Figure 179. Polyimide (SP-1) Cage from Bearing S/N C-1 After 7 Minutes at 48,000 rpm FE 68867

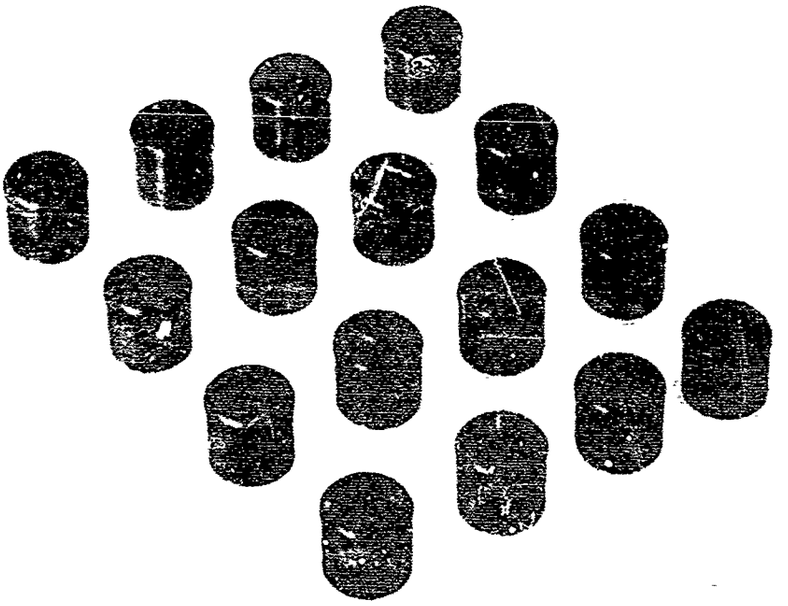


Figure 180. Rollers from Bearing S/N C-1 Showing Light (0.0005 inch) End Wear After 7 Minutes at 48,000 rpm FE 68869

(C) Test No. 4 incorporated shrouded Salox-M cages that were guided on inner race flanges in both bearings. The bearing in the reaction position used a standard flanged outer race. The loaded bearing incorporated roller end wear Scheme 3 (SP-4 Polyimide inserts in the outer race flanges as rub surfaces for the rollers). Figures 181 and 182 show the detail bearing parts prior to assembly. Test No. 4 was attempted on 9 May 1967; however, the test was terminated after one minute of operation at 40,000 rpm because of an increase of the reaction bearing outer race temperature. Inspection after disassembly revealed a cage failure of the reaction bearing. The post-test conditions of the test bearings are shown in figure 183 and 184. The Polyimide (SP-4) inserts of the flanged outer race showed no signs of distress and the rollers showed no end wear. The roller end wear was 0.011 and 0.015 in. on the two rollers from the failed pockets on the standard outer-race-flanged bearing in the reaction position. The other rollers from this bearing had no measurable end wear.

(U) The failure analysis of the shrouded Salox-M cage from bearing S/N F-1A used in test No. 4 revealed a fabrication problem. The cage failure originated at a crack in the aluminum shroud at a rivet location similar to those shown in figure 185. Figure 186 shows similar cracks in the cage from bearing S/N F-2A that did not fail. The aluminum alloy shroud was overheated in the areas of the rivets during hot upsetting operations. To alleviate this problem, the rivets were TIG-welded to the rivet heads. A cage was fabricated by this method, and a microstructure analysis showed no heat-affected zone at the rivet locations. This technique was used in the fabrication of the shrouded Salox-M cages used on subsequent tests.

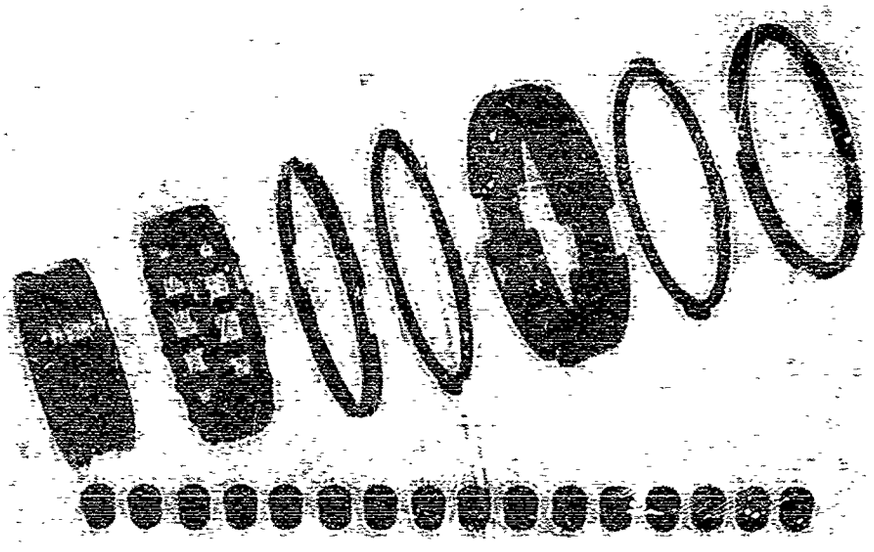


Figure 181. New Condition Bearing Details, S/N F-2A FE 69222

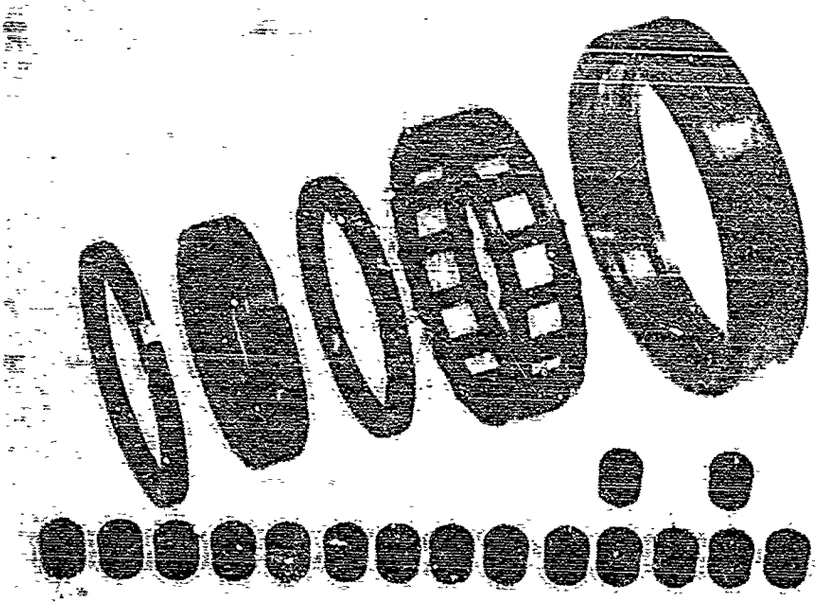


Figure 182. New Condition Bearing Details, S/N F-1A — FE 69223



Figure 183. Bearing S/N F-1A Post-Test Condition Showing Cage Failure After 1 Minute at 48,000 rpm — FE 69437

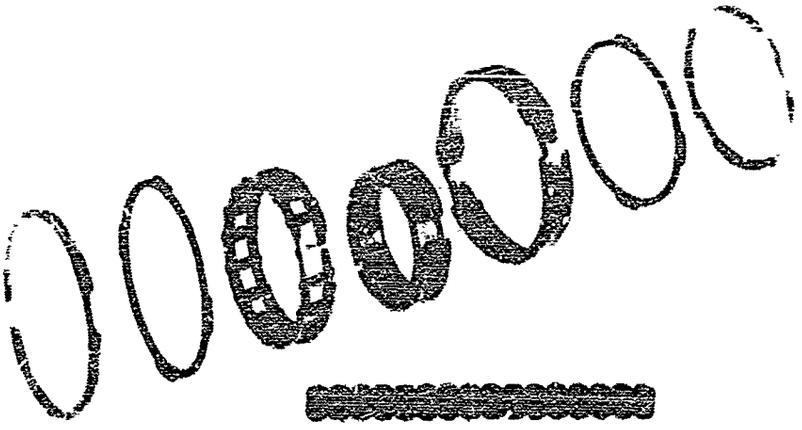


Figure 184. Bearing S/N F-2A Post-Test Condition Showing No Roller End Wear After 1 Minute at 48,000 rpm FE 69438

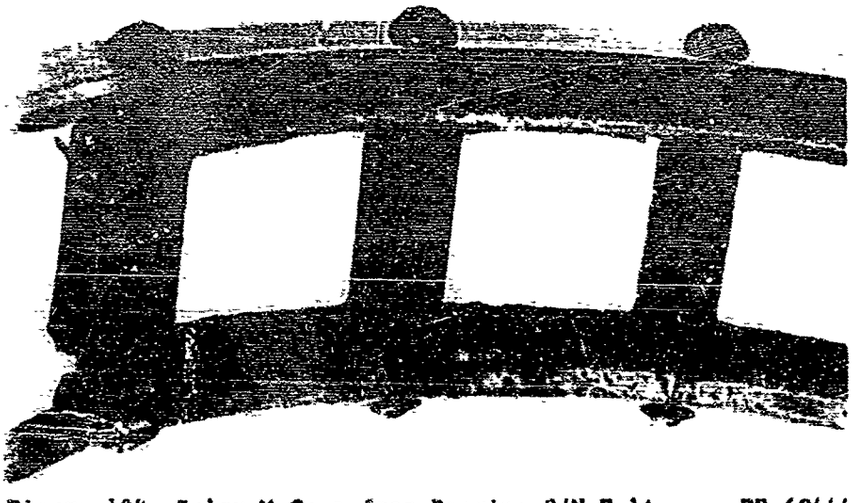


Figure 185. Salox-M Cage from Bearing S/N F-1A Showing Cracks at Rivet Locations After 1 Minute at 48,000 rpm FE 69444

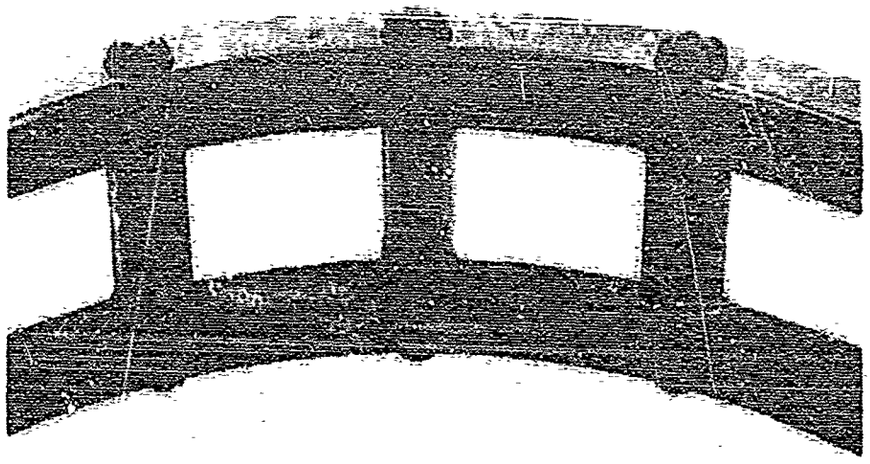


Figure 186. Salox-M Cage from Bearing S/N F-2A Showing Several Axial Cracks at Rivet Locations After 1 Minute at 48,000 rpm FR 69452

(U) A potential problem existed in the method of supplying coolant flow to the test bearings. The total rig flow was channeled through the two test bearings in series allowing debris from one bearing to contaminate the other. A rig modification to introduce the total coolant flow between the two test bearings and to discharge 50% through each bearing was completed following test No. 4 and was successfully used during test No. 5 and all subsequent tests.

(C) Test No. 5 was the first of two planned bearing tests under an IR&D program. This test was conducted as part of the evaluation of AISI 440C material roller bearings. This build incorporated AISI 440C material bearings with inner race flanges and Polyimide (SP-1) cages. The loaded bearing incorporated 0.0008-inch roller end clearance, and the reaction bearing had 0.040-inch roller end clearance to evaluate the effect of increased clearance. Both bearings incorporated an interference internal radial fit between the races and rollers to provide high radial stiffness. This configuration was tested on 26 May 1967. The test was terminated at 20,000 rpm during the acceleration because of an increase in the bearing outer race temperature and rig power requirements. A post-test inspection revealed that the Polyimide cage of the loaded bearing had failed. The failure occurred at one section of the cage as shown in figure 187. The rollers, except for the two from the failed roller pockets, had no measurable end wear. The two rollers in the failed pockets had 0.0003- and 0.001-inch end wear. The other bearing with 0.040-inch roller end clearance showed no end wear.

(C) The second of two planned tests under an IR&D program as part of the evaluation of AISI 440C material roller bearings was conducted as test No. 6. This test incorporated one AISI 440C bearing in the loaded position and one AISI 52100 bearing in the reaction location. Both used Armalon cages, 0.040-inch roller end clearance, and 0.001- and 0.0011-inch, respectively, interference internal radial fit at assembly between the

rollers and races. A post-test inspection after 15-minutes duration at 48,000 rpm indicated no measureable roller end wear on the AISI 440C rollers while the AISI 52100 rollers had an average total end wear of 0.0003 inch.

(U) Test No. 7 incorporated Polyimide SP-4 outer race side rail inserts and shrouded Salox-M cages. Testing of this build was attempted on 20 June 1967; however, the rig failed to accelerate following the LH_2 cooldown. A teardown inspection and the LN_2 testing indicated that the thermal contraction of the shrouded Salox-M cage was greater than predicted, and this prevented rotation.

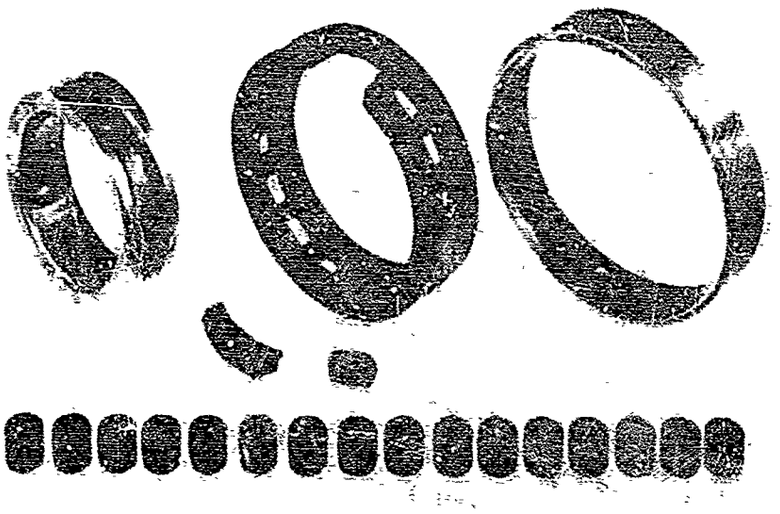


Figure 167. Bearing S/N H-2 Post-Test Condition Showing Polyimide (SP-1) Cage After Failure During Acceleration FE 69931

(U) Failure of the rig to rotate during test No. 7 was attributed to distortion during thermal contraction of the new design shrouded Salox-M cage configuration with 4 rivets instead of 16 to retain the aluminum shroud and the Salox-M. Liquid nitrogen testing of the original design cage with 16 rivets and the revised configuration with 4 rivets indicated a thermal contraction of approximately 0.035 inch for the revised cage, as opposed to 0.017 inch for the original cage. The original cage with rivets at 16 locations was able to restrain the Salox-M during thermal contraction. The new design shrouded Salox-M cage was revised to incorporate an additional 12 rivets and the thermal contraction was verified by liquid nitrogen testing to be satisfactory before use on test No. 9.

(C) Test No. 8, which incorporated flame-plated tungsten-carbide inner race side rails and an Armalon cage, was completed for the planned 15-minute duration on 27 June 1967. The bearing outer race temperature remained below 60°R, although a problem occurred in controlling the coolant flow. A teardown inspection indicated an average roller end wear of 0.0029 inch in the loaded bearing and 0.0043 inch in the reaction bearing. The rollers from both bearings were worn on both ends. The reaction bearing Armalon cage had signs of minor delamination at one location. A metallographic inspection of the tungsten-carbide side rails showed the hardcoat to be 0.0026-inch thick in unworn areas, which is within the print requirement of 0.002 to 0.003 inch. The rollers had worn the coating down to the basic metal in the areas of the highest wear near the outer diameter of the side rails. The tungsten-carbide coating was of good quality with a satisfactory hardness and good bonding to the base material.

(U) Test No. 9, which incorporated Polyimide (SP-4) outer race side rail inserts and shrouded Salox-M cages, was conducted on 12 July 1967. The test was terminated during the acceleration because of a temperature rise of the reaction bearing outer race. A post-test teardown inspection indicated that the cage of the reaction bearing failed as shown in figure 186. A failure analysis of the cage showed that the aluminum alloy armor failed because of overstress. The Polyimide (SP-4) side rail inserts of the reaction bearing were completely destroyed. The Polyimide (SP-4) side rail inserts of the loaded bearing failed at one location as shown in figure 189. A 30-degree segment of the Polyimide (SP-4) side rail insert was separated from the ring. The shrouded Salox-M cage of the loaded bearing showed no signs of distress as shown in figure 190.



Figure 188. Outer Race Assembly and Failed Shrouded Salox-M Cage (S/N M-1) FE 70858

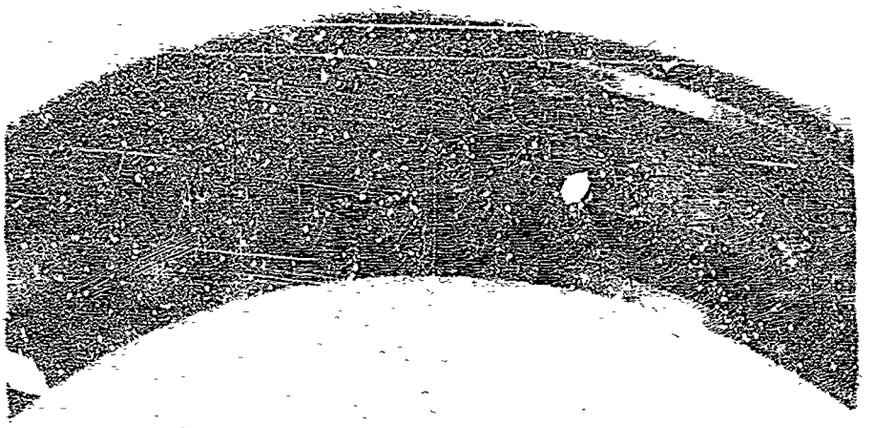


Figure 189. Outer Race Assembly Showing Damaged Polyimide SP-4 Insert (S/N N-2) FE 70865

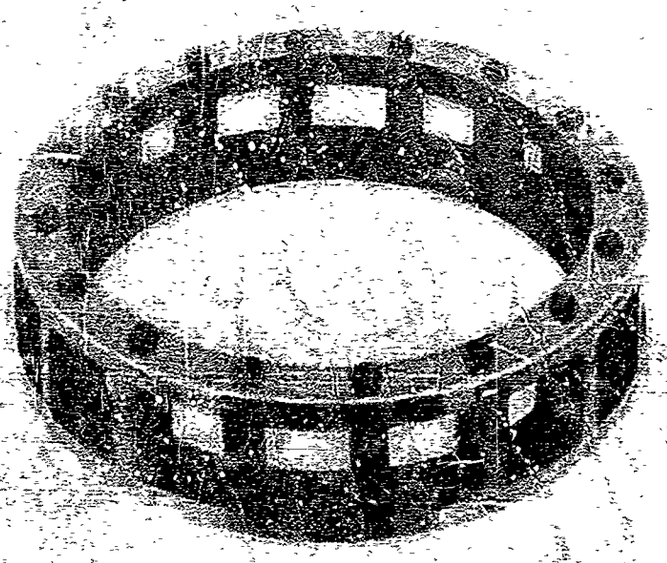


Figure 190. Salox-M Cage Assembly (S/N N-2) FE 70869

(C) Test No. 10, which incorporated leaded-bronze outer race side rail inserts as per roller-end-wear Scheme No. 2, with supplementary side-rail cooling and annular cages in both bearing locations, was conducted on 20 July 1967. The test was terminated after 1 minute at 46,000 rpm because of a sudden temperature rise of the reaction bearing outer race. A post-test teardown inspection indicated that the leaded-bronze side rails of the reaction bearing had failed as shown in figure 191. The failure analysis of the leaded-bronze side rails showed severe wear from roller end rub. The side rails from the reaction bearing had worn approximately 0.040 inch and the loaded bearing side rails had 0.020-inch wear. The rollers had an average end wear of 0.00075 inch on the reaction bearing and 0.00036 inch on the loaded bearing. Figure 192 shows a segment of the outer race with the worn leaded-bronze side rail. There are indications that a surface temperature of at least 500°F was experienced on the surface of the reaction bearing side rails as evidenced by the melted lead. The local yielding of the side rails appears to have resulted from the reduction in physical properties of the leaded-bronze at the elevated temperature. The most severe side rail wear occurred in two areas 180 degrees apart on the two side rails and in line with the applied 1700-lb radial load. This indicates that the rollers may have skewed when passing through the unloaded zone or that inner to outer race misalignment caused axial movement of the rollers into the side rails. This skewing or axial movement became progressively worse as a result of both side rail wear and local yielding.

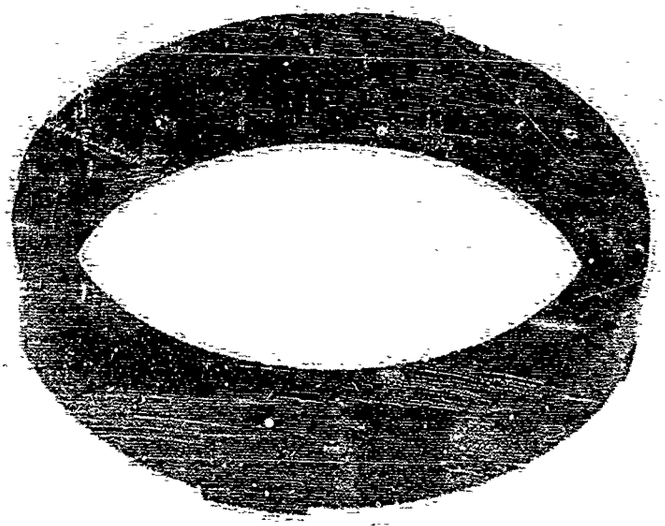


Figure 191. Outer Race Assembly Showing Failed Leaded-Bronze Inserts (S/N P-1) FE 70947

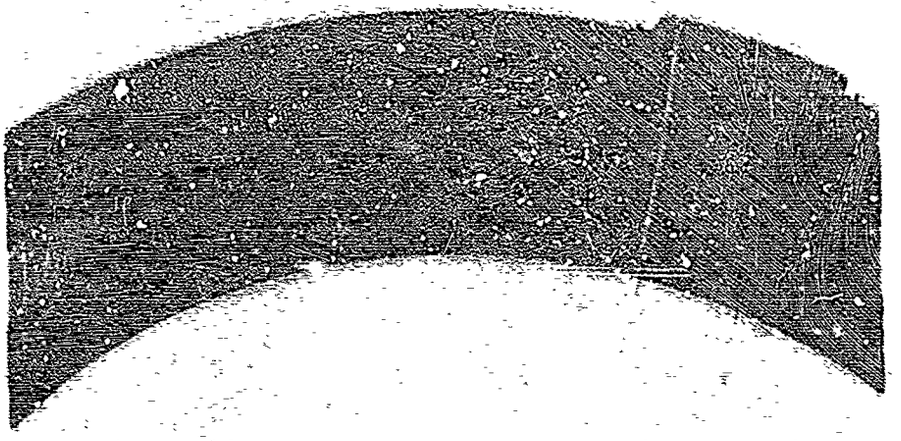


Figure 192. Outer Race Assembly Showing Side Rail Wear (S/N P-2) — PE 70958

(C) Test No. 11, which incorporated inner race piloted shrouded Salox-M cages per roller-and-wear Scheme No. 1, was conducted on 2 August 1967. The cage armor material was changed from aluminum (AMS 4121) to stainless steel (AMS 5664) to increase the cage strength. The cage assembly was riveted at 16 locations to reduce the thermal distortion experienced when only four rivets were used to attach the shroud, as occurred on test No. 7. The test was terminated after 9 minutes at 48,000 rpm, because of a vibration increase from a level of 6 g's to 30 g's. The bearing outer race thermocouples did not show a temperature increase during the test. A teardown inspection revealed that the reaction bearing inner race had cracked as shown in figure 193. The failure analysis of the detail parts indicates that the reaction bearing inner race cracked as a result of the propagation of a thermal crack in the AISI 440C material. The thermal cracks in the inner race side rail outer diameter were the result of rubbing of the AMS 5664 cage armor as shown in figure 194. The armor rubbed because the Salox-M in the area that guides the cage was worn as a result of cage unbalance.

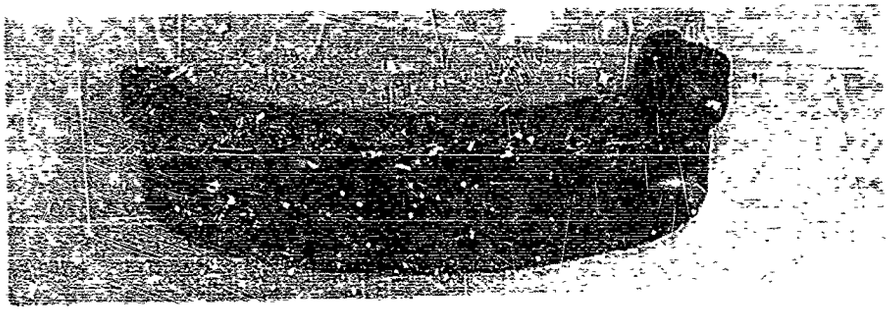


Figure 193. Post-Test No. 11 Condition of Inner Race from the Reaction Bearing — PE 71255

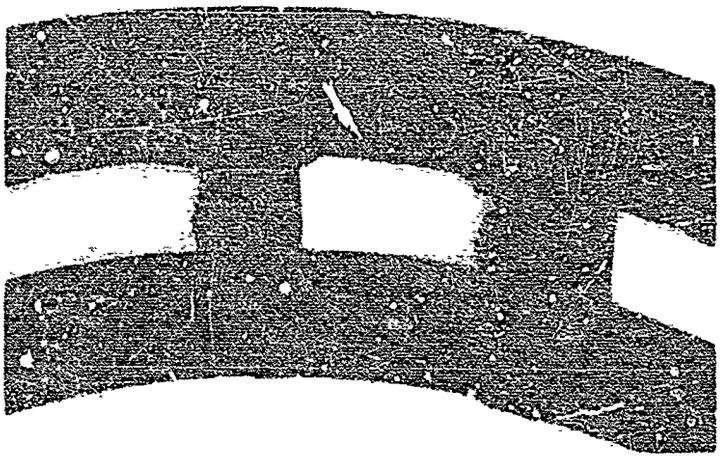


Figure 194. Post-Test No. 11 Condition of Cage from Reaction Bearing Showing Rub Area on Cage Armor FE 71259

3. Endurance Tests

(C) The bearing configuration selected for endurance testing consisted of AISI 440C material rollers and races, an outer-race-piloted Armalon cage, increased roller end clearance with the flanged inner race (0.040 inch total) and negative internal radial clearance (0.0013 inch at assembly on both bearings) to provide roller preload. Endurance testing of Build No. 12 was attempted on 11 August 1967. The test was terminated after 1 hour and 32 minutes of duration at 46,000 rpm because of excessive vibration. A teardown inspection revealed that the reaction bearing had one damaged roller, as shown in figure 195. The other rollers were in excellent condition with only 0.0002-inch wear on the roller with the maximum wear. The average roller end wear was 0.00006 inch. The inner race chipping shown in figure 195 was caused by impact from the damaged roller. The Armalon cage was in good condition except for the one pocket that contained the damaged roller. The bearing in the load ring location was in good condition as shown in figure 195, with slight roller end wear that averaged 0.0008 inch.

(C) An analysis of the bearing configuration tested in Build No. 12 indicated that the rollers opposite the applied load did not have an interference radial internal clearance when a 1700-lb radial load was applied with the test rig cold and not rotating. This condition could permit roller skewing or skidding during an acceleration to operating speed that could cause the failure noted. Analysis indicated that a further reduction in internal clearance would maintain a loaded condition on all the rollers under all operating conditions. This change was incorporated in Build No. 13 for the second endurance test.

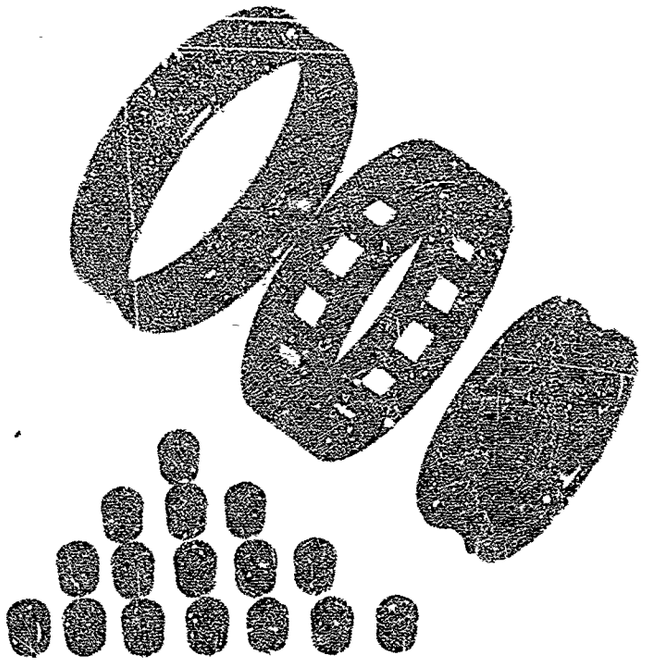


Figure 195. Post-Test No. 12 Condition of Reaction Bearing After 1 Hour and 32 Minutes at Design Speed — FE 71428

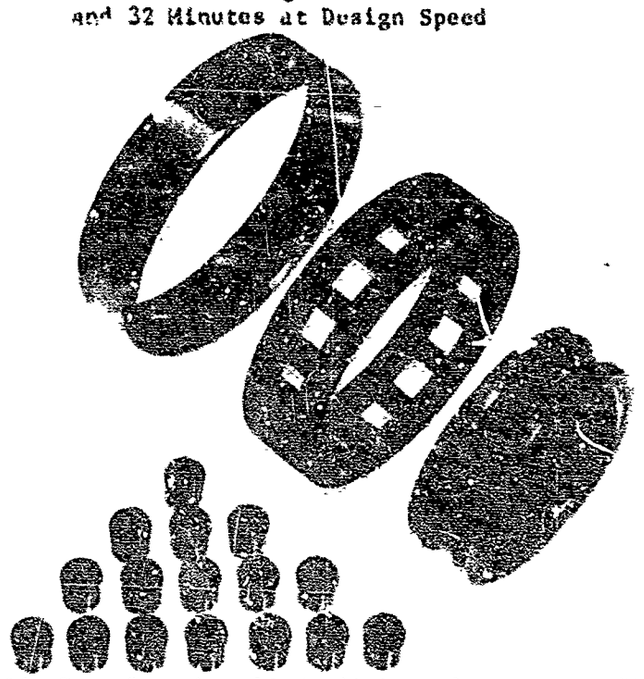


Figure 196. Post-Test No. 12 Condition of Load Bearing After 1 Hour and 32 Minutes at Design Speed — FE 71414

(C) Build No. 13 of the bearing rig incorporated the same configuration in both test bearing locations. This configuration consisted of AISI 440C material rollers and races an outer-race-piloted Armalon cage, 0.040-inch roller end clearance with the flanged inner race, and 0.0025-inch negative internal radial clearance at assembly between the rollers and races. The thickness of the outer race was approximately 0.155 inch on these bearings as compared to a thickness of approximately 0.227 inch on a standard outer race for a bearing of this size. This thinner outer race permits a larger negative internal radial clearance to be incorporated in the bearing without reducing the bearing fatigue life. This build of the rig accumulated 4 hours and 47 minutes and had two slave ball bearing failures on the turbine drive end of the rig. The first failure of the slave ball bearing occurred after 4 hours and 33 minutes of testing at design speed. This bearing was replaced without disassembly of the test roller bearings and the endurance testing was resumed. This test was terminated after 10 additional minutes of operation at design speed because a temperature rise on the slave bearing outer race indicated another failure of this bearing.

(U) The rig was disassembled to determine the cause of the slave bearing failures. A dynamic balance check indicated a high unbalance condition in the rotor assembly. The turbine retainer lug was worn such that indexing of the turbine was not properly maintained. This discrepancy and the inability to rebalance the rotor during the previous rebuild could cause the unbalance and produce the type of failures experienced on the slave ball bearing. The ball track on the races did not indicate a thrust load on the bearing. This thrust load on the ball bearing is desirable to provide capability for a radial load such as that generated by a dynamic unbalance condition of the rotor. Additional instrumentation was incorporated on the turbine drive unit to provide data for calculation of the axial thrust on the slave ball bearing.

(C) The test roller bearings were in good condition with an average of 0.0009-inch end wear and 0.0026-inch end wear on the roller with maximum wear in the load ring position. The reaction position bearing had an average roller end wear of 0.0003 inch and 0.0005-inch end wear on the roller with maximum end wear.

(U) The same two test bearings were incorporated in Build No. 14, which refurbished the turbine retainer lug, and included a new drive turbine, labyrinth seal, spacer and slave ball bearing. A dynamic balance of the turbine and shaft details was made prior to the final rotor assembly balance.

(C) Testing was resumed on 12 September 1967 and an additional 2 hours and 41 minutes were accumulated at design speed for a total of 7 hours and 26 minutes on both test bearings. The test was terminated because of an increase in rig power requirements. A teardown inspection revealed one damaged roller in the loaded bearing as shown in figure 197. This roller was worn on both ends, had a total of 0.055-inch roller end wear, and the roller diameter had worn 0.003 inch. This was the roller with maximum end wear on the previous test. The remaining rollers were in excellent condition with an average of 0.0011-inch end wear and 0.0027-inch

end wear on the roller with maximum end wear. The reaction bearing was in excellent condition with an average roller end wear of 0.0003 inch and 0.0006-inch end wear on the roller with maximum end wear.

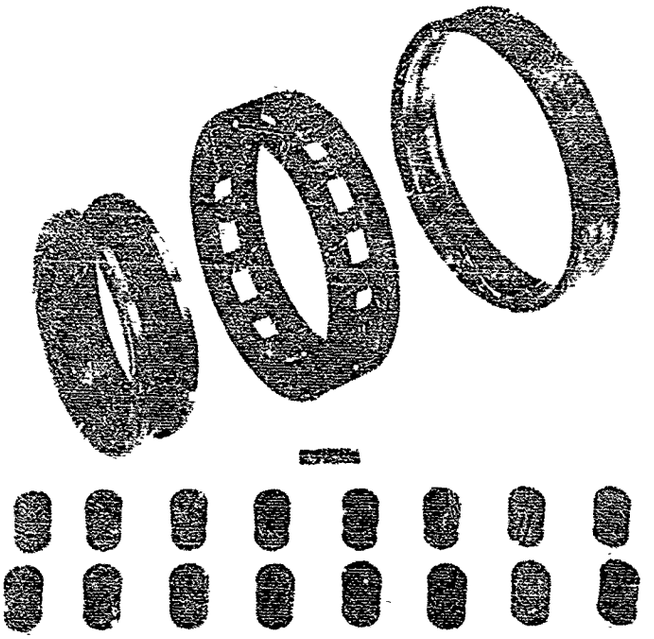


Figure 197. Post-Test No. 14 Condition of Load Bearing S/N S-2 After 7 Hours and 26 minutes at Design Speed FE 72598

(U) Pressure measurements taken during this test indicated a very low thrust load on the slave ball bearing. A valve was installed in the turbine discharge line to provide a method of adjusting the turbine back pressure and in turn the rotor thrust. This change and the improvements in the rotor dynamic balance appear to have solved the problem with the slave ball bearing that operated satisfactorily during the subsequent testing.

(C) Build No. 15 incorporated the same reaction bearing and a new bearing in the load ring position. The internal radial clearance of the new load bearing was reduced an additional 0.0002 inch for a total interference fit of 0.0027 inch at assembly in an attempt to prevent roller skewing in the unloaded zone of the bearing. One hour and 19 minutes of testing at design speed was accumulated on this configuration on 22 September 1967. This test was terminated when the power to drive the test rig increased. There was no indication of temperature rise on the bearing races or increase in the vibration level.

(C) Teardown inspection revealed one damaged roller in the load ring position which had been installed new for this build as shown in figure 198. The other rollers were in very good condition with no measurable end wear. The Armalon cage was in good condition except for the

one pocket that contained the failed roller. The reaction bearing that had accumulated a total of 8 hours and 45 minutes at design speed was still in excellent condition with an average roller end wear of 0.0004 inch and 0.0007-inch end wear on the roller with maximum end wear.

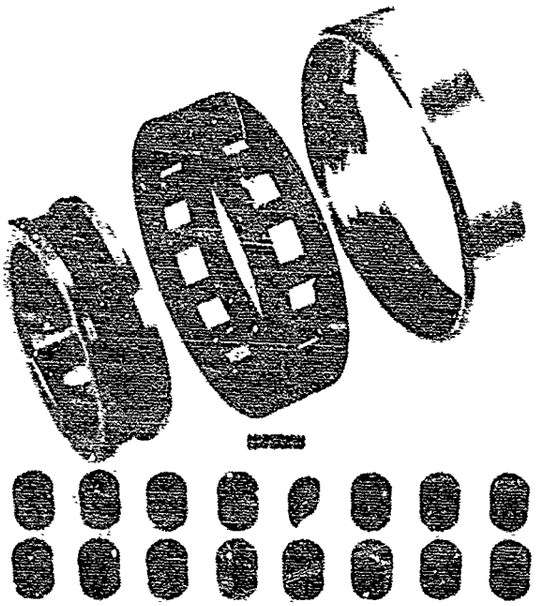


Figure 198. Post-Test No. 15 Condition of Load Bearing S/N T-2 After 1 Hour and 19 Minutes at Design Speed FE 72597

(C) On Build No. 16 the load bearing was replaced with a new bearing with a further reduction (0.0011 inch at assembly) in internal radial clearance for a total interference fit of 0.0038 inch to eliminate the unloaded zone of this bearing. It is calculated that a radial load of approximately 2300 lb would be required to deflect this bearing and create an unloaded zone with this 0.0038-inch interference fit. The same reaction bearing was used and an additional 3 hours and 50 minutes of testing was accumulated before the test was terminated because of an increase in rig power requirements and an increase in the outer race temperature on the load bearing.

(C) A teardown inspection revealed that the load bearing had a cracked outer race and one failed roller as shown in figures 199 and 200. The other rollers were in very good condition with no measureable roller end wear except for 0.00005-inch end wear on one roller. The cage was in good condition except for the one damaged roller pocket that contained the failed roller. The reaction bearing that had now accumulated 12 hours and 35 minutes at design speed was in excellent condition as shown in

figure 201. The average roller end wear was 0.00041 inch with 0.0007-inch wear on the roller with maximum end wear, which is the same wear recorded after 8 hours and 45 minutes of testing.

(U) An analysis of the cracked outer race indicates that the race failed as the result of a fatigue crack that started at the race outer diameter and progressed toward the inner diameter. This fatigue crack progressed approximately 75% of the thickness of the race before the race failed from tensile overstress. There is evidence that the outer race fretted in the load ring as shown in figure 202. Because this fretted area is almost directly under the applied radial load, it appears that the torque on the outer race retaining nut was not sufficient to retain the outer race relative to the load ring. The calculated combined stresses in the outer race that are generated by the rollers both in hoop and bending are not of sufficient magnitude to cause the failure. However, these stresses could be high enough to cause a failure if a large stress concentration was available as in the case of the fretting. Similar failures on oil lubricated bearings have been reported in literature.

(U) On future tests of this bearing configuration it is recommended that steps be taken to prevent or min mize this fretting. These steps could consist of increasing the torque on the race retaining nut and applying a coating to prevent the metal-to-metal contact between the race and load ring.

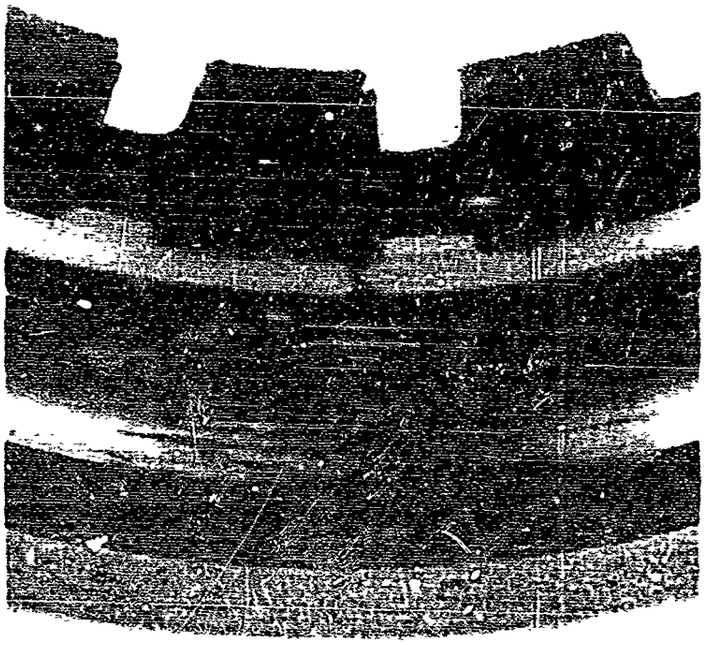


Figure 199. Post-Test No. 16 Condition of Outer Race from Load Bearing S/N U-2 Showing Cracked Outer Race After 3 Hours and 50 Minutes of Testing at 48,000 rpm FE 72502

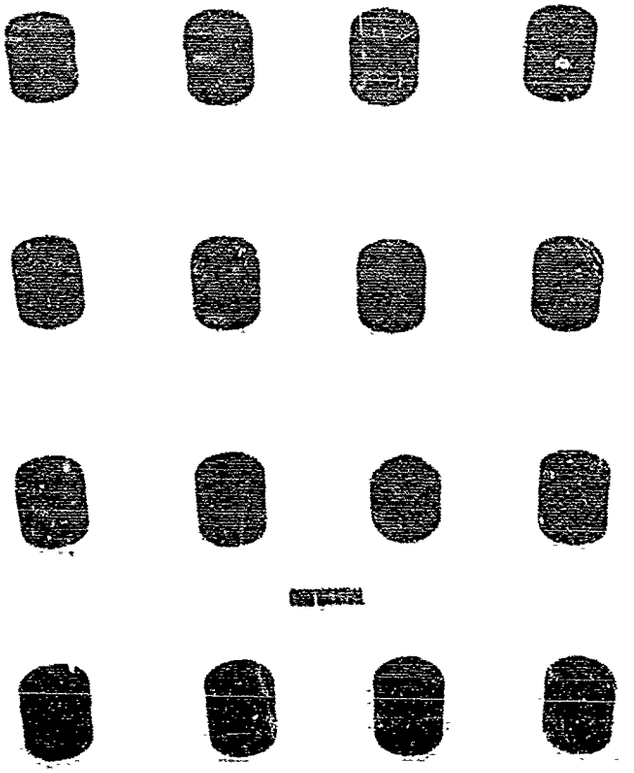


Figure 200. Post-Test No. 16 Condition of Rollers from Load Bearing S/N U-2 Showing One Failed Roller and the Good Condition of the Remaining Rollers After 3 Hours and 50 Minutes of Testing at 48,000 rpm

FR 72500

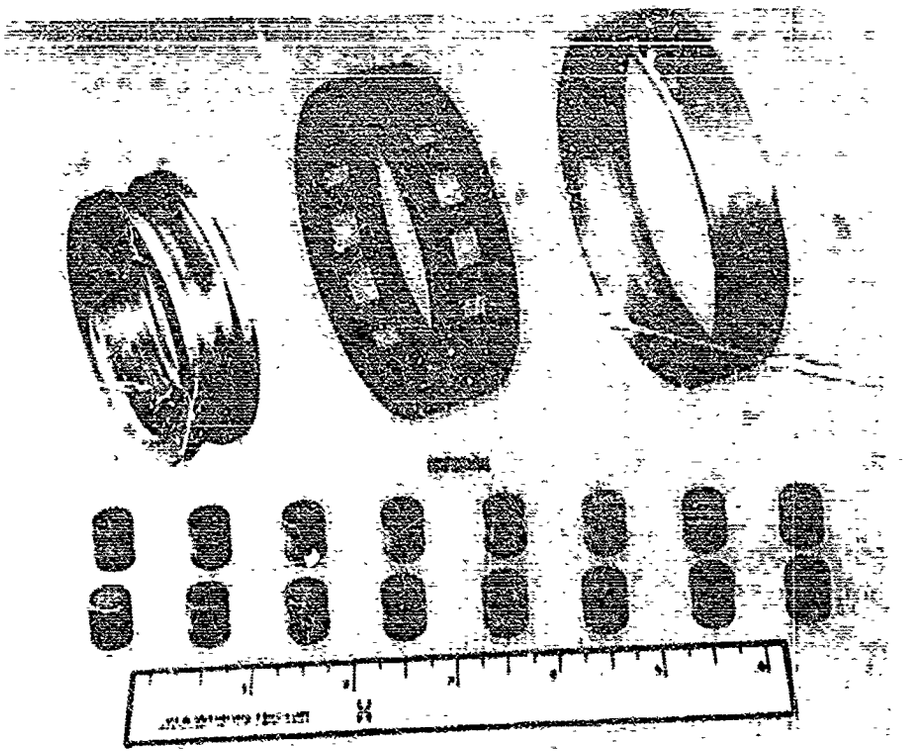


Figure 201. Post-Test No. 16 Condition of Bearing S/N S-1 Showing Good Condition After 12 Hours and 35 Minutes of Testing at 48,000 rpm FE 72577

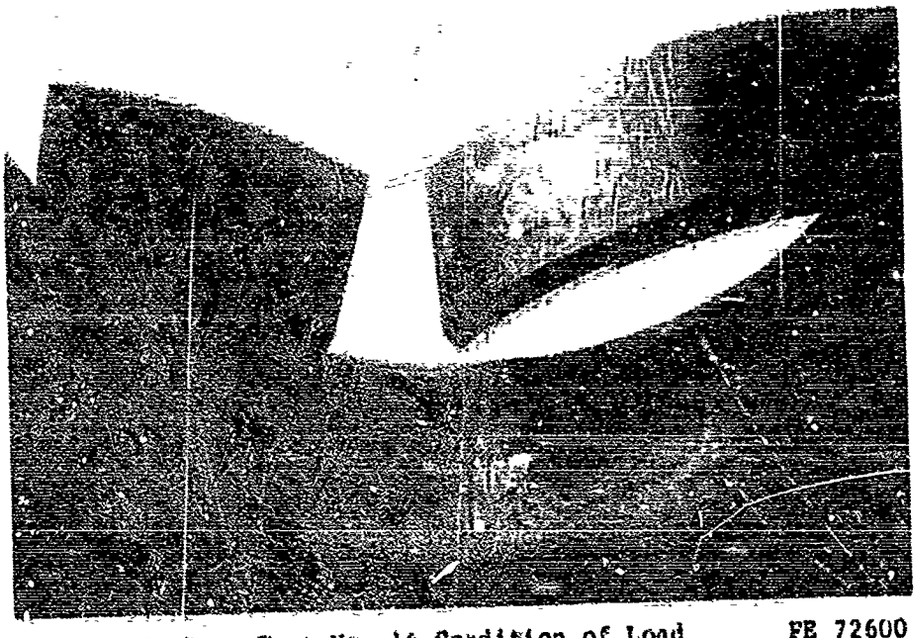


Figure 202. Post-Test No. 16 Condition of Load Ring and Outer Race OD Showing the Fretting Between These Two Parts in Area in Line With the Applied Radial Load FE 72600

B. TEST FACILITY AND PROCEDURES

1. Test Facility.

(U) Figure 203 is a schematic drawing of the test facility used for the bearing tests. This test facility is equipped with a vacuum jacketed supply dewar that furnishes the required liquid hydrogen to the test rig. The rig discharges into a vacuum jacketed recovery dewar that is vented to a burn stack as required to maintain the desired tank pressure. The total liquid hydrogen required for a test was reduced by recycling the liquid hydrogen from the recovery dewar back into the supply dewar following a test cycle.

(U) The facility is also equipped with a gaseous nitrogen supply for the pneumatic load piston and the drive turbine used to rotate the test rig. Gaseous nitrogen and gaseous hydrogen provisions are also available for purging the system and for tank pressurization, but these were not included on the schematic for clarity purposes. Instrumentation locations and types are also shown on figure 203.

2. Test Procedures

(C) Prior to a test, the rig and associated plumbing were purged with gaseous nitrogen for 40 minutes and then purged with gaseous hydrogen for 20 minutes. After the purge operation, liquid hydrogen was flowed through the rig by opening ROV 32, ROV 432, and closing ROV 332, ROV 331. The flow rate was set at 5-10 gpm for cooldown by controlling the supply dewar pressure and adjusting CV 330. The cooldown flow was continued until the temperature at rig discharge and bearing races reached 40°R.

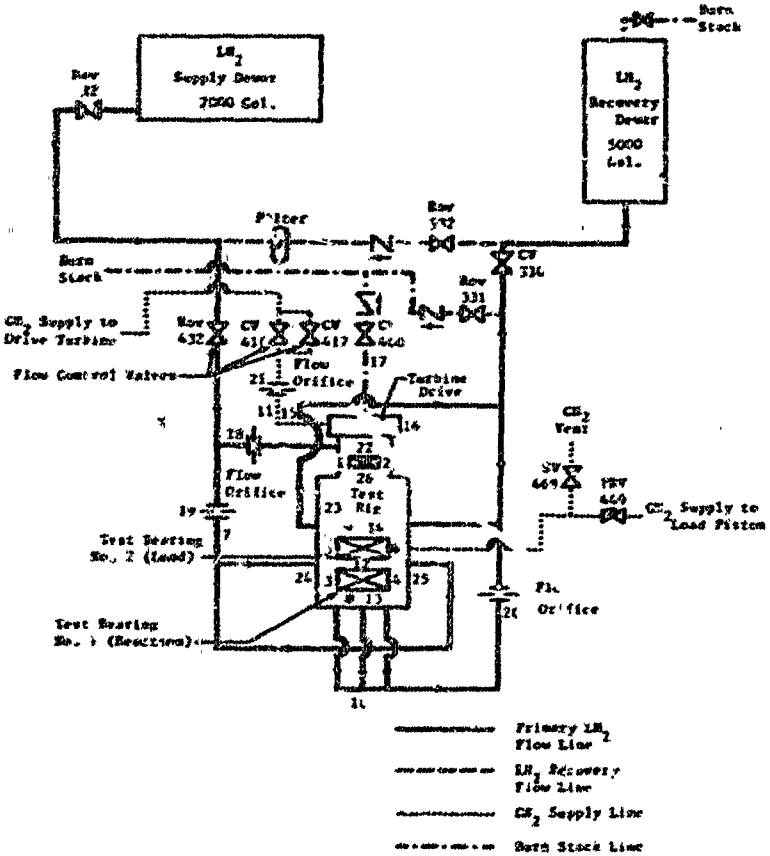
(U) After the cooldown period, the coolant flow rate was increased to 60-65 gpm for the test bearing supply cavity and 10-12 gpm for the slave bearing supply cavity by increasing the supply dewar pressure and opening CV 330. The radial load was applied to the test load bearing by closing SV 469 and adjusting PRV 449 to the required load piston pressure.

(C) For tests No. 1 through 12, the bearing load was applied in two increments. An initial (0 rpm) load of 500 lb was applied, the rig was accelerated to 10,000 rpm, and the final load of 1700 lb was applied while speed was held at 10,000 rpm. The rig was then accelerated to the test speed of 48,000 rpm. The 1700-lb load was not removed during rig shutdown. For test No. 13 through 16 the bearing load was applied and removed in four increments per the following schedule.

Speed, rpm	Load, lb
0	200
20,000	300
30,000	800
48,000	1700

Speed control of the rig was accomplished by adjusting CV 410 (coarse control) and CV 417 (fine control) to admit nitrogen gas to the turbine drive. The turbine discharge pressure was set at 70 psig by adjusting CV 400 to obtain the required axial load on the slave ball bearing. All speed, pressure, temperature, flow and vibration readouts were monitored during the run for indication of bearing failure. The test was terminated when a bearing failure was indicated or the required run conditions could not be maintained. All parameters not on continuous recording equipment (strip charts) were recorded manually every 2 minutes during the 15-minute screening tests and every 10 minutes during the longer duration endurance tests.

(U) The supply dewar provided enough coolant for rig cooldown and approximately one hour of continuous running before recycling of the liquid nitrogen. When the supply dewar was near depletion, the rig was shut down by closing CV 410 and CV 417 and adjusting PRV 449 in accordance with the speed-load schedule. The liquid hydrogen in the recovery dewar was recycled to the supply dewar through a filter by closing ROV 432 and CV 330, opening ROV 332, venting the supply dewar, and pressurizing the recovery dewar. After the liquid hydrogen was recovered in the supply dewar, cooldown flow was initiated and the run cycle was repeated.



INSTRUMENTATION

	Parameter	Type	Readout
1.	Temp, Slave Bearing Race	CC T/C, 0-10 MV	Potentiometer
2.	Temp, Slave Bearing Race	CC T/C, 0-10 MV	Potentiometer
3.	Temp, Test Bearing No. 1 Race	CC T/C, 0-10 MV	Strip Chart
4.	Temp, Test Bearing No. 1 Race	CC T/C, 0-10 MV	Strip Chart
5.	Temp, Test Bearing No. 2 Race	CC T/C, 0-10 MV	Strip Chart
6.	Temp, Test Bearing No. 2 Race	CC T/C, 0-10 MV	Strip Chart
7.	Temp, LH_2, Rig Inlet	Resistance Probe 37-70 K	Potentiometer
8.	Temp, LH_2, No. 1 Bearing Discharge	Resistance Probe 37-70 K	Strip Chart
9.	Temp, LH_2, No. 2 Bearing Discharge	Resistance Probe 37-70 K	Strip Chart
10.	Temp, Rig Discharge	CC T/C, 0-10 MV	Potentiometer
11.	Temp, GH_2 Turbine Supply	CA T/C, 0-10 MV	Potentiometer
12.	Pressure, Bearing Inlet	0-100 psig	Gage
13.	Pressure, No. 1 Bearing Discharge	0-100 psig	Gage
14.	Pressure, No. 2 Bearing Discharge	0-100 psig	Gage
15.	Pressure, Turbine Inlet	0-600 psig	Gage
16.	Pressure, Turbine Volute	0-600 psig	Gage
17.	Pressure, Turbine Discharge	0-200 psig	Gage
18.	Pressure, ΔP, Slave Bearing Flow	0-25 psig	Gage
19.	Pressure, ΔP, Test Bearing Flow	0-50 psig	Strip Chart
20.	Pressure, ΔP, Test Bearing Flow	0-25 psig	Strip Chart
21.	Pressure, ΔP, Turbine Drive Flow	0-100 psig	Gage
22.	Pressure, Seal Cavity	0-100 psig	Gage
23.	RPM	Magnetic	Reciprocal Counter, Strip Chart Tape Deck
24.	Vibration, Test Bearing, Vertical	Accelerometer	"G" Meter Tape Deck
25.	Vibration, Test Bearing, Horizontal	Accelerometer	"G" Meter Tape Deck
26.	Vibration, Slave Bearing, Vertical	Accelerometer	"G" Meter Tape Deck

Figure 203. B-13 Roller Bearing Test Facility

FD 23011

SUPPLEMENTARY

INFORMATION

AD-385910

DIVISION OF UNITED AIRCRAFT CORPORATION

OCT - 7 1968

In reply please refer to:
MFS:RPSto:Cont. Adm.

Mrs. Mary Racovich, FTMKR-3
Directorate of Materiel
Procurement Division
Edwards Air Force Base, California 93523

References: (a) PWA FP 67-11, 250K High Performance Reusable Oxygen/Hydrogen Rocket Engine, dated 21 August 1967.

(b) PWA FR-1810, Components Design Handbook, Advanced Development Program for a High Performance Oxygen/Hydrogen Rocket Engine, dated 30 June 1966.

(c) PWA FR-1911, Quarterly Report No. 1, Advanced Cryogenic Rocket Engine Program Staged - Combustion Concept, dated June 1966.

(d) PWA FR-1928, Quarterly Report No. 1, 250K Thrust Chamber Technology Program, dated 30 June 1966.

(e) PWA FR-2372, Final Report - Advanced Engine Design Study, Bell, (AEB), dated July 31, 1967.

(f) PWA FR-2397, Advanced Cryogenic Rocket Engine Program Staged - Combustion Concept - Final Report, dated December 1967.

Dear Mrs. Racovich:

The U. S. Patent Office has issued a Secrecy Order with a modifying "Security Requirements Permit" against United Aircraft Corporation's U. S. Patent Application No. 725,954, intitled "Dual Slot Swirler Injector Element." This Secrecy Order relates to a single throttleable injection element that provides a wide range of throttleability. You are advised that the referenced documents contain information relating to this concept.

A "Security Requirements Permit" limits disclosure of the subject matter involved to the security requirements of the Government contract which imposes the highest level of security classification thereon. The highest level of security classification on the subject matter of this application is "Confidential". Disclosure of the invention or any material information with respect thereto is prohibited except by written consent of the Commissioner of Patents or as authorized by the permit. By statute, violation of a Secrecy Order is punishable by a fine not to exceed $10,000 and/or imprisonment for not more than two years.

If this invention has been disclosed to others, the recipients of this letter are requested to notify them of the issuance of the Secrecy Order and "Security Requirements Permit" and of the penalties for violation.

Very truly yours,

UNITED AIRCRAFT CORPORATION
Pratt & Whitney Aircraft Division

M. F. Samples
Senior Contract Administrator
Florida Research and Development Center

cc: see attached.